Exploring the climate dependence of deep weathering in the Chilean Coastal Cordillera

Dissertation

zur Erlangung des Grades

eines Doktors der Naturwissenschaften (doctor rerum naturalium)

am Fachbereich Geowissenschaften

der Freien Universität Berlin

vorgelegt von

Laura Vivien Krone

Berlin 2024

Erstgutachter: Prof. Dr. Friedhelm von Blanckenburg
(Freie Universität Berlin)

Zweitgutachterin: Prof. Dr. Alida Perez-Fodich
(Universidad de Chile, Santiago)

Tag der Disputation: 07. Mai 2024

Eidesstaatliche Erklärung

Hiermit versichere ich, die vorliegende Dissertation selbstständig und ohne unerlaubte Hilfe angefertigt zu haben. Bei der Verfassung der Dissertation wurden keine anderen als die im Text aufgeführten Hilfsmittel verwendet. Beiträge von Koautor*innen zu publizierten und zur Publikation vorbereiteten Manuskripten sind im „Preface“ dieser Arbeit dargelegt. Ein Promotionsverfahren zu einem früheren Zeitpunkt an einer anderen Hochschule oder bei einem anderen Fachbereich wurde nicht beantragt.

Berlin, 01. Februar 2024

_____

Laura Krone

Danksagung – Acknowledgements

Mein größter Dank gilt meinem Doktorvater Prof. Dr. Friedhelm von Blanckenburg. Deine wissenschaftliche Kompetenz und fachliche Betreuung, aber vor allem Deine inspirierende wissenschaftliche Kreativität und Dein Enthusiasmus, waren mir immer eine große Hilfe und Motivation zugleich. Ich bin sehr dankbar für Deinen vertrauensvollen Umgang, Dein Verständnis und Deine Ermutigung, auch in schwierigeren Zeiten. Insbesondere im Schlussspurt der Anfertigung bin ich Dir sehr dankbar für all die Zeit, die Du in die schnellen Korrekturen investiert hat. Danke für die gemeinsame Zeit, Dein Vertrauen, die vielen Diskussionen, auch zu wissenschaftspolitischen Themen, und die hervorragende wissenschaftliche Ausbildung!

Ein besonderer Dank geht an Dr. Hella Wittmann-Oelze, die mich immer wissenschaftlich und persönlich unterstützt hat, ob bei Konferenzen oder im Laboralltag. Außerdem danke ich ihr für die vielen Anregungen zu dieser Arbeit, das Korrekturlesen einiger Kapitel, die Einführung und Hilfe im Labor sowie die Diskussionen über Resultate und das aufwändig ermittelte Detection Limit.

I would also like to thank the entire DeepEarthShape team, in particular, Dr. Kirstin Übernickel and Dr. Leandro Paulino for the organisation of the four drilling campaigns. I am also very grateful for the company of my two fellow doctoral students in all drilling campaigns: Dr. Ferdinand Hampl and Christopher Schwerdhelm. Vielen Dank an Euch beiden, vor allem für unseren Roadtrip in die Anden und die gute gemeinsame Zeit in Chile, Tübingen, Potsdam, Berlin und Obergurgl! The drilling campaigns would not have been possible without such a great and competent team: Dr. Kirstin Übernickel, Dr. Leandro Paulino, Dixie Rivera, Santiago Aldaz, Rahmantara Trichandi, Dr. Ferdinand Hampl, Christopher Schwerdhelm, Carolin Waldemer, Lucas Horstmann, Xiuling Wang, Diego Medina Caro, Axel Kitte, Oliver Burckhardt, Lea Sauter, Pablo - the stray dog, Dr. Casey Bryce, Dr. Lars Ganzert, Dr. María Chapela Lara, Dr. Rómulo Oses Pedraza, Dr. Klaus Bauer, Dr. Alida Perez-Fodich, Dr. Pablo Sanchez-Alfaro, Dr. Andrea Scheibe, Dr. habil. Nicole Stroncik, Prof. Dr. Dirk Wagner, Prof. Dr. Thomas Neumann, Prof. Dr. Marie Spohn, Prof. Dr. Charlotte Krawczyk, PD Dr. Ute Weckmann, Prof. Dr. Thomas Friedl, Prof. Dr. Andreas Kappler, Prof. Dr. Friedhelm von Blanckenburg, and the ARAOS drilling teams. I would like to express my gratitude to everyone for the great company during the drilling campaigns and valuable scientific discussions. I also want to thank the CONAF staff, the entire EarthShape family, and, in particular, all doctoral students in the project for the mutual support and the long-lasting memories.

I would like to express my great gratitude to my colleagues from Section 3.3 Geochemistry of the Earth's Surface. The scientific expertise, discussions, and input from such creative and intelligent people have always made working in this group exciting. I would like to thank everyone for the supportive, respectful, and cherishing atmosphere in the group. Für die organisatorische Hilfe und vielen lieben Worte möchte ich Cornelia Dettlaff danken. Außerdem gilt mein besonderer Dank Cathrin Schulz, Jutta Schlegel, Josefine Holtz und Sebastian Focke für die großartige Unterstützung und Hilfe in den verschiedenen Laboren. I would especially like to thank my two office mates Nestor Gaviria Lugo and Chenyu Wang. You always supported me, had kind words and time for scientific discussions and I am grateful to have you as friends during my entire time in the group and beyond! Special thanks go to my doctoral fellows, thanks for all the supportive words and memories! I especially thank Emma Lodes for proofreading the introduction of this thesis. I also thank Dr. habil. Nicole Stroncik for her support on sampling, core descriptions, and data acquisition; Dr. Patrick Frings for fruitful scientific discussions, his help with the ICP-OES and proof-reading parts of this thesis; Dr. David Uhlig for his advice and scientific discussions about the critical zone; and Dr. Kai Deng for scientific discussions about meteoric Be. I would like to thank all former and recent 3.3 members that I met during my time in the section for their scientific support but also for many fun Bier nach Vier's and Hot Pot dinners. It was great to be part of this wonderful group!

Zudem möchte ich einigen weiteren Personen und Sektionen am GFZ und an der Universität Köln danken: Thanks to Dr. Jeffrey Paulo H. Perez for they support and guidance with BET measurements and discussions about Beryllium. Ich danke außerdem der Sektion 4.2 Geomechanik und Wissenschaftliches Bohren für die Unterstützung bei den Porositäts- und Dichtemessungen. Auch der Sektion 3.1 Anorganische und Isotopengeochemie, insbesondere Sabine Tonn, möchte ich danken für die fachliche Betreuung und Nutzung des UV/VIS Spektrometers. Zudem möchte ich mich bei Dr. Stefan Heinze, Dr. Steven Binnie und Dr. Barbara Bock für die vielen Messungen am AMS und schnelle Bereitstellung meiner Ergebnisse bedanken. Außerdem gilt mein Dank Dr. Kirsten Elger und Simone Frenzel von GFZ Data Services, die für mich immer schnelle Hilfe und Lösungen für Medusa bereit hatten.

Besonders danke ich außerdem Prof. Dr. Anne Bernhardt für das mir entgegengebrachte Vertrauen und die gute Aufnahme in ihre Arbeitsgruppe. Ein herzlicher Dank gilt auch Dr. Ola Kwiecien und Dr. Sebastian Breitenbach, die insbesondere während der Pandemie mit dem PhD Sundowner einen Austausch mit anderen Doktorand*innen geschaffen haben, immer ein offenes Ohr für Probleme haben und mit kreativen Ideen zum Nachdenken anregen. Außerdem bin ich meinen Freund*innen aus der jDGGV sehr dankbar für ihre verständnisvollen Worte, Motivation und die wunderbaren letzten zwei Geo-Konferenzen in Köln und Berlin. Mein Dank gilt auch meinem guten Freund Nick, den ich durch Zufall bei fast jeder Konferenz getroffen habe und der immer eine geophysikalische Perspektive bereithält.

Außerdem danke ich meinem Cousin Adrian für das Korrekturlesen und wertvolle Anmerkungen.

Abschließend möchte ich noch einigen sehr wichtigen Leuten danken, die immer für mich da sind, aufmunternde Worte bereithalten und mich an das erinnern, was wichtig ist: Meinen besten Freundinnen Dörthe, Rilana und Silja, Fr. Singer, meinen Geschwistern Aaron und Jana, meinen Großeltern Silvia und Klaus, Norbert, meiner erweiterten Familie Barbara und Jan, Ilona und Wilhelm für die großartige Unterstützung in den ersten Jahren meines Studiums, und Petra und Thomas. Ganz besonderer Dank geht hier zuletzt an Yannick. Danke für deinen bedingungslosen Rückhalt und deine unermüdliche Unterstützung. Du bist mein unverwitterbarer Bedrock!

“We are each a patchwork quilt of those who have loved us, those who have believed in our futures, those who showed us empathy and kindness or told us the truth even when it wasn’t easy to hear. Those who told us we could do it when there was absolutely no proof of that.”
– Taylor Swift

Summary

Rock weathering is a fundamental geological process which primes fresh rock to form soil by chemical, physical and biological processes. However, despite the importance of weathering, little is known about deep weathering and its dependence on climatic factors.

In this thesis, deep weathering was investigated at four study sites in the Chilean Coastal Cordillera. For this purpose, drilling campaigns were performed to obtain undisturbed weathering profiles from fresh bedrock to soil. The sites are located in four climatically different settings (arid, semi-arid, mediterranean, humid), and thus permit investigation of the climate dependence of weathering depth and degree. The drill cores extend to a depth of ca. 90 m at the arid, semi-arid and mediterranean sites; at the humid site two ca. 50 m deep drill cores were obtained. In these five drill cores, deep weathering was analysed using geochemical methods, which include weathering parameters that indicate chemical mass loss. In addition, a new indicator for the retention of reactive elements in secondary weathering products is developed in this thesis using a sequential extraction procedure. Moreover, denudation rates (i.e. the rate of chemical and physical removal of material from a landscape) were determined with a method that has not yet been applied for this application: the isotope ratio ($^{10}Be_{met}/^{9}Be$) of meteoric beryllium-10 ($^{10}Be_{met}$), a cosmogenic radionuclide, and the stable isotope beryllium-9 (^{9}Be).

The weathering indicators define weathering profiles that differ in their depth and degree along the climate gradient. Deep weathering was identified at the semi-arid and mediterranean sites. At the arid site, no weathering was observed due to the lack of precipitation. Rather, alterations caused by hydrothermal overprinting were present. This drill core was therefore taken as a reference for hydrothermal alterations that have not been overprinted by meteoric processes. At the humid site, the two drill cores show weathering only in the upper 15 m of the weathering profile. Primary mineral dissolution and the concentration of extracted reactive elements like aluminium and iron that are incorporated into secondary weathering products are highest at this site. The comparison between the four sites therefore indicates that deep weathering is caused by a variety of different factors.

One main factor is the transport of water and gases (e.g. O_2) to depth, which occurs via diffusion through pore spaces or advection through open fractures in the rock. Primary mineral dissolution creates secondary porosity and introduces new transport pathways for water and gases. Tectonic fractures connect the Earth's surface with the subsurface and enable fast advective transport of water to depth. At the semi-arid site, deep weathering was observed to a depth of ca. 77 m – mainly located along tectonic fractures – but a continuous weathering gradient was found only in the upper 10 m. Therefore, the advective transport of water and gases through fractures facilitates deep weathering at this site. Tectonic fractures also enable deep weathering at the mediterranean site (to at least 75 m), where a continuous

weathering gradient was observed down to a depth of ca. 42 m. At the humid site, there are less open fractures and thus fewer direct transport pathways for water to depth are available. In addition, the high water availability results in intense precipitation of secondary weathering products that clog the porosity and prevent water flow to depth.

The pre-conditioning of bedrock can further promote deep weathering. Different processes can prime the minerals in bedrock: hydrothermal overprinting, post-magmatic cooling processes, mineral dissolution due to deep groundwater flow, and reactions with deeply diffused oxygen. These processes facilitate the mobilisation of elements from primary minerals. With sufficient water flow through the weathering profile, these mobilised and soluble elements can be removed and lost into the dissolved phase. The applied sequential extraction of reactive elements from secondary weathering products is a promising new indicator for this potential pre-conditioning of primary minerals.

Another factor is the time that is available for weathering processes. This time was determined by denudation rates derived from cosmogenic beryllium-10. Considering the time required for 10 m of the weathering profile to be removed, it takes ca. 900 000 years at the semi-arid location. Hence, deep weathering along fractures is possible even with the minute water flow at this site. At the mediterranean site, the denudation rate is significantly higher, such that the removal of 10 m takes ca. 200 000 years. Despite the shorter time available for weathering processes, a deep and continuous weathering gradient has formed due to the higher water flow in combination with tectonic fracturing, porosity formation and the pre-conditioning of primary minerals which was identified in this thesis by means of extractable elements. At the humid site, the removal of the upper 10 m of the weathering profile requires ca. 700 000 years. This time enables intensive near-surface weathering, as indicated by high primary mineral dissolution and precipitation of secondary phases, though the clogging of porosity prevents deep weathering.

The $^{10}Be_{met}/^{9}Be$ isotope system was developed for calculating denudation rates from surface samples and applied as an indicator for the time that is available for weathering processes and the depth-dependence of weathering. In this thesis, it was found that below an annual precipitation of 400 mm the depositional flux of cosmogenic $^{10}Be_{met}$ produced in the atmosphere cannot be determined with a global climate model, as these models overestimate precipitation and thus the deposition of the nuclide. Above this precipitation limit denudation rates determined from $^{10}Be_{met}$ /^{9}Be agree well with the more established method that uses *in situ* ^{10}Be produced in quartz. Furthermore, the depth distribution of both isotopes shows that reactive ^{9}Be can be used as an indicator of strong alteration, either by hydrothermal overprinting or intense primary mineral dissolution, even at depth. $^{10}Be_{met}$ only infiltrates into the upper meters of a weathering profile and adsorbs onto reactive weathering products, which prevents infiltration to depth.

This thesis presents new findings on deep weathering and tests new indicators to identify deep weathering. At two of four sites, the semi-arid and mediterranean, deep weathering was

identified in the drill cores. Tectonic fractures facilitate the transport of water and gases to depth at both sites. High water availability and the resulting high vegetation density enable intensive weathering, especially in the uppermost meters below the surface. As fractures connect the surface with the subsurface, microorganisms as well as water and gases can potentially migrate to depth. Moreover, the chemical extractions indicate that mineral nutrients and inorganic reaction partners for microbial growth are also present at great depth when minerals are pre-conditioned.

Zusammenfassung

Die Verwitterung von Gesteinen im Untergrund ist ein bedeutender geologischer Prozess, bei dem intaktes Gestein durch chemische, physikalische und biologische Prozesse umgewandelt wird, sodass daraus loses Substrat - der Boden - entstehen kann. Dennoch ist, trotz der großen Bedeutung von Verwitterung, wenig über tiefe Verwitterung und ihre Abhängigkeit von klimatischen Faktoren bekannt.

In der vorliegenden Doktorarbeit wurde tiefe Verwitterung an vier Standorten im chilenischen Küstengebirge untersucht. Dafür wurden Kernbohrungen durchgeführt, um ungestörte Verwitterungsprofile von unverwittertem Gestein bis zum Boden zu erhalten. Die Standorte befinden sich in vier klimatisch unterschiedlichen Bereichen (arid, semi-arid, mediterran, humid) und ermöglichen dadurch die Abhängigkeit der Verwitterungstiefe und der Art der Verwitterung von Niederschlag und Vegetation zu untersuchen. Die Bohrkerne reichen bis in ca. 90 m Tiefe am ariden, semi-ariden und mediterranen Standort; am humiden Standort wurden zwei ca. 50 m tiefe Bohrkerne gewonnen. In den fünf Bohrkernen wurde tiefe Verwitterung mit verschiedenen geochemischen Methoden untersucht. Dazu gehören unter anderem Verwitterungsparameter, die chemischen Massenverlust anzeigen. Zudem wurde in dieser Doktorarbeit ein Indikator für die Retention reaktiver Elemente in sekundären Verwitterungsprodukten aus einer sequenziellen Extraktion neu entwickelt. Außerdem wurden an Bodenprofilen Denudationsraten (chemische und physikalische Abtragung der Erdoberfläche) mit einer für diese Anwendung noch unerprobten Methode, dem Isotopenverhältnis ($^{10}Be_{met}/^{9}Be$) von meteorischem Beryllium-10 ($^{10}Be_{met}$), einem kosmogenen Radionuklid, und dem stabilen Isotop Beryllium-9 (^{9}Be) berechnet.

Die angewendeten Verwitterungsindikatoren zeigen für die vier Standorte unterschiedlich ausgeprägte Verwitterungsprofile. Tiefe Verwitterung wurde am semi-ariden und mediterranen Standort identifiziert. Am ariden Standort gibt es, bedingt durch das Fehlen von Niederschlag, keine eindeutigen Verwitterungsanzeichen; es gibt jedoch Alterationen, die durch hydrothermale Überprägung entstanden sind. Daher wurde dieser Bohrkern als Referenz für hydrothermale Alterationen, die nicht durch meteorische Einflüsse überprägt wurden, genutzt. Am humiden Standort zeigen in beiden Bohrkernen die Indikatoren

Verwitterung nur in den oberen 15 m des Profils an. An diesem Standort ist die Primärmineralauflösung am intensivsten und hohe Konzentrationen der extrahierbaren reaktiven Elemente Aluminium und Eisen zeigen die Bildung sekundärer Verwitterungsprodukte. Der Vergleich zwischen den vier Standorten ergab, dass die tiefe Verwitterung durch eine ganze Reihe unterschiedlicher Faktoren verursacht wird.

Ein solcher Faktor ist der Transport von Wasser und Gasen (z.B. O_2) in die Tiefe, der diffusiv durch den Porenraum oder advektiv durch offene Frakturen im Gestein vorkommt. Durch die Primärmineralauflösung erhöht sich die Porosität, wodurch sich neue Transportwege für Wasser und Gase erschließen. Tektonische Frakturen verbinden die Erdoberfläche mit dem Untergrund und ermöglichen schnellen advektiven Transport von Wasser in die Tiefe. Am semi-ariden Standort wurde tiefe Verwitterung bis in ca. 77 m Tiefe entlang tektonischer Frakturen beobachtet; ein kontinuierlicher Verwitterungsgradient fand sich jedoch nur in den oberen 10 m. Daraus folgt, dass der direkte Transport von Wasser und Gasen durch Frakturen an diesem Standort tiefe Verwitterung auslöst. Auch am mediterranen Standort ermöglichen tektonische Frakturen tiefe Verwitterung (bis mindestens 75 m), wobei hier ein kontinuierlicher Verwitterungsgradient bis in ca. 42 m Tiefe beobachtet wurde. Am humiden Standort gibt es nur wenige offene Frakturen, die Wasser in die Tiefe transportieren können. Zudem verschließt die intensive Ausfällung von Sekundärprodukten den Porenraum, sodass Wasserfluss in die Tiefe eingeschränkt und Verwitterung auf die obersten 15 m begrenzt ist.

Weiterhin kann tiefe Verwitterung erleichtert werden, wenn das Gestein in der Tiefe durch eine Reihe von Prozessen vorgeprägt wurde. Diese Prozesse umfassen hydrothermale Überprägung, post-magmatische Abkühlungsprozesse, Lösungsprozesse durch tiefen Grundwasserfluss und Reaktionen mit in die Tiefe diffundiertem Sauerstoff. Sie schaffen die Voraussetzung für die Mobilisierung von Elementen aus den Primärmineralen. Sobald der Wasserfluss im Verwitterungsprofil hoch genug ist, können diese löslichen Elemente abtransportiert werden. Die in dieser Doktorarbeit benutzte sequenzielle Extraktion von Elementen aus der reaktiven Phase ist ein vielversprechender neuer Indikator für diese potenzielle Vorprägung.

Ein weiterer Faktor ist die verfügbare Zeit, in der Verwitterungsprozesse stattfinden können. Diese Zeit wurde durch Denudationsraten aus kosmogenem Beryllium-10 bestimmt. Nimmt man für diese Überlegung die Zeit, in der als Beispiel 10 m des Verwitterungsprofils abgetragen werden, dauert dies am semi-ariden Standort ca. 900 000 Jahre. Somit ist selbst bei minimalem Wasserfluss tiefe Verwitterung entlang von Frakturen möglich. Am mediterranen Standort ist die Denudationsrate deutlich höher und die Abtragung von 10 m dauert nur ca. 200 000 Jahre. Trotz der für Verwitterungsprozesse verfügbaren kürzeren Zeit hat sich ein tiefer kontinuierlicher Verwitterungsgradient in den obersten 42 m ausgebildet. Gründe dafür sind der höhere Wasserfluss als am semi-ariden Standort in Kombination mit tektonischen Frakturen, Porositätsbildung und die in dieser Doktorarbeit mittels extrahierbarer Elemente identifizierte Vorprägung der Primärminerale. Am humiden Standort

dauert es ca. 700 000 Jahre, bis 10 m des Verwitterungsprofils abgetragen werden. Dadurch ist intensive oberflächennahe Verwitterung mit hoher Primärmineralauflösung und Ausfällung von Sekundärphasen möglich, das Verschließen des Porenraums verhindert jedoch tiefe Verwitterung.

Als Indikator für die Geschwindigkeit der Abtragungsprozesse und die Tiefenabhängigkeit der Verwitterung wurde das Isotopensystem $^{10}Be_{met}/^{9}Be$ für die Berechnung von Denudationsraten aus Oberflächenproben weiterentwickelt. Dabei wurde festgestellt, dass bei einem jährlichen Niederschlag von weniger als 400 mm die Depositionsrate des in der Atmosphäre produzierten kosmogenen $^{10}Be_{met}$ nicht mit einem globalen Klimamodell bestimmt werden kann, da diese Modelle Niederschläge und somit die Deposition des Nuklids überschätzen. Der Vergleich von Denudationsraten aus $^{10}Be_{met}/^{9}Be$ mit Raten, die mit der etablierten Methode des *in situ* produzierten ^{10}Be in Quarz bestimmt wurden, zeigt gute Übereinstimmung oberhalb dieser Niederschlagsgrenze. Weiterhin hat die Untersuchung der Tiefenverteilung beider Isotope ergeben, dass ^{9}Be ein Indikator für starke Alterationen, entweder durch hydrothermale Überprägung oder intensive Primärmineralauflösung, ist. $^{10}Be_{met}$ infiltriert hingegen nur in die oberen Meter eines Verwitterungsprofils und adsorbiert dabei an reaktive Verwitterungsprodukte, wodurch die tiefe Infiltration verhindert wird.

In der vorliegenden Doktorarbeit werden neue Erkenntnisse zu tiefer Verwitterung vorgestellt und neue Indikatoren zu deren Erforschung getestet. Tiefe Verwitterung wurde an zwei von vier Standorten identifiziert. An beiden Standorten ermöglichen tektonische Frakturen den Transport von Wasser und Gasen in die Tiefe. Hohe Wasserverfügbarkeit und die damit verbundene hohe Vegetationsdichte ermöglichen intensive Verwitterung vor allem in den obersten Metern unter der Oberfläche. Da Frakturen die Oberfläche mit dem Untergrund verbinden, können neben Wasser potenziell auch Mikroorganismen in die Tiefe gelangen. Die durchgeführten chemischen Extraktionen zeigen zudem, dass mineralische Nährstoffe und anorganische Reaktionspartner für das Wachstum von Mikroorganismen auch in großer Tiefe in vorgeprägten Mineralen vorliegen.

Preface

In this dissertation, I present in total four chapters whereof one is an introductory chapter and the further three chapters comprise scientific studies. Below, I briefly summarise each chapter, indicate the contribution of involved collaborators and co-authors, and provide information on the submission status.

Chapter 1 is the introduction chapter. In this chapter, I present a general overview of the factors that determine the weathering depth and weathering processes that advance the weathering front to depth. I also describe surface-subsurface interactions of weathering and erosion and weathering and biota. Furthermore, I present the research questions that are answered in this thesis and introduce the research project and study sites. Finally, I describe the used methods and provide a brief overview of the general concepts of the cosmogenic radionuclide meteoric Beryllium-10.

In **Chapter 2**, I present a geochemical and petrophysical description of drill core to 87 m depth from the study site Santa Gracia in semi-arid climate. In this study, various methods in combination with the analysis of tectonic fractures and the tectonic background of this region were applied to detect deep weathering in an eroding setting with minimal fluid flow. A continuous weathering gradient was only observed in the uppermost 10 m of the weathering profile. Deep weathering and multiple weathering fronts to a depth of ca. 77 m were observed along fractures and fracture zones. Furthermore, the hydrothermal overprint of the bedrock primes the minerals for weathering. The determined denudation rates derived by *in situ* ^{10}Be indicate a slow turn-over of the entire weathering profile (to a depth of 77 m), hence deep weathering along fractures is possible even with minute fluid flow.
F. J. Hampl provided the mineralogical composition and thin section photos, and C. Schwerdhelm and C. Bryce conducted the oxide extractions. L. Ganzert, A. Kitte and D. Wagner carried out the contamination control during the drilling campaign. F. von Blanckenburg, K. Übernickel and R. Oses-Pedraza organised and managed the drilling campaign, S. Aldaz helped to design the drilling campaign. A. Dielforder contributed the tectonic background for this study and J. P. H. Perez helped to perform the specific surface area analyses. P. Sanchez-Alfaro provided the characterisation of hydrothermal alteration of the samples. U. Weckmann contributed the well-logging data. The bulk geochemical analyses were conducted in a commercial laboratory (Activation Laboratories Ltd., Canada). I performed porosity and density measurements with the help of student assistants, calculated and interpreted the weathering parameters and wrote the chapter with inputs mainly from F. von Blanckenburg but also from all other co-authors. This chapter is published in *Scientific Reports*.

Chapter 3 outlines a study about the application of meteoric $^{10}Be/^{9}Be$ for the determination of denudation rates. For this study, I compared denudation rates determined with *in situ* ^{10}Be to rates determined with meteoric $^{10}Be/^{9}Be$ and ^{10}Be depositional flux derived from a global circulation model (ECHAM5-HAM). The meteoric $^{10}Be/^{9}Be$-derived denudation rates are in good agreement and thus reliable for the mediterranean and humid study sites but disagree at the arid and semi-arid sites. Calculations of depositional flux using meteoric ^{10}Be soil concentrations and inventories in combination with *in situ* ^{10}Be-derived denudation rates reveal a precipitation limit of ~400 mm yr^{-1} for the use of model-derived depositional fluxes. Below this precipitation limit, the depositional flux is overestimated due to the large spatial resolution of the model that does not cover small regional climatic variations, in particular in dry regions.
For this chapter, I performed *in situ* and meteoric ^{10}Be and ^{9}Be analyses, calculated denudation rates and depositional flux, interpreted the data and wrote the manuscript. H. Wittmann supported the laboratory procedure, analyses, and interpretation. F. von Blanckenburg helped with the interpretation of the results. Both co-authors contributed to the design of the manuscript and provided input. This chapter and the related data supplement (Chapter 6.2) is ready for submission.

In **Chapter 4,** I investigate deep weathering at all study sites by means of the reactive phase formed by secondary weathering products. Further, I test meteoric ^{10}Be as a deep infiltration proxy and explore the release of reactive ^{9}Be at depth as both isotopes are incorporated into the reactive phase and trace it indirectly. I identified three zones in the weathering profiles using the concentrations of the reactive phase that indicate the predominant weathering process. Moreover, I observed that meteoric ^{10}Be is readily adsorbed to secondary weathering products with high surface area and is thus not infiltrating to great depth. Reactive ^{9}Be concentrations at depth are increased when hydrothermal overprinting mobilised ^{9}Be from primary minerals. At the surface, reactive ^{9}Be concentrations indicate intense primary mineral dissolution, in particular plagioclase. The resulting isotope ratio $^{10}Be(meteoric)/^{9}Be$ at depth is zero. Finally, I summarise the factors that enable deep weathering, which are tectonic fractures, formation of secondary porosity, water availability, and time for weathering processes determined by denudation rates.
I conducted sequential extractions and measurements of extractable major elements, ^{9}Be and ^{10}Be. Further, I interpreted the data and wrote the manuscript. Roberts Blukis provided mineralogy data. Bulk element data was measured in a commercial laboratory (ALS Laboratory, UK). H. Wittmann helped with the laboratory procedure, in particular for meteoric ^{10}Be, and the data analyses. F. von Blanckenburg helped to design the manuscript and the interpretation. This chapter is under preparation for submission.

Table of contents

1 Introduction

Weathering is a fundamental geological process that affects both the subsurface and Earth's surface. The process of weathering comprises the chemical, physical and biological dissolution and disintegration of primary minerals and thus primes hard rock to form soft soil. In doing so, weathering consumes carbon dioxide (CO_2) from the atmosphere and thus modulates Earth's global climate over geologic time scales (Walker et al., 1981; Berner and Berner, 1997; Gaillardet et al., 1999). Furthermore, weathering releases mineral nutrients that are essential for the functioning of ecosystems, mainly by nourishing vegetation and microorganisms (Vitousek and Farrington, 1997; Chapin et al., 2002). Eventually, through erosion and redistribution of weathered, disintegrated substrate, the shape of Earth's surface is significantly influenced (Stallard, 1995; Lebedeva and Brantley, 2013). Moreover, weathering feeds global element cycles by transporting released mineral nutrients in the dissolved load of groundwater and rivers into the ocean (Gaillardet et al., 1999). The foundation of all these processes is the onset of weathering at depth. Hence it is fundamental to investigate the depth of weathering and the processes that advance weathering at depth.

Terminology

soil	mobile layer consisting of loose organic and inorganic material
saprolite	disaggregated chemically weathered rock, original texture is preserved
saprock	weathered rock, weathering mainly located at fractures
regolith	entire weathered material from soil to saprock
bedrock	unweathered rock
weathering front	interface between unweathered and weathered rock
reaction front	onset of a weathering reaction
weathering degree	Intensity of weathering processes in terms of mass loss and secondary phase formation
weathering rate	rate of chemical mass removal
erosion rate	rate of physical mass removal from the surface
denudation rate	sum of weathering and erosion rate
weathering advance rate	rate of weathering front propagation at depth

1.1 How deep is the weathering zone?

The maximum depth of weathering, defined as the weathering front, is the lower boundary of the critical zone. The critical zone spans from the weathering front at depth to the upper boundary of the vegetation canopy and is thus the zone where chemical, physical, geological and biological processes interact to enable life on Earth's surface (e.g. Brantley et al., 2007). The subsurface part of the critical zone consists of weathered rock (also called "saprock"), saprolite, and soil (jointly called "regolith") that together form the weathering zone (e.g. Chorover et al., 2007). Due to the inaccessible nature of the weathering front at the base of the critical zone, the determination of its depth is almost impossible from the surface or outcrops. Furthermore, the weathering zone thickness and thus the weathering front depth cannot be easily predicted as it depends on a multitude of factors (Figure 1-1): lithology (e.g. Bazilevskaya et al., 2013), tectonic preconditioning (e.g. Molnar et al., 2007), hydrothermal overprint (e.g. Hampl et al., 2022), erosion and weathering rate (e.g. Lebedeva and Brantley, 2013) and the resulting residence time of a weathering profile (e.g. Porder et al., 2007), water flow and temperature (e.g. Norton et al., 2014; Anderson et al., 2019; Wood et al., 2023), available weathering reactants (carbonic and sulfuric acid, organic complexing agents, oxygen (O_2), e.g. Fletcher et al., 2006; Kim et al., 2017), and the abundance and activity of vegetation and microorganisms (e.g. Chorover et al., 2007; Napieralski et al., 2019; Finlay et al., 2020; Maher and von Blanckenburg, 2023). The depth of weathering is a result of the complex interplay of these factors that also influence each other by numerous feedback mechanisms. Hence the effect of a single factor on the entire weathering front is difficult to determine (e.g. Anderson et al., 2002; Ghasera and Rashid, 2024). In the next paragraphs, I describe the individual influence on weathering depth of these factors.

1.1.1 Bedrock preconditioning

The geologic preconditioning of the bedrock predefines some relevant conditions influencing the weathering depth. Fractures resulting from tectonic preconditioning of the bedrock (Molnar et al., 2007; Lebedeva and Brantley, 2017) or from changes in topographic stress field (Slim et al., 2015; St. Clair et al., 2015), climate-dependent subcritical fracturing (Eppes and Keanini, 2017) or iron oxidation taking place during the weathering process itself (Bazilevskaya et al., 2015). Fractures provide preferential pathways for advective transport of weathering reactants to depth. These fractures connect the surface with the subsurface by introducing fluids and gases to depth, whereby fracture surfaces also serve as sites of mineral dissolution and secondary solid precipitation. Further, the density of tectonic fractures is an important control on gas chemistry in deep regolith (Kim et al., 2017). Another preconditioning of the bedrock is hydrothermal overprinting that alters the rock regarding mineralogy and porosity (Savage et al., 1987). In particular, hydrothermal overprinting can increase or decrease the initial bedrock porosity by dissolution and reprecipitation processes

and thus influences subsurface water flow (Schaefer et al., 2023, and references therein). Hydrothermally formed or replaced minerals might have different weatherability than their precursors and hence have strong effects on weathering (e.g. Kajdas et al., 2017; Hampl et al., 2022). Moreover, an essential prerequisite for weathering depth is lithology, including mineral composition, grain size, initial porosity, and permeability. Different minerals dissolve at different kinetic rates dependent on the strength of metal ion bonds in the mineral structure (White and Buss, 2014). The mineral grain size in different rock types affects the effective weathering rate of minerals with faster weathering of fine-grained material (White and Brantley, 2003; Heckman and Rasmussen, 2011). The initial porosity of the bedrock supplies pathways for the diffusion of weathering reactants to depth but also ensures further transport within the rock (e.g. Graham et al., 2010; Navarre-Sitchler et al., 2015). Thus porosity sets the permeability of the bedrock and determines the resulting fluid-rock interactions (e.g. Brantley et al., 2017b). The described geological prerequisites and processes interact through feedback mechanisms involving weathering reactants that influence the depth of weathering.

1.1.2 Surface processes, climate, water availability, and biota

Besides geologic preconditioning, the depth of weathering is also affected by erosion, topography, climate, and the availability of weathering reactants (e.g. Anderson et al., 2002; Lebedeva et al., 2010; Brantley et al., 2017b; Riebe et al., 2017; Lebedeva and Brantley, 2020; Brantley and Lebedeva, 2021; von Blanckenburg et al., 2021). The erosion rate determines the residence time of a weathering profile (the time over which a weathering profile is completely turned over by erosion) and thus influences the depth up to which weathering proceeds. In non-eroding landscapes, weathering creates thick zones that are fully depleted with respect to specific elements (e.g. laterites; Tardy and Roquin, 1992; Campodonico et al., 2019). In eroding landscapes, a steady state with constant weathering depth can be attained when the erosion rate at the surface equals the weathering front advance rate at depth (Lebedeva et al., 2010; Ackerer et al., 2016; Schoonejans et al., 2016; Lebedeva and Brantley, 2020). In addition, erosion shapes the topography, and thus influences water flow to depth; therefore, erosion, topography and weathering depth are interconnected (Riebe et al., 2017; Pedrazas et al., 2021). Various authors have observed thinner weathering zones under topographic heights (Heimsath et al., 1997; Anderson et al., 2002). However, Rempe and Dietrich (2014) propose that the weathering zone is thickest below the ridge and thins downslope where bedrock is exposed in channels. In any case, topographic position influences the depth of weathering (e.g. Anderson et al., 2002; Rempe and Dietrich, 2014; Riebe et al., 2017; Uecker et al., 2023).

Climate, the resulting water availability, and in particular, subsurface fluid flow are major controls on weathering front depth (e.g. Dixon et al., 2009; Maher, 2010, 2011; Norton et al., 2014; Brantley et al., 2017; Anderson et al., 2019; Gaillardet et al., 2019; Hayes et al., 2020; Riebe et al., 2021). The controls by climatic conditions are not unambiguous, however. For

example in humid climate, the weathering front in felsic lithology is typically observed to be located between 10 – 20 m (e.g. Behrens et al., 2015; Brantley et al., 2017; Hayes et al., 2020) while studies in arid to semi-arid regions suggest a deeper weathering front between 30 – 70 m (e.g. Stierman and Healy, 1985; Vázquez et al., 2016). Goodfellow and Hilley (2022) suggest that the weathering zone thickness in granitic lithology increases with fluid flow rates. Importantly, fluid flow in unweathered bedrock is a prerequisite for the dissolution of soluble primary minerals and secondary weathering products, and the removal of the dissolved constituents thus liberated. In the process, secondary porosity is created (White, 2002). In non-eroding settings, high water flow rates enhance primary mineral dissolution, and thus the weathering front is found at a greater depth compared to settings with low water flow rates (Maher, 2010). However, heterogeneous permeability in the subsurface might lead to preferential flow that creates weathering fronts in zones with high permeability (Pandey and Rajaram, 2016). Fluid flow generally occurs by vertical infiltration from the surface to depth followed by lateral transport as groundwater flow (Brantley et al., 2017b). Rempe and Dietrich (2014) suggest that the depth of the saturated zone, the groundwater level, coincides with the weathering front depth, whereas Anderson *et al.* (2019) propose that groundwater recharge rates are higher when the weathering front is located at the base of the groundwater system. However, Wang *et al.* (2021) observed that the weathering front is located above the groundwater table at the ridge but it is deeper than the groundwater table in the valley (in granitic lithology with semi-arid climate, Wyoming, USA). In another study, Wan *et al.* (2019) found that the deepest extent of seasonally fluctuating groundwater level defines the thickness of the weathering zone, and thus the depth of the weathering front, in a shale catchment in the Upper Colorado River Basin (USA). The groundwater flow and its extent thus strongly affect the weathering depth, though it remains difficult to identify the weathering depth only by groundwater level.

Vegetation has no immediate influence on the depth of the weathering front, yet the thickness of the regolith defines the nutrient inventory for plant uptake and microorganisms (Uhlig et al., 2020; Maher and von Blanckenburg, 2023). Nevertheless, in deep subsurface environments microorganisms induce biogeochemical processes that might directly influence the depth of weathering by inducing weathering (Wild et al., 2022). For example, Fe-reducing bacteria convert solid ferric (Fe(III)) oxyhydroxides to liquid phase ferrous iron (Fe(II)) using organic carbon as an electron donor, sulfide-reducing bacteria reduce sulfate, and microorganisms use hydrogen (H) as source to convert CO_2 to organic material (e.g. Banwart et al., 1994; Pedersen, 1997, and references therein).

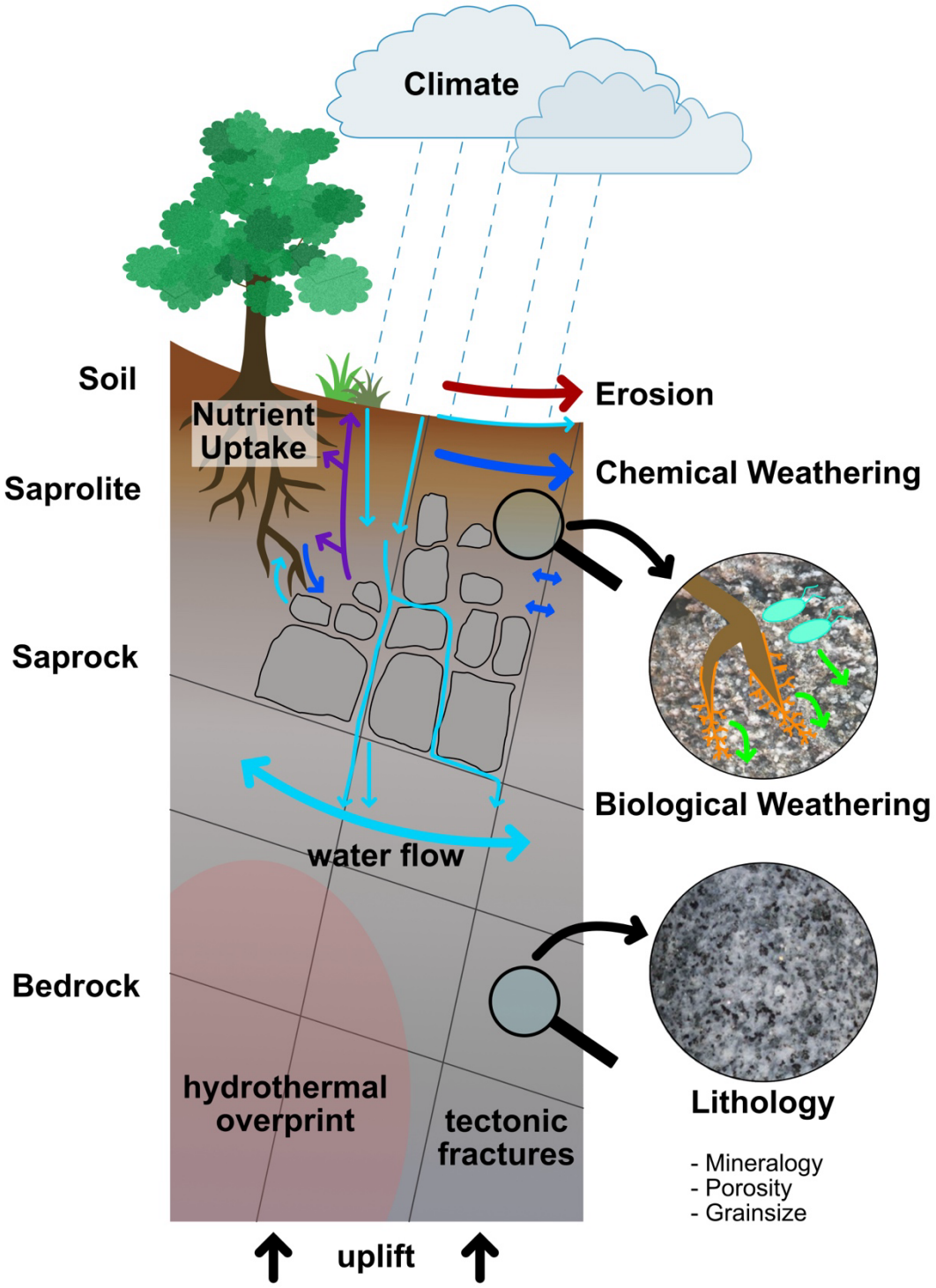

Figure 1-1. Conceptual weathering profile with parameters that influence weathering zone thickness and weathering front depth. Dark blue arrows indicate chemical weathering (biological-induced weathering, chemical weathering along fractures); light blue arrows indicate vertical water flow as surface infiltration through porosity and along fractures, surface flow, water uptake by roots, and lateral water flow at depth indicate groundwater flow; purple arrows indicate nutrient uptake; green arrows indicate biological weathering by root hyphae (orange) and microorganisms.

1.2 Which processes take place in the weathering zone?

In granitoid lithology, the main minerals relevant for weathering are feldspars and micas (biotite), but also amphiboles and trace calcite if these minerals are abundant. The following overview on weathering processes therefore focuses on these minerals, although some other minerals and elements play an essential role in weathering and in the related element cycles (sulphide weathering (e.g. pyrite) and release of sulphur: e.g. Jin et al., 2011; Brantley et al., 2017; Bufe et al., 2021).

1.2.1 Formation of secondary porosity

The formation of secondary porosity is an integral process for weathering at depth as it advances the weathering front, creates new pathways for weathering reactants and makes fresh mineral surfaces accessible for these reactants. One of the first weathering processes at depth that creates secondary porosity is the oxidation of Fe(II) to Fe(III) in Fe-bearing silicates like biotite or amphibole. The oxidation leads to a volume increase that induces micro-fractures within the minerals (e.g. Buss et al., 2008; Behrens et al., 2015; Kim et al., 2017). For this reaction, O_2 is transported to depth in gaseous form or dissolved in porewater through connected initial porosity and tectonic fractures (e.g. Fletcher et al., 2006; Behrens et al., 2015). The so-called weathering-induced fractures create new pathways for weathering reactants to fresh mineral surfaces and thus enhance weathering (Røyne et al., 2008). Because the oxidation of Fe-bearing silicates and the formation of Fe-oxyhydroxides consumes O_2, the O_2 concentration decreases with depth and restricts further oxidation processes (Fletcher et al., 2006; Behrens et al., 2015). Weathering-induced fractures in turn enable the introduction of fluids into fresh bedrock, leading to the dissolution of other silicate minerals like plagioclase. Bazilevskaya *et al.* (2015) observed a significant increase in porosity with plagioclase dissolution in granite and diabase and a decrease in porosity towards the surface due to the precipitation of secondary clay minerals. The precipitation of secondary weathering products (e.g. ferrihydrite as a product of biotite or clay minerals) is also a mechanism that induces microfractures caused by volume increase, which creates stress and builds up elastic strain (e.g. Fletcher et al., 2006; Jamtveit et al., 2011). Jamtveit *et al.* (2011) concluded that this process of micro-fracturing results in the formation of rindlets that are characteristic for spheroidal weathering (e.g. Buss et al., 2008). Moreover, grain size affects the secondary porosity formation as matrix cracking in coarse-grained rocks can extend to greater depth than in fine-grained rocks and thus provides additional pathways (Goodfellow and Hilley, 2022).

1.2.2 Dissolution of primary minerals

The dissolution of minerals, which results in element mobilisation into the dissolved phase or secondary weathering products, is an important weathering mechanism that, for example,

enables the uptake of mineral nutrients by vegetation and feeds element cycles. Minerals have specific dissolution rate constants that depend on pH, temperature, and the stoichiometry of the mineral (Brantley, 2008). However, mineral dissolution is a time-dependent process that is influenced by intrinsic mineral characteristics and extrinsic weathering environment factors. White and Brantley (2003) account increases in mineral surface area, simultaneous decreases in reactive surface area, and the clogging of pore spaces by secondary weathering products as intrinsic mineral characteristics, while extrinsic weathering environment factors include permeability and thus initial porosity, mineral/fluid ratios, solute composition, and biota. The authors identified the extrinsic factors as the main reason for varying dissolution rates between experimental laboratory and natural field studies (White and Brantley, 2003).

When Fe(II) in biotite is oxidised, not only is secondary porosity created, but also potassium (K) is released simultaneously from interlayers, resulting in oxidised biotite. The ratio of Fe(III) to K differs between fresh biotite, oxidised biotite and chlorite, and is thus indicative for this weathering process (Buss et al., 2008). During weathering of biotite to kaolinite, magnesium (Mg) is released from the mineral and lost into the dissolved phase (Murphy et al., 1998). In different weathering environments where biotite weathers to vermiculite and smectite before it eventually weathers to kaolinite, Mg is partially retained in vermiculite (Fordham, 1990). Further, the loss of elements during biotite weathering results in increasing aluminium (Al) to silica (Si) ratios with the progression of weathering. In contrast to biotite, muscovite contains only very little structural Fe(II), hence weathering of this mineral is much slower (White and Buss, 2014). The dissolution and release of elements in feldspars differ for plagioclase and K-feldspars according to their mineral chemistry. Generally, K-feldspar is much more weathering resistant than plagioclase and is therefore still abundant even when all plagioclase is weathered (Nesbitt et al., 1997; Zhang and Lüttge, 2009). When plagioclase weathers, calcium (Ca) and sodium (Na) are released and lost into the dissolved phase. Ca is preferentially released compared to Na because the Ca-rich core of anorthite-rich plagioclase weathers faster than the Na-rich outer part of albite-rich plagioclase (Clayton, 1986, in White and Buss, 2014). Studies on experimental dissolution of plagioclase suggest that an amorphous surface layer which is depleted in Al, Ca, and Na but enriched in SiO_2 forms at the solid-fluid boundary (Shotyk and Nesbitt, 1992; Zhang and Lüttge, 2009; Hellmann et al., 2012).

1.2.3 Formation of secondary weathering products and reactive surfaces

The formation of amorphous and weakly crystalline phases and the precipitation of secondary clay minerals further result from mineral dissolution and ensuing saturation of fluids. Biotite, as described earlier, eventually weathers to kaolinite or goethite with different weathering pathways: 1) biotite weathers directly to kaolinite, 2) mixed-layer clays (biotite mixed with secondary vermiculite, smectite, or hydrobiotite) form that further weather to

kaolinite or goethite, and 3) released Fe and Al form amorphous precursors and Fe-oxyhydroxides that weather to secondary clays like vermiculite or smectite and eventually to kaolinite or goethite (e.g. Fordham, 1990; Price and Velbel, 2014; Behrens et al., 2015). The weathering of feldspars produces kaolinite as weathering product; however, plagioclase and K-feldspar both form amorphous Al hydroxides during dissolution and precipitation processes at the mineral-fluid interface (Kawano, 1996; Zhang and Lüttge, 2009; Behrens et al., 2015). Reactive amorphous phases serve as sorption sites for dissolved metals (e.g. beryllium; Willenbring and von Blanckenburg, 2010), but also organic matter that is stabilised and stored within these phases (Kramer and Chadwick, 2018; Garcia Arredondo et al., 2023; Wu et al., 2023). All these secondary phases precipitate in open pore spaces which has two opposing effects on weathering propagation: The precipitation creates stress that leads to fracture formation and hence porosity formation (e.g. Fletcher et al., 2006), and precipitation fills available porosity and inhibits fluid infiltration, thus hampering further dissolution of primary minerals (e.g. Bazilevskaya et al., 2015; Kim et al., 2017). Moreover, the combination of increasing porosity, dissolution of primary minerals and precipitation of secondary phases changes the (reactive) surface area, which is an important control on solid-fluid interactions during weathering (e.g. White et al., 1996; Navarre-Sitchler et al., 2013; White and Buss, 2014; Bazilevskaya et al., 2015; Lai et al., 2015; Fisher et al., 2023). The weathering-available surface area increases with the formation of porosity and dissolution of primary minerals. However, the strongest increase in surface area is observed when secondary phases precipitate on mineral surfaces (e.g. Borggaard, 1982; Fisher et al., 2023).

1.2.4 Reaction fronts in the weathering zone

Several studies (e.g. Jin et al., 2010; Brantley et al., 2013, 2017b) suggest that depending on rock properties, i.e. initial porosity, mineralogy, and water flow to depth, the described weathering processes occur in different depths. The resulting reaction fronts of distinct processes form so-called nested weathering fronts and are separated from centimetres to tens of meters in different rock types. For granitic lithology, the nested weathering fronts reflect the depth of biotite oxidation (deepest reaction front), plagioclase dissolution (porosity-increasing reaction front) and alkali-containing mineral dissolution (soil-initiating reaction front) with distances between these fronts extending to tens of meters (Figure 1-2; Bazilevskaya et al., 2015; Brantley et al., 2017b; Hayes et al., 2020). For shale, (Brantley et al., 2013, 2017b) describe nested weathering fronts that also extend over tens of meters with pyrite oxidation (deepest reaction front), carbonate dissolution (porosity-increasing reaction front) and illite dissolution (soil-initiating reaction front). Separated reaction fronts are also observed in lithology with little porosity (pore size is too small for helium to enter) like charnockite, where oxidation of Fe(II)-minerals is the first weathering reaction followed by biotite, pyroxene and plagioclase dissolution (Behrens et al., 2015, 2021). However, in diabase, the observed reaction fronts for dissolution of Fe(II)-bearing augite, calcic augite and

plagioclase are located approximately at the same depth (Bazilevskaya et al., 2015; Brantley et al., 2017b). Further studies report that weathering processes occur at the same depth and one distinct weathering front is observed even in rock types where nested weathering fronts were previously observed. For example, Wan *et al.* (2019) identified overlapping reaction fronts for pyrite oxidation, carbonate dissolution and rock organic carbon degradation in shale. Therefore, whether nested weathering fronts develop is not necessarily a function of lithology.

To identify reaction fronts and the weathering depth, usually metrics based on mass loss either from chemical parameters (chemical depletion fraction CDF, Riebe et al., 2003; element-specific mass loss τ, Brimhall and Dietrich, 1987), petrophysical measurements (porosity, density, volumetric strain), clay mineralogy, and stable and radiogenic metal isotopes (e.g. strontium (Sr), Hewawasam et al., 2013; silicon (Si), Frings et al., 2021) are used. The combination of these parameters with measurements of Fe(III)/ Fe(total) and specific surface area combines mass loss with oxidation, porosity development and formation of secondary phases and thus yields well-constrained estimates on the weathering depth (e.g. Navarre-Sitchler et al., 2013; Bazilevskaya et al., 2015; Behrens et al., 2015; Hayes et al., 2019; Holbrook et al., 2019).

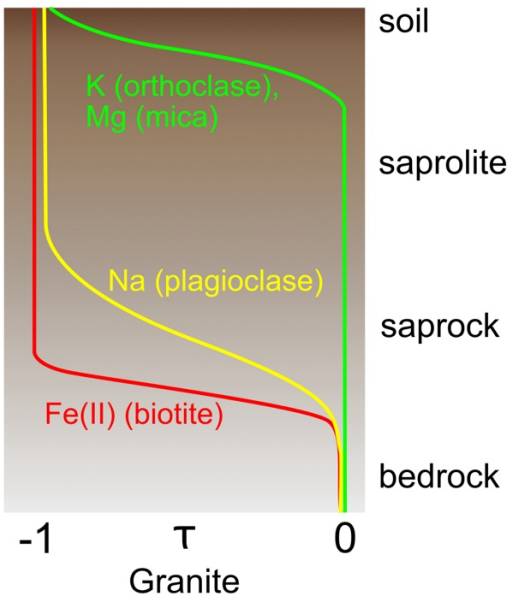

Figure 1-2. Concept of nested weathering fronts in granitic lithology. Observed reaction fronts in granite are separated by tens of meters starting with Fe(II)-oxidation at depth, followed by plagioclase dissolution releasing Na, and eventually the dissolution of alkali-containing minerals (modified after Brantley et al., 2017b).

1.3 Surface-subsurface interactions

1.3.1 Erosion and weathering

The interplay of mass removal by erosion and weathering front advance is an important connection between the Earth's surface and the subsurface. Anderson *et al.* (2007) described this connection as a "feed-through reactor" where mass is removed from the surface while in the subsurface fresh material enters the system. When the rates of mass removal at the surface (denudation rate) and fresh rock input at the weathering front (weathering front advance rate) are approximately equal, the system is in steady state with constant weathering zone thickness (e.g. Hack, 1960; Anderson et al., 2007; Lebedeva et al., 2010; Brantley and Lebedeva, 2011; Lebedeva and Brantley, 2020). In settings with high erosion rates, the weathering rate is decoupled and depends on fluid flow and saturation of the fluids (Anderson et al., 2002, 2007, 2021; Hilley et al., 2010). Slow erosion enables full mineral depletion and results in completely developed weathering profiles (Aarão Reis and Brantley, 2019). However, over a certain time scale, both processes may be balanced and are thus in steady state (Brantley and Lebedeva, 2011). If the denudation rate exceeds the weathering front advance rate, the system is no longer in steady state and bedrock is exposed at the surface (Aarão Reis and Brantley, 2019; Bufe et al., 2021). Climatic and tectonic changes may induce such disturbances that result in non-steady state weathering profiles (e.g. Nesbitt et al., 1997).

The development of weathering profiles in steady state requires feedback mechanisms that couple denudation at Earth's surface with the weathering front advance at depth. When surface material is removed due to erosion, for example, the formation of secondary porosity by Fe oxidation can advance to depth (e.g. Fletcher et al., 2006; Buss et al., 2008; Kim et al., 2017). In this feedback, erosion is thought to remove the weathered material from the surface, and thus the diffusion distance to unweathered bedrock is shorter. The weathering front can then advance through the formation of secondary porosity and the resulting new infiltration pathways for weathering reactants to depth. Moreover, a model by Lebedeva and Brantley (2020) indicates that steady state can be reached at any erosion rate independent of lithology because hydrological processes are coupled with weathering. The model shows that if the Darcy velocity decreases with depth the weathering advance rate decreases simultaneously.

1.3.2 Biota and weathering

Soil is a habitat for microorganisms and the base for vegetation that interact chemically, physically and mechanically with primary minerals (e.g. Berner et al., 2003; Brantley et al., 2017a; Ibarra et al., 2019; Napieralski et al., 2019; Oeser and von Blanckenburg, 2020a; Wild et al., 2022; Maher and von Blanckenburg, 2023). Chemical processes are caused by root respiration, organic ligand exudation, and pore water interactions (e.g. Kelly et al., 1998; Lee

and Boyce, 2010; Brantley et al., 2012; Lawrence et al., 2014; Perez-Fodich and Derry, 2019; Garcia Arredondo et al., 2023). Plant roots, microorganisms and mycorrhizal fungi enhance chemical weathering of fresh rock by influencing the dissolution of minerals (e.g. Banfield et al., 1999; Uroz et al., 2009; Graham et al., 2010) and using the minerals as energy sources through chemolithotrophic metabolism (Napieralski et al., 2019). The abundance and strategies of mineral weathering microorganisms depend on chemical composition and weatherability of the present minerals (Uroz et al., 2015) but also plant root exudates, nutrient availability, source of carbon (C) and nitrogen (N), and soil pH are important parameters (Uroz et al., 2022, and references therein). Organic acids and CO_2 from respiration are further reactants provided by plant roots and microorganisms that promote weathering (e.g. Kelly et al., 1998; Lawrence et al., 2014; Perez-Fodich and Derry, 2019). Ectomycorrhizal fungi have an important role in mineral dissolution as they release organic acids and chelators that aggressively weather minerals (Landeweert et al., 2001; Taylor et al., 2009; Banwart et al., 2019). In a study on biotite weathering by ectomycorrhizal fungi, the authors observed that acidification of fluids by organic acids, fungal respiration and cation complexation enhances mineral weathering rather than direct nutrient transfer from biotite to the fungi via hyphae (Balogh-Brunstad et al., 2008). Moreover, microorganisms in the soil form biofilms that affect the minerals by inducing chemical and physical changes and thus contribute to weathering (Finlay et al., 2020; Gerrits et al., 2020).

The formation of porosity, besides facilitating the transport of weathering reactants to depth, also creates habitats for microorganisms and makes the rock accessible for plant roots and associated mycorrhiza. The porosity is also essential for subsurface water storage from where plant roots and mycorrhizal fungi access water (Graham et al., 2010). The plant root depth thereby interacts with climate resulting in deep roots in semi-arid to humid tropical regions that are seasonally dry and shallow roots in arctic, boreal or cool-temperate regions (Schenk and Jackson, 2005). With the uptake of water, plant roots redistribute it in the soil (Brantley et al., 2011) and thus shape the water cycle (e.g. Ibarra et al., 2019). Uecker *et al.* (2023) observed that trees in a hilly landscape are more likely located at positions where the weathering front is shallow (<30 m) and water is accessible for the plant roots, and thus trees might be an indicator for subsurface water pathways.

Furthermore, vegetation and soil on top of saprolite influence chemical weathering. The presence of soil is crucial for the efficiency of chemical weathering (Dixon and von Blanckenburg, 2012). However, there is evidence that with increasing soil thickness, chemical weathering rates decrease in the underlying saprolite (Burke et al., 2007). Besides soil, vegetation cover also affects chemical weathering due to the accumulation of organic matter and the production of organic ligands in the soil (Egli et al., 2008). In ecosystems where soils are nutrient-depleted due to intense chemical weathering, vegetation shifts to a nutrient-recycling system (e.g. Oeser and von Blanckenburg, 2020; Maher and von Blanckenburg, 2023). Model results from Maher and von Blanckenburg (2023) suggest that biotic weathering

is, however, only effective in fresh regolith or in settings where erosion is high and thus regolith is rapidly renewed.

1.4 Research questions and main objectives

The overarching aim of this thesis is to investigate the depth of weathering, deep weathering processes and the climate dependence of both. Towards answering these questions several hypotheses can be formulated. 1) The weathering front depth is located deeper where more precipitation is available. 2) The degree of weathering is higher where more precipitation is available. 3) In granitoid weathering profiles, nested weathering fronts evolve that are independent of the depth of the weathering front. 4) Weathering is deepest, and intensity is highest, where the denudation rate is lowest.

The main question I address in this thesis is: "What is the depth of the weathering front in settings of similar lithology and differing climate?" The effect of climate, perceived as the combined effects of precipitation, vegetation cover, and microbial activity, on weathering and denudation, is tested at study sites along a steep gradient in the Chilean Coastal Cordillera (see Chapter 1.5).

Furthermore, I apply the novel isotope system meteoric $^{10}Be/^{9}Be$. Using this method, I answer the research question: "Can meteoric $^{10}Be/^{9}Be$ be used as a water infiltration proxy in a weathering profile to investigate the depth where primary minerals begin to dissolve?" Moreover, by combining this novel method with the standard technique to determine denudation rates (*in situ* ^{10}Be) I answer the question: "Does meteoric $^{10}Be/^{9}Be$ yield reliable denudation rates using surface samples?" Finally, I answer the question: "How does denudation affect the depth and degree of weathering along the investigated climate gradient?"

To answer these questions, I applied a wide range of geochemical and petrophysical methods on soil and drill core samples. A list of these methods is given in chapter 1.6 and detailed descriptions are provided in the according chapters.

1.5 Study sites and drilling campaigns

The thesis is embedded in the second phase of the project "EarthShape – Earth's surface shaping by Biota" funded by the Deutsche Forschungsgemeinschaft (DFG-SPP 1803). Within the framework of EarthShape, the subproject "DeepEarthShape" aimed to investigate processes in the subsurface that are connected to the surface and influence the shape of Earth's surface by using geochemical, mineralogical, geophysical, and geomicrobiological approaches.

The four EarthShape sites are located along an extreme climate gradient spanning from arid to humid climate in the Chilean Coastal Cordillera (Figure 1-3): Pan de Azúcar with an arid climate and mean annual precipitation (MAP) of 10 mm, Santa Gracia with a semi-arid climate

and MAP of 90 mm, La Campana with a mediterranean climate and MAP of 440 mm, and the southernmost site Nahuelbuta with a humid climate and MAP of 1100 mm (Oeser et al., 2018a). The mean annual temperature decreases from North (18.1 °C) to South (14.1 °C; Ministerio de Obras Públicas, 2017) while the vegetation cover increases from < 5% at the arid site to 100% at the humid site (Oeser and von Blanckenburg, 2020b). The study sites are similar in their lithology (Table 1-1; granitoid mineralogy including granite, diorite/monzodiorite, tonalites and granodiorites; (Oeser et al., 2018a) but also with respect to the absence of glaciation during the last glacial maximum (Hulton et al., 2002) and the absence of volcanic input. Due to these similarities, it is possible to investigate the control of climate in terms of precipitation on weathering at the study sites.

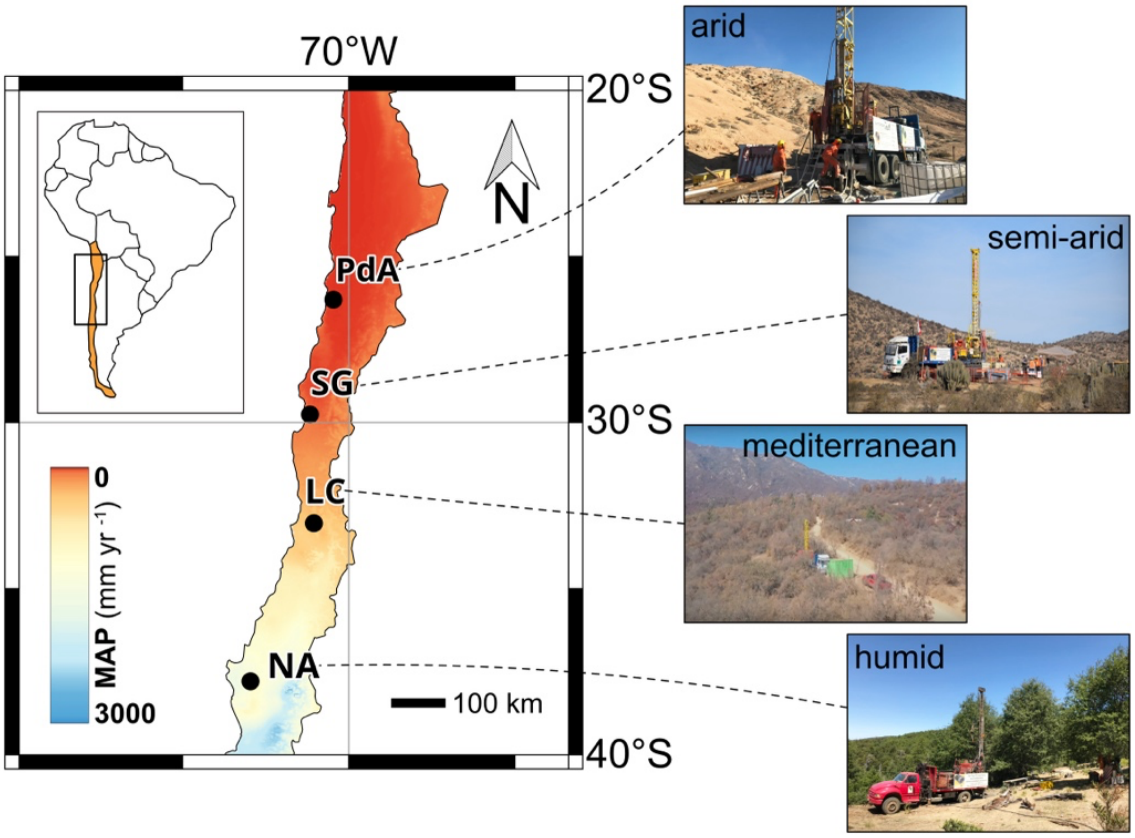

Figure 1-3. Study sites with mean annual precipitation (MAP averaged from 1970 - 2000, Fick & Hijmans, 2017: worldclim.org) in the Chilean Coastal Cordillera. Photos: arid, semi-arid, humid: L. Krone; Mediterranean: C. Conrady.

Table 1-1. Properties of the drill sites and published denudation rates (derived with *in situ* ^{10}Be). 1: Oeser et al., 2018a; 2: Oeser and von Blanckenburg, 2020a; 3: Luebert and Pliscoff, 2017; 4: Schaller et al., 2018; 5: van Dongen et al., 2019; 6:Godoy and Lara, 1998; 7: Jara et al., 2021; 8: SERNAGEOMIN, 2003; 9: Parada et al., 1999; 10: Parada et al., 2005; 11: Molina et al., 2015; 12: Parada et al., 2007; 13: Deckart et al., 2014; 14: Dallmeyer et al., 1996; 15: Acevedo Salinas, 2022.

Study site	**Latitude**	**Longitude**	**altitude**	**MAP[1]**	**Vegetation**
			[m.a.s.l.]	[mm yr^{-1}]	
Pan de Azúcar	-26.302717	-70.457350	732	10	Small shrubs, geophytes, annual plants[2]
Santa Gracia	-29.759037	-71.160226	618	90	interior mediterranean desert scrub of *Heliotropium stenophyllum* and *Flourensia thurifera*[3]
La Campana	-33.028375	-71.043710	894	440	coastal mediterranean sclerophyllous forest of *Lithraea caustica* and *Cryptocarya alba*[3]
Nahuelbuta 1	-37.793710	-72.950650	1113	1100	coastal temperate forest of *Araucaria araucana*[3]
Nahuelbuta 2	-37.795170	-72.952060	1084	1100	

Study site	**Soil pit denudation rates (S- and N-facing slope)[4]**	**Catchment-wide denudation rates[5]**	**Lithology**	**Preconditioning**	**Topographic position**
	]cm kyr^{-1}]	[cm kyr^{-1}]			
Pan de Azúcar	0.58 ± 0.03 0.46 ± 0.02	0.77 ± 0.07	Monzo- and Syenogranites (205-250 Myr)[6,7]	Hydrothermal overprint, mafic dikes (~130 Myr)[14,15]	downslope
Santa Gracia	1.63 ± 0.09 1.05 ± 0.05	0.92 ± 0.08	Diorite and Granodiorite (124-144 Myr)[8]	Hydrothermal overprint, tectonic fracturing related to Atacama Fault System	ridge
La Campana	4.25 ± 0.23 5.65 ± 0.30	20.0 ± 2.2	Granodiorite (93-97 Myr)[9,10,11]	Tectonic fracturing	ridge
Nahuelbuta 1	3.22 ± 0.13	2.74 ±0.24	Granitoid with mafic intrusions (~294 Myr)[12,13]	-	ridge
Nahuelbuta 2	na				mid-slope

Previous studies at the same sites only investigated the uppermost 2 m of the weathering profile and fresh unweathered bedrock was never encountered (e.g. Bernhard et al., 2018; Oeser et al., 2018a; Oeser and von Blanckenburg, 2020; Oeser and Von Blanckenburg, 2020). However, the observation of deep weathering in Central Chile (Vázquez et al., 2016) suggests that the weathering front is located much deeper. Because of this observation and the inaccessibility of the weathering front from the surface, four drilling campaigns were conducted along the climate gradient (Figure 1-4). The goal of these drilling campaigns was to recover entire undisturbed weathering profiles and at least 10 m of visual unweathered bedrock. The first drilling campaign was conducted in March and April 2019 at the semi-arid site Santa Gracia. The final depth of the main drill hole SG-N1 is 87.2 m and two drill holes SG-N1C and SG-N2 reached a depth of 10 m each. To recover the uppermost soil, three additional soil pits adjacent to the drill holes were sampled to a depth of 2 m. The second drilling campaign was conducted in November and December 2019 in the arid site Pan de Azúcar with a final depth of the main drill hole PdA-N1 of 93.45 m. At this site, no further drill holes were conducted. Three soil pits to a depth of 2 m were excavated; these samples were not used for the studies in this thesis. During a third drilling campaign in February 2020, two drill cores were obtained at the humid study site. The first drill hole NA-N1 has a final depth of 40.8 m and is located on a ridge while the second drill hole NA-N2 with a final depth of 48.3 m is located on a slope. Three additional soil pits were sampled to recover the uppermost meters. The soil pit adjacent to NA-N1 has a depth of 6 m and the soil pit next to NA-N2 is 4 m deep, the third soil pit has a depth of 2 m. The last drilling campaign was conducted at the mediterranean site La Campana in February and March 2020. The final depth of the drill hole LC-N1 is 88.25 m, and to recover the uppermost meters, three soil pits were sampled to 6 and 2 m depth. At all study sites, geophysical borehole logging (Weckmann et al., 2020) was performed, as well as geophysical imaging at the mediterranean, semi-arid, and arid sites (Trichandi et al., 2022, 2023a, 2023b). For geomicrobiological investigations of the drill core, a contamination control was implemented with an optical tracer (UV blue) with a particle size similar to the size of microbes. This control ensured that the sample material used for geomicrobiological analyses was not contaminated by microorganisms from drill fluids. A detailed description of the drilling procedure, contamination control of the used drill fluid and sampling of the drill cores is provided in Chapter 2.2.2.

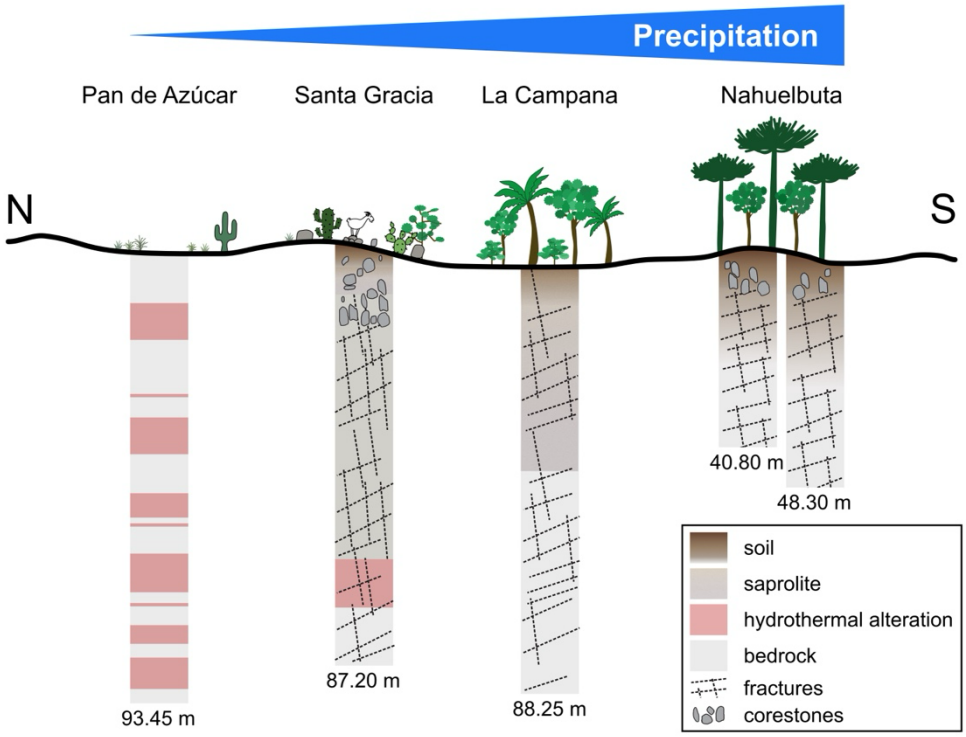

Figure 1-4. Schematic overview of the boreholes with the maximum drilled depth. Characteristics of the weathering profiles are derived from visual observations and core descriptions. In Nahuelbuta, the left profile with a depth of 40.80 m indicates N1, the right profile with a depth of 48.30 m indicates N2.

Several DeepEarthShape subprojects have already addressed specific questions (Trichandi et al., 2022, 2023a, 2023b; Hampl et al., 2022, 2023; Scheibe and Spohn, 2022; Scheibe et al., 2023). Geophysical analyses provided a 2-dimensional overview of the subsurface structures. On a much smaller scale, mineralogical and microbiological projects investigated deep weathering processes. Several articles from the DeepEarthShape project are already published: The geophysical imaging of the subsurface of Pan de Azúcar (Trichandi et al., 2023a), Santa Gracia (Trichandi et al., 2022), and La Campana (Trichandi et al., 2023b); mineralogical investigations of Fe-bearing silicates on weathering at fractures in Santa Gracia (Hampl et al., 2022); investigation of feedbacks between secondary minerals and porosity (Hampl et al., 2023); and microbial fixation of nitrogen (Scheibe and Spohn, 2022) and carbon (Scheibe et al., 2023) in soils.

1.6 Overview of methods

In this thesis, I applied a wide range of geochemical and petrophysical methods. The methods are explained in detail in the respective chapters. This overview briefly summarises all of the main methods applied. The meteoric $^{10}Be/^{9}Be$ method is described in more detail in the following section.

Method	Description	Chapter	Reference
Bulk element analysis (ICP-MS/ ICP-OES)	bulk element concentration for major and trace elements measured with inductively coupled plasma – mass spectrometry (ICP-MS) and inductively coupled plasma – optical spectrometry (ICP-OES)	2, 3	-
CDF	Chemical depletion fraction (CDF), bulk mass loss relative to an immobile element	2, 3, 4	Riebe et al., 2004
τ (tau)	Element-specific mass loss relative to an immobile element	2, 3	Brimhall and Dietrich, 1987
Fe(III)/Fe(total)	Ratio of ferric Fe (Fe(III)) to total Fe	2, 3	Schuessler et al., 2008
BET/specific surface area	Gas sorption method (BET – Brunauer, Emmett, Teller) to estimate the specific surface area	2, 3	Brunauer et al., 1938
Buoyancy, helium (He) pycnometry and water porosimetry	Determination of total rock and matrix density, He-available porosity, water-available porosity	2	-
Volumetric strain ε	Calculation of expansion or collapse of a weathering profile using density and an immobile element	2	Brimhall and Dietrich, 1987
in situ ^{10}Be	In quartz produced cosmogenic radionuclide	2, 4	von Blanckenburg et al., 2004
Meteoric $^{10}Be/^{9}Be$	In atmosphere produced cosmogenic radionuclide	3, 4	Willenbring and von Blanckenburg, 2010b
Sequential extractions	Combined hydrochloride acid and hydroxylamine hydrochloride leach to extract reactive elements	4	Tessier et al., 1979; Wittmann et al., 2012

1.6.1 Basic principles and applications of meteoric $^{10}Be/^{9}Be$

Beryllium (Be) is a rare alkaline earth metal with three main isotopes, of which only one is stable (^{9}Be). Stable ^{9}Be is present in the continental crust in most rock types with an average concentration of ca. 2.5 ppm (von Blanckenburg et al., 2012, and references therein). Only two isotopes have half-lives ($T_{1/2}$) that are longer than seconds and are thus relevant for geologic processes. The isotope ^{7}Be has a $T_{1/2}$ of ca. 53.2 days. The other isotope is ^{10}Be with $T_{1/2}$ = 1.387 ± 0.012 Myr (Chmeleff et al., 2010; Korschinek et al., 2010), which is applicable as isotope tracer to investigate long-term processes in the atmosphere and on Earth's surface. These applications encompass, for example, measuring soil residence time and soil ages (e.g. Pavich et al., 1984, 1986; Maejima et al., 2005; Bacon et al., 2012), soil erosion rate and transport (e.g. Brown et al., 1988; Schaller et al., 2002; Balco et al., 2008; Graly et al., 2010; Schoonejans et al., 2017; Calitri et al., 2021; Zhang et al., 2023), determining trace metal scavenging, incorporation into sediments and water mass movements in the oceans (e.g. Kusakabe and Ku, 1984; Anderson et al., 1990; von Blanckenburg et al., 1996; Lal et al., 2006; Kaste and Baskaran, 2012), and reconstructions of the paleomagnetic field strength and solar activity (e.g. Field et al., 2006; Muscheler et al., 2007; Steinhilber et al., 2012; Heikkilä and Smith, 2013; Simon et al., 2018; Jena et al., 2021, 2023).

Both isotopes, ^{7}Be and ^{10}Be, are produced in the atmosphere by interactions of high-energy cosmic rays (mostly protons and secondary neutrons) that induce spallation reactions (Lal and Peters, 1967). The isotope ^{10}Be occurs in two varieties that differ in their production mechanism: *in situ* ^{10}Be ($^{10}Be_{insitu}$) is produced in the crystal lattice of quartz while meteoric ^{10}Be ($^{10}Be_{met}$) is produced in the atmosphere (Figure 1-5; Lal, 1991). In both production mechanisms, cosmic rays collide with target nuclei of oxygen in quartz, or oxygen, nitrogen, and other atmospheric gases in the atmosphere resulting in spallation of these nuclei and production of lighter particles (Lal and Peters, 1967). The production rate of ^{10}Be is a function of the primary cosmic ray flux defined by solar activity and geomagnetic field strength and orientation (Masarik and Beer, 1999, 2009). The production rate of $^{10}Be_{insitu}$ further depends on altitude, latitude, irradiation geometry, and shielding (Lal, 1991; Balco et al. 2008). The geometry of the geomagnetic field of the Earth determines a higher production rate in high latitudes where more cosmic rays can penetrate the atmosphere (Masarik and Beer, 2009; Willenbring and von Blanckenburg, 2010b). Due to the different production mechanisms for $^{10}Be_{insitu}$ and $^{10}Be_{met}$, the abundance of the latter variety is much higher, and less sample material is required for analysis. Furthermore, $^{10}Be_{met}$ is not limited to quartz-bearing lithologies and thus offers considerable advantages over $^{10}Be_{insitu}$ (von Blanckenburg et al., 2012). The following section focuses on the meteoric variety, which is a main topic in this thesis.

Most of the production of $^{10}Be_{met}$ takes place in altitudes above 3 km. The produced $^{10}Be_{met}$ nuclides are mixed in the atmosphere and hydrolysed to ^{10}BeO or $^{10}Be(OH)_2$ with a stratospheric residence time of about one year. $^{10}Be_{met}$ is eventually attached to aerosol

particles (Willenbring and von Blanckenburg, 2010b). These aerosol particles are then transported to Earth's surface via dry (e.g. dust) or wet (e.g. precipitation) deposition so that the depositional flux is dependent on aerosol loading and climate and can thus vary spatially and temporarily (Field et al., 2006; Willenbring and von Blanckenburg, 2010b; Deng et al., 2020a).

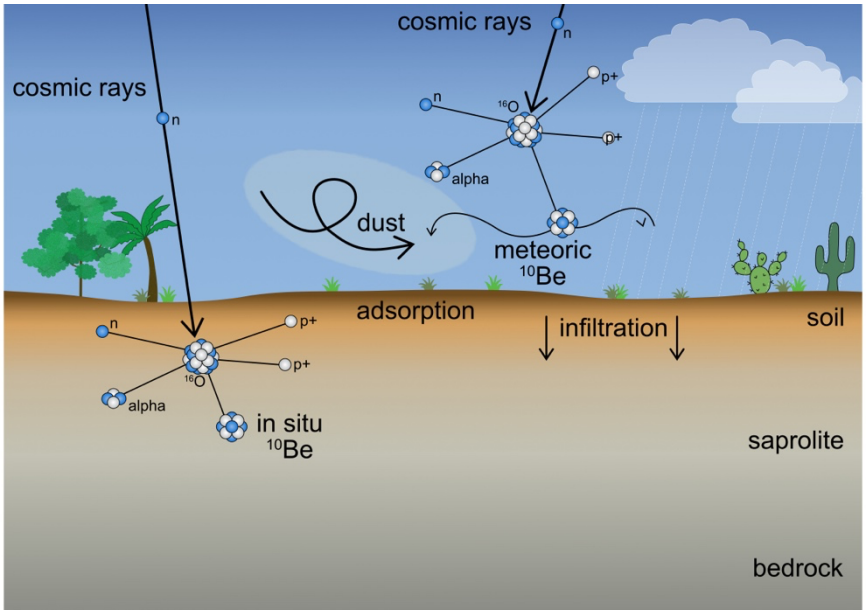

Figure 1-5. Production mechanisms of both ^{10}Be isotope varieties. $^{10}Be_{insitu}$ is produced in the crystal lattice of quartz in a soil profile while $^{10}Be_{met}$ is delivered to Earth's surface by wet and dry deposition, adsorbs to soil particles and infiltrates into the soil profile (modified after Willenbring and von Blanckenburg, 2010b).

After the deposition at Earth's surface, $^{10}Be_{met}$ infiltrates into the soil profile and adsorbs to soil and sediment particles (McHargue and Damon, 1991). The retentivity in the soil profile is influenced by the presence of humic acids and pH, though in most soils with a pH higher than five, $^{10}Be_{met}$ is present in the hydrolysed form. Adsorption sites are provided by secondary weathering products with high surface areas, in particular clay minerals as well as Fe and Al hydroxides (Takahashi et al., 1999). In soil, Be and other metals compete with Al for adsorption sites which may cause partial release of adsorbed $^{10}Be_{met}$. In that case and with sufficient water flow, the released $^{10}Be_{met}$ is transported into the groundwater (Willenbring and von Blanckenburg, 2010b). The infiltration of $^{10}Be_{met}$ commonly forms two different concentration profiles: 1) an exponential profile with highest $^{10}Be_{met}$ concentration at the surface (e.g. Egli et al., 2010; Reusser et al., 2010; Deng et al., 2021a (river terraces)), and 2) a bulge-shape profile with highest concentration in a clay-rich soil layer (e.g. Pavich et al., 1986; Schoonejans et al., 2017). The exponential profile indicates highest retentivity and thus highest $^{10}Be_{met}$ concentration at the surface while the bulge-shape profile is less retentive at the surface so that the concentration increases with depth and shows a maximum concentration in a clay-rich soil layer that provides adsorption sites (Graly et al., 2010). The shape of both depth profiles also correlates with grain-size distribution in soil profiles, where

the highest $^{10}Be_{met}$ concentrations indicate the smallest grain sizes (clay size; Willenbring and von Blanckenburg, 2010 and references therein). However, the mobility and retention of $^{10}Be_{met}$ in these depth profiles are strongly affected by water availability, and above a certain rainfall amount (for example >1400 mm in Hawaii island, USA; Dixon et al., 2018) $^{10}Be_{met}$ can be mobilised, as water changes the adsorption capacity of the soil.

The pH and grain size dependence of $^{10}Be_{met}$ limits the applicability of the method for dating surfaces or determining erosion rates if sediment is sorted. This problem can be circumvented by normalising its concentration to that of the stable isotope ^{9}Be with similar chemical behaviour and using the resulting isotope ratio (Wittmann et al., 2012, 2015; Bacon et al., 2012; von Blanckenburg et al., 2012; Maher and von Blanckenburg, 2016; Dannhaus et al., 2018). ^{9}Be is present in most rock types with average concentrations of ca. 2.5 ppm and is released during silicate weathering. The released ^{9}Be is either in the dissolved ($^{9}Be_{diss}$) or reactive ($^{9}Be_{reac}$) phase. Furthermore, a fraction of ^{9}Be is locked in primary minerals ($^{9}Be_{min}$). In this dissertation, however, dissolved concentrations of $^{9}Be_{diss}$ in water were never measured. Reactive ^{9}Be mixes with $^{10}Be_{met}$ and partitions between solid and solution (von Blanckenburg et al., 2012). The ratio of $^{10}Be_{met}$ and ^{9}Be ($^{10}Be_{met}/^{9}Be$) therefore depends on the bedrock ^{9}Be concentration and its release during weathering, and the depositional flux of $^{10}Be_{met}$ to Earth's surface (von Blanckenburg et al., 2012; Maher and von Blanckenburg, 2016). To apply the isotope ratio $^{10}Be_{met}/^{9}Be$ for denudation rate determination from soil profiles and bedload sediment, von Blanckenburg *et al.* (2012) developed a conceptual mathematical framework. Wittmann *et al.* (2012) developed the laboratory method by modifying the sequential leaching protocol by Tessier *et al.* (1979). With this method, $^{10}Be_{met}$ and ^{9}Be contained in amorphous and weakly crystalline oxyhydroxides (operationally defined as "reactive" Be) are separated from the sample material and ^{9}Be is afterwards measured using Inductively Coupled Plasma-Optical Emission Spectroscopy (ICP-OES). For $^{10}Be_{met}$ measurements, the sample is spiked with a ^{9}Be carrier of known Be amount and separated from other elements by anion and cation columns followed by alkaline Be precipitation (von Blanckenburg et al., 2004). For the measurement of the few (10^5 to 10^8) atoms of ^{10}Be by an accelerator mass spectrometer (AMS), the Be sample is oxidised and pressed into AMS cathodes. The conceptual framework and the laboratory method for the isotope ratio $^{10}Be_{met}/^{9}Be$ were successfully applied to determine denudation rates from the Amazon River basin (Wittmann et al., 2015), from the George River basin (Tasmania, Australia; with modified method; VanLandingham et al., 2022), and in forested catchments in the Czech Republic (Dannhaus et al., 2018), to constrain the upper limit of denudation rate in the Liwu Basin in Taiwan (Deng et al., 2021b), to track global silicate fluxes from rivers into the ocean in marine sediment deposits (Willenbring and von Blanckenburg, 2010a; von Blanckenburg et al., 2015), and to track the nutrient uptake depth by plants (Uhlig et al., 2020). In this thesis, I applied $^{10}Be_{met}$ and $^{10}Be_{met}/^{9}Be$ to soil profiles to 1) investigate the potential of the isotope as a water infiltration tracer, 2) develop the release and retention of ^{9}Be as a weathering intensity proxy;

and 3) determine denudation rates from soil samples. In doing so, I applied the previously described method to samples from the obtained drill cores and calculated denudation rates using the equations by von Blanckenburg *et al.* (2012). Moreover, to compare and validate the newly derived $^{10}Be_{met}/^{9}Be$ denudation rates I additionally determined denudation rates using $^{10}Be_{insitu}$ concentrations in quartz samples.

2. Deep weathering in the semi-arid Coastal Cordillera, Chile

Abstract

The weathering front is the boundary beneath Earth's surface where pristine rock is converted into weathered rock. It is the base of the "critical zone", in which the lithosphere, biosphere, and atmosphere interact. Typically, this front is located no more than 20 m deep in granitoid rock in humid climate zones. Its depth and the degree of rock weathering are commonly linked to oxygen transport and fluid flow. By drilling into fractured igneous rock in the semi-arid climate zone of the Coastal Cordillera in Chile we found multiple weathering fronts of which the deepest is 76 m beneath the surface. Rock is weathered to varying degrees, contains core stones, and strongly altered zones featuring intensive iron oxidation and high porosity. Geophysical borehole measurements and chemical weathering indicators reveal more intense weathering where fracturing is extensive, and porosity is higher than in bedrock. Only the top 10 metres feature a continuous weathering gradient towards the surface. We suggest that tectonic preconditioning by fracturing provided transport pathways for oxygen to greater depths, inducing porosity by oxidation. Porosity was preserved throughout the weathering process, as secondary minerals were barely formed due to the low fluid flow.

This chapter is published in:
Scientific Reports Vol. 11, 13057

Krone, L. V., Hampl, F. J., Schwerdhelm, C., Bryce, C., Ganzert, L., Kitte, A., Übernickel, K., Dielforder, A., Aldaz, S., Oses-Pedraza, R., Perez, J. P. H., Sanchez-Alfaro, P., Wagner, D., Weckmann, U. & von Blanckenburg, F. (2021); https://doi.org/10.1038/s41598-021-90267-7

2.1 Introduction

Rock weathering, the conversion of coherent rock through contact with atmospheric gases, water, or organisms into weathered rock and mobile soil is a fundamental geologic process. Weathering disintegrates rock for transport by erosion (Lebedeva and Brantley, 2013) and consumes global atmospheric CO_2, thereby modulating global climate over geological timescales (Walker et al., 1981). In addition, the release of nutrients by weathering provides nutrients for microorganisms and plants (Graham et al., 2010). The deep weathering zone is the lower part of the "critical zone", which is defined as the section of Earth's surface extending vertically from the depth where weathering begins to the top of the vegetation canopy, the zone "where rock meets life" (Dawson et al., 2020).

The thickness of weathering zones occurs in a defined depth interval for given lithologies in eroding landscapes (Bazilevskaya et al., 2013). In felsic lithologies, the weathering zone and associated reaction fronts are much thicker and found deeper than in mafic lithologies (Bazilevskaya et al., 2013; Brantley et al., 2017). This observation requires the advance of the weathering front at depth to be coupled to erosion at the surface through a feedback Lebedeva et al., 2010). Recent studies suggest that the locus of the weathering front is governed by the maximum depth of O_2 diffusion (Kim et al., 2017) or the depth of the saturated zone (Rempe and Dietrich, 2014; Riebe et al., 2017) besides the lithological precondition (Brantley et al., 2017b). Deeper still, groundwater may induce localised weathering up to 250 m and consequentially may have significant impact on weathering (Calmels et al., 2011).

Yet, pathways are needed that connect the depth with the surface to transport fluid and gaseous reactants to depth. Fractures and porosity serve as such pathways for diffusive and advective transport (Brantley et al., 2017; Kim et al., 2017; Behrens et al., 2015). Weathering-induced fracturing enhances the porosity and acts as a positive feedback in propagating the weathering front to depth (Kim et al., 2017; Jamtveit et al., 2011; Fletcher et al., 2006). In particular, it drives Fe oxidation generating strain that leads to the formation of fractures (Brantley et al., 2017; Fletcher et al., 2006; Buss et al., 2008; Goodfellow et al., 2016). Due to advancing weathering, secondary mineral formation may in turn fill pores (Jamtveit et al., 2011), a process that inhibits a deeper advance of the weathering front (Behrens et al., 2015). Also, the activity of chemolithoautotrophic microorganisms contributes to weathering at depth (Napieralski et al., 2019) as well as other microorganisms such as fungi (Bonneville et al., 2016).

Non-weathering-related processes generate pathways resulting from tectonic pre-fracturing (Molnar et al., 2007; St. Clair et al., 2015), which often involves the development of planar faults and macrofractures on the metre-scale (Holbrook et al., 2019). Such macroscale structures are thus distinct from weathering-induced fractures that are typically developed on nano- to micro-scale within mineral grains and along grain boundaries (Bazilevskaya et al.,

2015). Nevertheless, tectonic pre-fracturing also causes microfractures in minerals (Anders et al., 2014).

Weathering fronts in granitoid rocks exposed to humid climate are typically observed at about 10 to 20 m depth (Bazilevskaya et al., 2013; Behrens et al., 2015; Brantley et al., 2017; Hayes et al., 2020; White et al., 2001; Uhlig and von Blanckenburg, 2019). Studies on the depth of the weathering front in semi-arid and arid climate though are rare. Vázquez *et al.* (2016) and Stierman and Healy (1985) reported much deeper weathering fronts of 30 and 70 m for Central Chile and the Mojave Desert, USA, respectively. These sites both have a similar climate and are located close to an active plate boundary and have thus experienced tectonic deformation. Even though tectonic processes are thought to promote later weathering through fracturing (Molnar et al., 2007) whether they also result in deeper weathering is still an open question. In this regard locations in dry climate are particularly promising to disclose processes that promote weathering and that set of the depth of the weathering front, as their imprints are impacted by only minimal amounts of fluid.

To close this knowledge gap, this study aims to identify the depth and degree of weathering in granitoid rock in a semi-arid climate. Here, we present the first results of a drilling campaign conducted in the framework of the "EarthShape" project at the field site Santa Gracia (Coastal Cordillera, Chile; Oeser et al., 2018a). We drilled an 87 m deep well and performed geological, geochemical, and geophysical investigations. In further studies the samples will be used to investigate the diversity and impact of microbial communities for deep weathering front, and thus full contamination control was employed during drilling. In this paper, we present a description of drilling activities results on the porosity, specific surface area, the geometry of fractures, Fe oxidation, the degree of chemical weathering, volumetric strain and the weathering rate using cosmogenic nuclides. We provide a first interpretation of the impact of fracturing based on these weathering features and borehole geophysics.

2.2 Geological setting and drilling procedure

2.2.1 Geological setting

The Chilean Coastal Cordillera is the westernmost mountain range of the Andean orogen and extends from north to south along the Pacific coast of South America. In northern Chile, the elevation of the range is about 0.5 to 2 km and its width up to 50 km. The lithological basement units exposed in the Coastal Cordillera were part of the Jurassic to early Cretaceous magmatic arc, comprising plutons of granitoid composition and andesitic volcanic rocks (Figure 2-1a; SERNAGEOMIN, 2003). At present, the Coastal Cordillera is situated within the forearc. One of the largest tectonic structure of the Coastal Cordillera is the Atacama Fault System (AFS) that can be traced for more than 1000 km between Iquique at 20°S and La Serena at 30°S (Cembrano et al., 2005; Scheuber and Gonzalez, 1999; Figure 2-1a). This fault system consists of steeply dipping, northwest, north, and northeast oriented strike-slip faults which

are striking over tens to hundreds of kilometres. The faults formed mainly during the Late Jurassic and Early Cretaceous and record predominantly sinistral arc-parallel strike-slip movements suggesting that the AFS accommodated oblique plate convergence (Scheuber and Andriessen, 1990). Initial deformation was ductile under amphibolite to greenschist facies conditions, followed by brittle deformation during the mid-Cretaceous. Cooling and exhumation of the magmatic arc occurred mainly during the late Mesozoic development of the AFS, but also during the Cenozoic phase of Andean mountain building (Cembrano et al., 2005; Scheuber and Gonzalez, 1999; Juez-Larré et al., 2010). Faulting in the study area along N-S trending faults continued at least until the Early Miocene and resulted in an uplift of the eastern Cordillera relative to the western part (Rodríguez et al., 2015). This study's drill site northeast of La Serena is located in the western Coastal Cordillera in an Early Cretaceous pluton of dioritic to granodioritic composition (Figure 2-1b). The pluton is faulted by steeply dipping, northwest to northeast oriented faults that can be traced over several kilometres and represent the southernmost part of the AFS.

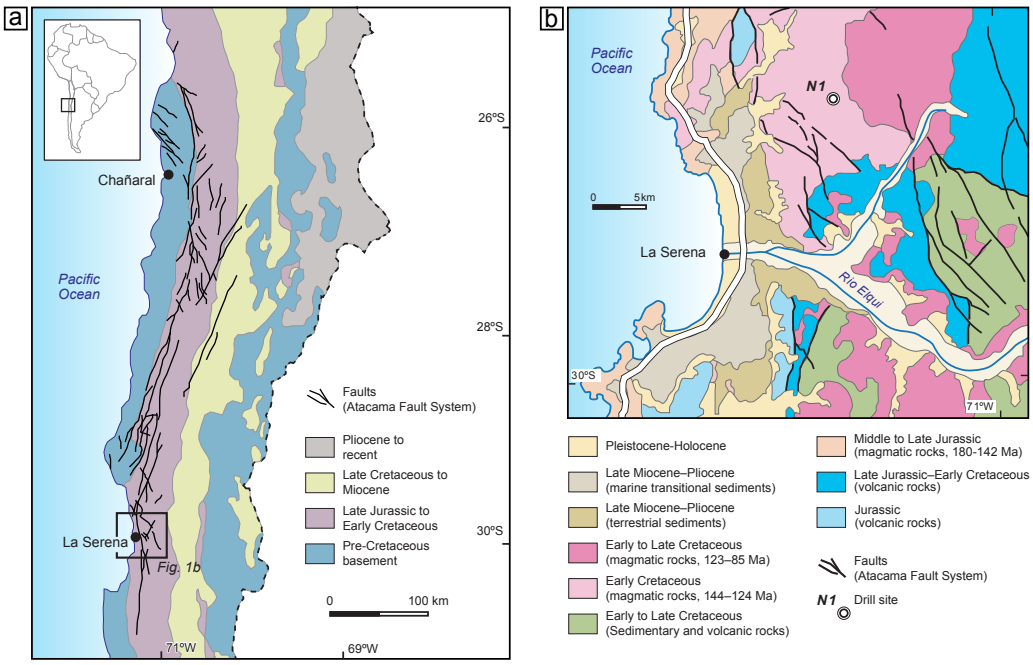

Figure 2-1. a) Simplified geological map of northern Chile between 25ºS and 31ºS indicating the Atacama Fault System in the present-day forearc as based on maps in Tornos *et al*. (2020). Traces of the Atacama fault system are based on Cembrano *et al.* (2005). The study area near La Serena is indicated by the black rectangle. **b)** Simplified geological map of the study area near La Serena as based on SERNAGEOMIN (2003). The NW- and N-trending faults are features of the southernmost part of the Atacama Fault System.

The Early Cretaceous activity of the AFS was coupled to the formation of the "Chilean Iron Belt", a cluster of mineral deposits of Cretaceous age that is spatially and genetically related to the AFS. This cluster is rich in iron oxide, copper, gold, iron oxide, apatite, and stratabound silver deposits, which are hosted in thick mafic-to-intermediate subaerial volcanic units of Middle Jurassic to Early Cretaceous age (Rojas et al., 2018). Hydrothermal alteration in the

country rocks is extensive and consists of a mineral assemblage of actinolite, scapolite, biotite, tourmaline, chlorite, chlorapatite, sphene, minor amounts of garnet, and pyrite. One of the largest iron oxide–apatite deposits of the coastal range, “El Romeral”, is located 10 km to the northwest of the study site. The deposit formed about 128 Ma during extensional sinistral NNW strike-slip faulting along the AFS (Rojas et al., 2018). There is no documentation on supergene formation processes in the study area, however such processes have been documented for the Atacama Desert further north (Rojas et al., 2018; Arancibia et al., 2006). There, supergene processes have been dated using alunite-group minerals indicating an extended period between ~45 and 9 Ma of supergene oxidation, with a peak at ~21–14 Ma that is dominated by downward circulation of meteoric water under semi- arid to arid climate conditions (Arancibia et al., 2006).

The study site Santa Gracia (29.76°S, 71.16°W) is characterised by semi-arid climate with a mean annual precipitation of 87 mm a^{-1} and mean annual temperature of 16.1 °C (Ministerio de Obras Públicas, 2017). The sparse vegetation is dominated by shrubs and cacti and is highly influenced by livestock grazing. Luebert and Pliscoff (2017) describe the native vegetation in Santa Gracia as Mediterranean desertic shrubs. Dominant plant species are *Proustia cuneifolia*, *Senna cumingii* and *Cordia decandra* for shrubs and *Cumulopuntia sphaerica* and *Eulychnia acida* for cacti (Oeser et al., 2018a). Soils in the study area are thin with an A and B-horizon thickness of 30 to 55 cm, underlain by saprolite (Oeser et al., 2018a). The drill sites are located on a ridge at 622 m. a. s. l., surrounded by hillslopes with dipping angles of 5 to 20°.

2.2.2 Drilling procedure

The wireline diamond drilling of hole N1 was conducted in March and April 2019, using a standard industry truck-mounted PQ3-sized (85 mm core diameter, 123 mm hole diameter) rotary drilling rig (Sondajes Araos E.I.R.L.). A Long Year Series 4 diamond drilling crown suitable for abrasive rock and a Long Year Series 9 crown for moderately abrasive rock were used. The final true vertical well depth reached 87.2 m, using a standard wireline continuous coring system recovering up to 1.5 m long core runs contained in stainless steel liners. Potable water with added contamination control tracer (fluorescent particles at a size range similar to microorganisms, according to the procedure of Friese *et al.*, 2017) was used to drill and to monitor potential contamination of samples by microorganisms introduced by the drilling fluid. The contamination control is necessary for microbiological studies to be conducted on these samples. A detailed description of the contamination control and the results can be found in the methods section and the results in the data supplement (Table S2-8).

Increasing sample recovery in the uppermost unconsolidated saprolite was attempted by using additives (AMC GEL XTRA bentonite, AMC CR 650 polymer, both Imdex Ltd, Australia) in the topmost 11.45 m was unsuccessful and was omitted for the remainder of the coring to avoid contamination (see Methods). The circulating drilling fluid was recycled by decantation

into a settling pit. Due to substantial drilling fluid losses into the rock fresh potable water was added daily to the circulating system. To stabilize the borehole in the shallow section, a conductor casing was installed from surface to 6.92 m depth. The average rate of penetration was 3.32 m d^{-1} in soil and saprolite, and up to 6.45 m d^{-1} in rock. The average recovery was 1.67 m d^{-1} in soil, and 6.45 m d^{-1} in crystalline rock. Because of low recovery in the uppermost soil and loose saprolite two additional boreholes N1C (surface – 5.6 m) and N2 (surface – 6.85 m) were cored by a hammer sampler equipped with a core catcher ("cuchara española", Spanish spoon) with a maximum run length of 500 mm and a diameter of 30 mm. Both holes N1C and N2 were drilled from 5.6 and 6.85 m, respectively, to a final depth of 10 m with the rotary drilling and wireline coring equipment described above. The drilling advance with the hammer technique was 2.5 m d^{-1} and the average recovery was 1.46 m d^{-1}. After completion of the drilling, geophysical well logging data was acquired using downhole wireline logging tools.

Mineralogical, petrophysical, and geochemical analytical procedures are described in the methods section. All data are contained in an accompanying data publication (Krone et al., 2021b) and tables therein are here referred to as Tables S2-1 – S2-8.

2.3 Results

2.3.1 Core description

The drilled core from borehole N1 reveals distinct zones (I-VI) from the surface to bedrock (Figure 2-2a). The upper 0.3 – 0.5 m are soil (zone I), followed by zone II of highly weathered loose saprolite containing core stones to a depth of 10 m. Between 10 and 36 m, we found more consolidated saprolite featuring fractures, red-stained parts, and a moderate porosity (2.8 ± 2%; average ± 1 standard deviation (SD)) in zone III. In zone IV (36 and 66 m), less strongly fractured and only moderately altered rock (or "saprock") is intermingled with slightly red-stained rock of lower porosity (1.3 ± 1%). In zone V between 66 and 76.5 m, a highly altered, intensely fractured, red-coloured rock featuring high porosity up to 7.5% (average 3.5 ± 3%) was found. Some sections in this zone are of unconsolidated fabric and yield zones of dark red, presumably hydrothermal alteration (Figure 2-2c). This zone is rich in what likely are Fe oxides and oxyhydroxides. Zones III to V are referred to as saprock. Zone VI from 76.5 to 87.5 m comprises what appears to be unweathered grey bedrock with low porosity (0.3 ± 0.2%) and only few fractures and zones of red alteration.

Acoustic televiewer images display weathered zones and brittle rock in blue colours (Figure 2-2b, 2-3a). Fractures are also recognizable on these images: sinusoidal structures indicate inclined fractures whereas planar structures show horizontal fractures (Figure 2-3a). Detailed results from all measured downhole logging tools are reported in Weckmann *et al.* (2020).

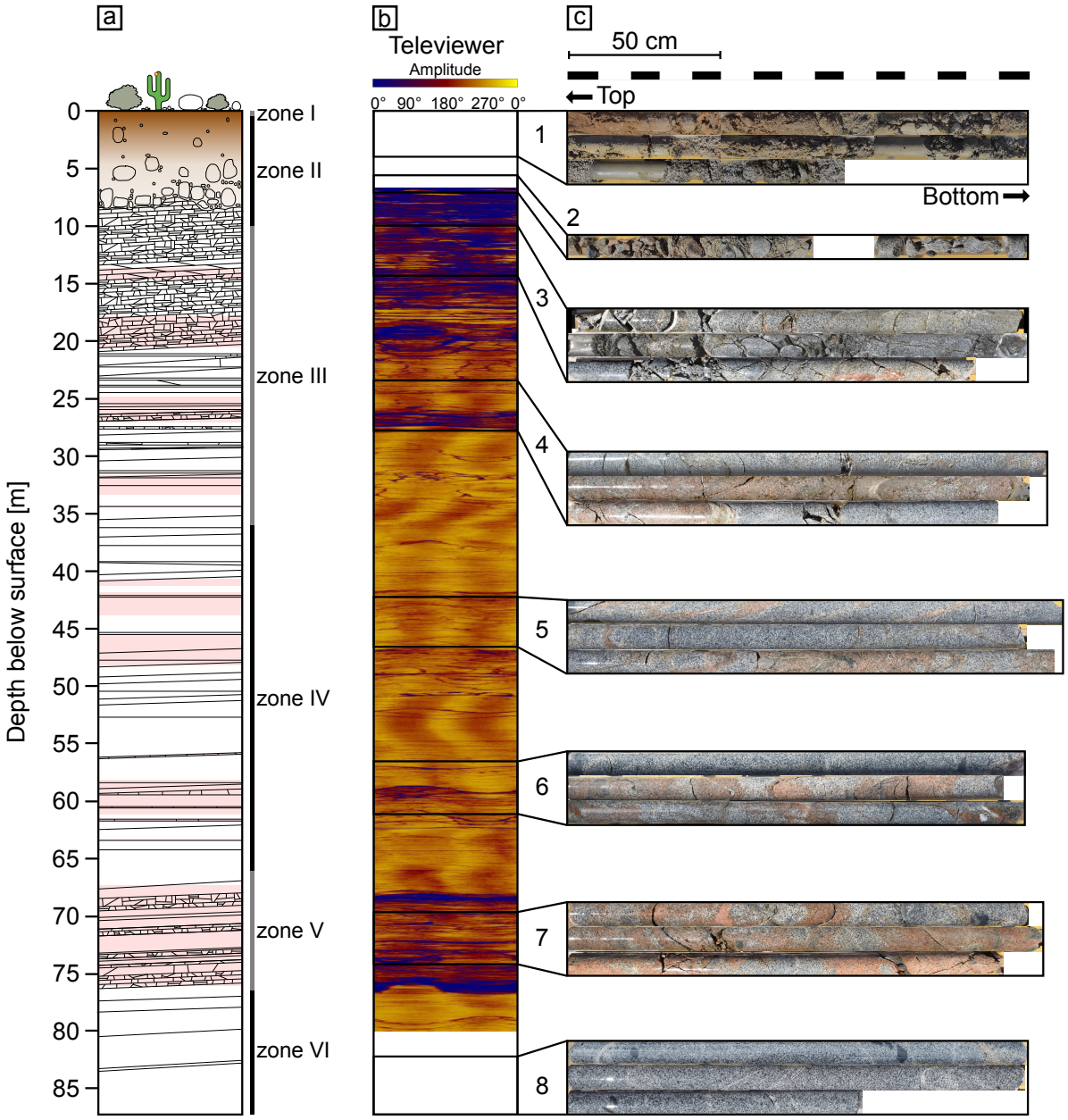

Figure 2-2. a) Schematic core log compiled from core descriptions and -photos. Brown part in the upper metres indicates soil, pink parts indicate red-stained zones. Black lines indicate fractures but are not showing their orientation. **b)** Acoustic televiewer image of the unrolled borehole wall from well logging. Fractures are shown as horizontal lines. Oblique fractures were projected onto the 0° azimute angle at their shallowest depth. The colours imply different amplitudes due to the varying velocity of the acoustic signal with blue indicating a low amplitude (0) and yellow a high amplitude (50000). Details are described in the method section. **c)** Core photos of selected zones: 1: Soil and saprolite (zone I-II); 2: Saprolite (zone II); 3: Transition between saprolite and saprock (zone II-III); 4-7: saprock (zone III - V); 6: fresh bedrock (zone VI). Photos of the uppermost metres of the profile (panel 1) show drill cores from the well N1C.

2.3.2 Fracture orientation

Drill cores recovered from well N1 show a dense network of planar fractures with an average spacing of less than 0.5 m. Most fractures are less than a few mm thick. Larger fracture zones can reach a thickness of a few decimetres and are commonly bound to shear zones and faults, or other compositional anisotropies in the magmatic host rock. Fracture orientations were compiled from televiewer data from borehole N1 (n = 283). The contour diagram for poles of fracture planes indicates three main sets of fractures (Figure 2-3b). The first and dominant group comprises fractures that strike predominantly NNE-SSW and dip at high angle toward the WNW, and to a lesser degree toward the ESE (G1 in Figure 2-3b). The second group includes fractures that strike approximately NW-SE and dip at moderate angles toward the NE (G2 in Figure 2-3b). In comparison, the third group includes fractures that also strike approximately NW-SE, but dip at low angle toward the SW. In addition, the data comprises some fractures that appear randomly oriented and cannot be assigned to one of the three groups above.

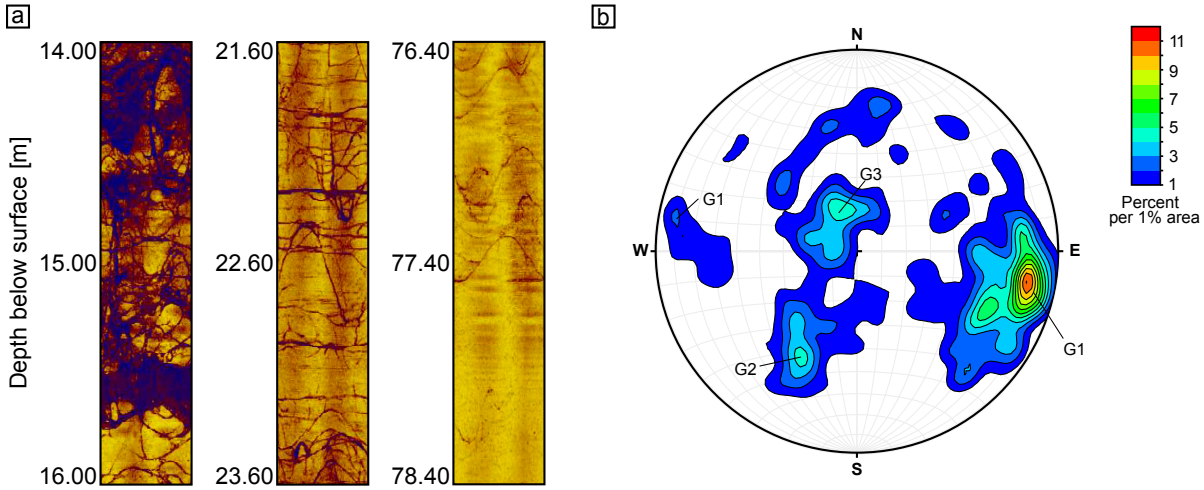

Figure 2-3. a) Detailed acoustic televiewer images showing different types of fractures, where sinusoidal and planar patterns are mainly attributed to a tectonic origin. Left: Both planar and non-planar intensely branched fractures are forming a network where the rock is subjected to a high degree of weathering. Centre: Planar and non-planar fractures in saprolite of a low weathering degree. Oblique and horizontal planar fractures are intersected. Right: Bedrock featuring neither strong branched nor planar fractures. **b)** Lower hemisphere stereographic projection illustrating the orientation of fractures as obtained from the televiewer data (poles to fracture planes, n = 283). The fractures can be grouped into three groups, G1, G2, and G3. Group 1 is the dominant group and comprises fractures that are steeply inclined and dominantly strike NNE-SSW. Groups 2 and 3 comprise gently to moderately inclined fractures that strike NW-SE. Data plotted with OSXStereonet (Cardozo and Allmendinger, 2013).

2.3.3 Bedrock composition and hydrothermal alteration

The primary lithology changes little with depth apart from secondary hydrothermal features (Figure 2-4). However, occasional mafic xenoliths and more felsic zones can be found. The bedrock is characterised by ~58% SiO_2, ~6% for both Na_2O and K_2O, ~6% CaO, ~3% MgO, ~7% Fe_2O_3 and ~17% Al_2O_3, respectively, all in percentages by weight (Table S2-2). Major and trace elements show slight variations (SD < 13%). Some elements show higher bedrock variations (SD Cu: 27%, Cs: 24%). The average Zr concentration in the bedrock is 166 ± 11 ppm (SD) with a relative uncertainty of 8% calculated from reference material measurements. For comparison, the average Zr concentration from relatively unweathered bedrock specimens collected previously near the study area was 115 ± 68 (SD) ppm (Oeser et al., 2018a). Element distribution maps of a polished bedrock slab were used to calculate a modal mineral composition (in area% as an approximation of volume%) of ~44% plagioclase, ~16% hornblende, ~16% K-feldspar, ~11% quartz, and ~6% biotite. Accessory minerals are apatite (~2%), magnetite (~1%), zircon (~0.5%), titanite (~0.4%), and copper-bearing sulphides (mainly chalcopyrite, ~0.3%). Minor abundances of chlorite, calcite, pumpellyite, ilmenite, sericite, and epidote were detected. According to this composition the bedrock can be classified as quartz monzodiorite. Large parts of the core are hydrothermally altered which is evident from the presence of hematite (also martite), chlorite, laumontite, and sericite occurring mainly as a replacement of plagioclase. Anhydrite is present in minor abundance as infilling in veins and fractures and is sometimes intergrown with secondary K-feldspar. Late calcite veins crosscut previous alteration zones. Fracture surfaces in red zones are covered with hematite, chlorite, and carbonates.

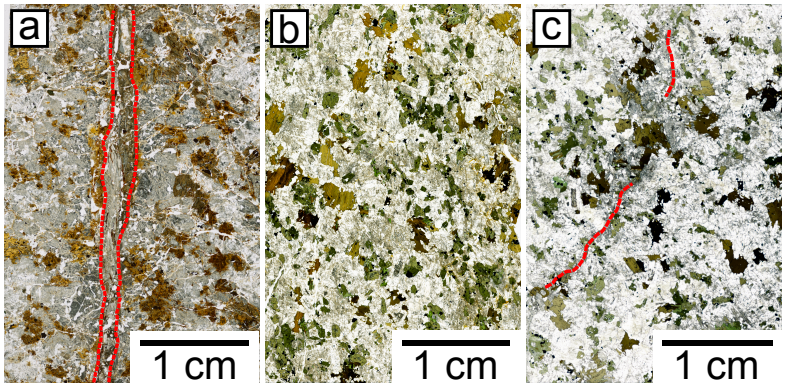

Figure 2-4. Thin sections of **a)** The strongest degree of weathering found in a sample from a nearby soil pit showing a carbonate vein delineated in red (sample depth: 1.74 m). **b)** Moderately weathered sample from zone C (average depth: 11.8 m). **c)** Bedrock sample (zone VI) with a carbonate veinlet (average depth: 82.6 m).

2.3.4 Physical properties

The average bulk bedrock density below 80 m is 2.757 ± 0.005 g cm^{-3} (Table S2-1). In the strongly altered zone V, the average bulk density decreases to 2.64 ± 0.06 g cm^{-3}. At 26 m the density is as low as 2.58 g cm^{-3} (Figure 2-5a). The uncertainty of density measurements is within 0.2%. We did not capture the decrease in bulk density expected at the surface because our method required coherent samples which also have low porosity. To counter a potential decrease in density the abundance of secondary minerals with higher density also increases towards the surface. This is also reflected in the higher matrix density data (Figure 2-5b, Table S2-1). Densities as low as 2.3 g cm^{-3} were calculated from p-wave velocity measurements. Soil densities from 0 to 60 cm depth are on average at 1.5 g cm^{-3}(Oeser et al., 2018a).

The average porosity of bedrock determined by helium (He) porosimetry is 0.3 ± 0.2% (SD). The He porosity is increasing to 7.5% (average 3.5 ± 3%) in the strongly altered zone V. Higher porosity was found at 42 m (4%), 30 m (4.8%), at 26 m (7%), and at 15.5 m (4.8%) (Figure 2-5c; Table S2-1). Surface porosities remain low (0.7 – 2.7%) as samples needed to be coherent for the measurement and thus do not reflect unconsolidated saprolite. He porosity measurements are within an uncertainty of 1%. Values for water- available porosity are consistent with He porosity, whereas the water available porosity calculated from saturation is lower than He porosity. Some samples with extremely low He porosity show higher values for water available porosity; these differences are within uncertainty, however. We assume the water-available porosity reflects the connected porosity.

For bedrock in zone VI, the average value of the specific surface area (SSA) is 2.0 ± 0.5 m^2 g^{-1} (Figure 2-5d). The strongly altered zone V shows higher SSA ranging from 2.36 to 5.21 m^2 g^{-1}. In zones III and IV, higher SSA around 6.5 m^2 g^{-1} occur locally in zone III but most of the measured SSA ranges between 1.5 and 4.5 m^2 g^{-1}. Towards the surface, the SSA increases from 6.0 to 11.0 m^2 g^{-1} (Table S2-1).

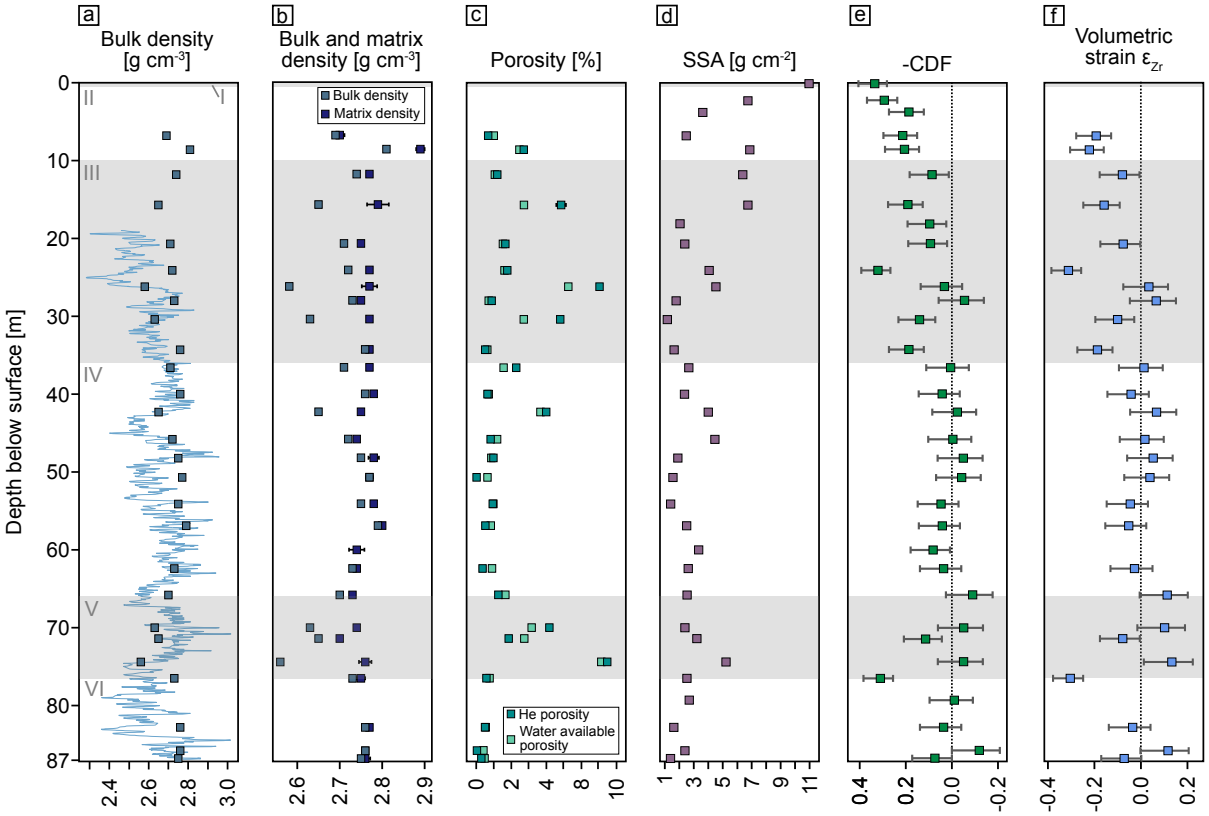

Figure 2-5. a) Measured bulk density (dark blue) and calculated bulk density from p-wave velocities (light blue). **b)** Matrix density indicates the density rock density without pores; bulk density the density including pore volume. Error bars indicate the standard deviation of 10 replicate measurements of the same sample. **c)** Porosity measured with He pycnometry ("He Porosity") and water saturation ("Water available porosity"). **d)** Specific surface area (SSA) of powdered samples measured by N_2 sorption analysis using the BET equation. **e)** Chemical depletion fraction (CDF) shows Fractional mass loss relative to the average of four bedrock samples (negative CDF). Dotted reference line for zero mass loss. Values < 0 indicate elemental loss. **f)** Calculated volumetric strain (ε_{Zr}) for the weathering profile. Positive values indicate dilation whereas negative values denote the collapse of the profile. The accuracy of the CDF and of ε_{Zr} is limited by the variability in bedrock Zr concentration which is shown as error bars on all samples in panel E and F. Grey and white shades denote the core zones (I-VI) described in the results.

2.3.5 Weathering indicators

The chemical depletion fraction (CDF, see Methods) quantifies the fraction of mass lost by weathering relative to the bedrock. In zone V, CDF values between 0.11 and 0.31 indicate a loss of more soluble elements. Zone IV appears to be virtually unweathered with CDF values between 0.08 and -0.09. Starting with zone III, the CDF is constantly decreasing towards the surface. At 24 m below the surface (zone III), a high-weathering degree zone with a CDF of -0.32 was found (Figure 2-5e; Table S2-4). A continuous gradient in CDF was only encountered in zone II where also the shallowest sample yielded the lowest CDF of 0.33. Generally, positive CDF values were found where fracturing is more pervasive as seen by televiewer data. The fractional elemental mass loss (τ, see methods) generally reflects the CDF. Most elements are

depleted in the deep altered zones III and V, except for potassium (K) and uranium (U). The most strongly depleted elements at the surface compared to the bedrock are K (-0.46), U (-0.43), and Ca (-0.41) (Figure 2-6, 2-7a; Table S2-4).

Strain (ε_{Zr}), the change in volume relative to bedrock (Brimhall and Dietrich, 1987), yields values near zero for saprock in zone IV (0.11 to -0.05). More weathered zones (zone III and V) show variable strain (Figure 2-5f). Towards the surface, especially in zone II, the calculated values are negative (-0.08 to -0.22), indicating collapse.

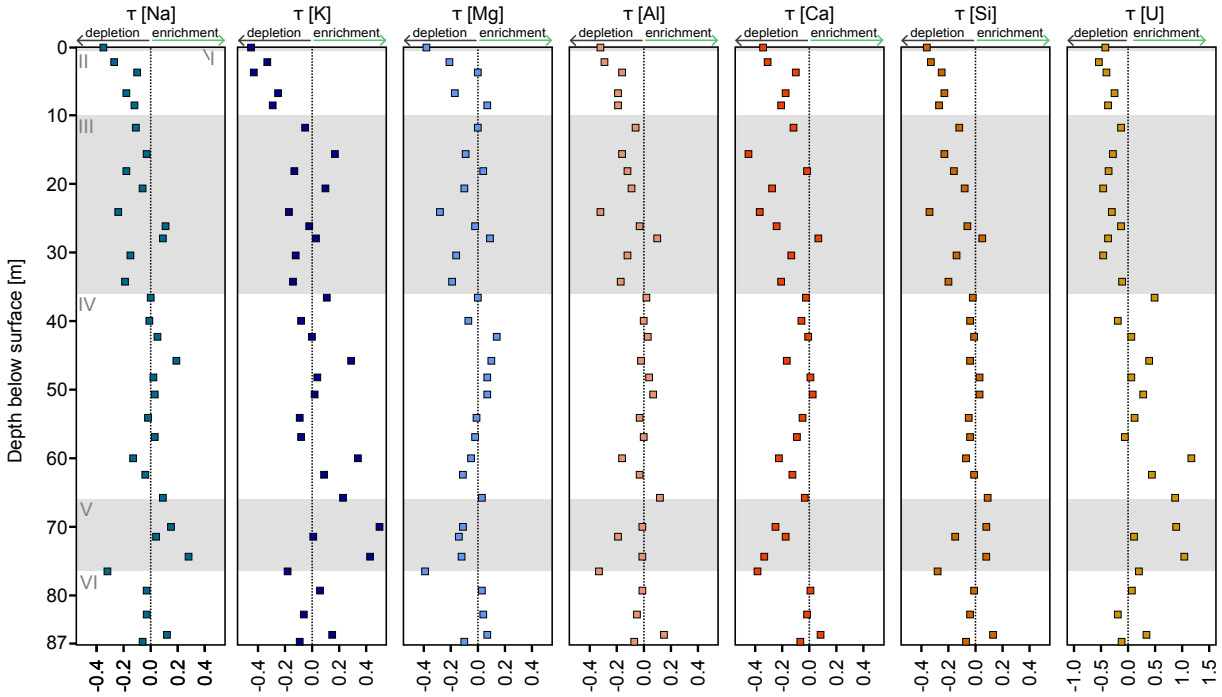

Figure 2-6. Elemental mass transfer coefficient (τ) calculated relative to four averaged bedrock samples. Values < 0 indicate depletion of an element whereas values > 0 indicate enrichment relative to bedrock. Dotted reference line indicates zero mass loss. Grey and white shades denote the core zones (I-VI) described in the results.

2.3.6 Redox state and extractable oxides

$Fe(III)/Fe_{total}$ in bedrock is 0.37 ± 0.05 (Table S2-5). An overall trend of increasing $Fe(III)/Fe_{total}$ ratios towards the surface is recognizable, with Fe being more oxidised in almost all weathered samples compared to bedrock (Figure 2-7b). In the highly altered zones V and III, $Fe(III)/Fe_{total}$ increases to 0.42 – 0.50, whereas $Fe(III)/Fe_{total}$ ratios in zone IV depict similar values as bedrock. Highest $Fe(III)/Fe_{total}$ is found at the surface (0.66) where the loss of total Fe is also highest as denoted by τ_{Fe}.

In deep bedrock, 3.68 mg Fe g^{-1} was extracted by citrate bicarbonate dithionite (CBD; reducible oxides). In weathered rock the amount of extracted Fe ranges from 4.24 – 8.94 mg Fe g^{-1} rock powder (Figure 2-7; Table S2-5). When compared to the total amount of iron in each sample, we extracted 7.8 – 18.3% of total iron. With CBD extractable Si concentrations

obtained from bedrock are 0.750 - 1.55 mg Si g^{-1} rock powder. In weathered rock, the concentrations range from 0.552 – 1.25 mg Si g^{-1} rock powder. Extractable Al concentrations in bedrock are 0.516 – 0.900 mg Al g^{-1} rock powder. In weathered rock they range from 0.750 – 1.51 mg Al g^{-1} rock powder (Figure 2-7d, e). Compared to total Si, CBD extractable Si accounts for 0.23 – 0.56% (CBD). CBD extractable Al accounts for 0.64 – 1.98% of the total Al.

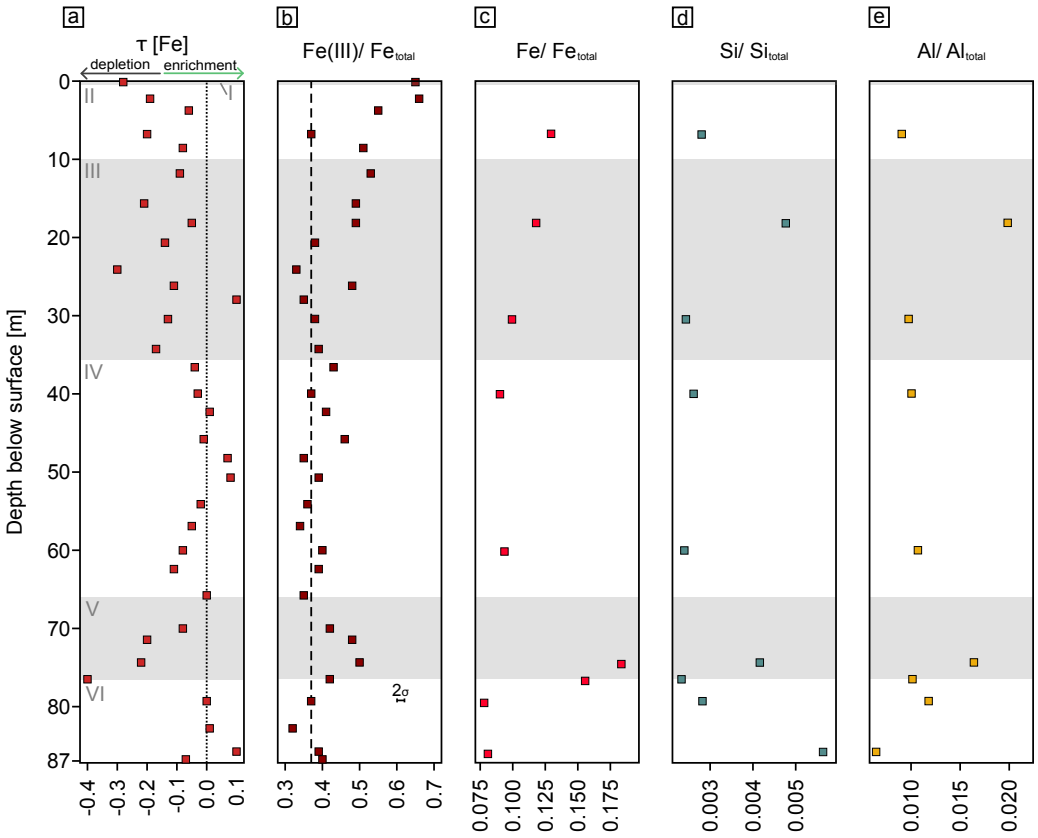

Figure 2-7. Weathering degree characterization by using Fe, Si, and Al. **a)** Elemental mass transfer coefficient (τ) of Fe, dotted line indicates zero loss. Values < 0 show relative depletion of Fe, values > 0 enrichment of Fe relative to bedrock. **b)** Redox state of bulk drill core samples, here shown as Fe(III)/Fe_{total} ratios. Dashed line indicates the average bedrock value of 0.37. **c)** Ratio of reactive Fe mineral fraction (extractable by citrate bicarbonate dithionite, (CBD)) to total Fe content here expressed as Fe/Fe_{total}. **d)** Si/Si_{total} ratios representing ratio of CBD extractable Si to total Si. **e)** Al/Al_{total} ratios representing ratio of CBD extractable Al to total Al. Grey and white shades denote the different zones (I-VI) described in the results.

2.3.7 *In situ* ^{10}Be

Soil denudation rates from *in situ* cosmogenic ^{10}Be at the drill site range between 24.8 and 35.6 t km^{-2} yr^{-1} (mean 29.6 ± 4.0 t km^{-2} yr^{-1}, *n* = 4). Their integration time is 56 ± 7 kyr (see Methods). By comparison, denudation rates from soil pits nearby range from 16 to 22 t km^{-2} yr^{-1} (Schaller et al., 2018), whereas catchment-average denudation rates in the study area are 20 to 29 t km^{-2} yr^{-1} (van Dongen et al., 2019). Using the topsoil CDF of 0.33 a core-integrated weathering rate of 9.9 ± 1.3 t km^{-2} yr^{-1} results. Using the CDF of 0.21 at the

bottom of zone II (8.6 m depth) a weathering rate integrating from 80 m to 10 of 6.1 ± 0.8 t km^{-2} yr^{-1} is obtained.

2.4 Discussion

The main difference between our study site in arid climate and study sites in temperate and humid climate (Bazilevskaya et al., 2013) is the great depth in the granitoid rocks (as deep as 76 m) to which weathering proceeds. Rather than a continuous gradient in weathering indicators, we found several distinct weathering fronts at 20, 36, and 76 m depth that, unlike those set by chemical reactions driven by top-down inputs (Brantley et al., 2017b), repeat each other in style and intensity.

A key observation is that the depletion of the most soluble major elements is concomitant with high fracture density, high porosity, and low bulk regolith density. Moreover, the highest elemental loss is detected in the proximity of planar fractures or fracture zones. In particular, many observed fractures are rimmed by weathered halos. We therefore assume that fractures act as a major pathway for the advective transport of reactants to depth (Lebedeva and Brantley, 2017). Many of these fractures are part of the first and second fracture group identified in the televiewer data. The approximate N-S orientation and moderate to high dip angles of these fractures are consistent with the orientation of faults in the study area and the general strike and kinematics of the Atacama fault system. We interpret these fractures to have formed during the Late Mesozoic activity of the fault system and to record damage offside larger faults, although we cannot exclude that some of these fractures relate to the cooling of the diorite. The remaining fracture sets may be modern, and have formed either by stress relief during denudation (St. Clair et al., 2015), or through Fe oxidation.

The described events have preconditioned the distinct weathering zones (Figures 2-5, 2-6). The unweathered zone IV is identical in all parameters to zone VI (bedrock). Zone III and V represent two weathered intervals, as indicated by mass loss (negative CDF), increased surface area, loss of soluble elements Na and Ca (τ), and volumetric dilation (positive strain ε) that is correlated with increasing porosity (Figure 2-8). Porosity likely forms by dissolution of plagioclase and hornblende without precipitation of pore-filling secondary minerals. In these zones, Fe oxidation, for example in biotite, is the most likely explanation for the increase in volume. Positive volumetric strain is found in zone V (Figure 2-5f). In contrast, zone III shows a collapse of the profile indicated by negative volumetric strain. As this is an unlikely process, we assume a bias in Zr concentration caused by a different bedrock type.

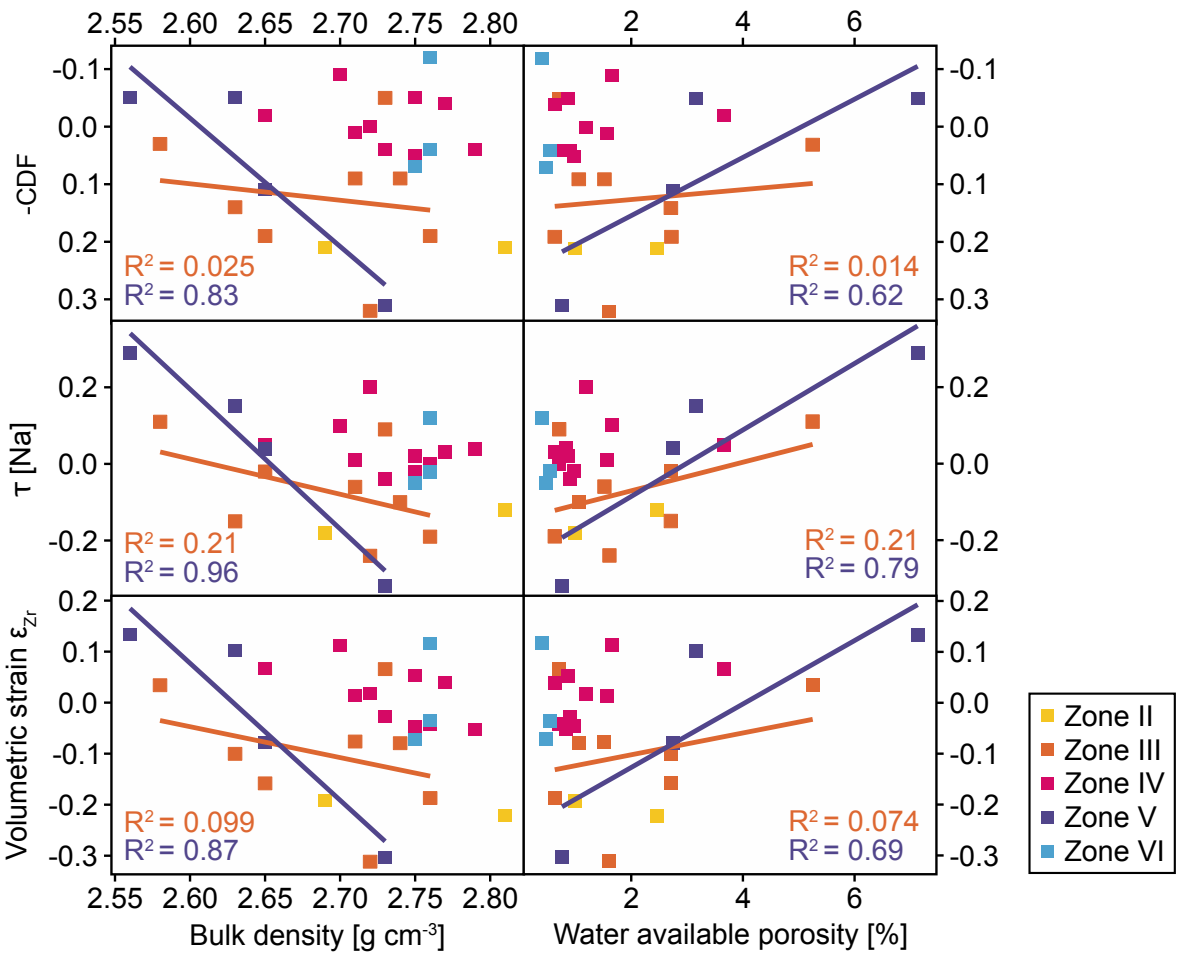

Figure 2-8. Chemical weathering indicators CDF and τ, and volumetric strain ε_{Zr} versus bulk density and water-available porosity. Chemical loss in the more strongly weathered zones III and V (orange and purple) shows a significant dependance on density and porosity, whereas less weathered (pink) and unweathered (blue) zones IV and VI shows no dependance. Physical weathering indicated by volumetric strain ε_{Zr} shows a dependence on density and porosity but variations in porosity cannot completely traced back to an increase in strain. More coherent and therefore less weathered samples are over-represented because the petrophysical analysis could not be conducted on disintegrated samples.

In zone II, the topmost 7 m, all elements get significantly depleted except for U (Figure 2-6, 2-7a). Because these samples consist of incoherent saprolite, most weathering indicators exceed those in the deeper alteration zones III and V, and because similar mass losses have been found in soil profiles over the same rock type close to the drill site (Oeser et al., 2018a), we attribute this increased weathering intensity to decreasing lithostatic pressure during exhumation (Martel, 2011) , root wedging, and infiltration of meteoric fluid contribute to weathering rather than this zone merely reflecting a repetition of the deep features (Hayes et al., 2019).

The first weathering reaction taking place in the rock matrix in the vicinity of the faults is then *in situ* Fe oxidation of Fe-bearing minerals like biotite and hornblende which induces an increase in volume (Buss et al., 2008). Fe oxidation of these minerals produces strain which in

turn can lead to the formation of weathering-induced micro-fractures (Behrens et al., 2015; Fletcher et al., 2006).

That *in situ* Fe oxidation of bulk rock represents the dominating alteration process throughout the core is supported by the citrate bicarbonate dithionite extractable Fe. This fraction represents the reducible Fe(III) (oxyhydr)oxides and reflects the general trend indicated by the $Fe(III)/Fe_{total}$ ratios. The amount of reducible and poorly crystalline oxides is substantial: it represents about 10 -20% of the Fe pool of the entire drilling core and is particularly prominent in the highly altered zone V. However, the total amount of extractable iron is higher than reported in Oeser *et al.* (2018a). This is likely a result of increased extraction efficiency from the smaller grain size of our powdered rock samples compared to their sieved soil samples. Yet this substantial oxidation cannot unequivocally be attributed to weathering as sole cause. Hydrothermal alteration, as evidenced by martitised magnetite in association with chlorite and laumontite, might have led to some of the pronounced Fe oxidation, and would have pre-conditioned the deep rock for later weathering.

Following from the sum of these observations we group the alteration features into three categories: 1) obviously hydrothermal, characterised by minerals clearly of hydrothermal origin like chlorite, laumontite, and sericite. 2) Obviously weathering-related, mainly characterised by chemical mass loss found in the upper 7 m towards the surface. 3) Not unequivocally attributable, as characterised by Fe oxides that can be of either hydrothermal or weathering-induced origin. The origin of these Fe oxides is subject of future studies.

2.5 Implications

The absence of a continuous weathering gradient in the drill core implies that here water flow through porous media might not be the main driver of weathering. We rather hypothesise that advection of fluids and gases through tectonic fractures sets deep weathering at multiple weathering fronts, since we found elevated degrees of chemical depletion close to larger fractures. Furthermore, the high abundance of magnetite might serve as a redox couple for deep microbial communities, enhancing silicate weathering in the process. Compared to semi-arid climates, weathering zones in humid climate show a higher chemical depletion and a shallower weathering zone (Behrens et al., 2015; Goodfellow et al., 2016; Uhlig and von Blanckenburg, 2019). In such settings, the formation of secondary minerals might in fact reduce the porosity and thereby limits the depth of fluid infiltration to the reaction front (Behrens et al., 2015; Jamtveit et al., 2011). In contrast, in Santa Gracia this is not the case due to the lack of secondary minerals.

Finally, at this stage we cannot fully discount that the deep weathering fronts at Santa Gracia are ancient features. For example, the development of deep weathering could possibly date back to before the aridification of the Atacama Desert initiated in the Miocene (Dunai et al., 2005). We regard this possibility as unlikely, however. Such ancient weathering features may not have survived in the Chilean Coastal Cordillera due to the steady tectonic uplift, and

likely ensuing erosion. For the drill sites' steady state denudation rate of 29.6 t km^{-2} yr^{-1}, corresponding to about 11 m Myr^{-1}, the entire weathering zone is turned over about every 7 Myr. Thus, the zone might contain only a brief memory of the Miocene. Yet, this slow turnover allows generation of the observed weathering features even with minute fluid flow.

2.6 Methods

2.6.1 Geophysical borehole logging

After coring, geophysical well logging was conducted including gyroscope, acoustic televiewer, spectral gamma ray, full wave sonic, induced polarization/ resistivity, vertical seismic profile (VSP), and single point resistance (SPR). Detailed data sets for all used tools are available in Weckmann *et al.* (2020). The televiewer data (acoustic Televiewer BHTV 42 from Electromind S.A.) was spatially oriented using a north-seeking Fiber Optic Gyro (Beijing Liuhe Greatness Technology, China). Representing the dip directions of structures, the azimuth was measured clockwise with respect to magnetic North. Azimuth and dip information allows to investigate fractures, borehole breakouts, and information on lithological features and boundaries. It utilizes the surface reflectivity of the wall in a fluid-filled borehole and the reflectance of ultrasonic pulses. The deviation from verticality between the surface drill location and the total depth of 87.2 m was about 1.3 m Southeast.

2.6.2 Sample preparation and processing

Directly following the retrieval of each 1.5 m core run from the well, 20 – 30 cm long samples were separated from the core runs by using an angle grinder, hammer and chisel under sterile conditions. Samples were immediately stored in cooled (4 °C) vacuum-sealed bags. After shipment, we divided the samples by using a mechanical rock trimmer into a sample used for geochemical analyses (3-4 kg) and an archive sample that comprises the outer part of the core. The inner part of the core (0.5-1 kg), exposed to the lowest amount of drill fluid, is used as a sample for geomicrobiological analyses since a contamination by the drilling fluid should be minimal. Geochemical samples were further processed using a jaw breaker and subsequently a ball mill whereas microbiological samples were ground to a final grain size of < 2 mm by using a flame-sterilised disk mill. Every instrument in direct contact with the sample was first cleaned with ethanol and then treated with a Bunsen burner. The size of the samples and depth interval sampled (20-30 cm) are considered to average out variations, being representative in mineral abundance and fracture occurrence for the respective depth intervals.

2.6.3 Contamination control

To assess the infiltration of drilling fluid into the drill core, a tracer was added to the fluid. We used a well-established protocol (Friese et al., 2017), employing a fluorescent pigment dispersion (SPL-594N, Day-Glo, Cleveland OH, USA) and detection by fluorescence microscopy. Ranging from 0.25 to 0.45 µm, the pigment particles are similar sized to environmental microorganisms. The pigment dispersion had a particle concentration of about 1 $x10^{15}$ particles L^{-1} in undiluted form and was added to the drilling fluid that obtained a final particle concentration between 1.1 $x10^{11}$ to 6 $x10^{11}$ particles L^{-1}. Particle concentration in the drilling fluid was checked and adjusted regularly. Each time a core was retrieved from the well, a drilling fluid sample ("liner fluid") was collected from the liner into a 15 mL centrifuge tube. A subsample of 0.5 mL was mixed with 9.5 mL particle-free water and 10 µL of the diluted sample were filtered on 0.2 µm polycarbonate membrane filters (Whatman Cyclopore) resulting in at least 200 countable particles using a Leica DM2000 fluorescence microscope with a UV filter set (Leica Filter Cube A, excitation BP340-380nm, dichromatic mirror 400 nm, suppression LP425 nm). To estimate drilling fluid infiltration into inner core sections, about 250 mg of previously homogenised, crushed inner core samples were ground in a porcelain mortar and suspended in 1 mL MilliQ water. The suspension was shaken vigorously for 30 min and allowed to settle for 5 min. Tracer particles do not settle because of their small size and specific gravity of 1 - 1.1 g mL^{-1}. 200 µL of the supernatant were then processed and analysed using the same method as for the liner fluid described above. Particle counts were converted to volume of drill fluid infiltration per mass of material, considering liner fluid concentration and a reduced count efficiency for this sample preparation, caused by mineral particles covering tracer particles and quantified by control experiments. The detection limit of the method is 0.02 µL drilling fluid infiltration per gram of sample.

2.6.4 Element concentrations and modal mineral composition

Element concentrations were determined with inductively coupled plasma mass spectrometry (ICP-MS) and inductively coupled plasma optical emission spectrometry (ICP-OES) in a commercial laboratory (Activation Laboratories Ltd., Canada). On pulverised samples (< 74 µm), lithium metaborate and tetraborate fusions were performed using a robotic system. Sample analysis was performed by ELAN 6000, 6100 or 9000 ICP-MS (Perkin Elmer Sciex). For data quality control, replicates were analysed every 17 samples and reference material were measured before and after every sample batch (reference: actlabs.com, 2020). The measured element concentrations were corrected for the loss on ignition (LOI):

$$[X]_{corr} = \frac{[X]_{measured} * SUM_{measured}}{SUM_{measured} - (LOI_{measured} - \overline{LOI}_{bedrock})} \quad [2\text{-}1]$$

where $[X]_{corr}$ and $[X]_{measured}$ are the corrected and the measured concentration of an element, respectively, $SUM_{measured}$ is the sum of all analysed elements (including LOI), $LOI_{measured}$ is the measured loss on ignition of a sample, and $\overline{LOI}_{bedrock}$ the averaged loss on ignition of bedrock samples.

The modal mineral composition of a bedrock sample was investigated using a micro x-ray fluorescence device (µ-XRF M4 Tornado, Bruker, USA) at the Technische Universität Berlin. An area of 57 times 57 mm of a bedrock sample slab (cut perpendicular to the drilling direction) was mapped. A measuring spot size of 20 µm with a distance between spots of 50 µm were chosen and the integration time was 30 ms point^{-1}. The maps were analysed with the open-source image processing program ImageJ and element combinations were attributed to the different minerals (i.e. calculation of area shares which are occupied by the respective element combinations). The modal mineral composition is complemented by ordinary point counting with an optical light microscope.

2.6.5 Fe(III)/Fe$_{total}$ ratios

To determine Fe(III)/Fe$_{total}$ ratios, we used a colorimetric method as described by Schuessler *et al.* (2008). 8 to 10 mg of powdered sample aliquots were decomposed in a HF-vanadate mixture using V^{5+}. After addition of 2:2’ bipyridyl solution Fe(II) concentrations were measured on 10 mL of this solution by spectroscopy using a UV/VIS SPEKOL 1500 (Analytik Jena, Germany) in 1 cm transmission cells at 523 nm. After the Fe(II) measurement, hydroxylamine hydrochloride was added to the solution. Hydroxylamine hydrochloride acts as reducing agent and converts all Fe^{3+} to Fe^{2+} such that total Fe is obtained. By dividing the measured absorbances of Fe^{2+} and total Fe, the Fe(II)/Fe$_{total}$ ratio and the Fe(III)/Fe$_{total}$ ratio can be calculated. Weighing and dilution errors thus cancel out and uncertainties are primarily from spectroscopic measurements. Reference materials (GA and AC-E granite reference materials) and procedure blanks were run for quality control. Repeated measurements of standard solutions result in an uncertainty of ± 0.02 (2SD) for Fe(III)/Fe$_{total}$ ratios.

2.6.6 Oxide extractions

We extracted Fe in duplicates following a modified protocol of Mehra and Jackson (1958) using citrate bicarbonate dithionite (CBD; pH 7). CBD extracts crystalline and poorly crystalline iron (easily reducible oxides) such as ferrihydrite, goethite and powdered hematite[48]. For each sample, 30 mL CBD were added to 0.5 g powdered samples from 1 to 86 m depth. Extractions were done on a rolling shaker at 10 rpm for 24 h anoxically in the dark. Extractions were centrifuged at 4000 rpm for 10 min, the supernatant removed anoxically and fixed with 1 M HCl in 1:10 dilutions. Finally, we quantified Fe$_{CBD}$ -concentrations with the ferrozine assay and converted it into mg Fe g^{-1} rock powder. Al and Si concentrations were determined on the supernate by microwave plasma atomic emission spectrometry (MP-AES), and Fe

concentrations by the ferrozine assay. All concentrations were converted into mg element g^{-1} rock powder.

2.6.7 *In situ* ^{10}Be

We processed samples for *in situ* ^{10}Be separation in the *HELGES* laboratory at the GFZ German Research Centre for Geosciences (Potsdam, Germany) using the revised methods of von Blanckenburg *et al.* (2004). For ^{10}Be analysis, we added ca. 150 µg of ^{9}Be carrier to each sample. For this carrier, we determined a ^{10}Be/^{9}Be ratio of 3.4×10^{-15} (± 4.4×10^{-15}) which we used for blank correction of measured ^{10}Be/^{9}Be ratios. After Fe and Be column chemistry and alkaline precipitation, Be was oxidised and pressed into accelerator mass spectrometer (AMS) cathodes and ^{10}Be/^{9}Be ratios were measured at the AMS at the University of Cologne relative to standards KN1-6-2 and KN1-5-3 (having nominal ^{10}Be/^{9}Be ratios of 5.35×10^{-13} and 6.32×10^{-12}, respectively; which are consistent with the 07KNSTD standardization.

In order to derive denudation rates *D* (Eq. 2), we calculated nuclide production using the time-dependent scaling scheme of Lal/Stone (St; Balco et al., 2008) calibrated to a sea-level high latitude (SLHL) neutron spallation ^{10}Be production rate of 4.01 at g^{-1} yr^{-1} and solved the equation for *D*,

$$\left[{}^{10}Be\right] = \frac{P_N}{\lambda + \frac{D}{\Lambda_N}} + \frac{P_\mu}{\lambda + \frac{D}{\Lambda_\mu}} \qquad [2\text{-}2]$$

where $[{}^{10}Be]$ is the measured ^{10}Be nuclide concentration (at $g_{(Quartz)}^{-1}$), P_N is the scaled ^{10}Be neutron production rate and P_μ that for muons (at g_{qtz}^{-1} yr^{-1})), Λ_N and Λ_μ are the e-folding absorption lengths for neutrons and muons, respectively (g cm^{-2}), and λ is the decay constant of ^{10}Be (5×10^{-7} yr^{-1}). The absorption of muons is calculated by a single exponential function derived from Beacon Heights, Antarctica (Balco, 2017). The term ρ/Λ is often replaced by z*, the absorption depth scale (cm), which is the distance over which the cosmic-ray flux decreases over the *e*-folding length, or 63%. This vertical distance, divided by the denudation rate, gives the integration timescale of the method.

2.6.8 Density, porosity, water available porosity

Buoyancy, He porosimetry, and water porosimetry were used to determine density, porosity, and water-available porosity of physically coherent samples. We first calculated a samples' bulk Volume V_{bulk} by assuming $V_{bulk} = V_{water}$, with V_{water} being volume of the fluid displaced by a rock sample.

$$V_{bulk} = V_{water} = \frac{m_{water}}{\rho_{\text{fluid}}}. \qquad [2\text{-}3]$$

Here m_{water} is the mass of the displaced fluid (e.g. water) and ρ_{fluid} is the density of the fluid at a certain temperature. With this volume V_{bulk} , the sample density ρ_{bulk} can be calculated:

$$\rho_{bulk} = \frac{m_{\mathrm{dry}}}{V_{bulk}} \quad [2\text{-}4]$$

where m_{dry} is the dry rock sample mass. The estimated uncertainty of the density measurements is < 0.3%.

He pycnometry was used to estimate the matrix volume V_{matrix} of the solid part of a sample. The measurements were conducted on the same samples as used for density determination. Samples were dried and weighed before placing them in an AccuPyc 1030 He pycnometer (Micromeritics, USA). The sample was placed into a sealed chamber which was then flooded with He. Because the volume of the chamber is known, V_{matrix} can be calculated from the difference in chamber fill volume. Porosity ϕ_{He} can be obtained with:

$$\phi_{\mathrm{He}} = \frac{V_{\mathrm{bulk}} - V_{\mathrm{matrix}}}{V_{\mathrm{bulk}}} \quad [2\text{-}5]$$

Uncertainty of the measurements are < 0.03% of gas displacement reading plus 0.03% for the chamber volume.

The water-available porosity measured with water porosimetry ϕ_{con} can be calculated from the sample weight before and after saturation with deionised water for 48 h:

$$\phi_{\mathrm{con}} = \frac{V_{\mathrm{sat}}}{V_{\mathrm{bulk}}} \quad [2\text{-}6]$$

where V_{sat} is the volume of pores saturated with water. The uncertainty of the connected porosity is < 0.14%.

For comparison we used the measured P wave velocity from the sonic log to derive a calculated density log. We applied a parameterised velocity-density relationship based on global petrophysical studies for sedimentary, igneous, and metamorphic rocks (Ludwig et al., 1970; Christensen and Mooney, 1995).

2.6.9 Specific surface area (SSA)

The specific surface area (SSA) was determined by nitrogen gas sorption using the BET equation (Brunauer et al., 1938). About 3 g of powdered sample material was degassed in a Vac Prep Q61 Sample Degas System (Micromeritics, USA). During the degassing process, bedrock samples were heated up to 250 °C, samples from zones C-E up to 60 °C for durations of 8 to 20 hours, and samples from zona A and B up to 120 °C for 16h. After degassing, the

SSA was measured by N_2 sorption in a Gemini VII Surface Area and Porosity analyser (Micromeritics, USA). The uncertainty of the SSA measurement is ~1.1% based on repeat analysis (n = 3, relative SD = 0.29%) of a certified reference material (Carbon Black, SSA_{BET} = 21.52 ± 0.75 $m^2\ g^{-1}$). The detection limit is 0.01 $m^2\ g^{-1}$.

2.6.10 Calculations of weathering indicators

Weathering indicators have been calculated from elemental concentrations. The chemical depletion fraction (CDF) represents the relative mass loss due to chemical weathering of the bedrock (Riebe et al., 2003):

$$CDF = 1 - \frac{[X_i]_{\mathrm{p}}}{[X_i]_{\mathrm{w}}} \qquad [2\text{-}7]$$

where $[X_i]_{\mathrm{p}}$ and $[X_i]_{\mathrm{w}}$ are the concentration of the immobile element $[X_i]$ in the weathered saprolite (w) and the unweathered parent bedrock (p), respectively. We used Zr as immobile element. Zero elemental loss during chemical weathering from parent bedrock to saprolite yields as a CDF of zero. We used four samples without visible weathering features as the average value for bedrock. In granitic rocks, the CDF can attain a maximum value of 0.5 if weathering is complete and only quartz, clay minerals, and secondary oxides remain. The loss of individual elements during chemical weathering can be calculated with the mass transfer coefficient $\tau_{j,w}$ (tau; Anderson et al., 2002). The ratio of the concentration X of in weathered rock to that in parent bedrock material depends on the loss of the element j , but also on the loss of other elements. Thus, the calculation $\tau_{j,\mathrm{w}}$ includes concentrations of an immobile element $X_{i,\mathrm{p/w}}$:

$$\tau_{j,\mathrm{w}} = \frac{[X_j]_{\mathrm{w}}\,[X_i]_{\mathrm{p}}}{[X_j]_{\mathrm{p}}\,[X_i]_{\mathrm{w}}} - 1 \qquad [2\text{-}8]$$

where $[X_j]_{\mathrm{w}}$and $[X_j]_{\mathrm{p}}$ are the concentrations of an element j in weathered saprolite and unweathered parent bedrock. $\tau = 0$ indicates zero loss of an element relative to the bedrock, $\tau < 0$ shows loss of a certain element whereas $\tau > 0$ means gain. Because the sense of τ is opposite to that of CDF we plot - CDF in figures 2-2 to 2-5 to facilitate comparison.

A weathering rate W assuming steady state denudation is calculated from the cosmogenic nuclide-derived soil denudation rate D and CDF:

$$W = D * CDF \qquad [2\text{-}9]$$

2.6.11 Volumetric strain ε_{Zr}

To calculate the volumetric strain ε_{Zr}, we used the average bedrock Zr concentration $[X_i]_\mathrm{p}$ and the average bedrock bulk density ρ_{bulk_p} as well as the Zr concentration $[X_i]_\mathrm{w}$ and the bulk density ρ_{bulk_w} of a weathered sample (Table S2-1, S2-2; Brimhall and Dietrich, 1987):

$$\varepsilon_{Zr} = \frac{\rho_{bulk_p}}{\rho_{bulk_\mathrm{w}}} * \frac{[X_i]_\mathrm{p}}{[X_i]_\mathrm{w}} - 1 \qquad [10]$$

Values close to zero indicate isovolumetric weathering. Positive values show dilation whereas negative values indicate a collapse of a profile.

2.7 Acknowledgements

This project is funded by German Science Foundation (DFG) grants within the priority program 1803 “EarthShape – Earth surface shaping by biota”. The authors would like to thank L. Paulino and T. Ehlers for their support in planning and performing the drilling campaign. Further, the authors are grateful to J. Kück for advice and assistance on the televiewer data, to K. Bauer for implementing the density calculation from logging data, and to J. Kallmeyer for assisting with the contamination control. The authors also thank the section *Geomechanics and Scientific Drilling* at the Helmholtz Centre Potsdam GFZ German Research Centre for Geosciences for using their facilities.

3. Exploring soil denudation along an extreme climate gradient with in-situ cosmogenic ^{10}Be and meteoric $^{10}Be/^{9}Be$

Abstract

Along an extreme climate gradient in the Chilean coastal mountains, we investigated denudation and weathering rates using the meteoric cosmogenic nuclide ^{10}Be and its ratio to stable ^{9}Be. Given the novelty of this proxy, we compared the denudation rates to those determined by the established *in situ* cosmogenic ^{10}Be system and chemical depletion fractions (CDFs). Our results show that the fraction of ^{9}Be released from bedrock is a sensitive indicator of weathering with a depth distribution similar to CDF. In contrast, meteoric ^{10}Be decreases exponentially with depth, reflecting the reactive nature of this tracer. Denudation rates are consistent between both methods in the mediterranean and humid areas. However, in arid to semi-arid sites, the soil inventory of ^{10}Be indicates a deficit in the depositional flux of meteoric ^{10}Be, suggesting a lower limit for the use of the $^{10}Be/^{9}Be$ method at an annual precipitation of 400 mm.

Plain language summary

Quantifying the rates of soil denudation by erosion and weathering over the time scale of soil formation (e.g. kiloyears) is essential towards identifying controls over mass fluxes at Earth's surface. Today, the state-of-the-art technique used towards this aim is *in-situ* cosmogenic ^{10}Be. However, this method is limited to quartz-bearing rocks, thus rendering the method unsuited to studies of soils formed on mafic rock, limestone, or fine-grained sediment. To expand the portfolio of rate meters we explored the cosmogenic radionuclide meteoric ^{10}Be produced in the atmosphere in combination with the stable isotope ^{9}Be that is released during rock weathering. The $^{10}Be/^{9}Be$ ratio allows to estimate denudation rates, provided the depositional flux of meteoric ^{10}Be is known. As test, we analysed soil samples from four study sites along an extreme climate gradient in Chile from granitoid rock that permitted the comparison with *in situ* ^{10}Be to estimate this flux. We found that stable weathering-released ^{9}Be indicates the degree of alteration which depends on infiltration by water. The deposition of meteoric ^{10}Be in dry regions is not consistent with deposition fluxes predicted by cosmogenic production functions coupled to climate models. We attribute this difference to an overestimation of dry precipitation in these models. Above a precipitation threshold, however, $^{10}Be/^{9}Be$ ratio yields reliable denudation rate estimates.

This chapter is ready for submission. The co-authors are Hella Wittmann and Friedhelm von Blanckenburg.

3.1 Introduction

The depth of the weathering zone, fluid flow through this zone, and turnover of primary and secondary solids by erosion all represent interdependent controls over rock weathering and soil formation. The ^{10}Be(meteoric)/^{9}Be cosmogenic isotope system is a novel yet underexplored proxy capable to track all of these controls (von Blanckenburg et al., 2012). Application of this proxy to determine basin-wide denudation rates in river samples yielded denudation rates (D_{met}) that are in good agreement with rates determined by the well-understood *in situ* cosmogenic ^{10}Be system (D_{insitu}; e.g. Portenga et al., 2019; Wittmann et al., 2015). Here, we apply meteoric $^{10}Be/^{9}Be$ to depth profiles in soil and weathered rock to evaluate the method's suitability for determining denudation rates from single soil samples.

Meteoric ^{10}Be ($^{10}Be_{met}$), with a half-life of 1.39 Myr (Chmeleff et al., 2010), is produced in the atmosphere by cosmic ray-induced spallation, attaches to atmospheric aerosols and is delivered to Earth's surface by wet and dry deposition (Lal and Peters, 1967; summary in Willenbring and von Blanckenburg, 2010b). After deposition, it is incorporated into amorphous and weakly crystalline (Mn-Fe)-(hydr)oxides (Willenbring and von Blanckenburg, 2010b). Such so-called reactive (reac) phases can be extracted from soils or sediments via sequential extraction. The ^{10}Be fraction retained in the solid depends on pH and grain size. Normalisation of the reactive ^{10}Be concentration to stable ^{9}Be concentration that is released from rock during weathering largely removes this dependence (Wittmann et al., 2012). The resulting isotope ratio of meteoric ^{10}Be to ^{9}Be ($^{10}Be_{met}/^{9}Be_{reac}$) is a proxy for weathering and denudation (von Blanckenburg et al., 2012). Compared to $^{10}Be_{insitu}$, which is produced in the mineral lattice of e.g. quartz by cosmic-ray induced spallation (Lal, 1991), $^{10}Be_{met}$ is present in higher concentrations, can be applied to quartz-free lithologies like mafic rock (Dannhaus et al., 2018) or slate (Deng et al., 2020b), and requires much smaller sample amounts.

To apply $^{10}Be_{met}/^{9}Be_{reac}$, three parameters need to be known: 1), the concentration of stable ^{9}Be in unweathered bedrock ($[^{9}Be]_{parent}$). 2) The fraction of ^{9}Be released from weathering $f^{9}Be_{reac}$+$f^{9}Be_{diss}$ which reveals mobilisation of ^{9}Be from primary minerals comprising ^{9}Be precipitated or adsorbed onto reactive mineral surfaces ($f^{9}Be_{reac}$) or lost into the dissolved phase ($f^{9}Be_{diss}$). $f^{9}Be_{reac}$+$f^{9}Be_{diss}$ can be determined from the ratio of the concentration of ^{9}Be ($[^{9}Be]_{reac}$) adsorbed to or precipitated with reactive phases such as (Mn-Fe)-(hydr)oxides) to the concentration of ^{9}Be ($[^{9}Be]_{min}$) in the mineral-bound phase (von Blanckenburg et al., 2012), provided that dissolved loss of ^{9}Be is negligible which is the case if pH is high or runoff is low. 3) The depositional flux (F_{met}^{10Be}) of $^{10}Be_{met}$ to Earth's surface. Globally, F_{met}^{10Be} depends on atmospheric production rate, geomagnetic field intensity and solar activity (Masarik and Beer, 1999, 2009). $^{10}Be_{met}$ is well-mixed in the stratosphere and therefore latitudinal production variations are averaged out (Heikkilä et al., 2013). Within a residence time of ~1 year, $^{10}Be_{met}$ attaches to atmospheric aerosol particles and is delivered to Earth's surface (McHargue & Damon, 1991). The deposition constitutes three distinct pathways: ^{10}Be by precipitation as wet delivery, by dry delivery on aerosol particles, and by dust which is,

however, recycled ^{10}Be (Deng et al., 2020a). Some studies suggest that the depositional flux correlates with precipitation (Field et al., 2006; Graly et al., 2011; Heikkilä et al., 2013; Heikkilä & Smith, 2013). Other studies noted dilution of $^{10}Be_{met}$ with higher precipitation (e.g. Yiou et al., 1997). These two effects, the "additive" and the "dilution" effect, are explored in detail in Willenbring and von Blanckenburg (2010b) and Deng et al. (2020a). Mostly, these effects operate in combination, where their relative weight depends on the ratio of the area of vapour condensation to area of precipitation (Deng et al., 2020a).

A variety of approaches are used to estimate F_{met}^{10Be}: General Circulation Models (GCM) combined with ^{10}Be production functions and aerosol dynamics; 2) ^{10}Be in precipitation collections; 3) ^{10}Be inventories in dated soil profiles; 4) riverine ^{10}Be exported by solids and in the dissolved form (summarised in Deng et al., 2020a). GCMs provide F_{met}^{10Be} on a large spatial scale (Heikkilä & von Blanckenburg, 2015) while precipitation collection provides local short-term fluxes influenced by seasonal variations and stratosphere-troposphere exchange of air masses (Graly et al., 2011). Deng *et al.* (2020a) found that precipitation-derived F_{met}^{10Be} mostly exceed GCM-derived fluxes. Therefore, F_{met}^{10Be} estimated with the empirical equation by Graly *et al.* (2011) based on precipitation-collections might overestimate long-term deposition where precipitation is high. F_{met}^{10Be} from soil profile measurements and GCMs are generally in good agreement (Deng et al., 2020a).

Here we explored the climate dependence of $^{10}Be_{met}$ deposition and identified possible limitations of the $^{10}Be_{met}/^{9}Be_{reac}$ denudation rate meter by comparing D_{insitu} and D_{met} on eroding soil profiles, an approach previously employed only once (Clow et al., 2020). The principle is based on assuming that $D_{insitu} = D_{met}$ so that F_{met}^{10Be} can be calculated from known D_{insitu}. To do so we measured $^{10}Be_{insitu}$, the inventory of $^{10}Be_{met}$, $^{9}Be_{parent}$, $^{9}Be_{reac}$, and $^{9}Be_{min}$ concentrations in soil and drill core samples, and calculated denudation, erosion, and weathering rates, as well as F_{met}^{10Be}. By employing this method along an extreme climate gradient in the Chilean Coastal Cordillera, and by comparison with published catchment-wide and soil pit-derived D_{insitu}, we show that weathering intensity depends on precipitation, and therefore on the accumulation and mobilisation of Be in depth profiles. We also show below a lower limit of precipitation large spatial-scale estimates of F_{met}^{10Be} from atmospheric models are unsuited to determine denudation rates.

3.2 Study sites and previous work

The study sites Pan de Azúcar (PdA), Santa Gracia (SG), La Campana (LC), and Nahuelbuta (NA) are located along an extreme climate gradient between 26° S and 38° S in the Chilean Coastal Cordillera that was studied by the research program "Earthshape – Earth Surface Shaping by Biota" (Figure 3-1). This gradient covers arid (PdA, 10 mm yr^{-1} average precipitation rate), semi-arid (SG, 90 mm yr^{-1}), mediterranean (LC, 440 mm yr^{-1}), and humid (NA, 1100 mm yr^{-1}) climate with vegetation cover ranging from <5% in arid to 100% in humid climate (Oeser et al., 2018a). The lithology consists of granodiorites, tonalites and quartz

diorites (Oeser et al., 2018a, and references therein). Hydrothermal alteration of the granite is strong at the arid study site, and mild at the semi-arid site as apparent by a high degree of Fe-oxidation and fracture fillings by both carbonates and amorphous Fe-(hydr)oxides (Chapter 2.3.2 and Krone et al., 2021a; Hampl et al., 2022). A detailed geologic description is available in Oeser *et al.* (2018a) and Krone *et al.* (2021a). Previous studies also report on soil-pit-derived (Schaller et al., 2018) and river-sediment-derived (van Dongen et al., 2019) D_{insitu}.

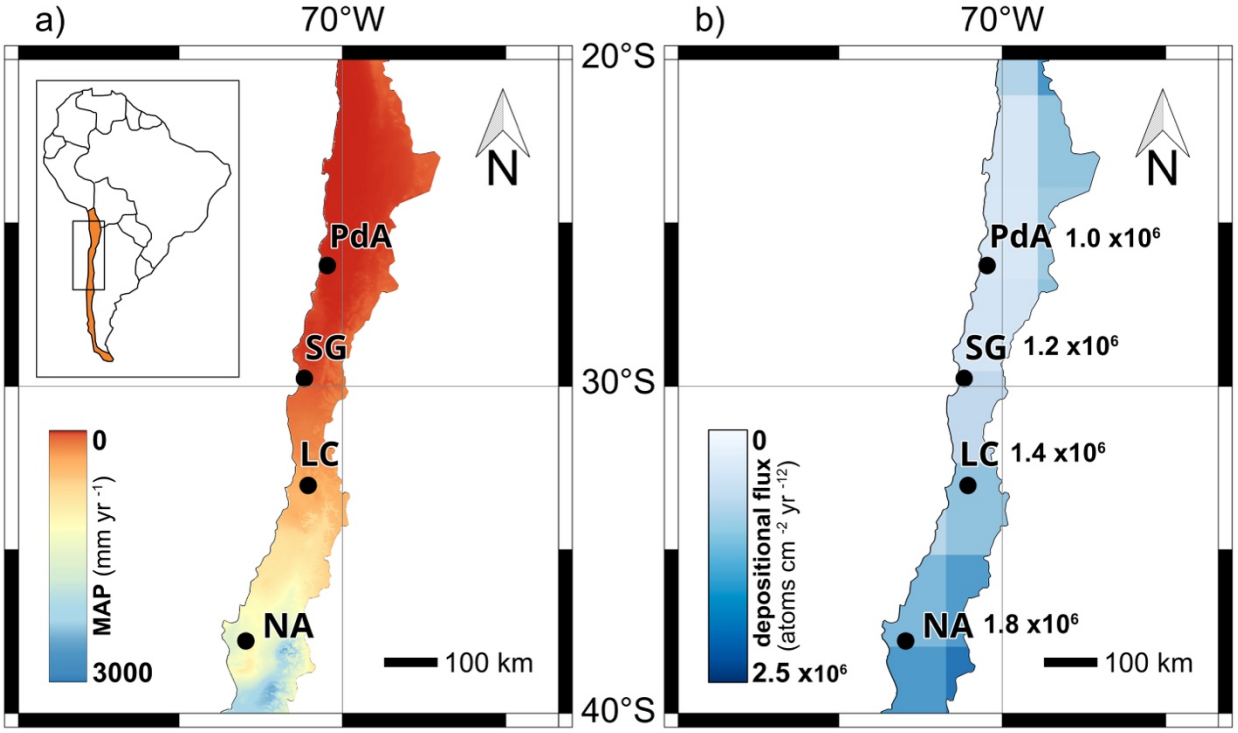

Figure 3-1. Sampling locations in Chile. a) Mean annual precipitation (MAP) averaged from 1970 – 2000 (Fick & Hijmans, 2017: worldclim.org). b) Meteoric ^{10}Be depositional flux map from production functions implemented in the ECHAM5-HAM GCM model (Heikkilä, 2007; Heikkilä & von Blanckenburg, 2015) which also shows the cell size of model values which is about 200 x 200km.

3.3 Materials and Methods

We sampled the upper 2-6 m for soil depth profiles and used visually unweathered parent rock from drill core samples of bedrock from >10 m below the weathering front recovered during wireline diamond drilling campaigns (03/2019 to 03/2020; Chapter 2.2.2 and Krone et al., 2021) .

The detailed procedure for *in situ* and meteoric ^{10}Be analyses is provided as supplementary material. To determine denudation rates D_{insitu}, we used the CRONUS online exposure age calculator (Balco et al., 2008) using the time-dependent scaling scheme of Lal/Stone (St) (Lal, 1991; Stone, 2000) and a sea-level high latitude (SLHL) neutron spallation ^{10}Be production rate of 4.01 at $g^{-1}\ yr^{-1}$ (Borchers et al., 2016). The denudation rate D_{insitu} (in g $cm^{-2}\ yr^{-1}$) can be calculated using equation 1 shown in a simplified form (Lal, 1991):

$$D_{insitu} = \left(\frac{P}{[^{10}Be_{insitu}]} - \lambda \right) \Lambda \quad [1]$$

where [$^{10}Be_{insitu}$] is the ^{10}Be nuclide concentration (atoms g_{qtz}^{-1}), P the scaled ^{10}Be production rate (atoms g_{qtz}^{-1} yr^{-1}), and λ the decay constant of ^{10}Be ($5x10^{-7}$ yr^{-1}). Λ includes the e-folding absorption length for neutrons and muons, respectively.

Denudation rates D_{met} (g cm^{-2} yr^{-1}) were calculated using equation 12 from von Blanckenburg *et al.* (2012) solved for D_{met} with an additional term to account for decay of meteoric reactive ^{10}Be (hereafter $^{10}Be_{reac}$) that may reduce the soil inventory if the infiltration depth is deep and denudation rate is slow:

$$D_{met} = \frac{F_{met}^{10Be} - I * \lambda}{\left(\frac{^{10}Be}{^{9}Be}\right)_{reac} * [^{9}Be]_{parent} * (f\,^{9}Be_{reac} + f\,^{9}Be_{diss})} \quad [2]$$

with F_{met}^{10Be} as meteoric ^{10}Be depositional flux (atoms cm^{-2} yr^{-1}), ^{9}Be concentrations (denoted as [^{9}Be], in atoms g^{-1}) for the reac and min fractions, and parent bedrock, respectively, I as the $^{10}Be_{reac}$ inventory of the soil profile (atoms cm^{-2}) and λ as decay constant of ^{10}Be (yr^{-1}). We calculated the depositional flux by solving equation 2 for F_{met}^{10Be} assuming that $D_{insitu} = D_{met}$. $f^{9}Be_{reac}$+$f^{9}Be_{diss}$ is calculated from [^{9}Be]$_{reac}$ and [^{9}Be]$_{min}$, assuming dissolved loss of ^{9}Be is negligible:

$$f\,^{9}Be_{reac} + f\,^{9}Be_{diss} = \frac{[^{9}Be]_{reac}}{([^{9}Be]_{min} + [^{9}Be]_{reac})} \quad [3]$$

To derive the weathering rate W from a denudation rate D, we use the chemical depletion fraction (CDF):

$$CDF = 1 - \frac{[X_i]_{parent}}{[X_i]_{weathered}} \quad [4]$$

with $[X_i]_{parent}$ and $[X_i]_{weathered}$ as the concentration of an immobile element (PdA, LC, NA: Nb; SG: Zr) in parent and weathered material. The weathering rate $W_{met\ or\ insitu}$ is calculated using the mean CDF (Table S3-1; Chapter 2.3.5 and Krone et al., 2021a) from surface samples according to equation 4.

$$W_{met\ or\ insitu} = D_{met\ or\ insitu} * CDF \quad [5]$$

The erosion rate E_{insitu} can be calculated from D_{situ} and W.

$$E_{insitu} = D_{insitu} - W \quad [6]$$

3.4 Results

We provide all results in supplementary tables (Tables S3-1 – S3-6); main results are listed in Table 3-1. Denudation rates from $^{10}Be_{insitu}$ are 7.1 ± 0.5 t km^{-2} yr^{-1} at the arid (uncertainty is the standard deviation of 3 measured D_{insitu} at the study sites), 29.6 ± 4.0 t km^{-2} yr^{-1} at the semi-arid (Chapter 2.3.7 and Krone et al., 2021a), 126 ± 32 t km^{-2} yr^{-1} at the mediterranean, and 38 ± 10 t km^{-2} yr^{-1} at the humid site. The new D_{insitu} from our soil sites are in good agreement with published *in situ* denudation rates (Schaller et al., 2018; van Dongen et al., 2019).

$[^{9}Be]_{parent}$ is 1.9 ± 0.5 µg g^{-1} at the arid, 1.2 ± 0.1 µg g^{-1} at the semi-arid, 1.0 ± 0.1 µg g^{-1} at the mediterranean, and 1.4 ± 0.4 to 2.1 ± 0.1 µg g^{-1} at the humid site (relative uncertainty 5%). These concentrations are at the lower end of 3.1 ± 1.5 µg g^{-1} $[^{9}Be]_{parent}$ compiled for granitoid lithology (von Blanckenburg et al., 2012). $f^{9}Be_{reac}+f^{9}Be_{diss}$ is highest with 0.46 at the arid site and lowest at the semi-arid and mediterranean sites with 0.11 and 0.12, respectively, and 0.26 at the humid site (Figure 3-2B). $[^{9}Be]_{reac}$ shows no gradient with depth. $[^{10}Be]_{met}$ in topsoil samples correlates with precipitation by showing an increasing concentration from the arid (1.2 ± 0.21 x10^{7} atoms g^{-1}) to the humid (4.5 ± 0.15 x10^{8} atoms g^{-1}) site (Figure 3-2C). In the depth profiles, reactive $[^{10}Be]_{reac}$ decreases exponentially from surface to depth at all study sites (Figure 3-2C).

For the calculation of D_{met}, we used the GCM model-derived F_{met}^{10Be} by Heikkilä and von Blanckenburg (2015) for the respective study sites (Table 3-1). At the mediterranean and humid sites, D_{met} are 169 ± 39 and 30 ± 8 t km^{-2} yr^{-1}, respectively. D_{met} for the arid site is 1235 and for the semi-arid site 210 t km^{-2} yr^{-1}. These latter two rates disagree strongly with D_{insitu}. We discuss the reasons below and do not consider these two D_{met} as meaningful estimates any further.

By inserting D_{insitu} and solving equation 2 for F_{met}^{10Be}, we obtain F_{met}^{10Be} values covering 3 orders of magnitude of (6.3 ± 2.0)x10^{3} at the arid, (1.6 ± 0.3)x10^{5} at the semi-arid, (1.1 ± 0.3)x10^{6} at the mediterranean, and (1.1 ± 0.3 to 3.3 ± 0.3)x10^{6} atoms cm^{-2} yr^{-1} at the humid site.

Table 3-1. Main results for all study sites. CDF: chemical depletion fraction; $F^{10}Be_{met}$: depositional flux; D: total denudation rate; E: physical erosion rate. PdA: arid, SG: semi-arid, LC: mediterranean, NA ridge: humid-ridge, NA slope: humid-slope; NA_{avg}: average humid.

						in situ ^{10}Be		*meteoric* $^{10}Be/^{9}Be$
	$F^{10}Be_{met}$ (GCM-derived)	**$(^{10}Be/^{9}Be)$**	**$[^{9}Be]_{parent}$**	**$f^{9}Be_{reac}$ + $f^{9}Be_{min}$**	**CDF**	**D**	**E**	**D**
	[x10^{6} atoms cm^{-2} yr^{-1}]	[x10^{-9} atoms $atoms^{-1}$]	[µg g^{-1}]			[t km^{-2} yr^{-1}]	[t km^{-2} yr^{-1}]	[t km^{-2} yr^{-1}]
PdA	1.0 ± 0.2	0.14 ± 0.03	1.9 ± 0.5	0.46	0.00 ± 0.00	7.1 ± 0.5	7.1 ± 0.5	(1235 ± 460)*
SG	1.2 ± 0.01	6.4 ± 0.4	1.21 ± 0.07	0.11	0.33 ± 0.02	30 ± 4	19.7 ± 2.7	(210 ± 22)*
LC	1.4 ± 0.3	11.3 ± 0.7	0.97 ± 0.05	0.12	0.21 ± 0.05	126 ± 32	99 ± 25	169 ± 39
NA ridge	1.8 ± 0.4	19 ± 1	1.4 ± 0.4	0.25	0.50 ±0.06	24 ± 1	11.9 ± 2.4	40 ± 14
NA slope	1.8 ± 0.4	19 ± 1	2.14 ± 0.07	0.27	0.56 ± 0.02	45 ± 2	19.8 ± 2.6	24 ± 5
NA_{avg}	1.8 ±0.4	19 ± 1	1.8 ± 0.4	0.26	0.53 ± 0.02	38 ± 10	17.5± 3.9	30 ± 8

*These denudation rates are overestimated because of flux deficits (see Discussion).

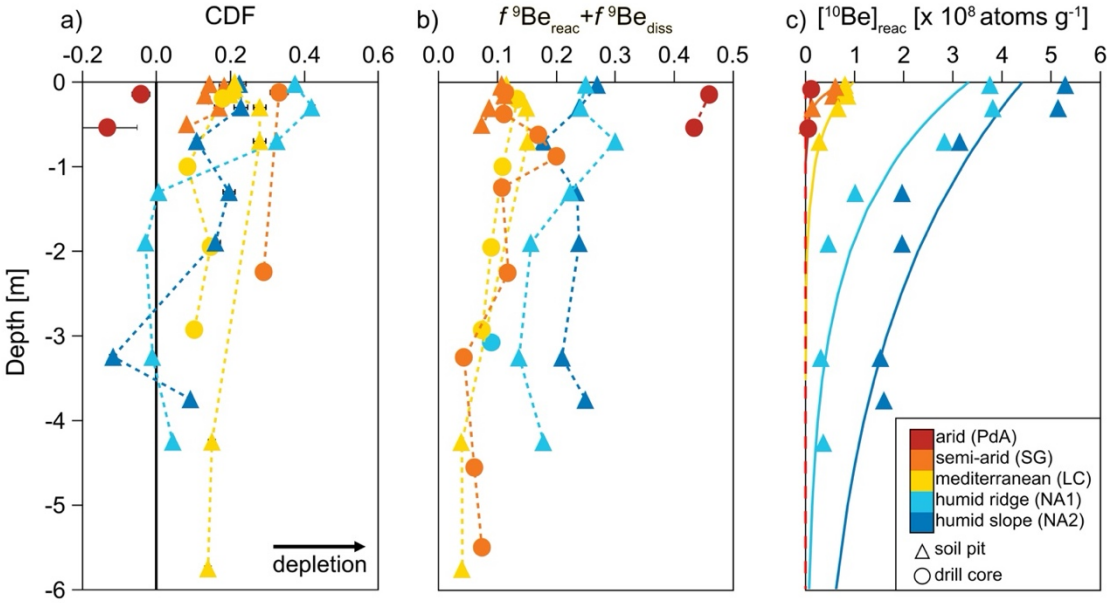

Figure 3-2. a) Chemical depletion fraction CDF, black line indicates bedrock values, positive values indicate depletion. Used immobile element: Nb for arid, mediterranean, humid, Zr for semi-arid. Uncertainties are calculated from bedrock variability of Zr or Nb. b) $f^{9}Be_{reac}+f^{9}Be_{diss}$ as an indicator for the degree of ^{9}Be mobilisation from primary mineral and retention in the reactive phase with depth (zero values denote no mobilisation, unity denotes quantitative transfer from primary to reactive phases. c) meteoric $[^{10}Be]_{reac}$ with depth (dashed line indicates detection limit of 9.3 x10^{5} atoms g^{-1}, solid lines show exponential fits used to calculate ^{10}Be inventories). Symbol sizes exceed the size of most uncertainty bars. These are provided in Table 3-1.

3.5 Discussion

3.5.1 *Weathering proxies from surface soil and soil profiles*

Both the mediterranean and humid sites reveal the highest $f^{9}Be_{reac}+f^{9}Be_{diss}$ and CDF along the gradient (where the arid site provides an outlier discussed below; Figure 3-2A). At these two sites, precipitation is highest which leads to highest degree of bulk element loss (as indicated by CDF) and of ^{9}Be mobilisation from bedrock into the reactive phase ($f^{9}Be_{reac}+f^{9}Be_{diss}$). This pattern does not hold at the semi-arid site where a high abundance of soluble plagioclase results in a high weatherability of bedrock (Table S3 in Oeser et al., 2018b). Both water flow and mineral assemblage of parent rock are therefore controls over the degree of weathering, indicated by both CDF and $f^{9}Be_{reac}+f^{9}Be_{diss}$. Compared to the CDF, ^{9}Be mobilisation as quantified by $f^{9}Be_{reac}+f^{9}Be_{diss}$ offers a practical advantage as it does not require knowing the concentration of an insoluble index element in both regolith and unweathered bedrock. The Be-specific weathering degree $f^{9}Be_{reac}+f^{9}Be_{diss}$ can be determined on a single soil sample.

In this context, it is unexpected that highest $f^{9}Be_{reac}+f^{9}Be_{diss}$ was found at the arid site, given the lack of water flow. At this site, no chemical mass loss by weathering is detected by the CDF, and geophysical subsurface imaging does not reveal a weathered zone at the top of the profile. However, fractured bedrock is imaged from the surface to ~20 m depth (Trichandi et al., 2023a). Along these fractures parent rock is strongly hydrothermally overprinted. This hydrothermal activity likely mobilised ^{9}Be (Barton and Young, 2002), rendering $f^{9}Be_{reac}+f^{9}Be_{diss}$ an indicator for hydrothermalism rather than for weathering at this site. Potentially a mild hydrothermal overprint at the semi-arid site might have also caused ^{9}Be mobilisation (Chapter 2.3.1 and Krone et al., 2021a).

For meteoric $[^{10}Be]_{reac}$ in soil profiles, “decline-type” profiles emerge if Be movement to depth is retarded (Willenbring and von Blanckenburg, 2010b; Graly et al., 2010; Maher and von Blanckenburg, 2016) and regolith mixing with depth is absent (McKean et al., 1993). We identified decline-type profiles throughout with exponential decrease of $[^{10}Be]_{reac}$ attaining a zero value in ca. 2 m (arid), ca. 1 m (semi-arid), ca. 2.5 m (mediterranean) and ca. 6 to 12 m (humid; Figure 3-2C) depths. The infiltration depth is correlated with the amount of precipitation. This observation corresponds to models that predict deeper infiltration depths at higher flow rates (Maher and von Blanckenburg, 2016).

The infiltration depth is deepest at the humid site with 5 m, despite the high abundance of clay minerals (Hampl et al., 2023) that are thought to adsorb ^{10}Be. Three independent controls over adsorption and infiltration and of ^{10}Be likely favour the deep infiltration at the humid site, as predicted by reactive flow models of Maher and von Blanckenburg (2016): First, at the humid site fluid flow is highest, second, soil pH is lowest (4 to 5 at the humid site compared to 6 to 7 at the mediterranean site and 7 to 8 at the other sites), and third, the residence time of a given length interval of regolith (and thus the time available for depth

migration) as calculated from denudation rates (see below) is about three times as long at the humid site than at the mediterranean site.

3.5.2 *Denudation rates and ^{10}Be depositional flux estimates*

Denudation rates calculated from $^{10}Be_{met}/^{9}Be_{reac}$ and the GCM-derived F_{met}^{10Be} agree with $^{10}Be_{insitu}$-derived denudation rates at the mediterranean and humid sites. In contrast, they strongly disagree at the semi-arid and arid sites (Table 3-1). The disagreement is most pronounced at the arid site, where the calculated D_{met} exceeds D_{insitu} ~170-fold. The cause of the disagreement is an overestimation of F_{met}^{10Be} from the GCM model at these dry sites. This finding becomes apparent from when D_{met} is equated with D_{insitu} to estimate F_{met}^{10Be} (eq. 2, Table 3-1). At the arid sites, the derived F_{met}^{10Be} then is only 5700 atoms cm^{-2} yr^{-1} which is ~2 orders of magnitude lower than GCM-derived F_{met}^{10Be} (Heikkilä, 2007; Heikkilä & von Blanckenburg, 2015). In contrast, at the mediterranean and humid sites, the D_{insitu}-estimated and the GCM-derived F_{met}^{10Be} are in good agreement (Figure 3-3, Table S3-5). At the humid site, the ridge position (N1) yields higher D_{met} (40 t km^{-2} yr^{-1}) than D_{insitu} (24 t km^{-2} yr^{-1}) and vice versa at the slope position (N2; D_{met} is 25 t km^{-2} yr^{-1} and D_{insitu} is 45 t km^{-2} yr^{-1}; Table 3-1). Downslope transport of surface-derived soil particles rich in $^{10}Be_{met}$ might cause loss of $^{10}Be_{met}$ at the ridge and its accumulation on the slope (Schoonejans et al., 2017). The precipitation-derived flux by Graly *et al.* (2011), however, closely matches the F_{met}^{10Be} estimated from equating denudation rates at the arid, semi-arid and mediterranean sites. At the humid site, the precipitation-derived flux overestimates F_{met}^{10Be}.

We consider the lack of precipitation as the main cause for the observed deficit in $^{10}Be_{met}$ deposition at the dry sites. A similar observation was made in a previous study from the Atacama Desert, where F_{met}^{10Be} of (3.7 ± 0.6)x10^4 atoms cm^{-2} yr^{-1} was estimated, which is only 6% of the corresponding GCM-model flux for this region (Wang et al., 2015). Taken together, while these two studies for the first time quantify the low depositional ^{10}Be fluxes in arid areas, they also offer two consistent explanations for the GCM-derived F_{met}^{10Be} overestimating $^{10}Be_{met}$ deposition in arid and semi-arid regions. First, although in the model the fraction of dry in total ^{10}Be deposition is 0.4-0.2 in this region (Heikkilä et al., 2013), dry deposition does not appear to be a significant delivery mechanism. Second, fine-scale spatial variations in the aridity in the Atacama Desert are not adequately represented by the coarse resolution of the GCM-model which has a cell size of ca. 200 x 200 km.

However, even the arid and semi-arid sites are subjected to occasional influx of moisture in the form of coastal fog that, however, does not cause $^{10}Be_{met}$ deposition. In this region, the coastal fog is transported from the Pacific Ocean towards the Coastal Cordillera (Lehnert et al., 2018). If the travel distance is sufficiently long, the additive effect operates on ^{10}Be, meaning that the fog accumulates ^{10}Be scavenged from the atmosphere (Deng et al., 2020a). Deuterium/hydrogen isotope ratios (in δ^2H, seawater has a ratio of 0) measured on the land surface indicate the travel distance of the precipitation as they fractionate during rainfall

(Araguás-Araguás et al., 2000). Near the coast, a ratio of -34 ± 5 ‰ indicates a proximal source of the moisture (in arid study site; Bowen, 2023); further inland the δ^2H ratio decreases to ca. -70 to -90 ‰ in the Andes as the heavy isotopes are preferentially lost during precipitation (Araguás-Araguás et al., 2000). We can therefore exclude coastal fog as a main supplier of $^{10}Be_{met}$ in the arid site. Comparing the arid and semi-arid to the mediterranean and humid sites, convective precipitation appears to be the relevant deposition mechanism for $^{10}Be_{met}$ at the latter sites.

Because of the discrepancy between our calculated and GCM-derived F_{met}^{10Be}, we postulate a precipitation limit between semi-arid and mediterranean climate for the applicability of $^{10}Be_{met}/^{9}Be_{reac}$. Above a precipitation limit of approximately 400 mm yr^{-1}, a GCM-derived F_{met}^{10Be} can be used to determine denudation rates.

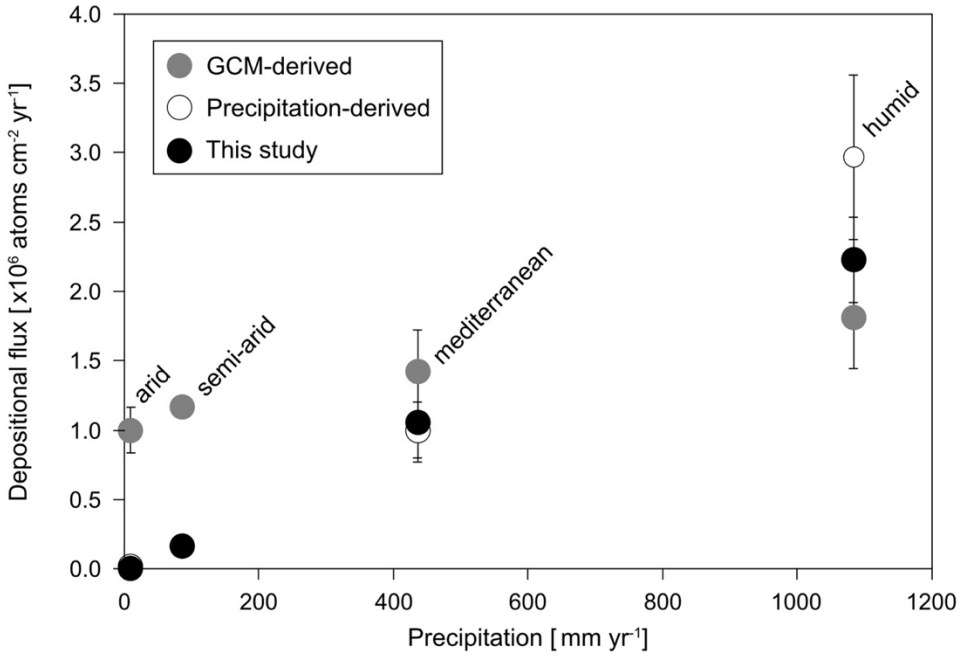

Figure 3-3. Depositional flux for $^{10}Be_{met}$ derived from GCMs, precipitation and from combined D_{insitu} and $^{10}Be_{met}$ in soil surface samples (this study).

3.6 Implications

Both isotopes of Be are sensitive indicators of the controls over weathering in the critical zone, albeit in different ways: Meteoric ^{10}Be indicates the depth extent of infiltration of particle-reactive elements, as controlled by fluid flow, reactive surfaces, pH, and soil residence time. The fraction of ^{9}Be released from primary minerals, in contrast, serves as a sensitive indicator of regolith alteration, either from hydrothermal overprinting as is the case at our arid site, or from meteoric water-induced weathering, as at the sites exposed to higher rainfall. At these latter sites, this fraction is a sensitive indicator of the weathering degree, even where bulk mass loss in the dissolved form is not observed.

Our findings suggest that above a precipitation limit of approximately 400 mm yr^{-1} F_{met}^{10Be} determined using $[^{10}Be]_{met}$ and soil inventories agree with F_{met}^{10Be} predicted by GCM-derived estimates. Therefore, in such climate of sufficient precipitation these models are suited as input for denudation rate determination with meteoric ^{10}Be. In areas of arid and semi-arid climate with high variability in precipitation over short distances, F_{met}^{10Be} from coarse-resolution atmospheric transport models fail to resolve gradients and also appear to overestimate dry deposition of ^{10}Be. Further investigation of this potential precipitation limit is needed to map out the application of $^{10}Be_{met}/^{9}Be_{reac}$ in such dry regions.

Our comparison with *in situ*-derived denudation rates shows that when knowing the F_{met}^{10Be}, the ^{9}Be concentration of local bedrock, and the mobilisation of ^{9}Be from primary minerals into the reactive phase, reliable denudation rates result from $^{10}Be_{met}/^{9}Be_{reac}$. In that case a single sample from surface soil is sufficient to determine a local denudation rate.

3.7 Acknowledgements

This project is funded by German Science Foundation (DFG) grant BL562-16/2 within the priority program 1803 “EarthShape – Earth surface shaping by biota”. We are grateful to the “DeepEarthShape” team for assistance during the drilling campaigns.

4. The reactive phase as indicator for deep granitoid weathering

Abstract

Reactive phases are intermediate weathering products that result from primary mineral dissolution and transform into crystalline secondary phases like clays during rock weathering. They play an important role in fixation of organic matter and adsorption of metals in soils, yet their abundance in deeper sections of the weathering zone, the saprolite, is rarely investigated. We therefore studied these reactive phases in five granitoid drill cores from a climate gradient in the Chilean Coastal Cordillera by means of sequential extractions to determine the concentrations of the elements they contain. At the surface, their concentration strongly correlates with rainfall, but this correlation is diminished at depth. With beryllium, we employ an innovative trace element contained in these reactive phases. We use the stable isotope ^{9}Be that traces the reactive phase, as ^{9}Be is released from rock where alteration is strong either by hydrothermal overprint or by intense dissolution of plagioclase and eventually adsorbs to reactive phases. In contrast, the depth distribution of the meteoric cosmogenic nuclide ^{10}Be, incorporated into these phases up to a certain depth, depends on the abundance of reactive surfaces, on rainfall, and on the rates of weathering and erosion processes.

Unexpectedly, we find non-negligible concentrations of extractable elements even in visually classified fresh bedrock. A comparison to primary mineral element composition and dissolution rates suggests that likely micro-scale pre-weathering of primary minerals has primed release of these elements. Higher in the profile, when sufficient fluid flow enables solubilisation of elements from pre-weathered minerals, loss of these elements into the dissolved phase (quantified by elemental loss balances) is the main process driving the evolution of the weathering profile. We use this information to assign different zones in the weathering profile. These zones show distinguishable weathering processes that are reflected in the concentration of extractable Al and Fe: in soil and subsoil both dissolution and formation of reactive secondary weathering products are most important; in saprolite dissolution is the main mechanism; and in bedrock, pre-weathering of primary minerals induced by post-magmatic processes, hydrothermalism, groundwater flow or gaseous O_2 diffusion primes elements such that, during denudation, water flow higher in the profile mobilise these elements.

This chapter is under preparation for submission with Friedhelm von Blanckenburg as co-author.

4.1 Introduction

Reactive phases play an important role in the weathering zone. These secondary weathering products with high reactive surface area are a substrate for fixation of soil organic matter and thereby impact global carbon cycling (Kramer and Chadwick, 2018; Roering et al., 2023), influence the bioprocessing of organic matter (Uroz et al., 2015; Wu et al., 2023), and provide adsorption sites for trace metals and soil contaminants like uranium (Fischer et al., 2009; Wang et al., 2022). Reactive phases bound to suspended particulate matter in rivers affect the cation flux and thus silicate weathering fluxes from the continent to the ocean (Clow and Mast, 2010; Tipper et al., 2021). Despite the strong impact on carbon release, fixation, and global element cycles, reactive and other amorphous phases like Al-Si oxyhydroxides are rarely studied in weathering studies (e.g. Frings et al., 2021). In particular, in saprolite and saprock (weathered, fractured rock) their contribution to deep weathering remains unknown. In this study, we investigate the occurrence, formation, behaviour, and climate dependency of reactive secondary weathering products in granitoid lithology along a climate gradient.

Reactive phases, formed by the dissolution of primary minerals during weathering, lead to the precipitation of reactive secondary solids. These solids are commonly operationally defined as amorphous aluminium (Al)-, silicon (Si)-, iron (Fe)-, and manganese (Mn)-oxides or weakly crystalline oxyhydroxides that contain mobilised and adsorbed Fe (Tessier et al., 1979; Fantle and DePaolo, 2004; Wiederhold et al., 2007; Wittmann et al., 2012; Frings et al., 2021). These amorphous and weakly crystalline reactive phases are precursors for clay minerals (Schwertmann, 1964; Behrens et al., 2015; Frings et al., 2021). Both, clay minerals and their precursors are characterised by high specific surface area, hence with the progression of weathering the surface area increases and thus presents an indicator of the degree of weathering (e.g. White et al., 1996; Navarre-Sitchler et al., 2013; Fisher et al., 2023). Therefore, the abundance of reactive phases and related surface area depends also on the weathering rate (White and Brantley, 2003; Caves Rugenstein et al., 2019).

The precipitation of reactive phases in pore spaces results in feedback mechanisms that either enhance or reduce weathering processes. For example, the precipitation of ferrihydrite in pore spaces leads to increasing strain that produces microfractures and thus secondary porosity, enhancing weathering (Fletcher et al., 2006; Røyne et al., 2008). However, weathering can also be mitigated by the precipitation of secondary weathering products that clog available pores and hence inhibit water flow through the porous medium (Bazilevskaya et al., 2015; Kim et al., 2017). Moreover, in deep saprolite profiles, kaolinite coating of plagioclase minerals is suspected to decrease dissolution and thus retard further weathering (White and Brantley, 2003; Vázquez et al., 2016).

Several procedures to extract reactive phases are commonly applied in soil and critical zone science. A common procedure is ammonium oxalate extraction, partly in combination with hydroxylamine hydrochloride as sequential extraction (Ross et al., 1985; Parfitt and Childs, 1988; Lee et al., 1989; Von Fromm et al., 2021). With this method, ferrihydrite and

other amorphous and organic Al, Fe, and Si phases are extracted (e.g. Parfitt and Childs, 1988). Furthermore, the extraction with citrate bicarbonate dithionite is applied to extract crystalline and weakly crystalline oxides (Mehra and Jackson, 1958; Fisher et al., 2021; Chapter 2.3.3). The combination of both methods is also used to investigate extractable elements (Itami et al., 1996; Stoppe et al., 2015). Sequential extractions with sodium hydroxide (NaOH) are used to extract amorphous Si and Al in secondary clays (Frings et al., 2021). Another common method to extract amorphous and weakly crystalline phases is a sequential extraction using hydrochloride (HCl) and hydroxylamine hydrochloride (e.g. Tessier et al., 1979; Poulton and Canfield, 2005; Wiederhold et al., 2007; Wittmann et al., 2012). We use the latter sequential extraction method in this study to extract all amorphous and weakly crystalline reactive phases in soil, saprolite, and bedrock samples.

We also examined the behaviour and abundance of the cosmogenic radionuclide meteoric ^{10}Be ($^{10}Be_{met}$) and the stable isotope ^{9}Be as both isotopes are interconnected with the formation of secondary weathering products. $^{10}Be_{met}$ is exclusively produced in the atmosphere and transported to Earth's surface by wet and dry delivery thus the only possible input source is infiltration with rainwater (Willenbring and von Blanckenburg, 2010b). In contrast, ^{9}Be is released during weathering of primary minerals (reactive ^{9}Be) hence its concentration in the weathering profile is determined by the parent bedrock concentration and weathering intensity (von Blanckenburg et al., 2012). However, both isotopes behave chemically similar, and both reactive ^{9}Be and $^{10}Be_{met}$ adsorb readily to available adsorption sites (von Blanckenburg et al., 2012). Therefore, the concentration of the two isotopes depends on reactive phases that provide these adsorption sites, making ^{9}Be and $^{10}Be_{met}$ potential indirect tracers of reactive phases in weathering profiles. We hypothesise that the concentration of $^{10}Be_{met}$ with depth indicates the depth migration of trace elements in a soil profile where secondary weathering products are present. We further assume that the concentration of reactive ^{9}Be correlates with the depth where these secondary weathering products begin to form. Furthermore, because $^{10}Be_{met}$ enters the weathering zone at known flux and thus determines residence times of regolith, the ratio of both isotopes $^{10}Be_{met}/^{9}Be$ is a denudation rate meter (von Blanckenburg et al., 2012). In this regard, knowing the interval over which the $^{10}Be_{met}/^{9}Be$ ratio is set is a prerequisite for the application of $^{10}Be_{met}/^{9}Be$ denudation rate meter in surface samples. To this end, we examine whether the assumption that the weathering release flux of ^{9}Be, the deposition and depth migration of $^{10}Be_{met}$ at the surface are reflected by the $^{10}Be_{met}/^{9}Be$ ratio is justified.

The aim of this study is to investigate the role of reactive phases especially in deep saprolite in four study sites from arid to humid climate. This climate gradient allows to investigate the control of water availability on the formation and abundance of reactive phases. We investigated five drill cores to a depth of 50 to 90 m using a sequential extraction method to measure the concentration of the extractable phase of major elements Al, calcium (Ca), Fe, potassium (K), magnesium (Mg), and sodium (Na) together with ^{9}Be and $^{10}Be_{met}$

assuming that extractable elements reflect the abundance of reactive secondary weathering products. We compared the concentrations of the leached extractable phase in bedrock samples to those of soil samples and identified element distribution patterns for hydrothermal overprint, bedrock, and secondary weathering products. Using the concentrations of extractable Al and Fe, we defined different zones in the weathering profiles that agree with other weathering parameters. We show that, unless reactive ^{9}Be was released by hydrothermal activity, the isotope ratio $^{10}Be_{met}/^{9}Be$ faithfully records the denudation rate over the interval at which reactive ^{9}Be and ^{10}Be reside in the weathering zone.

4.2 Study Site and Material

Along an extreme gradient from arid to humid climate in the Chilean Coastal Cordillera (26° S to 38° S), we conducted drilling campaigns to obtain complete weathering profiles from soil to unweathered bedrock. The four study sites have been explored in the network project "EarthShape – Earth Surface Shaping by Biota" and are Pan de Azúcar (PdA, arid, mean annual precipitation (MAP): 10 mm yr^{-1}), Santa Gracia (SG, semi-arid, MAP: 90 mm yr^{-1}), La Campana (LC, mediterranean, MAP: 440 mm yr^{-1}), and Nahuelbuta (NA, humid, MAP: 1100 mm yr^{-1}). The lithology at all sites consists mainly of granitoids, tonalites, and quartz diorites (Oeser et al., 2018a, and references therein).

The arid site (Pan de Azúcar) is located in the Cerros del Vetado pluton consisting of coarse-grained (almost pegmatitic) monzo- and syenogranites of Late Triassic age (205 – 250 Myr; Godoy and Lara, 1998; Jara et al., 2021). The pluton is intruded by NE – SW oriented mafic dikes (grabbroic to dioritic composition) of Late Cretaceous age (ca. 130 Myr; Dallmeyer et al., 1996; Acevedo Salinas, 2022) that are also abundant at the drill site and observed by geophysical subsurface imaging (Trichandi et al., 2023a). At both the arid and semi-arid sites, the presence of Fe-hydroxides and carbonatic fracture fillings in the drilled cores indicates hydrothermal overprinting. Visual observation suggests that the hydrothermal overprint is stronger at the arid site. Because that site was not subjected to any meteoric weathering due to its dry climate, we consider this site to be a reference location for studying the impact of hydrothermal alteration and how this differs from the impacts of weathering.

At the semi-arid site (Santa Gracia), the fine-grained lithology is of dioritic to granodioritic composition in a pluton of Early Cretaceous age (124 – 144 Myr; SERNAGEOMIN, 2003; Chapter 2.2.1). The pluton is affected by tectonic fracturing with steeply dipping NW to NE oriented faults (Chapter 2.3.2).

The mediterranean site (La Campana) is located in the Caleu pluton of Late Cretaceous age (ca. 93 – 97 Myr; Parada et al., 1999, 2005; Molina et al., 2015), that consists of fine-grained granodiorites. For this site, reported uplift rates are highest among all sites (ca. 0.13 ± 0.04 mm yr^{-1}; (Melnick, 2016), and rocks were subjected to tectonic fracturing (Trichandi et al., 2023b).

The humid site (Nahuelbuta) is located in granitoid rocks in a pluton that belongs to the Nahuelbuta complex of Late Carboniferous age (294 Myr; Parada et al., 2007; Deckart et al., 2014). The observed coarse-grained lithology is heterogenous and contains small mafic intrusions (Oeser et al., 2018a; Hampl et al., 2023).

The depth of the drill holes extends to ca. 90 m at the arid, semi-arid, and mediterranean sites; at the humid site, two drill holes to a depth of ca. 50 m were cored. The wireline diamond drilling procedure is described in Chapter 2.2.2. In most cases, the upper meters of the drilled material could not be recovered. To obtain continuous weathering profiles, nevertheless, we manually sampled soil profiles adjacent to the drill holes from soil pits dug by friendly workers called e.g. “el topo”. Sampling of the drill cores is described in Chapter 2.6.2.

4.3 Methods

We performed sequential extractions on ca. 1 g of powdered sample material (grain size <20 µm) that was previously oven-dried for 72 h at 60 °C following the leaching protocol designed by Tessier *et al.* (1979) for deep ocean sediment and modified by Wittmann *et al.* (2012) for extraction of reactive meteoric cosmogenic ^{10}Be and stable ^{9}Be. The used leaching reagents were 0.5 M hydrochloric acid (HCl) followed by a hydroxylamine hydrochloride (HxHCl) leach (1 M $NH_2OH \times HCl$ in 1 M HCl). The phase that is extracted by 0.5 M HCl is operationally defined as amorphous Fe and Mn oxyhydroxides (Tessier et al., 1979; Wittmann et al., 2012) or weakly crystalline Fe oxides, including adsorbed and organically bound Fe that was mobilised in a soil profile (Fantle and DePaolo, 2004; Wiederhold et al., 2007). However, the 0.5 M HCl leach also dissolves calcium carbonate ($CaCO_3$; Wittmann et al., 2012), and, depending on the lithology, it can dissolve up to 20% of Fe from biotite and chlorite (Kiczka et al., 2010). The phase that is attacked by 1 M HxHCl is operationally defined as crystalline oxides (Tessier et al., 1979), consisting for example of Fe-Mn-oxides or easily reducible oxides like ferrihydrite and lepidocrite (Poulton and Canfield, 2005).

For several reasons samples were pulverized before performing the sequential extractions: 1) The pulverisation ensures the representativeness and comparability of the samples as the grain size of the plutonic bedrock strongly differs between the study sites (Oeser et al., 2018a; Hampl et al., 2023). 2) Pulverisation avoids sample heterogeneity from sorting effects due to different grain size. 3) The complete extraction of the leachable phase is ensured. And 4) possible sample defects and alterations of primary minerals in the bedrock are accessible to the extraction to disclose whether the defined bedrock has experienced micro-scale weathering (e.g. described in Buss et al., 2008; Yuguchi et al., 2021; Behrens et al., 2021). In this regard, the employed method differs from the original method designed to extract reactive cosmogenic ^{10}Be and stable ^{9}Be (Wittmann et al., 2012) where the objective is to avoid including primary mineral-bound Be in the leacheates. We performed the sequential extractions on 5 drill core samples from the arid site, 5 soil and 16 drill core samples from the semi-arid site, 7 soil and 19 drill core samples from the mediterranean site, and 14

soil and 14 drill core samples from the humid site. A bias is apparent in mineralogical and chemical properties between soil and drill core samples. This bias can be attributed to the drilling technique that flushes core material with water: Fine and very fine particles in the drill core samples might be lost in the drilling fluid whereas in manually taken soil samples these fine particles remain.

After the sequential extraction, we measured major elements (Al, Ca, Fe, K, Mg, Na) and ^{9}Be in the separate HCl and HxHCl splits by Inductively Coupled Plasma – Optical Emission Spectroscopy (ICP-OES, uncertainty 5%) and combined the concentration results of both splits to the "extractable phase". For ^{10}Be measurements, each sample was spiked with a ^{9}Be carrier. After anion and cation column separation and alkaline precipitation of Be (von Blanckenburg et al., 2004), Be was oxidised and pressed into accelerator mass spectrometer (AMS) cathodes and measured at the AMS facility at the University of Cologne (Dewald et al., 2013). For blank correction, we used a pooled blank from all (^{10}Be/^{9}Be) AMS measurements of 6.5 ± 5.7 * 10^{-15} (n=11), but also applied batch-blank corrections.

Bulk element analyses were conducted in a commercial laboratory (ALS Global, UK) using ICP-OES. To account for the addition of weathering-derived inputs (water, carbon) into weathered samples, we corrected their bulk element concentrations for loss on ignition (LOI, $X_{LOI_{corr}}$) according to:

$$X_{LOI_{corr}} = \frac{X_{measured} * (SUM_{measured} + LOI)}{SUM_{measured} + LOI_{average\ parent}} \quad [1]$$

with $X_{measured}$ as the measured element concentration, $SUM_{measured}$ as the sum of all measured element concentrations, LOI of the analysed sample, and $LOI_{average\ parent}$ as average LOI from all bedrock samples. For the mediterranean site, we applied a correction for magnetite according to Hampl *et al.* (2023) by subtracting 0.7 wt% from total Fe_2O_3 for 1 wt% magnetite. This is done to account for the high Fe content in inert magnetite that is not susceptible to weathering processes.

The fractional elemental mass loss was calculated using the equation for tau (τ) by (Anderson et al., 2002) for an immobile (e.g. Zr, Nb) element $X_{i,weathered/parent}$:

$$\tau = \frac{X_{j,weathered} * X_{i,parent}}{X_{j,parent} * X_{i,weathered}} - 1 \quad [2]$$

with $X_{j,weathered}$ and $X_{j,parent}$ as the concentrations of an element j in a weathered sample and in parent bedrock, respectively. $\tau = 0$ indicates no loss or enrichment of an element, $\tau > 0$ indicates enrichment and $\tau < 0$ means loss of an element, relative to parent bedrock, respectively. τ depends on bedrock homogeneity with respect to the immobile element thus variations around a zero τ value in bedrock samples indicate the deviation of the natural element distribution.

We calculated the fractions of the extractable phase (F_{ex}, in %) using the measured concentration of a given leached reactive element X_{ex} (in %) and the bulk average bedrock concentration of the same element X_{parent} (in %) following the equation:

$$F_{ex} = \frac{X_{ex}}{X_{parent}} \quad [3]$$

The fraction of an element lost from unweathered bedrock (F_{diss}) into the dissolved phase is given by τ (see above). From these calculations we can set up a mass balance of an element in a weathered sample:

$$F_{residual} = 1 - F_{ex} - F_{diss} \quad [6]$$

with $F_{residual}$ as the fraction of the element that is neither dissolved nor incorporated into the reactive phase. This fraction contains the silicate residue and any other primary or secondary phase that is not dissolved in either 0.5 M HCl or HxHCl.

To identify whether in the extractions primary minerals were potentially dissolved, we compared the concentrations of leached elements in weathered and bedrock samples to hypothetical element patterns assuming stoichiometric mineral dissolution, in particular for biotite and hornblende. We calculated mineral dissolution rates for the HCl (24 h, pH < 2) leaching step and compared these to published primary mineral dissolution rates reported for similar conditions to single out whether upon leaching of the powders any (micro-) alterations or, alternatively, pristine primary minerals were dissolved. To distinguish between patterns arising from hydrothermal alteration from those of weathering, we used the patterns resulting from extractions of samples from the arid site.

4.4 Results

4.4.1 Extractable phase

All concentrations in the two extractions are provided in supplementary tables (Tables S4-1 to S4-4). We note that in the HxHCl step considerably less mass was extracted than in the HCl step (average % of total sample leached with HxHCl: 5-15% Al, 14-38% Ca, 11-26% Fe, 9-25% K, 15-36% Mg, 12-31% Na). Thus, for simplicity in the presentations, the concentrations from the two sequential extraction steps were mathematically pooled into the “extractable phase”.

For the extracted major elements Al, Ca, Fe, Na, K, and Mg, we observed three different depth patterns at all study sites (except for the arid site where hydrothermal overprinting prevails) (Figure 4-1): 1) Complete solubilisation and absence of partitioning into the extractable phase (Na); 2) High concentrations in both bedrock and at the surface whereas concentrations are lower in between (Al, Fe); and 3) Monotonously decreasing concentrations

from bedrock towards the surface (Ca, K, Mg). These depth patterns disclose element mobilisation from primary minerals followed by loss into the dissolved phase or incorporation into secondary weathering products. Commonly, only Al and Fe, which show increasing concentrations in the extractable phase towards the surface, are incorporated into secondary weathering products. In contrast, Ca, K, and Mg are much less partitioned into the extractable phase, and Na is not incorporated at all. At all sites, increasing concentrations in the extractable phase are only detected in the upper 5 -10 m. With increasing rainfall, the concentration of elements in the extractable phase and total F_{ex} increases. In surface samples at the humid site, ca. 20% Al and 40% Fe were extracted whereas at the semi-arid and mediterranean sites, only 5-8% Al and 20% Fe were extracted.

From jumps in the concentrations of extractable Al and Fe, we identified distinct zones in the weathering profiles. We used extractable Al and Fe as indicators for the zones as both elements are incorporated into secondary weathering products and are commonly not lost into the dissolved phase. We defined that a difference of 20% in Al and Fe concentration indicates the shift from one zone into another. We identified three distinguishable zones in all weathering profiles (Table 4-1), consisting of soil and subsoil (zone 1), weathered saprolite and saprock (zone 2), and bedrock (zone 3). We note that the defined depths are not precise as the analysed sample intervals do not have sufficient depth resolution.

Table 4-1. Zones in weathering profiles defined by a minimum 20% jump in the concentration of extractable Al and Fe within the profile.

	Consisting of	**Site**				
		arid	**semi-arid**	**mediterranean**	**humid-ridge**	**humid-slope**
			[m]	[m]	[m]	[m]
Zone 1	soil and subsoil	hydrothermal reference, no zones	0.0 - 0.9	0.0 - 2.9	0.0 - 3.1	0 - 1.9
Zone 2	saprolite and saprock		0.9 - 65.8	2.9 - 42.2	3.1 - 14.1	1.9 - 13.5
Zone 3	bedrock		> 65.8	> 42.2	> 14.1	> 13.5

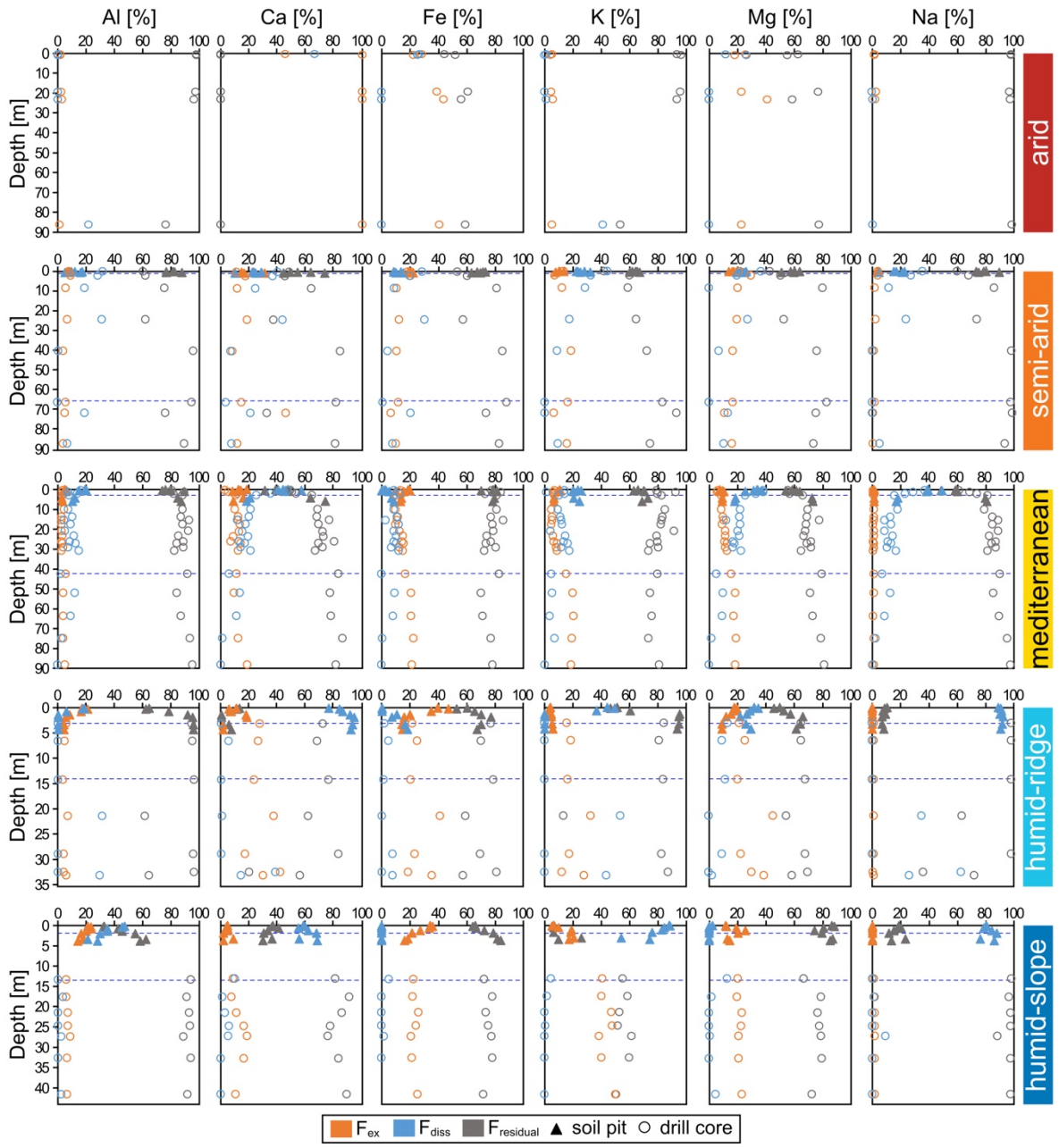

Figure 4-1. Extractable (F_{ex}), dissolved (F_{diss}) and residual ($F_{residual}$) fractions for analysed major elements with depth at all study sites. The dashed lines indicate the defined zones in the weathering profile.

4.4.2 Bedrock leaching

In bedrock, for most analysed elements (except Na) the concentrations of elements in the extractable phase are surprisingly high (Figure 4-1). The shape of the element distribution pattern for the extractable phase of bedrock at the semi-arid, mediterranean, and humid sites is compatible, to some extent, with the stoichiometrically-defined element distribution pattern for both biotite and hornblende. Yet, the extracted concentrations from bedrock are much smaller and account for only ca. 10% of the stoichiometrically mineral composition. From this approximate fit, ca. 10% of biotite, that is present at all sites, and hornblende is

dissolved from bedrock samples by the leach (Figure 4-2). At the semi-arid and mediterranean sites, the modal abundance of hornblende is ca. 15-20% while it is absent at the humid site (Hampl et al., 2023; pers. comm. R. Blukis). Fe and K are leached preferentially relative to Mg, consistent with previously detected removal of interlayer K in biotite (e.g. Price and Velbel, 2014). We cannot exclude that these minerals are pre-weathered and that these e.g. micro-scale alterations are preferentially leached. We return to this question in the discussion section below. Moreover, we detect extractable Ca in bedrock samples that likely originate from leaching of trace amounts of calcite in granitoid lithology (White et al., 1999, 2005) but might also indicate plagioclase dissolution.

The comparison of element distribution patterns for leached bedrock to the patterns of samples from the profiles' surface yields two distinct groups. While, as shown above, in bedrock potentially primary minerals (possibly mixed with micro-scale reactive alteration products) are moderately leached, in surface samples the leach extracts secondary reactive phases formed during weathering (Figure 4-3). These phases consist of amorphous or weakly crystalline Fe and Al phases and concentrations in the extractable phase are roughly twice as high as those from bedrock whereas hardly any Ca or K are contained in the extractable phase.

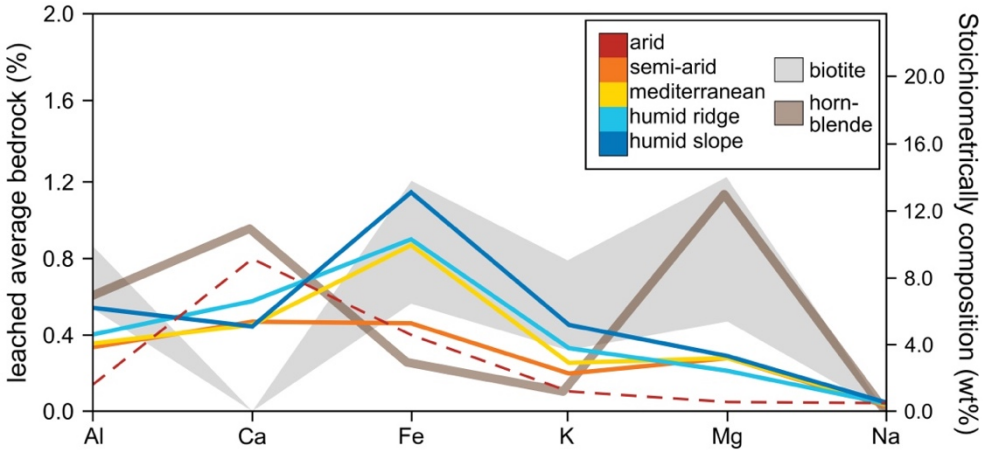

Figure 4-2. Element distribution patterns for leached bedrock samples compared to stoichiometrically-defined biotite (using 4 biotite compositions: Biotite Mineral Data from www.webmineral.com; Ingamells (1976); Savko *et al.* (2015); Biotite composition from www.mineralienatlas.de) and hornblende (Mg-hornblende Mineral Data from www.webmineral.com) composition. The leach from the arid study site indicates hydrothermal overprint (dashed line), whereas the other leacheates indicate primary mineral dissolution (solid lines).

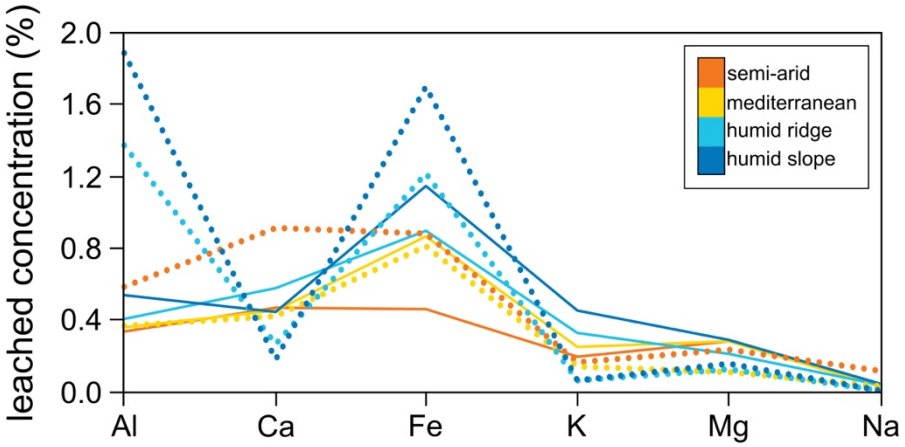

Figure 4-3. Element distribution pattern for leached bedrock (solid lines) and samples from the profiles' surface (dotted lines). Only the weathering-dominated samples are shown (the arid site is not shown).

4.4.3 Hydrothermal overprint

In bedrock from the arid site, serving as reference site for hydrothermal overprint, we found a concentration peak for leached Ca that exceeds the concentration of leached Al, Fe and Mg (Figure 4-2). This Ca concentration peak is also pronounced in the extractable fraction in surface samples (ca. 45% reactive Ca; Figure 4-1). In all deeper samples, all Ca is quantitatively extracted and is thus contained exclusively in the extractable phase. Abundances of extractable Fe (ca. 28%), and Mg (ca. 26%) are also high in surface samples and increase with depth (Figure 4.1). The element distribution pattern for this site is distinct from the patterns for bedrock from the other sites (Figure 4-2).

4.4.4 Dissolved loss

The loss of elements in the dissolved phase, as denoted by τ or F_{diss}, is highest in the topsoil samples (Figure 4-1). Only for Fe, the dissolved phase decreases towards the surface. At the mediterranean and humid sites, no Fe was lost in the dissolved form. At the semi-arid site, some loss of Fe is apparent at the surface. We observe loss of Fe between bedrock and soil at the semi-arid site (between ca. 70 m until surface) and at the mediterranean site (between ca. 65 and 5 m). The dissolved loss is highest for the elements that are not incorporated into reactive secondary phases, in particular Ca and Na. At the surface, F_{diss} of Ca amounts to ca. 23% at the semi-arid, ca. 40% at the mediterranean, ca. 80% at the humid-ridge and ca. 60% at the humid-slope site. For Na, F_{diss} is also highest at the humid sites with ca. 92% at the ridge and ca. 81% at the slope position. At the mediterranean site, F_{diss} is ca. 40% in the uppermost sample. K and Mg are also lost into the dissolved phase albeit to a lower degree than Ca and Na. In general, there is a trend towards higher dissolved loss with increasing rainfall along the climate gradient.

At all study sites, the proportions of F_{ex} and F_{diss} flip over at a certain depth (Figure 4-1). In the uppermost meters, F_{diss} exceeds F_{ex} and constitutes the predominant mobile pool at the surface. We observe this flip-over for all elements except for Fe where F_{ex} is dominating in saprolite and soil, and Na which is not partitioned into the extractable phase. At a given site, the flip-over depth is similar for all elements and is located at ca. 24 m at the semi-arid site, ca. 42 m at the mediterranean site, and ca. 5 m at both humid sites.

4.4.5 *^{9}Be and meteoric ^{10}Be*

The reactive ^{9}Be concentration in the uppermost surface samples shows no correlation with increasing rainfall along the climate gradient (arid: 1.26 ± 0.06 µg g^{-1}, semi-arid: 0.14 ± 0.01 µg g^{-1}, mediterranean: 0.094 ± 0.005 µg g^{-1}, humid-ridge: 0.30 ± 0.01 µg g^{-1}, humid-slope: 0.42 ± 0.02 µg g^{-1}). With depth, reactive ^{9}Be concentrations decrease until they attain a constant concentration at ca. 10 m depth at the mediterranean and humid sites (Figure 4-4). At the arid and semi-arid sites, reactive ^{9}Be appears in higher concentrations at depth than at the other sites. We attribute these elevated concentrations to hydrothermal mobilisation of Be in primary minerals. Samples at depth that originate from strongly fractured zones indicate slightly higher reactive ^{9}Be concentrations than the surrounding samples (e.g. at humid-ridge site samples between 28 to 32 m).

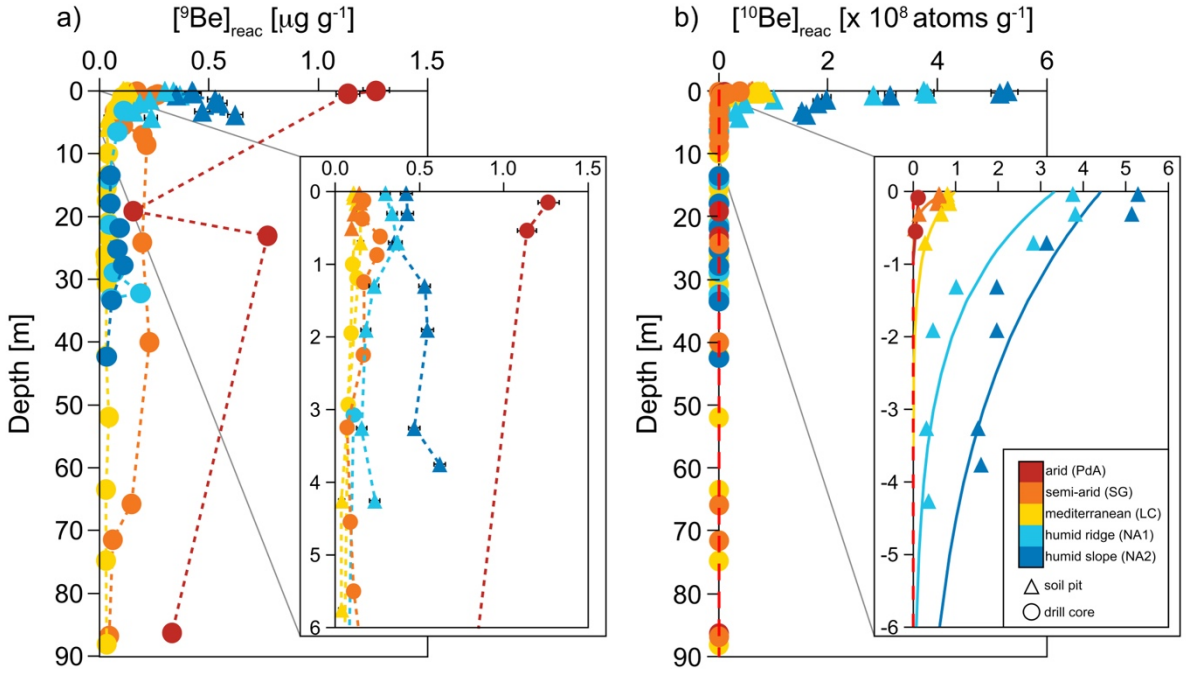

Figure 4-4. Reactive Be concentrations with depth. The insets show a close-up of the upper 6 m of the weathering profile. a) Reactive ^{9}Be with depth. The uncertainty is 5% which is mostly smaller than symbol sizes. b) Meteoric ^{10}Be with depth. The inset shows an exponential fit of concentrations that serves to quantify the infiltration depth. The dashed red line indicates the detection limit for $^{10}Be_{met}$ of ca. 9 x10^{5} atoms g^{-1}.

The $^{10}Be_{met}$ concentration in the uppermost samples increases with increasing rainfall along the gradient (arid: 1.2 ± 0.2 x10^7 atoms g^{-1}, semi-arid: 6.1 ± 0.2 x10^7 atoms g^{-1}, mediterranean: 8.1 ± 0.3 x10^7 atoms g^{-1}, humid-ridge: 3.8 ± 0.1 x10^8 atoms g^{-1}, humid-slope: 5.3 ± 0.2 x10^8 atoms g^{-1}; Chapter 3.4). The concentration with depth decreases exponentially, and the depth until where $^{10}Be_{met}$ can be measured extends with increasing rainfall (Figure 4-4). Below 7 m, no sample indicates $^{10}Be_{met}$ concentrations that exceed the detection limit (9 x10^5 atoms g^{-1}). From these depth profiles, we calculated the characteristic e-folding depth for each profile using the intersection of the exponential fit at the surface and determined the adsorption coefficient *k* from this depth (Table 4-2). The adsorption coefficient *k* correlates with increasing rainfall and is smaller where rainfall is higher (arid: 1.54 m^{-1}, semi-arid: 5.71 m^{-1}, mediterranean: 2.17 m^{-1}, humid-ridge: 0.65 m^{-1}, humid-slope: 0.33 m^{-1}). At the arid site, *k* is smaller than at the semi-arid and mediterranean sites. This effect is likely an artifact due to the low number of samples and thus a less precise exponential fit at the arid site.

Table 4-2. The characteristic e-folding depth and the calculated adsorption coefficient for $^{10}Be_{met}$ for all study sites.

Study site	e-folding depth	*k*
	[m]	[m^{-1}]
arid	0.65	1.54
semi-arid	0.175	5.71
mediterranean	0.46	2.17
humid-ridge	1.55	0.65
humid-slope	3.00	0.33

4.5 Discussion

4.5.1 *Primary mineral leaching*

The bedrock samples reveal high concentrations in the extractable phase for nearly all analysed leached elements except Na, corresponding to the equivalent of ca. 10% of biotite or hornblende in bedrock. In the discussion of this phenomenon, it must be kept in mind that samples were ground to a powder < 20 µm and are thus more readily attacked by the used reagents than that would be the case in extractions of soil or sediment that was sieved but not ground. Three possible explanations for this observation are: 1) The sequential leaching procedure attacks and dissolves primary minerals; 2) Primary minerals are pre-weathered and the sequential extraction thus leaches elements from nano- to micrometer-scale alterations; or 3) Hydrothermal overprinting preconditioned the primary minerals so that the elements from the secondary phases formed in the process are extracted.

With respect to explanation 3), hydrothermal overprinting, we investigated the element distribution pattern for hydrothermally overprinted lithology at the arid site. This extraction yields a pattern that is distinct from the other patterns where in particular the high concentration of extractable Ca is significant (Figure 4-2). We can therefore exclude this explanation. With respect to explanation 1), dissolution of primary minerals, we compared the elemental distribution pattern of the extractable phase in bedrock to the pattern of the stoichiometric composition of biotite and hornblende. Even though much lower in general, the patterns and relative changes amongst the elements resemble those patterns emerging from extractions in bedrock to some extent. The element distributions fit roughly for extractable Fe and K which potentially indicate biotite leaching. However, the leached amounts of Al and Mg do not fit the primary mineral composition. Some plagioclase may have been attacked, as indicated by the extractable Ca found. Na cannot be used to evaluate plagioclase dissolution as it is not incorporated into reactive phases but is lost into solution. F_{diss} for Na would inform on Na loss; however, this cannot be evaluated in bedrock as it serves as the reference material for elemental loss τ (eq. 2). As a result, both explanations 1) primary mineral attack, and 2) micro-scale pre weathering, are potential explanations.

To resolve this question, we evaluated whether the dissolution rates from our extraction method agree with published biotite, hornblende, and anorthite dissolution rates. We calculated mineral dissolution rates using the first sequential leaching step (0.5 M HCl for 24h at room temperature) for grain sizes of 1 and 20 μm, respectively, assuming that all K and all Fe originate from biotite, all Mg originates from hornblende, and all Ca originates from anorthite (Table 4-3). The comparison to published mineral dissolution rates compiled in Brantley *et al.* (2008) shows that our calculated rates are up to 1000 times faster. We thus regard it unlikely that the extractable phase consists only of leached primary minerals. Hence, we suggest that minerals in the defined bedrock are pre-weathered and contain nano- and micrometer-scale alterations that are dissolved in the extraction. This pre-weathering in granitoid lithology can be of different origins: #1) post-magmatic, #2) hydrothermal overprint, #3) groundwater, or #4) diffusing oxygen. The first two origins of pre-weathering potentially result in the same alterations but can occur at different times after the cooling of the intrusion, however, we already excluded hydrothermal overprint as pre-conditioning. During cooling and hydrothermal fluid circulation, biotite can be chloritized which forms microfractures that enable hydrothermal fluids to penetrate the fractured minerals and induce further alteration (Yuguchi et al., 2021). This might be the case at our study sites though further microscopic investigation of minerals in bedrock samples is required to identify pre-weathering. Pre-weathering by groundwater (#3) might have taken place at all study sites as we detected a shallow groundwater table of ca. 6 m at the humid site, whereas we never encountered the groundwater table at the semi-arid and mediterranean sites. Thus, groundwater is located deeper than our bedrock samples and weathering is possible at greater depth. Groundwater flowing at depth is thought to contribute to weathering only to a minor extent, however, it

accounts for, for example, < 4% of total weathering fluxes in the French Strengbach catchment (Ackerer et al., 2021). This low extent may be due to the high solute concentrations and low fluid flow rates, such that weathering-induced dissolution-precipitation reactions occur close to equilibrium. The depth diffusion of gaseous O_2 (#4) and pore waters with minor amounts of O_2 induces alteration by Fe oxidation resulting in micro-fractures (Kim et al., 2017; Stinchcomb et al., 2018). These micro-fractures are observed in shallow samples but also partly in bedrock at all our study sites (Hampl et al., 2022, 2023). At depth, the induced alterations by groundwater and O_2 prime the minerals so that the sequential leaching is able to extract elements. Above a certain depth, sufficient infiltration and shallow water flow remove the extractable elements, and the dissolution becomes the predominant process. We conclude that extractable elements at depth most likely indicate pre-weathering of minerals.

Table 4-3. Mineral dissolution rates calculated from bedrock average K and Fe for biotite, Mg for hornblende, and Ca for anorthite. Uncertainty is calculated from all bedrock samples.

Site	Mineral	Sphere size	Used acid	pH	Dissolution rate	Reference
		[µm]			[mol m^{-2} s^{-1}]	
semi-arid	Biotite (K)	1	0.5 M HCl	< 2	5.6E-09	this study
mediterranean	Biotite (K)	1	0.5 M HCl	< 2	7.4 ± 0.6 E-09	this study
humid-ridge	Biotite (K)	1	0.5 M HCl	< 2	9.8 ± 2.3 E-09	this study
humid-slope	Biotite (K)	1	0.5 M HCl	< 2	1.4 ± 0.2 E-08	this study
semi-arid	Biotite (K)	20	0.5 M HCl	< 2	1.1E-07	this study
mediterranean	Biotite (K)	20	0.5 M HCl	< 2	1.5 ± 0.1 E-07	this study
humid-ridge	Biotite (K)	20	0.5 M HCl	< 2	2.0 ± 0.5 E-07	this study
humid-slope	Biotite (K)	20	0.5 M HCl	< 2	2.7 ± 0.3 E-07	this study
semi-arid	Biotite (Fe)	1	0.5 M HCl	< 2	6.3E-09	this study
mediterranean	Biotite (Fe)	1	0.5 M HCl	< 2	1.4 ± 0.1 E-08	this study
humid-ridge	Biotite (Fe)	1	0.5 M HCl	< 2	1.5 ± 0.3 E-08	this study
humid-slope	Biotite (Fe)	1	0.5 M HCl	< 2	2.0 ± 0.1 E-08	this study
semi-arid	Biotite (Fe)	20	0.5 M HCl	< 2	1.3E-07	this study
mediterranean	Biotite (Fe)	20	0.5 M HCl	< 2	2.8 ± 0.3 E-07	this study
humid-ridge	Biotite (Fe)	20	0.5 M HCl	< 2	3.1 ± 0.6 E-07	this study
humid-slope	Biotite (Fe)	20	0.5 M HCl	< 2	3.9 ± 0.3 E-07	this study
-	Biotite	10-20	0.1 M HCl	1.1	3.08E-09	Kalinowski and Schweda, (1996)
-	Biotite	10-20	0.01 M HCl	2.0	3.05E-10	Kalinowski and Schweda, (1996)
-	Biotite	10-20	0.001 M HCl	3.0	1.19E-10	Kalinowski and Schweda, (1996)

Table 4-3 continued.

Site	Mineral	Sphere size	Used acid	pH	Dissolution rate	Reference
		[µm]			[mol m^{-2} s^{-1}]	
semi-arid	Hornblende	1	0.5 M HCl	< 2	6.2E-09	this study
mediterranean	Hornblende	1	0.5 M HCl	< 2	7.5 ± 0.8 E-09	this study
humid-ridge	Hornblende	1	0.5 M HCl	< 2	7.2 ± 2.1 E-09	this study
humid-slope	Hornblende	1	0.5 M HCl	< 2	8.4 ± 0.1 E-09	this study
semi-arid	Hornblende	20	0.5 M HCl	< 2	1.2E-07	this study
mediterranean	Hornblende	20	0.5 M HCl	< 2	1.5 ± 0.2 E-08	this study
humid-ridge	Hornblende	20	0.5 M HCl	< 2	1.4 ± 0.4 E-08	this study
humid-slope	Hornblende	20	0.5 M HCl	< 2	1.7 ± 0.03 E-08	this study
-	Hornblende	125-250	HCl	1	1.86E-12	(Frogner and Schweda, 1998)
-	Hornblende	125-250	HCl	2	1.33E-12	(Frogner and Schweda, 1998)
semi-arid	Anorthite	1	0.5 M HCl	< 2	4.6E-09	this study
mediterranean	Anorthite	1	0.5 M HCl	< 2	4.4 ± 1.2 E-09	this study
humid-ridge	Anorthite	1	0.5 M HCl	< 2	4.8 ± 2.9 E-09	this study
humid-slope	Anorthite	1	0.5 M HCl	< 2	6.0 ± 0.9 E-09	this study
semi-arid	Anorthite	20	0.5 M HCl	< 2	9.3E-08	this study
mediterranean	Anorthite	20	0.5 M HCl	< 2	8.9 ± 2.3 E-08	this study
humid-ridge	Anorthite	20	0.5 M HCl	< 2	9.6 ± 5.8 E-08	this study
humid-slope	Anorthite	20	0.5 M HCl	< 2	12.0 ± 1.7 E-08	this study
-	Anorthite	25-75	0.01 M HCl	2.6	2.50E-10	(Hodson, 2003)
-	Anorthite	< 30	0.001 M HCl	3	3.25E-10	(Holdren and Speyer, 1987)
-	Anorthite		0.01 M HCl	2	6.43E-09	(Casey et al., 1991)

4.5.2 *The extent of weathering from the surface area of secondary weathering products*

The leaching of samples from different depths in the weathering profile indicated that the largest fraction of elements, most pronounced for Al and Fe, are extracted in samples near the profile's surface which indicates the presence of reactive secondary weathering products. These secondary weathering products are the result of element mobilisation into the dissolved phase and subsequent precipitation of secondary amorphous and weakly crystalline oxyhydroxides like ferrihydrite. Also, clay minerals like kaolinite and vermiculite are found here (pers. comm. R. Blukis). The most abundant clay mineral at the mediterranean and humid sites is kaolinite with a surface concentration of ca. 15 wt%. Minor amounts of vermiculite (0.4-1.3 wt%) and montmorillonite (1.0-2.2 wt%) are also abundant at the surface of all

weathering profiles. Yet, in the uppermost soil samples of all sites, we detected a higher abundance in extractable Fe than in clay minerals. Both extractable Fe and clay minerals have a high specific surface area (SSA) in contrast to unweathered primary minerals. Thus, they provide adsorption sites for metals and organic matter. However, the SSA is also a weathering indicator in itself (Fisher et al., 2023). The SSA of clay minerals such as kaolinite (ca. 18-26 $m^2 g^{-1}$; Mbey et al., 2019) is smaller than that of Fe hydroxides like ferrihydrite (ca. 270-640 $m^2 g^{-1}$; Filip et al., 2007; Mendez and Hiemstra, 2020). When calculating the SSA contributed by kaolinite, vermiculite, montmorillonite (pers. comm. R. Blukis), and ferrihydrite (assuming that all extractable Fe is ferrihydrite; Table S4-1) the SSA contributed by ferrihydrite to bulk regolith is significantly higher (Table 4-4). Fisher *et al.* (2023) also observed that already < 0.1% of secondary Al and Fe oxides provide 36-81% of additional surface area which supports our interpretation that reactive Al and Fe hydroxides provide more surface area and thus adsorption sites due to their higher abundance in soil samples at all study sites.

Table 4-4. Comparison of the contribution of specific surface area (SSA) to bulk regolith from kaolinite, vermiculite, montmorillonite, and ferrihydrite at the semi-arid, mediterranean and humid sites (mineral composition provided by pers. comm. with R. Blukis). 1: Mbey et al., 2019; 2: Raman and Mortland, 1966; 3: Kuila and Prasad, 2013; 4: Helmy et al., 1999; 5: Filip et al., 2007; 6: Mendez and Hiemstra, 2020.

Secondary weathering products	**Published SSA**	**semi-arid**	**mediterranean**	**humid**
	$[m^2 g^{-1}]$	$[m^2 g^{-1}]$	$[m^2 g^{-1}]$	$[m^2 g^{-1}]$
Kaolinite[1]	18 – 26	0.0 – 0.0	2.6 – 3.7	2.8 – 4.1
Vermiculite[2]	2 – 56	0.03 – 0.73	0.01 – 0.22	0.01 – 0.34
Montmorillonite[3,4]	30 – 700	0.3 – 7.0	0.7 – 15.4	0.5 – 11.2
Ferrihydrite[5,6]	270 – 640	50 – 119	54 – 127	107 – 253

4.5.3 *Indication of weathering by dissolved loss*

The dissolved loss is highest in surface samples due to the input of rainwater with its low solute concentration. Loss is lowest in bedrock where fluid residence times are highest and mineral dissolution rates are accordingly lower (Maher, 2010; Brantley and Lebedeva, 2011). The resulting gradient is a typical pattern for weathering profiles (e.g. Brantley and Lebedeva, 2011). The only exception is presented by dissolved loss of Fe that decreases at the surface concomitant with an increase in extractable Fe. This vertical pattern can be explained with two weathering mechanisms: 1) In bedrock, Fe is pre-weathered and with increasing water flow the mobile Fe is lost into the dissolved phase (see Discussion – Primary mineral leaching).

Hence, where dissolution is predominant in the weathering profile, the concentrations of extractable Fe decrease. 2) Fe is stabilised due to oxidation of ferrous (Fe(II)) to ferric (Fe(III)) Fe by O_2 or by organic complexation (e.g. Kim et al., 2017; Song et al., 2022; Wu et al., 2023) and is thus not readily dissolvable. Nevertheless, the finding of Fe loss in our weathering profiles is surprising as in Fe-poor lithology, Fe(II) is usually oxidised by the available O_2 in gaseous form or dissolved in pore water (e.g. Fletcher et al., 2006; Buss et al., 2008; Behrens et al., 2015). As an explanation, Kim *et al.* (2017) suggested for Fe-rich lithology that Fe is lost into the dissolved phase if the capacity of minerals to consume O_2 is higher than the availability of O_2 in the weathering profile. In Fe-poor lithology, Fe is commonly retained and stabilised due to oxidation (Kim et al. 2017). However, even in our granitoid rock, where the total Fe contents are only 2- 5%, which is roughly half of the total Fe compared to the analysed diabase (10%) in Kim *et al.* (2017), still 10-15% Fe as indicated by τ is lost into the dissolved phase. The loss from the Fe-poor granitoid can thus be explained firstly by the aforementioned pre-alteration of minerals and subsequent loss where water flow is higher. Further, the loss can be explained by limited O_2 diffusion in gaseous or dissolved form such that O_2 is consumed in shallower depths. Alternatively, the activity of Fe-reducing microorganisms at depth might enhance the mobilisation of Fe and thus contribute to loss into the dissolved phase (e.g. Colombo et al., 2014; Mejia et al., 2016). Finally, dissolved organic matter complexes Fe(III) thereby increasing its solubility (e.g. Kaiser and Kalbitz, 2012; Scott and Rothstein, 2014), although this mechanism may not be effective at depth below the upper soil meters.

For all elements except for Fe, F_{ex} and F_{diss} flip over in a certain depth (Figure 4-1). Below this depth, the extractable phase indicates potential element mobilisation from primary minerals without significant loss. The flip-over depth marks the depth where water flow is sufficiently high to enable the dissolution of previously immobile elements. However, the flip-over depth as well as other weathering indicators (Fe oxidation indicated by Fe(III)/Fe(total), porosity; Chapter 2.3.6, 2.3.4; Hampl et al., 2022) suggest that reaction fronts are located at the same depth. Only dissolution and formation of secondary weathering products take place at variable depths. However, we do not observe nested weathering fronts as identified, even for granitic lithology, in other studies (Brantley et al., 2014, 2017b).

4.5.4 *The ^{9}Be, $^{10}Be_{met}$ and $^{10}Be_{met}/^{9}Be$ ratio as indicators for weathering*

We detected increasing concentrations of reactive ^{9}Be where dissolution of Na is high or hydrothermal overprint preconditioned the bedrock. For example, at the mediterranean site, the loss of Na at the surface is ca. 40% with a reactive ^{9}Be concentration of ca. 0.15 µg g^{-1} whereas at the humid-ridge site, ca. 90% of Na is lost and the surface reactive ^{9}Be concentration is ca. 0.4 µg g^{-1} (Figure 4-2; assuming that Na loss indicates plagioclase dissolution). As plagioclase is one of the main carriers of Be (Grew, 2002), the reactive ^{9}Be concentration depends on the intensity of plagioclase dissolution. In addition, at the arid and semi-arid sites, high concentrations of reactive ^{9}Be indicate that hydrothermal fluids may have

transported allochthonous Be to the core sites (Figure 4-2; Barton and Young, 2002). For reactive ^{9}Be, the depth distribution is set by the downward migration in soils, which is favoured by pH < 5, sufficient fluid flow, and a low abundance of reactive surfaces (Maher and von Blanckenburg, 2016). As shown below, the same principles hold for meteoric cosmogenic ^{10}Be that is not sourced in rocks. That ^{9}Be is released where primary minerals dissolve and immobilised where the abundance of reactive phases with high surface area is high, is supported by the observed increase in reactive ^{9}Be concentrations with increasing concentrations of extractable Al and Fe in the uppermost zone. In deep saprolite and bedrock, high reactive ^{9}Be concentrations only appear when the rock is hydrothermally overprinted. ^{9}Be in weathering profiles is also shifted by fluid flow. At the humid slope site, we observe increasing concentrations with depth (Figure 4-4), indicating that slope-parallel water flow pathways beneath hillslopes affect the redistribution of Be. Thus, the depth distribution and mobilisation of ^{9}Be are not only dependent on water infiltration but also on water flow within a hillslope. Further, we have shown that extractable concentrations in bedrock possibly contain a fraction released from pre-weathered primary minerals. For reactive ^{9}Be concentrations, this issue is likely negligible as only 0.03 to 0.07 µg g^{-1} are extracted from bedrock with the sequential extraction procedure. Not only is this a negligible fraction of bedrock Be, but also in the standard ^{10}Be/^{9}Be denudation rate method (Wittmann et al., 2012) unpowdered samples with a grain size > 20 µm are processed, at which case no ^{9}Be should be released from primary minerals.

For $^{10}Be_{met}$, the depth of infiltration is limited to the upper meters of the weathering profile at all study sites. Yet, the depth of infiltration is deeper where rainfall is high (Figure 4-4). This climate dependence of the $^{10}Be_{met}$ infiltration depth was also observed in a compilation of soil profiles (summarised in Graly et al., 2010; Bacon et al., 2012). Beneath this upper zone, the measured ^{10}Be concentrations are negligible. Even in fractured samples (where one might expect fast advective transport of ^{10}Be) the concentrations do not significantly exceed the detection limit. In soil, concentrations of $^{10}Be_{met}$ indicate a good correlation with extractable Al and Fe at the mediterranean and humid sites - both increase towards the surface (Figure 4-5). Hence, $^{10}Be_{met}$ infiltrates only in the uppermost zone consisting of soil and subsoil where the concentrations of extractable Al and Fe are high. Extractable Al and Fe in the form of Fe and Al hydroxides provide higher surface area that increase the capacity to adsorb the infiltrating $^{10}Be_{met}$ (Maher and von Blanckenburg, 2016). At the humid site, however, $^{10}Be_{met}$ infiltrates into the upper part of the second zone consisting of saprolite where concentrations of extractable Al and Fe are lower (Figure 4-1). At all sites, the high abundance of extractable Al and Fe close to the surface explains why no significant $^{10}Be_{met}$ is found at depth, not even in deeply fractured samples. We exclude the semi-arid site from this analysis (showing a moderate negative correlation of $^{10}Be_{met}$ with reactive Al and Fe) as the $^{10}Be_{met}$ depositional flux to Earth's surface is not comparable to the humid and mediterranean sites due to limited rainfall (Chapter 3.5.2). For all sites, we suggest that

reactive Al and Fe hydroxides form a soil trap for $^{10}Be_{met}$ due to the high surface area of these weathering products (Table 4-4) and prevent the infiltration to the depth at which open fractures appear within saprolite. Thus, $^{10}Be_{met}$ is not tracing deep water infiltration into a weathering profile but the $^{10}Be_{met}$ infiltration depth in combination with the concentration of extractable Al and Fe is a tracer for weathering intensity.

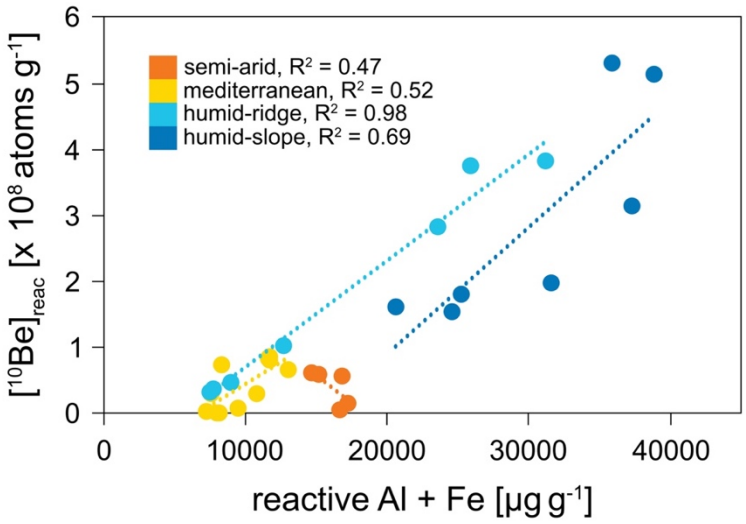

Figure 4-5. Correlation between the concentrations of $^{10}Be_{met}$ and leached reactive Al and Fe.

The isotope ratio of ^{9}Be and $^{10}Be_{met}$ ($^{10}Be_{met}/^{9}Be$) provides information on release by weathering and the input of meteoric ^{10}Be from the atmosphere and can thus be used as a denudation rate meter (von Blanckenburg et al., 2012). Direct inter-site comparison of $^{10}Be_{met}/^{9}Be$ ratios is difficult because, in reality, $^{10}Be_{met}$ depositional fluxes differ, as shown in Chapter 3.5.2. To compare the processes that set the isotope ratios at the different sites nevertheless, we normalised ratios to a uniform depositional flux of 1.5 x10^6 atoms cm^{-2} yr^{-1}. To infer the integration time of this erosion and weathering rate meter, we need to know the residence time within the depth interval in which both isotopes are mixed. This depth increases with rainfall along the study sites and is 0.1 m at the semi-arid, 0.15 m at the mediterranean, and 0.3 m at both humid sites. The resulting residence time for this depth depends on the denudation rate that was independently determined using *in situ* ^{10}Be (Chapter 3.4). The resulting residence times are ca. 3 kyrs at the mediterranean site where denudation rates are highest along the gradient, ca. 9 kyrs at the semi-arid site, and ca. 21 kyrs at the humid sites. As shown above, the $^{10}Be_{met}$ concentration is zero below the uppermost 5 m, and consequently, the $^{10}Be_{met}/^{9}Be$ ratio is also zero at all sites. Only one sample from the humid-slope site indicates a ratio that is significantly higher than detection limit (Figure 4-6). Knowledge of the depth distribution of $^{10}Be_{met}/^{9}Be$ is important as the ratio in groundwater likely resembles the depth ratio from the weathering profile. As groundwater will contribute Be to rivers, groundwater might lower the $^{10}Be_{met}/^{9}Be$ ratio from surface waters

when it is mixed in rivers. This might affect denudation rates calculated from $^{10}Be_{met}/^{9}Be$ in river sediment.

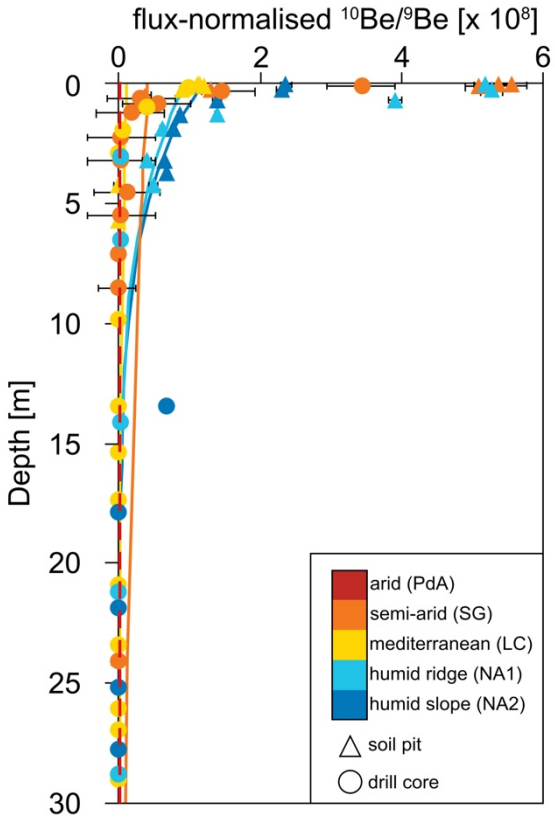

Figure 4-6. Depth profile of the isotope ratio $^{10}Be_{met}/^{9}Be$. The dashed line indicates the detection limit. The solid lines show exponential fits.

4.5.5 *Depth zones in weathering profiles*

We have quantitatively assigned distinct zones assuming that a change of 20% in total concentration of extractable Al and Fe in a sample relative to the sample directly below indicates a different zone in the weathering profile. We have also shown that the concentration of infiltrated $^{10}Be_{met}$ correlates with these zones (Figure 4-5). In summary, we identified three zones in the weathering profiles using extractable Al and Fe: The uppermost zone contains soil and subsoil and indicates high concentrations of extractable Al and Fe, high loss of Ca and Na, and highest concentrations of reactive ^{9}Be and $^{10}Be_{met}$. Below, the second zone consists of moderately to highly weathered saprolite with strong gradients that indicate increasing loss of all elements except for Fe, increasing concentrations of extractable Al, Fe, and reactive ^{9}Be, but no significant concentrations of infiltrated $^{10}Be_{met}$ are detected. This zone further comprises weakly weathered deep saprolite and fractured saprock that is indicated by gradually increasing dissolution of primary minerals towards the surface, although, this increase is small and extends over several meters (semi-arid: ca. 55 m, mediterranean: ca. 40 m, humid: ca. 10 m). The concentration of the extractable phase decreases towards the

surface as dissolution removes elements from pre-weathered and primary minerals. The deepest zone consists of bedrock that is likely pre-weathered by deep or old processes (see Discussion – Primary mineral leaching) and thus reveals high concentrations in the extractable phase.

The zones determined with extractable Al and Fe (Figure 4-7) match with zones identified by other weathering parameters like elemental mass loss τ and Fe(III)/Fe(total) (Chapter 2.3; Hampl et al., 2022), with the visual description and classification of different zones, and also with zones identified by geophysical subsurface imaging using seismic velocities (Trichandi et al., 2022, 2023b). This match can be explained by the interrelated weathering processes: primary mineral dissolution at depth mobilises elements that are subsequently precipitated into secondary weathering products and thus the concentration of extractable Al and Fe increases. The oxidation of Fe(II) to Fe(III) and the precipitation of amorphous Fe hydroxides stabilises Fe and thus we observe a concentration increase in extractable Fe at the depth where the oxidation takes place. In bedrock, no dissolution occurs but gaseous O_2 can induce Fe oxidation (that we observe as high extractable Fe concentrations). As soon as sufficient water flow enables dissolution, we observe loss of Fe and other elements (indicated by τ). Furthermore, dissolution of primary minerals and Fe oxidation create secondary porosity while the precipitation of secondary weathering products clogs porosity so that water flow at depth is affected which is observable in different seismic velocities of the defined zones.

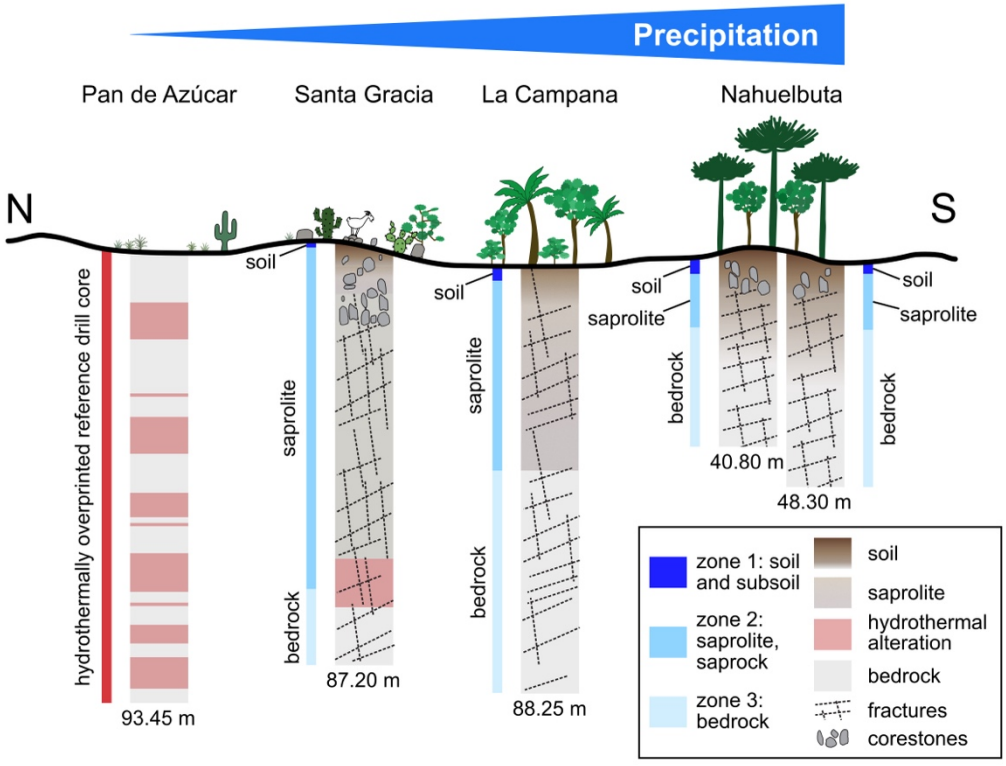

Figure 4-6. Schematic overview of the drill cores from visual core descriptions at the four study sites with identified weathering zones (blue) calculated from the concentration of leached reactive Al and Fe.

4.5.6 *External factors controlling processes and depth of the weathering zone*

With increasing rainfall, the concentrations of extractable Al and Fe as well as the dissolved loss of Ca, K, and Na in surface samples increase. Yet, the depth at which concentrations of extractable elements and dissolution increase does not correlate with increasing rainfall. At the mediterranean site with approximately half of the rainfall available relative to the humid site, τ_{Na} indicates much deeper loss (ca. 40 m) than at the humid site (< 10 m). In surface samples, however, τ_{Na} indicates nearly complete loss (ca. 90%) at the humid site while at the mediterranean site, τ_{Na} only accounts for ca. 40% loss. We ascribe the higher near-surface dissolution at the humid site to the higher input of rainwater leading to more intense weathering (Hayes et al., 2020). Moreover, the dense vegetation cover and microbial activity (Oeser and von Blanckenburg, 2020a; Rodriguez et al., 2022) in soil at the humid site provide organic acids that might promote mineral dissolution which also explains the high dissolution identified with τ_{Na}. Rodriguez *et al.* (2022) detected the highest amount of specialised microorganisms that enhance dissolution of minerals at the humid site. Oeser and von Blanckenburg (2020) suggested that the dense vegetation cover prevents more intense weathering by inducing secondary mineral formation. However, this study and Hampl *et al.* (2023) observed that weathering is most intense at the humid site but deep weathering is inhibited due to pore clogging by formation of secondary weathering products.

For a weathering profile situated in the same climatic setting in Central Chile like our mediterranean site that is also characterised by a thick saprolite zone (> 30 m), the authors suggest that kaolinite coating of plagioclase inhibits more intense weathering (Vázquez et al., 2016). At the mediterranean site, Hampl *et al.* (2023) suggested that the evolution of a deep weathering profile is determined by Fe oxidation that induces micro-scale fracturing due to volume expansion and by the absence of swelling clay minerals that might else clog the porosity and inhibits water flow. Both explanations facilitate deep weathering at the mediterranean site. In conclusion, this comparison suggests that available rainfall does not determine the weathering depth, that is rather controlled by tectonic pre-conditioning, whereas water availability controls the weathering intensity as indicated by concentration of reactive Al and Fe and elemental mass loss of Na at the surface.

The denudation rate determines the time available for a weathering profile to develop over a certain depth and thus determines the available time for mineral dissolution and precipitation of secondary weathering products. Since the weathering depth varies strongly between the study sites, we calculated the residence time for the upper 10 meters (arbitrarily chosen to allow for direct comparison of relative regolith residence times) using denudation rates derived with *in situ* ^{10}Be from Chapter 2.3.7 (Krone et al., 2021a) and Chapter 3.4. The resulting residence time for 10 m of regolith is ca. 900 kyr at the semi-arid site, ca. 200 kyr at the mediterranean site, and ca. 700 kyr at the humid sites. The significantly shorter time for minerals to be weathered in the mediterranean site further explains the lower weathering intensity. There, the fast denudation leads to supply of fresh bedrock at the bottom of the

weathering zone that is as fast as the measured denudation rate assuming that the denudation rate and the weathering front advance rate are in steady state (Lebedeva and Brantley, 2020). The long residence time at the semi-arid site explains why elemental mass loss and reactive phase concentrations are similar to those at the mediterranean site despite vastly different rainfall. Furthermore, at the humid sites, the intense formation of secondary reactive phases and clay minerals is facilitated by the long residence time.

4.6 Conclusion and Implications

Our investigation of reactive secondary weathering products measured by extractable elements and combined with elemental mass loss balances in weathering profiles suggests that the reactive phase is a novel and sensitive weathering indicator of solid transformations at depth even in the absence of detectable mass loss. The new proxy serves to assign zones defined by distinct alteration processes in a weathering profile. We defined three different zones that are in good agreement with visual characterisation, other weathering parameters like Fe(III)/Fe(total), and geophysical subsurface imaging. While the weathering depth along the climate gradient is not controlled by rainfall, the weathering intensity (concentration of extractable Al and Fe, dissolution of Na) is. Therefore, transport pathways provided by porosity and tectonic fractures enable fluid flow to greater depth and control the weathering depth rather than climate. Potentially, these fractures provide migration pathways for microorganisms with the ability to participate in weathering (e.g. Napieralski et al., 2019; Finlay et al., 2020). Weatherable minerals like accessory calcite or pre-weathered biotite serve as suppliers of essential elements (C from calcite, K and Mg from biotite) in such a deep biosphere. We conclude that at the investigated study sites the conditions for deep microbiological activity prevail, rendering these sites suited for further investigation on the abundance and strategy of these microorganisms, including their contribution to mineral transformations and Fe stabilisation mechanisms.

Concerning the mechanisms that form the backbone of the denudation rate meter meteoric cosmogenic ^{10}Be and its ratio to weathering-released stable ^{9}Be, we identified that infiltrated $^{10}Be_{met}$ is adsorbed to reactive phases provided mostly by Fe hydroxides, but also clay minerals serve as adsorption sites. These reactive secondary weathering products are increasingly abundant towards the surface where $^{10}Be_{met}$ readily attaches to these provided adsorption sites. Neither in settings with tectonic fractures connecting Earth's surface with the subsurface nor with sufficient rainfall does $^{10}Be_{met}$ appear to infiltrate to great depth. The soil and upper weathering zone, containing reactive Al and Fe hydroxides and clay minerals, serve as an apparent complete trap for this nuclide. Reactive ^{9}Be concentration indicates intense alteration by previous hydrothermal activity (arid and semi-arid sites) or by a high degree of plagioclase dissolution (humid site). Thus, both ^{9}Be and $^{10}Be_{met}$ are indicators for both weathering intensity and weathering rate.

5. References

Aarão Reis, F.D.A., and Brantley, S.L., 2019, The impact of depth-dependent water content on steady state weathering and eroding systems: Geochimica et Cosmochimica Acta, v. 244, p. 40–55, doi:10.1016/j.gca.2018.09.028.

Acevedo Salinas, J.G., 2022, Análisis petrológico/mineralógico y estructural del Plutón Cerros del Vetado, comuna de Chañaral, región de Atacama:

Ackerer, J., Chabaux, F., Van der Woerd, J., Viville, D., Pelt, E., Kali, E., Lerouge, C., Ackerer, P., di Chiara Roupert, R., and Négrel, P., 2016, Regolith evolution on the millennial timescale from combined U–Th–Ra isotopes and in situ cosmogenic 10Be analysis in a weathering profile (Strengbach catchment, France): Earth and Planetary Science Letters, v. 453, p. 33–43, doi:10.1016/j.epsl.2016.08.005.

Ackerer, J., Ranchoux, C., Lucas, Y., Viville, D., Clément, A., Fritz, B., Lerouge, C., Schäfer, G., and Chabaux, F., 2021, Investigating the role of deep weathering in critical zone evolution by reactive transport modeling of the geochemical composition of deep fracture water: Geochimica et Cosmochimica Acta, v. 312, p. 257–278, doi:10.1016/j.gca.2021.07.017.

Anders, M.H., Laubach, S.E., and Scholz, C.H., 2014, Microfractures: A review: Journal of Structural Geology, v. 69, p. 377–394, doi:10.1016/j.jsg.2014.05.011.

Anderson, S.P., von Blanckenburg, F., and White, A.F., 2007, Physical and Chemical Controls on the Critical Zone: Elements, v. 3, p. 315–319, doi:10.2113/gselements.3.5.315.

Anderson, S.P., Dietrich, W.E., and Brimhall, G.H., Jr., 2002, Weathering profiles, mass-balance analysis, and rates of solute loss: Linkages between weathering and erosion in a small, steep catchment: GSA Bulletin, v. 114, p. 1143–1158, doi:10.1130/0016-7606(2002)114<1143:WPMBAA>2.0.CO;2.

Anderson, S.P., Kelly, P.J., Hoffman, N., Barnhart, K., Befus, K., and Ouimet, W., 2021, Is This Steady State? Weathering and Critical Zone Architecture in Gordon Gulch, Colorado Front Range, *in* Hunt, A., Egli, M., and Faybishenko, B. eds., Geophysical Monograph Series, Wiley, p. 231–252, doi:10.1002/9781119563952.ch13.

Anderson, R.F., Lao, Y., Broecker, W.S., Trumbore, S.E., Hofmann, H.J., and Wolfli, W., 1990, Boundary scavenging in the Pacific Ocean: a comparison of ^{10}Be and ^{231}Pa: Earth and Planetary Science Letters, v. 96, p. 287–304, doi:10.1016/0012-821X(90)90008-L.

Anderson, R.S., Rajaram, H., and Anderson, S.P., 2019, Climate driven coevolution of weathering profiles and hillslope topography generates dramatic differences in critical zone architecture: Hydrological Processes, v. 33, p. 4–19, doi:10.1002/hyp.13307.

Araguás-Araguás, L., Froehlich, K., and Rozanski, K., 2000, Deuterium and oxygen-18 isotope composition of precipitation and atmospheric moisture: Hydrological Processes, v. 14, p. 1341–1355, doi:10.1002/1099-1085(20000615)14:8<1341::AID-HYP983>3.0.CO;2-Z.

Arancibia, G., Matthews, S.J., and Pérez de Arce, C., 2006, K–Ar and ^{40} Ar/ ^{39} Ar geochronology of supergene processes in the Atacama Desert, Northern Chile: tectonic and climatic relations: Journal of the Geological Society, v. 163, p. 107–118, doi:10.1144/0016-764904-161.

Bacon, A.R., Richter, D. deB., Bierman, P.R., and Rood, D.H., 2012, Coupling meteoric ^{10}Be with pedogenic losses of ^{9}Be to improve soil residence time estimates on an ancient North American interfluve: Geology, v. 40, p. 847–850, doi:10.1130/G33449.1.

Balco, G., 2017, Production rate calculations for cosmic-ray-muon-produced ^{10}Be and ^{26}Al benchmarked against geological calibration data: Quaternary Geochronology, v. 39, p. 150–173, doi:10.1016/j.quageo.2017.02.001.

Balco, G., Stone, J.O., Lifton, N.A., and Dunai, T.J., 2008, A complete and easily accessible means of calculating surface exposure ages or erosion rates from ^{10}Be and ^{26}Al measurements: Quaternary Geochronology, v. 3, p. 174–195, doi:10.1016/j.quageo.2007.12.001.

Balogh-Brunstad, Z., Kent Keller, C., Thomas Dickinson, J., Stevens, F., Li, C.Y., and Bormann, B.T., 2008, Biotite weathering and nutrient uptake by ectomycorrhizal fungus, Suillus tomentosus, in liquid-culture experiments: Geochimica et Cosmochimica Acta, v. 72, p. 2601–2618, doi:10.1016/j.gca.2008.04.003.

Banfield, J.F., Barker, W.W., Welch, S.A., and Taunton, A., 1999, Biological impact on mineral dissolution: Application of the lichen model to understanding mineral weathering in the rhizosphere: Proceedings of the National Academy of Sciences, v. 96, p. 3404–3411, doi:10.1073/pnas.96.7.3404.

Banwart, S., Gustafsson, E., Laaksoharju, M., Nilsson, A., Tullborg, E., and Wallin, B., 1994, Large-scale Intrusion of shallow water into a vertical fracture zone in crystalline bedrock: Initial hydrochemical perturbation during tunnel construction at the Äspö Hard Rock Laboratory, southeastern Sweden: Water Resources Research, v. 30, p. 1747–1763, doi:10.1029/94WR00155.

Banwart, S.A., Nikolaidis, N.P., Zhu, Y.-G., Peacock, C.L., and Sparks, D.L., 2019, Soil Functions: Connecting Earth's Critical Zone: Annual Review of Earth and Planetary Sciences, v. 47, p. 333–359, doi:10.1146/annurev-earth-063016-020544.

Barton, M.D., and Young, S., 2002, Non-pegmatitic Deposits of Beryllium: Mineralogy, Geology, Phase Equilibria and Origin: Reviews in Mineralogy and Geochemistry, v. 50, p. 591–691, doi:10.2138/rmg.2002.50.14.

Bazilevskaya, E., Lebedeva, M., Pavich, M., Rother, G., Parkinson, D.Y., Cole, D., and Brantley, S.L., 2013, Where fast weathering creates thin regolith and slow weathering creates thick regolith: Earth Surface Processes and Landforms, v. 38, p. 847–858, doi:10.1002/esp.3369.

Bazilevskaya, E., Rother, G., Mildner, D.F.R., Pavich, M., Cole, D., Bhatt, M.P., Jin, L., Steefel, C.I., and Brantley, S.L., 2015, How Oxidation and Dissolution in Diabase and Granite Control Porosity during Weathering: Soil Science Society of America Journal, v. 79, p. 55–73, doi:10.2136/sssaj2014.04.0135.

Behrens, R., Bouchez, J., Schuessler, J.A., Dultz, S., Hewawasam, T., and von Blanckenburg, F., 2015, Mineralogical transformations set slow weathering rates in low-porosity metamorphic bedrock on mountain slopes in a tropical climate: Chemical Geology, v. 411, p. 283–298, doi:10.1016/j.chemgeo.2015.07.008.

Behrens, R., Wirth, R., and Von Blanckenburg, F., 2021, Rate limitations of nano-scale weathering front advance in the slow-eroding Sri Lankan Highlands: Geochimica et Cosmochimica Acta, v. 311, p. 174–197, doi:10.1016/j.gca.2021.06.003.

Berner, R.A., and Berner, E.K., 1997, Silicate Weathering and Climate, *in* Ruddiman, W.F. ed., Tectonic Uplift and Climate Change, Boston, MA, Springer US, p. 353–365, doi:10.1007/978-1-4615-5935-1_15.

Berner, E.K., Berner, R.A., and Moulton, K.L., 2003, Plants and Mineral Weathering: Present and Past, *in* Treatise on Geochemistry, Elsevier, p. 169–188, doi:10.1016/B0-08-043751-6/05175-6.

Bernhard, N. et al., 2018, Pedogenic and microbial interrelations to regional climate and local topography: New insights from a climate gradient (arid to humid) along the Coastal Cordillera of Chile: CATENA, v. 170, p. 335–355, doi:10.1016/j.catena.2018.06.018.

Biotite Mineral Data, http://webmineral.com/data/Biotite.shtml (accessed January 2024).

von Blanckenburg, F., Bouchez, J., Ibarra, D.E., and Maher, K., 2015, Stable runoff and weathering fluxes into the oceans over Quaternary climate cycles: Nature Geoscience, v. 8, p. 538–542, doi:10.1038/ngeo2452.

von Blanckenburg, F., Bouchez, J., and Wittmann, H., 2012, Earth surface erosion and weathering from the ^{10}Be (meteoric)/^{9}Be ratio: Earth and Planetary Science Letters, v. 351–352, p. 295–305, doi:10.1016/j.epsl.2012.07.022.

von Blanckenburg, F., Hewawasam, T., and Kubik, P.W., 2004, Cosmogenic nuclide evidence for low weathering and denudation in the wet, tropical highlands of Sri Lanka: Journal of Geophysical Research, v. 109, p. F03008, doi:10.1029/2003JF000049.

von Blanckenburg, F., O'Nions, R.K., Belshaw, N.S., Gibb, A., and Hein, J.R., 1996, Global distribution of beryllium isotopes in deep ocean water as derived from Fe-Mn crusts: Earth and Planetary Science Letters, v. 141, p. 213–226, doi:10.1016/0012-821X(96)00059-3.

von Blanckenburg, F., Schuessler, J.A., Bouchez, J., Frings, P.J., Uhlig, D., Oelze, M., Frick, D.A., Hewawasam, T., Dixon, J., and Norton, K., 2021, Rock weathering and nutrient cycling along an erodosequence: American Journal of Science, v. 321, p. 1111–1163, doi:10.2475/08.2021.01.

Bonneville, S., Bray, A.W., and Benning, L.G., 2016, Structural Fe(II) Oxidation in Biotite by an Ectomycorrhizal Fungi Drives Mechanical Forcing: Environmental Science & Technology, v. 50, p. 5589–5596, doi:10.1021/acs.est.5b06178.

Borchers, B., Marrero, S., Balco, G., Caffee, M., Goehring, B., Lifton, N., Nishiizumi, K., Phillips, F., Schaefer, J., and Stone, J., 2016, Geological calibration of spallation production rates in the CRONUS-Earth project: Quaternary Geochronology, v. 31, p. 188–198, doi:10.1016/j.quageo.2015.01.009.

Borggaard, O.K., 1982, The influence of iron oxides on the surface area of soil: Journal of Soil Science, v. 33, p. 443–449, doi:10.1111/j.1365-2389.1982.tb01779.x.

Bowen, G.J., 2023, The Online Isotopes in Precipitation Calculator, version 3.2:, http://www.waterisotopes.org (accessed September 2023).

Brantley, S.L., 2008, Kinetics of Mineral Dissolution, *in* Brantley, S.L., Kubicki, J.D., and White, A.F. eds., Kinetics of Water-Rock Interaction, New York, NY, Springer New York, p. 151–210, doi:10.1007/978-0-387-73563-4_5.

Brantley, S.L. et al., 2017a, Reviews and syntheses: on the roles trees play in building and plumbing the critical zone: Biogeosciences, v. 14, p. 5115–5142, doi:10.5194/bg-14-5115-2017.

Brantley, S.L. et al., 2011, Twelve testable hypotheses on the geobiology of weathering: Geobiology, v. 9, p. 140–165, doi:10.1111/j.1472-4669.2010.00264.x.

Brantley, S.L., Goldhaber, M.B., and Ragnarsdottir, K.V., 2007, Crossing Disciplines and Scales to Understand the Critical Zone: Elements, v. 3, p. 307–314, doi:10.2113/gselements.3.5.307.

Brantley, S.L., Holleran, M.E., Jin, L., and Bazilevskaya, E., 2013, Probing deep weathering in the Shale Hills Critical Zone Observatory, Pennsylvania (USA): the hypothesis of nested chemical reaction fronts in the subsurface: NESTED REACTION FRONTS: Earth Surface Processes and Landforms, v. 38, p. 1280–1298, doi:10.1002/esp.3415.

Brantley, S.L., Kubicki, J.D., and White, A.F. (Eds.), 2008, Kinetics of Water-Rock Interaction: New York, NY, Springer New York, doi:10.1007/978-0-387-73563-4.

Brantley, S.L., and Lebedeva, M., 2011, Learning to Read the Chemistry of Regolith to Understand the Critical Zone: Annual Review of Earth and Planetary Sciences, v. 39, p. 387–416, doi:10.1146/annurev-earth-040809-152321.

Brantley, S.L., and Lebedeva, M.I., 2021, Relating land surface, water table, and weathering fronts with a conceptual valve model for headwater catchments: Hydrological Processes, v. 35, doi:10.1002/hyp.14010.

Brantley, S.L., Lebedeva, M.I., Balashov, V.N., Singha, K., Sullivan, P.L., and Stinchcomb, G., 2017b, Toward a conceptual model relating chemical reaction fronts to water flow paths in hills: Geomorphology, v. 277, p. 100–117, doi:10.1016/j.geomorph.2016.09.027.

Brantley, S.L., Lebedeva, M., and Bazilevskaya, E., 2014, Relating Weathering Fronts for Acid Neutralization and Oxidation to pCO_2 and pO_2, *in* Treatise on Geochemistry, Elsevier, p. 327–352, doi:10.1016/B978-0-08-095975-7.01317-6.

Brantley, S.L., Lebedeva, M., and Hausrath, E.M., 2012, A Geobiological View of Weathering and Erosion, *in* Knoll, A.H., Canfield, D.E., and Konhauser, K.O. eds., Fundamentals of Geobiology, Wiley, p. 205–227, doi:10.1002/9781118280874.ch12.

Brimhall, G.H., and Dietrich, W.E., 1987, Constitutive mass balance relations between chemical composition, volume, density, porosity, and strain in metasomatic hydrochemical systems: Results on weathering and pedogenesis: Geochimica et Cosmochimica Acta, v. 51, p. 567–587, doi:10.1016/0016-7037(87)90070-6.

Brown, L., Pavich, M.J., Hickman, R.E., Klein, J., and Middleton, R., 1988, Erosion of the eastern United States observed with ^{10}Be: Earth Surface Processes and Landforms, v. 13, p. 441–457, doi:10.1002/esp.3290130509.

Brunauer, S., Emmett, P.H., and Teller, E., 1938, Adsorption of Gases in Multimolecular Layers: Journal of the American Chemical Society, v. 60, p. 309–319, doi:10.1021/ja01269a023.

Bufe, A., Hovius, N., Emberson, R., Rugenstein, J.K.C., Galy, A., Hassenruck-Gudipati, H.J., and Chang, J.-M., 2021, Co-variation of silicate, carbonate and sulfide weathering drives CO_2 release with erosion: Nature Geoscience, v. 14, p. 211–216, doi:10.1038/s41561-021-00714-3.

Burke, B.C., Heimsath, A.M., and White, A.F., 2007, Coupling chemical weathering with soil production across soil-mantled landscapes: Earth Surface Processes and Landforms, v. 32, p. 853–873, doi:10.1002/esp.1443.

Buss, H.L., Sak, P.B., Webb, S.M., and Brantley, S.L., 2008, Weathering of the Rio Blanco quartz diorite, Luquillo Mountains, Puerto Rico: Coupling oxidation, dissolution, and fracturing: Geochimica et Cosmochimica Acta, v. 72, p. 4488–4507, doi:10.1016/j.gca.2008.06.020.

Calitri, F., Sommer, M., van der Meij, W.M., Tikhomirov, D., Christl, M., and Egli, M., 2021, ^{10}Be and ^{14}C data provide insight on soil mass redistribution along gentle slopes and reveal ancient human impact: Journal of Soils and Sediments, doi:10.1007/s11368-021-03041-7.

Calmels, D., Galy, A., Hovius, N., Bickle, M., West, A.J., Chen, M.-C., and Chapman, H., 2011, Contribution of deep groundwater to the weathering budget in a rapidly eroding mountain belt, Taiwan: Earth and Planetary Science Letters, v. 303, p. 48–58, doi:10.1016/j.epsl.2010.12.032.

Campodonico, V.A., Pasquini, A.I., Lecomte, K.L., García, M.G., and Depetris, P.J., 2019, Chemical weathering in subtropical basalt-derived laterites: A mass balance interpretation (Misiones, NE Argentina): CATENA, v. 173, p. 352–366, doi:10.1016/j.catena.2018.10.027.

Cardozo, N., and Allmendinger, R.W., 2013, Spherical projections with OSXStereonet: Computers & Geosciences, v. 51, p. 193–205, doi:10.1016/j.cageo.2012.07.021.

Casey, W.H., Westrich, H.R., and Holdren, G.R., 1991, Dissolution rates of plagioclase at pH = 2 and 3: American Mineralogist, v. 76, p. 211–217.

Caves Rugenstein, J.K., Ibarra, D.E., and von Blanckenburg, F., 2019, Neogene cooling driven by land surface reactivity rather than increased weathering fluxes: Nature, v. 571, p. 99–102, doi:10.1038/s41586-019-1332-y.

Cembrano, J., González, G., Arancibia, G., Ahumada, I., Olivares, V., and Herrera, V., 2005, Fault zone development and strain partitioning in an extensional strike-slip duplex: A case study from the Mesozoic Atacama fault system, Northern Chile: Tectonophysics, v. 400, p. 105–125, doi:10.1016/j.tecto.2005.02.012.

Chapin, F.S., Matson, P.A., Mooney, H.A., and Vitousek, P.M., 2002, Principles of terrestrial ecosystem ecology:

Chmeleff, J., Von Blanckenburg, F., Kossert, K., and Jakob, D., 2010, Determination of the ^{10}Be half-life by multicollector ICP-MS and liquid scintillation counting: Nuclear Instruments and Methods in Physics Research Section B: Beam Interactions with Materials and Atoms, v. 268, p. 192–199, doi:10.1016/j.nimb.2009.09.012.

Chorover, J., Kretzschmar, R., Garcia-Pichel, F., and Sparks, D.L., 2007, Soil Biogeochemical Processes within the Critical Zone: Elements, v. 3, p. 321–326, doi:10.2113/gselements.3.5.321.

Christensen, N.I., and Mooney, W.D., 1995, Seismic velocity structure and composition of the continental crust: A global review: Journal of Geophysical Research, v. 100, p. 9761–9788.

Clarke, J.D.A., 2006, Antiquity of aridity in the Chilean Atacama Desert: Geomorphology, v. 73, p. 101–114, doi:10.1016/j.geomorph.2005.06.008.

Clayton, J.L., 1986, An estimate of plagioclase weathering rate in the Idaho batholith based upon geochemical transport rates.: Rates of chemical weathering of rocks and minerals, p. 453–466.

Clow, D.W., and Mast, M.A., 2010, Mechanisms for chemostatic behavior in catchments: Implications for CO_2 consumption by mineral weathering: Chemical Geology, v. 269, p. 40–51, doi:10.1016/j.chemgeo.2009.09.014.

Clow, T., Willenbring, J.K., Schaller, M., Blum, J.D., Christl, M., Kubik, P.W., and Von Blanckenburg, F., 2020, Calibrating a long-term meteoric ^{10}Be delivery rate into eroding western US glacial deposits by comparing meteoric and in situ produced ^{10}Be depth profiles: Geochronology, v. 2, p. 411–423, doi:10.5194/gchron-2-411-2020.

Colombo, C., Palumbo, G., He, J.-Z., Pinton, R., and Cesco, S., 2014, Review on iron availability in soil: interaction of Fe minerals, plants, and microbes: Journal of Soils and Sediments, v. 14, p. 538–548, doi:10.1007/s11368-013-0814-z.

Dallmeyer, R.D., Brown, M., Grocott, J., Taylor, G.K., and Treloar, P.J., 1996, Mesozoic Magmatic and Tectonic Events within the Andean Plate Boundary Zone, 26°-27°30'S, North Chile: Constraints from ^{40} Ar/ ^{39} Ar Mineral Ages: The Journal of Geology, v. 104, p. 19–40, doi:10.1086/629799.

Dannhaus, N., Wittmann, H., Krám, P., Christl, M., and von Blanckenburg, F., 2018, Catchment-wide weathering and erosion rates of mafic, ultramafic, and granitic rock from cosmogenic meteoric ^{10}Be/^{9}Be ratios: Geochimica et Cosmochimica Acta, v. 222, p. 618–641, doi:10.1016/j.gca.2017.11.005.

Dawson, T.E., Hahm, W.J., and Crutchfield-Peters, K., 2020, Digging deeper: what the critical zone perspective adds to the study of plant ecophysiology: New Phytologist, v. 226, p. 666–671, doi:10.1111/nph.16410.

Deckart, K., Hervé, F., Fanning, C.M., Ramírez, V., Calderón, M., and Godoy, E., 2014, Geocronología U-Pb e isótopos de Hf-O en circones del batolito de la Costa Pensilvaniana, Chile.: Andean Geology, v. 41, p. 49–82, doi:10.5027/andgeoV41n1-a03.

Deng, K., Wittmann, H., and von Blanckenburg, F., 2020a, The depositional flux of meteoric cosmogenic ^{10}Be from modeling and observation: Earth and Planetary Science Letters, v. 550, p. 116530, doi:10.1016/j.epsl.2020.116530.

Deng, K., Wittmann, H., Hsieh, M.-L., Yang, S., and von Blanckenburg, F., 2021a, Deposition and retention of meteoric ^{10}Be in Holocene Taiwan river terraces: Quaternary Science Reviews, v. 265, p. 107048, doi:10.1016/j.quascirev.2021.107048.

Deng, K., Wittmann, H., Yang, S., and Blanckenburg, F., 2021b, The Upper Limit of Denudation Rate Measurement from Cosmogenic ^{10}Be(Meteoric)/^{9}Be Ratios in Taiwan: Journal of Geophysical Research: Earth Surface, doi:10.1029/2021JF006221.

Deng, K., Yang, S., Von Blanckenburg, F., and Wittmann, H., 2020b, Denudation Rate Changes Along a Fast-Eroding Mountainous River With Slate Headwaters in Taiwan From ^{10}Be(Meteoric)/^{9}Be Ratios: Journal of Geophysical Research: Earth Surface, v. 125, p. e2019JF005251, doi:10.1029/2019JF005251.

Dewald, A. et al., 2013, CologneAMS, a dedicated center for accelerator mass spectrometry in Germany: Nuclear Instruments and Methods in Physics Research Section B: Beam Interactions with Materials and Atoms, v. 294, p. 18–23, doi:10.1016/j.nimb.2012.04.030.

Dixon, J.L., and von Blanckenburg, F., 2012, Soils as pacemakers and limiters of global silicate weathering: Comptes Rendus Geoscience, v. 344, p. 597–609, doi:10.1016/j.crte.2012.10.012.

Dixon, J.L., Chadwick, O.A., and Pavich, M.J., 2018, Climatically controlled delivery and retention of meteoric ^{10}Be in soils: Geology, v. 46, p. 899–902, doi:10.1130/G45176.1.

Dixon, J.L., Heimsath, A.M., Kaste, J., and Amundson, R., 2009, Climate-driven processes of hillslope weathering: Geology, v. 37, p. 975–978, doi:10.1130/G30045A.1.

van Dongen, R., Scherler, D., Wittmann, H., and von Blanckenburg, F., 2019, Cosmogenic ^{10}Be in river sediment: where grain size matters and why: Earth Surface Dynamics, v. 7, p. 393–410, doi:10.5194/esurf-7-393-2019.

Dunai, T.J., González López, G.A., and Juez-Larré, J., 2005, Oligocene–Miocene age of aridity in the Atacama Desert revealed by exposure dating of erosion-sensitive landforms: Geology, v. 33, p. 321, doi:10.1130/G21184.1.

Egli, M., Brandová, D., Böhlert, R., Favilli, F., and Kubik, P.W., 2010, ^{10}Be inventories in Alpine soils and their potential for dating land surfaces: Geomorphology, v. 119, p. 62–73, doi:10.1016/j.geomorph.2010.02.019.

Egli, M., Mirabella, A., and Sartori, G., 2008, The role of climate and vegetation in weathering and clay mineral formation in late Quaternary soils of the Swiss and Italian Alps: Geomorphology, v. 102, p. 307–324, doi:10.1016/j.geomorph.2008.04.001.

Eppes, M.-C., and Keanini, R., 2017, Mechanical weathering and rock erosion by climate-dependent subcritical cracking: WEATHERING BY SUBCRITICAL CRACKING: Reviews of Geophysics, v. 55, p. 470–508, doi:10.1002/2017RG000557.

Fantle, M.S., and DePaolo, D.J., 2004, Iron isotopic fractionation during continental weathering: Earth and Planetary Science Letters, v. 228, p. 547–562, doi:10.1016/j.epsl.2004.10.013.

Fick, S.E., and Hijmans, R.J., 2017, WorldClim 2: new 1-km spatial resolution climate surfaces for global land areas: International Journal of Climatology, v. 37, p. 4302–4315, doi:10.1002/joc.5086.

Field, C.V., Schmidt, G.A., Koch, D., and Salyk, C., 2006, Modeling production and climate-related impacts on ^{10}Be concentration in ice cores: Journal of Geophysical Research, v. 111, p. D15107, doi:10.1029/2005JD006410.

Filip, J., Zboril, R., Schneeweiss, O., Zeman, J., Cernik, M., Kvapil, P., and Otyepka, M., 2007, Environmental Applications of Chemically Pure Natural Ferrihydrite: Environmental Science & Technology, v. 41, p. 4367–4374, doi:10.1021/es062312t.

Finlay, R.D. et al., 2020, Reviews and syntheses: Biological weathering and its consequences at different spatial levels – from nanoscale to global scale: Biogeosciences, v. 17, p. 1507–1533, doi:10.5194/bg-17-1507-2020.

Fischer, C., Karius, V., and Lüttge, A., 2009, Correlation between sub-micron surface roughness of iron oxide encrustations and trace element concentrations: Science of The Total Environment, v. 407, p. 4703–4710, doi:10.1016/j.scitotenv.2009.04.026.

Fisher, B.J., Faust, J.C., Moore, O.W., Peacock, C.L., and März, C., 2021, Technical note: Uncovering the influence of methodological variations on the extractability of iron-bound organic carbon: Biogeosciences, v. 18, p. 3409–3419, doi:10.5194/bg-18-3409-2021.

Fisher, B.A., Yoo, K., Aufdenkampe, A.K., Nater, E.A., Feinberg, J.M., and Nyquist, J.E., 2023, Mineral surface area in deep weathering profiles reveals the interrelationship of iron oxidation and silicate weathering: Earth Surface Dynamics, v. 11, p. 51–69, doi:10.5194/esurf-11-51-2023.

Fletcher, R., Buss, H., and Brantley, S., 2006, A spheroidal weathering model coupling porewater chemistry to soil thicknesses during steady-state denudation: Earth and Planetary Science Letters, v. 244, p. 444–457, doi:10.1016/j.epsl.2006.01.055.

Fordham, A.W., 1990, Weathering of biotite into dioctahedral clay minerals: Clay Minerals, v. 25, p. 51–63, doi:10.1180/claymin.1990.025.1.06.

Friese, A., Kallmeyer, J., Axel Kitte, J., Montaño Martínez, I., Bijaksana, S., Wagner, D., and the ICDP Lake Chalco Drilling Science Team and the ICDP Towuti Drilling Science Team, 2017, A simple and inexpensive technique for assessing contamination during drilling operations: A simple and inexpensive technique: Limnology and Oceanography: Methods, v. 15, p. 200–211, doi:10.1002/lom3.10159.

Frings, P.J., Oelze, M., Schubring, F., Frick, D.A., and Von Blanckenburg, F., 2021, Interpreting silicon isotopes in the Critical Zone: American Journal of Science, v. 321, p. 1164–1203, doi:10.2475/08.2021.02.

Frogner, P., and Schweda, P., 1998, Hornblende dissolution kinetics at 25°C: Chemical Geology, v. 151, p. 169–179, doi:10.1016/S0009-2541(98)00078-3.

Gaillardet, J., Calmels, D., Romero-Mujalli, G., Zakharova, E., and Hartmann, J., 2019, Global climate control on carbonate weathering intensity: Chemical Geology, v. 527, p. 118762, doi:10.1016/j.chemgeo.2018.05.009.

Gaillardet, J., Dupré, B., Louvat, P., and Allègre, C.J., 1999, Global silicate weathering and CO_2 consumption rates deduced from the chemistry of large rivers: Chemical Geology, v. 159, p. 3–30, doi:10.1016/S0009-2541(99)00031-5.

Garcia Arredondo, M., Fang, Y., Jones, M., Yabusaki, S., Cardon, Z., and Keiluweit, M., 2023, Resolving dynamic mineral-organic interactions in the rhizosphere by combining in-situ microsensors with plant-soil reactive transport modeling: Soil Biology and Biochemistry, v. 184, p. 109097, doi:10.1016/j.soilbio.2023.109097.

Gerrits, R., Pokharel, R., Breitenbach, R., Radnik, J., Feldmann, I., Schuessler, J.A., Von Blanckenburg, F., Gorbushina, A.A., and Schott, J., 2020, How the rock-inhabiting fungus *K. petricola* A95 enhances olivine dissolution through attachment: Geochimica et Cosmochimica Acta, v. 282, p. 76–97, doi:10.1016/j.gca.2020.05.010.

Ghasera, K.M., and Rashid, S.A., 2024, Influence of micro-scale factors in weathering and elements mobility: Evidence from a comparative study of granite and basalt weathering profiles across India: CATENA, v. 235, p. 107680, doi:10.1016/j.catena.2023.107680.

Godoy, E., and Lara, L., 1998, Hojas Chañaral y Diego de Almagro, Región de Atacama: Servicio nacional de geología y minería.

Goodfellow, B.W., and Hilley, G.E., 2022, Climatic and lithological controls on the structure and thickness of granitic weathering zones: Earth and Planetary Science Letters, v. 600, p. 117890, doi:10.1016/j.epsl.2022.117890.

Goodfellow, B.W., Hilley, G.E., Webb, S.M., Sklar, L.S., Moon, S., and Olson, C.A., 2016, The chemical, mechanical, and hydrological evolution of weathering granitoid: Granite Weathering: Journal of Geophysical Research: Earth Surface, v. 121, p. 1410–1435, doi:10.1002/2016JF003822.

Graham, R., Rossi, A., and Hubbert, R., 2010, Rock to regolith conversion: Producing hospitable substrates for terrestrial ecosystems: GSA Today, p. 4–9, doi:10.1130/GSAT57A.1.

Graly, J.A., Bierman, P.R., Reusser, L.J., and Pavich, M.J., 2010, Meteoric ^{10}Be in soil profiles – A global meta-analysis: Geochimica et Cosmochimica Acta, v. 74, p. 6814–6829, doi:10.1016/j.gca.2010.08.036.

Graly, J.A., Reusser, L.J., and Bierman, P.R., 2011, Short and long-term delivery rates of meteoric ^{10}Be to terrestrial soils: Earth and Planetary Science Letters, v. 302, p. 329–336, doi:10.1016/j.epsl.2010.12.020.

Grew, E.S., 2002, Mineralogy, Petrology and Geochemistry of Beryllium: An Introduction and List of Beryllium Minerals: Reviews in Mineralogy and Geochemistry, v. 50, p. 1–76, doi:10.2138/rmg.2202.50.01.

Hack, J.T., 1960, Interpretation of erosional topography in humid temperate regions: Bobbs-Merrill Washington, DC, USA.

Hampl, F.J., Schiperski, F., Byrne, J.M., Schwerdhelm, C., Kappler, A., Bryce, C., von Blanckenburg, F., and Neumann, T., 2022, The role of iron-bearing minerals for the deep weathering of a hydrothermally altered plutonic rock in semi-arid climate (Chilean Coastal Cordillera): Chemical Geology, v. 604, p. 120922, doi:10.1016/j.chemgeo.2022.120922.

Hampl, F.J., Schiperski, F., Schwerdhelm, C., Stroncik, N., Bryce, C., von Blanckenburg, F., and Neumann, T., 2023, Feedbacks between the formation of secondary minerals and the infiltration of fluids into the regolith of granitic rocks in different climatic zones (Chilean Coastal Cordillera): Chemical: Chemical weathering preprint, doi:10.5194/esurf-2022-71.

Hayes, N.R., Buss, H.L., Moore, O.W., Krám, P., and Pancost, R.D., 2020, Controls on granitic weathering fronts in contrasting climates: Chemical Geology, v. 535, p. 119450, doi:10.1016/j.chemgeo.2019.119450.

Hayes, J.L., Riebe, C.S., Holbrook, W.S., Flinchum, B.A., and Hartsough, P.C., 2019, Porosity production in weathered rock: Where volumetric strain dominates over chemical mass loss: Science Advances, v. 5, p. eaao0834, doi:10.1126/sciadv.aao0834.

Heckman, K., and Rasmussen, C., 2011, Lithologic controls on regolith weathering and mass flux in forested ecosystems of the southwestern USA: Geoderma, v. 164, p. 99–111, doi:10.1016/j.geoderma.2011.05.003.

Heikkilä, U., 2007, Modeling of the atmospheric transport of the cosmogenic radionuclides ^{10}Be and ^{7}Be using the ECHAM5-HAM general circulation model: ETH Zurich, doi:10.3929/ETHZ-A-005560259.

Heikkilä, U., Beer, J., Abreu, J.A., and Steinhilber, F., 2013, On the Atmospheric Transport and Deposition of the Cosmogenic Radionuclides (^{10}Be): A Review: Space Science Reviews, v. 176, p. 321–332, doi:10.1007/s11214-011-9838-0.

Heikkilä, U., and von Blanckenburg, F., 2015, The global distribution of Holocene meteoric ^{10}Be fluxes from atmospheric models. Distribution maps for terrestrial Earths surface applications: , p. 1291716 Bytes, 2 Files, doi:10.5880/GFZ.3.4.2015.001.

Heikkilä, U., and Smith, A.M., 2013, Production rate and climate influences on the variability of ^{10}Be deposition simulated by ECHAM5-HAM: Globally, in Greenland, and in Antarctica: PRODUCTION AND CLIMATE INFLUENCE ON ^{10}BE: Journal of Geophysical Research: Atmospheres, v. 118, p. 2506–2520, doi:10.1002/jgrd.50217.

Heimsath, A.M., Dietrich, W.E., Nishiizumi, K., and Finkel, R.C., 1997, The soil production function and landscape equilibrium: Nature, v. 388, p. 358–361, doi:10.1038/41056.

Hellmann, R., Wirth, R., Daval, D., Barnes, J.-P., Penisson, J.-M., Tisserand, D., Epicier, T., Florin, B., and Hervig, R.L., 2012, Unifying natural and laboratory chemical weathering with interfacial dissolution–reprecipitation: A study based on the nanometer-scale chemistry of fluid–silicate interfaces: Chemical Geology, v. 294–295, p. 203–216, doi:10.1016/j.chemgeo.2011.12.002.

Helmy, A.K., Ferreiro, E.A., and De Bussetti, S.G., 1999, Surface Area Evaluation of Montmorillonite: Journal of Colloid and Interface Science, v. 210, p. 167–171, doi:10.1006/jcis.1998.5930.

Hewawasam, T., von Blanckenburg, F., Bouchez, J., Dixon, J.L., Schuessler, J.A., and Maekeler, R., 2013, Slow advance of the weathering front during deep, supply-limited saprolite formation in the tropical Highlands of Sri Lanka: Geochimica et Cosmochimica Acta, v. 118, p. 202–230, doi:10.1016/j.gca.2013.05.006.

Hilley, G.E., Chamberlain, C.P., Moon, S., Porder, S., and Willett, S.D., 2010, Competition between erosion and reaction kinetics in controlling silicate-weathering rates: Earth and Planetary Science Letters, v. 293, p. 191–199, doi:10.1016/j.epsl.2010.01.008.

Hodson, M.E., 2003, The influence of Fe-rich coatings on the dissolution of anorthite at pH 2.6: Geochimica et Cosmochimica Acta, v. 67, p. 3355–3363, doi:10.1016/S0016-7037(02)01370-4.

Holbrook, W.S., Marcon, V., Bacon, A.R., Brantley, S.L., Carr, B.J., Flinchum, B.A., Richter, D.D., and Riebe, C.S., 2019, Links between physical and chemical weathering inferred from a 65-m-deep borehole through Earth's critical zone: Scientific Reports, v. 9, p. 4495, doi:10.1038/s41598-019-40819-9.

Holdren, G.R., and Speyer, P.M., 1987, Reaction rate-surface area relationships during the early stages of weathering. II. Data on eight additional feldspars: Geochimica et Cosmochimica Acta, v. 51, p. 2311–2318, doi:10.1016/0016-7037(87)90284-5.

Hulton, N.R.J., Purves, R.S., McCulloch, R.D., Sugden, D.E., and Bentley, M.J., 2002, The Last Glacial Maximum and deglaciation in southern South America: Quaternary Science Reviews, v. 21, p. 233–241, doi:10.1016/S0277-3791(01)00103-2.

Ibarra, D.E., Rugenstein, J.K.C., Bachan, A., Baresch, A., Lau, K.V., Thomas, D.L., Lee, J.-E., Boyce, C.K., and Chamberlain, C.P., 2019, Modeling the consequences of land plant evolution on silicate weathering: American Journal of Science, v. 319, p. 1–43, doi:10.2475/01.2019.01.

Ingamells, C., 1976, Preparation, analysis, and sampling constants for a biotite: Nat. Bur. Stand., Spec. Pub., v. 422, p. 401–419.

Itami, K., Kitagawa, Y., Kyuma, K., and Kosaki, T., 1996, Effect of removal of free oxides on changes in dispersibility and charge characteristics of soils: Soil Science and Plant Nutrition, v. 42, p. 593–602, doi:10.1080/00380768.1996.10416328.

Jamtveit, B., Kobchenko, M., Austrheim, H., Malthe-Sørenssen, A., Røyne, A., and Svensen, H., 2011, Porosity evolution and crystallization-driven fragmentation during weathering of andesite: Journal of Geophysical Research, v. 116, p. B12204, doi:10.1029/2011JB008649.

Jara, J.J., Barra, F., Reich, M., Morata, D., Leisen, M., and Romero, R., 2021, Geochronology and petrogenesis of intrusive rocks in the Coastal Cordillera of northern Chile: Insights from zircon U-Pb dating and trace element geochemistry: Gondwana Research, v. 93, p. 48–72, doi:10.1016/j.gr.2021.01.007.

Jena, P.S., Bhushan, R., Ajay, S., Dabhi, A.J., Gaddam, M., and Sudheer, A.K., 2023, Applicability of meteoric ^{10}Be in dating marine sediment cores: Marine Chemistry, v. 254, p. 104275, doi:10.1016/j.marchem.2023.104275.

Jena, P.S., Bhushan, R., Shivam, A., Nambiar, R., and Bharti, N., 2021, Production rate variation and changes in sedimentation rate of marine core dated with meteoric ^{10}Be and ^{14}C: Journal of Environmental Radioactivity, v. 237, p. 106678, doi:10.1016/j.jenvrad.2021.106678.

Jin, L., Ravella, R., Ketchum, B., Bierman, P.R., Heaney, P., White, T., and Brantley, S.L., 2010, Mineral weathering and elemental transport during hillslope evolution at the Susquehanna/Shale Hills Critical Zone Observatory: Geochimica et Cosmochimica Acta, v. 74, p. 3669–3691, doi:10.1016/j.gca.2010.03.036.

Jin, L., Rother, G., Cole, D.R., Mildner, D.F.R., Duffy, C.J., and Brantley, S.L., 2011, Characterization of deep weathering and nanoporosity development in shale--A neutron study: American Mineralogist, v. 96, p. 498–512, doi:10.2138/am.2011.3598.

Juez-Larré, J., Kukowski, N., Dunai, T.J., Hartley, A.J., and Andriessen, P.A.M., 2010, Thermal and exhumation history of the Coastal Cordillera arc of northern Chile revealed by thermochronological dating: Tectonophysics, v. 495, p. 48–66, doi:10.1016/j.tecto.2010.06.018.

Kaiser, K., and Kalbitz, K., 2012, Cycling downwards – dissolved organic matter in soils: Soil Biology and Biochemistry, v. 52, p. 29–32, doi:10.1016/j.soilbio.2012.04.002.

Kajdas, B., Michalik, M.J., and Migoń, P., 2017, Mechanisms of granite alteration into grus, Karkonosze granite, SW Poland: CATENA, v. 150, p. 230–245, doi:10.1016/j.catena.2016.11.026.

Kalinowski, B.E., and Schweda, P., 1996, Kinetics of muscovite, phlogopite, and biotite dissolution and alteration at pH 1-4, room temperature: Geochimica et Cosmochimica Acta, v. 60, p. 367–385, doi:10.1016/0016-7037(95)00411-4.

Kaste, J.M., and Baskaran, M., 2012, Meteoric ^{7}Be and ^{10}Be as Process Tracers in the Environment, *in* Baskaran, M. ed., Handbook of Environmental Isotope Geochemistry, Berlin, Heidelberg, Springer Berlin Heidelberg, Advances in Isotope Geochemistry, p. 61–85, doi:10.1007/978-3-642-10637-8_5.

Kawano, M., 1996, Amorphous Aluminum Hydroxide Formed at the Earliest Weathering Stages of K-Feldspar: Clays and Clay Minerals, v. 44, p. 672–676, doi:10.1346/CCMN.1996.0440510.

Kelly, E.F., Chadwick, O.A., and Hilinski, T.E., 1998, The Effect of Plants on Mineral Weathering: Biogeochemistry, v. 42, p. 21–53, doi:10.1023/A:1005919306687.

Kiczka, M., Wiederhold, J.G., Frommer, J., Kraemer, S.M., Bourdon, B., and Kretzschmar, R., 2010, Iron isotope fractionation during proton- and ligand-promoted dissolution of primary phyllosilicates: Geochimica et Cosmochimica Acta, v. 74, p. 3112–3128, doi:10.1016/j.gca.2010.02.018.

Kim, H., Stinchcomb, G., and Brantley, S.L., 2017, Feedbacks among O_2 and CO_2 in deep soil gas, oxidation of ferrous minerals, and fractures: A hypothesis for steady-state regolith thickness: Earth and Planetary Science Letters, v. 460, p. 29–40, doi:10.1016/j.epsl.2016.12.003.

Korschinek, G. et al., 2010, A new value for the half-life of ^{10}Be by Heavy-Ion Elastic Recoil Detection and liquid scintillation counting: Nuclear Instruments and Methods in Physics Research Section B: Beam Interactions with Materials and Atoms, v. 268, p. 187–191, doi:10.1016/j.nimb.2009.09.020.

Kramer, M.G., and Chadwick, O.A., 2018, Climate-driven thresholds in reactive mineral retention of soil carbon at the global scale: Nature Climate Change, v. 8, p. 1104–1108, doi:10.1038/s41558-018-0341-4.

Krone, L.V. et al., 2021a, Deep weathering in the semi-arid Coastal Cordillera, Chile: Scientific Reports, v. 11, p. 13057, doi:10.1038/s41598-021-90267-7.

Krone, L.V. et al., 2021b, Physical and geochemical data on a drill core from the semi-arid Coastal Cordillera, Chile: GFZ Data Publications, doi:10.5880/GFZ.3.3.2021.002.

Kuila, U., and Prasad, M., 2013, Specific surface area and pore-size distribution in clays and shales: Geophysical Prospecting, v. 61, p. 341–362.

Kusakabe, M., and Ku, T.-L., 1984, Incorporation of Be isotopes and other trace metals into marine ferromanganese deposits: Geochimica et Cosmochimica Acta, v. 48, p. 2187–2193, doi:10.1016/0016-7037(84)90215-1.

Lai, P., Moulton, K., and Krevor, S., 2015, Pore-scale heterogeneity in the mineral distribution and reactive surface area of porous rocks: Chemical Geology, v. 411, p. 260–273, doi:10.1016/j.chemgeo.2015.07.010.

Lal, D., 1991, Cosmic ray labeling of erosion surfaces: in situ nuclide production rates and erosion models: Earth and Planetary Science Letters, v. 104, p. 424–439, doi:10.1016/0012-821X(91)90220-C.

Lal, D., Charles, C., Vacher, L., Goswami, J.N., Jull, A.J.T., McHargue, L., and Finkel, R.C., 2006, Paleo-ocean chemistry records in marine opal: Implications for fluxes of trace elements, cosmogenic nuclides (^{10}Be and ^{26}Al), and biological productivity: Geochimica et Cosmochimica Acta, v. 70, p. 3275–3289, doi:10.1016/j.gca.2006.04.004.

Lal, D., and Peters, B., 1967, Cosmic Ray Produced Radioactivity on the Earth, *in* Sitte, K. ed., Kosmische Strahlung II / Cosmic Rays II, Berlin, Heidelberg, Springer Berlin Heidelberg, Handbuch der Physik / Encyclopedia of Physics, v. 9 / 46 / 2, p. 551–612, doi:10.1007/978-3-642-46079-1_7.

Landeweert, R., Hoffland, E., Finlay, R.D., Kuyper, T.W., and Van Breemen, N., 2001, Linking plants to rocks: ectomycorrhizal fungi mobilize nutrients from minerals: Trends in Ecology & Evolution, v. 16, p. 248–254, doi:10.1016/S0169-5347(01)02122-X.

Lawrence, C., Harden, J., and Maher, K., 2014, Modeling the influence of organic acids on soil weathering: Geochimica et Cosmochimica Acta, v. 139, p. 487–507, doi:10.1016/j.gca.2014.05.003.

Lebedeva, M.I., and Brantley, S.L., 2020, Exploring an 'ideal hill': how lithology and transport mechanisms affect the possibility of a steady state during weathering and erosion: Earth Surface Processes and Landforms, v. 45, p. 652–665, doi:10.1002/esp.4762.

Lebedeva, M.I., and Brantley, S.L., 2013, Exploring geochemical controls on weathering and erosion of convex hillslopes: beyond the empirical regolith production function: Earth Surface Processes and Landforms, v. 38, p. 1793–1807, doi:10.1002/esp.3424.

Lebedeva, M.I., and Brantley, S.L., 2017, Weathering and erosion of fractured bedrock systems: Earth Surface Processes and Landforms, v. 42, p. 2090–2108, doi:10.1002/esp.4177.

Lebedeva, M.I., Fletcher, R.C., and Brantley, S.L., 2010, A mathematical model for steady-state regolith production at constant erosion rate: Earth Surface Processes and Landforms, p. 508–524, doi:10.1002/esp.1954.

Lee, J., and Boyce, K., 2010, Impact of the hydraulic capacity of plants on water and carbon fluxes in tropical South America: Journal of Geophysical Research: Atmospheres, v. 115, p. 2010JD014568, doi:10.1029/2010JD014568.

Lee, R., Taylor, M., Daly, B., and Reynolds, J., 1989, The extraction of Al, Fe and Si from a range of New Zealand soils by hydroxylamine and ammonium oxalate solutions: Soil Research, v. 27, p. 377, doi:10.1071/SR9890377.

Lehnert, L.W. et al., 2018, A Case Study on Fog/Low Stratus Occurrence at Las Lomitas, Atacama Desert (Chile) as a Water Source for Biological Soil Crusts: Aerosol and Air Quality Research, v. 18, p. 254–26, doi:10.4209/aaqr.2017.01.0021.

Ludwig, W.J., Nafe, J.E., and Drake, C.L., 1970, Seismic refraction, *in* Maxwell, A.E. ed., The Sea, New York, Wiley-Interscience, v. 4, Part 1, p. 53–84.

Luebert, F., and Pliscoff, P., 2017, Sinopsis bioclimática y vegetacional de Chile:

Maejima, Y., Matsuzaki, H., and Higashi, T., 2005, Application of cosmogenic ^{10}Be to dating soils on the raised coral reef terraces of Kikai Island, southwest Japan: Geoderma, v. 126, p. 389–399, doi:10.1016/j.geoderma.2004.10.004.

Magnesiohornblende Mineral Data, http://webmineral.com/data/Magnesiohornblende.shtml (accessed January 2024).

Maher, K., 2010, The dependence of chemical weathering rates on fluid residence time: Earth and Planetary Science Letters, v. 294, p. 101–110, doi:10.1016/j.epsl.2010.03.010.

Maher, K., 2011, The role of fluid residence time and topographic scales in determining chemical fluxes from landscapes: Earth and Planetary Science Letters, v. 312, p. 48–58, doi:10.1016/j.epsl.2011.09.040.

Maher, K., and von Blanckenburg, F., 2016, Surface ages and weathering rates from ^{10}Be (meteoric) and ^{10}Be/^{9}Be: Insights from differential mass balance and reactive transport modeling: Chemical Geology, v. 446, p. 70–86, doi:10.1016/j.chemgeo.2016.07.016.

Maher, K., and von Blanckenburg, F., 2023, The circular nutrient economy of terrestrial ecosystems and the consequences for rock weathering: Frontiers in Environmental Science, v. 10, p. 1066959, doi:10.3389/fenvs.2022.1066959.

Martel, S.J., 2011, Mechanics of curved surfaces, with application to surface-parallel cracks: Geophysical Research Letters, v. 38, p. L20303, doi:10.1029/2011GL049354.

Masarik, J., and Beer, J., 2009, An updated simulation of particle fluxes and cosmogenic nuclide production in the Earth's atmosphere: Journal of Geophysical Research, v. 114, p. D11103, doi:10.1029/2008JD010557.

Masarik, J., and Beer, J., 1999, Simulation of particle fluxes and cosmogenic nuclide production in the Earth's atmosphere: Journal of Geophysical Research: Atmospheres, v. 104, p. 12099–12111, doi:10.1029/1998JD200091.

Mbey, J.A., Thomas, F., Razafitianamaharavo, A., Caillet, C., and Villiéras, F., 2019, A comparative study of some kaolinites surface properties: Applied Clay Science, v. 172, p. 135–145, doi:10.1016/j.clay.2019.03.005.

McHargue, L.R., and Damon, P.E., 1991, The global beryllium 10 cycle: Reviews of Geophysics, v. 29, p. 141, doi:10.1029/91RG00072.

McKean, J.A., Dietrich, W.E., Finkel, R.C., Southon, J.R., and Caffee, M.W., 1993, Quantification of soil production and downslope creep rates from cosmogenic 10Be accumulations on a hillslope profile: Geology, v. 21, p. 343, doi:10.1130/0091-7613(1993)021<0343:QOSPAD>2.3.CO;2.

Mehra, O., and Jackson, P., 1958, Iron oxide removal from soils and clays in a dithionite-citrate-bicarbonate system buffered with sodium: Clays and Clay Minerals, v. 7, p. 317–327.

Mejia, J., Roden, E.E., and Ginder-Vogel, M., 2016, Influence of Oxygen and Nitrate on Fe (Hydr)oxide Mineral Transformation and Soil Microbial Communities during Redox Cycling: Environmental Science & Technology, v. 50, p. 3580–3588, doi:10.1021/acs.est.5b05519.

Melnick, D., 2016, Rise of the central Andean coast by earthquakes straddling the Moho: Nature Geoscience, v. 9, p. 401–407, doi:10.1038/ngeo2683.

Mendez, J.C., and Hiemstra, T., 2020, Surface area of ferrihydrite consistently related to primary surface charge, ion pair formation, and specific ion adsorption: Chemical Geology, v. 532, p. 119304, doi:10.1016/j.chemgeo.2019.119304.

Mineralienatlas - Fossilienatlas, https://www.mineralienatlas.de/lexikon/index.php/MineralData?lang=de&mineral=Biotit (accessed January 2024).

Ministerio de Obras Públicas, M., 2017, Información Oficial Hidrometeorológica y de Calidad de Aguas en Línea.:

Molina, P.G., Parada, M.A., Gutiérrez, F.J., Ma, C., Li, J., Yuanyuan, L., Reich, M., and Aravena, Á., 2015, Protracted late magmatic stage of the Caleu pluton (central Chile) as a consequence of heat redistribution by diking: Insights from zircon data and thermal modeling: Lithos, v. 227, p. 255–268, doi:10.1016/j.lithos.2015.04.008.

Molnar, P., Anderson, R.S., and Anderson, S.P., 2007, Tectonics, fracturing of rock, and erosion: Journal of Geophysical Research, v. 112, p. F03014, doi:10.1029/2005JF000433.

Murphy, S.F., Brantley, S.L., Blum, A.E., White, A.F., and Dong, H., 1998, Chemical Weathering in a Tropical Watershed, Luquillo Mountains, Puerto Rico: II. Rate and Mechanism of Biotite Weathering: Geochimica et Cosmochimica Acta, v. 62, p. 227–243, doi:10.1016/S0016-7037(97)00336-0.

Muscheler, R., Joos, F., Beer, J., Müller, S.A., Vonmoos, M., and Snowball, I., 2007, Solar activity during the last 1000yr inferred from radionuclide records: Quaternary Science Reviews, v. 26, p. 82–97, doi:10.1016/j.quascirev.2006.07.012.

Napieralski, S.A., Buss, H.L., Brantley, S.L., Lee, S., Xu, H., and Roden, E.E., 2019, Microbial chemolithotrophy mediates oxidative weathering of granitic bedrock: Proceedings of the National Academy of Sciences, v. 116, p. 26394–26401, doi:10.1073/pnas.1909970117.

Navarre-Sitchler, A., Brantley, S.L., and Rother, G., 2015, How Porosity Increases During Incipient Weathering of Crystalline Silicate Rocks: Reviews in Mineralogy and Geochemistry, v. 80, p. 331–354, doi:10.2138/rmg.2015.80.10.

Navarre-Sitchler, A.K., Cole, D.R., Rother, G., Jin, L., Buss, H.L., and Brantley, S.L., 2013, Porosity and surface area evolution during weathering of two igneous rocks: Geochimica et Cosmochimica Acta, v. 109, p. 400–413, doi:10.1016/j.gca.2013.02.012.

Nesbitt, H.W., Fedo, C.M., and Young, G.M., 1997, Quartz and Feldspar Stability, Steady and Non-Steady-State Weathering, and Petrogenesis of Siliciclastic Sands and Muds: The Journal of Geology, v. 105, p. 173–192, doi:10.1086/515908.

Norton, K.P., Molnar, P., and Schlunegger, F., 2014, The role of climate-driven chemical weathering on soil production: Geomorphology, v. 204, p. 510–517, doi:10.1016/j.geomorph.2013.08.030.

Oeser, R.A. et al., 2018a, Chemistry and microbiology of the Critical Zone along a steep climate and vegetation gradient in the Chilean Coastal Cordillera: CATENA, v. 170, p. 183–203, doi:10.1016/j.catena.2018.06.002.

Oeser, R.A. et al., 2018b, Data supplement to: Chemistry and Microbiology of the Critical Zone along a steep climate and vegetation gradient in the Chilean Coastal Cordillera: , p. 3237982 Bytes, 5 Files, doi:10.5880/GFZ.3.3.2018.001.

Oeser, R.A., and von Blanckenburg, F., 2020a, Do degree and rate of silicate weathering depend on plant productivity? Biogeosciences, v. 17, p. 4883–4917, doi:10.5194/bg-17-4883-2020.

Oeser, R.A., and von Blanckenburg, F., 2020b, Strontium isotopes trace biological activity in the Critical Zone along a climate and vegetation gradient: Chemical Geology, v. 558, p. 119861, doi:10.1016/j.chemgeo.2020.119861.

Pandey, S., and Rajaram, H., 2016, Modeling the influence of preferential flow on the spatial variability and time-dependence of mineral weathering rates: Water Resources Research, v. 52, p. 9344–9366, doi:10.1002/2016WR019026.

Parada, M.A. et al., 2007, Andean magmatism, *in* Moreno, T. and Gibbons, W. eds., The Geology of Chile, The Geological Society of London, p. 115–146, doi:10.1144/GOCH.4.

Parada, M.A., Nyström, J.O., and Levi, B., 1999, Multiple sources for the Coastal Batholith of central Chile (31–34°S): geochemical and Sr–Nd isotopic evidence and tectonic implications: Lithos, v. 46, p. 505–521, doi:10.1016/S0024-4937(98)00080-2.

Parada, M.A., Roperch, P., Guiresse, C., and Ramírez, E., 2005, Magnetic fabrics and compositional evidence for the construction of the Caleu pluton by multiple injections, Coastal Range of central Chile: Tectonophysics, v. 399, p. 399–420, doi:10.1016/j.tecto.2004.12.032.

Parfitt, R., and Childs, C., 1988, Estimation of forms of Fe and Al - a review, and analysis of contrasting soils by dissolution and Mossbauer methods: Soil Research, v. 26, p. 121, doi:10.1071/SR9880121.

Pavich, M.J., Brown, L., Harden, J., Klein, J., and Middleton, R., 1986, ^{10}Be distribution in soils from Merced River terraces, California: Geochimica et Cosmochimica Acta, v. 50, p. 1727–1735, doi:10.1016/0016-7037(86)90134-1.

Pavich, M.J., Brown, L., Klein, J., and Middleton, R., 1984, ^{10}Be accumulation in a soil chronosequence: Earth and Planetary Science Letters, v. 68, p. 198–204, doi:10.1016/0012-821X(84)90151-1.

Pedersen, K., 1997, Microbial life in deep granitic rock: FEMS Microbiology Reviews, v. 20, p. 399–414, doi:10.1111/j.1574-6976.1997.tb00325.x.

Pedrazas, M.A., Hahm, W.J., Huang, M., Dralle, D., Nelson, M.D., Breunig, R.E., Fauria, K.E., Bryk, A.B., Dietrich, W.E., and Rempe, D.M., 2021, The relationship between topography, bedrock weathering, and water storage across a sequence of ridges and valleys: Journal of Geophysical Research: Earth Surface, doi:10.1029/2020JF005848.

Perez-Fodich, A., and Derry, L.A., 2019, Organic acids and high soil CO_2 drive intense chemical weathering of Hawaiian basalts: Insights from reactive transport models: Geochimica et Cosmochimica Acta, v. 249, p. 173–198, doi:10.1016/j.gca.2019.01.027.

Porder, S., Hilley, G.E., and Chadwick, O.A., 2007, Chemical weathering, mass loss, and dust inputs across a climate by time matrix in the Hawaiian Islands: Earth and Planetary Science Letters, v. 258, p. 414–427, doi:10.1016/j.epsl.2007.03.047.

Portenga, E.W., Bierman, P.R., Trodick, C.D., Greene, S.E., DeJong, B.D., Rood, D.H., and Pavich, M.J., 2019, Erosion rates and sediment flux within the Potomac River basin quantified over millennial timescales using beryllium isotopes: GSA Bulletin, v. 131, p. 1295–1311, doi:10.1130/B31840.1.

Poulton, S.W., and Canfield, D.E., 2005, Development of a sequential extraction procedure for iron: implications for iron partitioning in continentally derived particulates: Chemical Geology, v. 214, p. 209–221, doi:10.1016/j.chemgeo.2004.09.003.

Price, J.R., and Velbel, M.A., 2014, Rates of Biotite Weathering, and Clay Mineral Transformation and Neoformation, Determined from Watershed Geochemical Mass-Balance Methods for the Coweeta Hydrologic Laboratory, Southern Blue Ridge Mountains, North Carolina, USA: Aquatic Geochemistry, v. 20, p. 203–224, doi:10.1007/s10498-013-9190-y.

Raisbeck, G.M., Yiou, F., Fruneau, M., Loiseaux, J.M., Lieuvin, M., and Ravel, J.C., 1981, Cosmogenic ^{10}Be/^{7}Be as a probe of atmospheric transport processes: Geophysical Research Letters, v. 8, p. 1015–1018, doi:10.1029/GL008i009p01015.

Raman, K.V., and Mortland, M.M., 1966, External specific surface area of vermiculite1: American Mineralogist, v. 51, p. 1787–1792.

Rempe, D.M., and Dietrich, W.E., 2014, A bottom-up control on fresh-bedrock topography under landscapes: Proceedings of the National Academy of Sciences, v. 111, p. 6576–6581, doi:10.1073/pnas.1404763111.

Reusser, L., Graly, J., Bierman, P., and Rood, D., 2010, Calibrating a long-term meteoric ^{10}Be accumulation rate in soil: LONG-TERM METEORIC ^{10}Be ACCUMULATION: Geophysical Research Letters, v. 37, p. n/a-n/a, doi:10.1029/2010GL044751.

Riebe, C.S., Callahan, R.P., Granke, S.B.-M., Carr, B.J., Hayes, J.L., Schell, M.S., and Sklar, L.S., 2021, Anisovolumetric weathering in granitic saprolite controlled byclimate and erosion rate: Geology, doi:10.1130/G48191.1.

Riebe, C.S., Hahm, W.J., and Brantley, S.L., 2017, Controls on deep critical zone architecture: a historical review and four testable hypotheses: Four Testable Hypotheses about the Deep Critical Zone: Earth Surface Processes and Landforms, v. 42, p. 128–156, doi:10.1002/esp.4052.

Riebe, C.S., Kirchner, J.W., and Finkel, R.C., 2004, Erosional and climatic effects on long-term chemical weathering rates in granitic landscapes spanning diverse climate regimes: Earth and Planetary Science Letters, v. 224, p. 547–562, doi:10.1016/j.epsl.2004.05.019.

Riebe, C.S., Kirchner, J.W., and Finkel, R.C., 2003, Long-term rates of chemical weathering and physical erosion from cosmogenic nuclides and geochemical mass balance: Geochimica et Cosmochimica Acta, v. 67, p. 4411–4427, doi:10.1016/S0016-7037(03)00382-X.

Rodríguez, M.P., Aguilar, G., Urresty, C., and Charrier, R., 2015, Neogene landscape evolution in the Andes of north-central Chile between 28 and 32°S: interplay between tectonic and erosional processes: Geological Society, London, Special Publications, v. 399, p. 419, doi:10.1144/SP399.15.

Rodriguez, V., Moskwa, L.-M., Oses, R., Kühn, P., Riveras-Muñoz, N., Seguel, O., Scholten, T., and Wagner, D., 2022, Impact of Climate and Slope Aspects on the Composition of Soil Bacterial Communities Involved in Pedogenetic Processes along the Chilean Coastal Cordillera: Microorganisms, v. 10, p. 847, doi:10.3390/microorganisms10050847.

Roering, J.J., Hunter, B.D., Ferrier, K.L., Chadwick, O.A., Yoo, K., Wackett, A.A., Almond, P.C., Silva, L., and Jellinek, A.M., 2023, Quantifying erosion rates and weathering pathways that maximize soil organic carbon storage: Biogeochemistry, v. 164, p. 319–333, doi:10.1007/s10533-023-01054-7.

Rojas, P.A., Barra, F., Reich, M., Deditius, A., Simon, A., Uribe, F., Romero, R., and Rojo, M., 2018, A genetic link between magnetite mineralization and diorite intrusion at the El Romeral iron oxide-apatite deposit, northern Chile: Mineralium Deposita, v. 53, p. 947–966, doi:10.1007/s00126-017-0777-x.

Ross, G.J., Wang, C., and Schuppli, P.A., 1985, Hydroxylamine and Ammonium Oxalate Solutions as Extractants for Iron and Aluminum from Soils: Soil Science Society of America Journal, v. 49, p. 783–785, doi:10.2136/sssaj1985.03615995004900030051x.

Røyne, A., Jamtveit, B., Mathiesen, J., and Malthe-Sørenssen, A., 2008, Controls on rock weathering rates by reaction-induced hierarchical fracturing: Earth and Planetary Science Letters, v. 275, p. 364–369, doi:10.1016/j.epsl.2008.08.035.

Savage, D., Cave, M.R., Milodowski, A.E., and George, I., 1987, Hydrothermal alteration of granite by meteoric fluid: an example from the Carnmenellis Granite, United Kingdom: Contributions to Mineralogy and Petrology, v. 96, p. 391–405, doi:10.1007/BF00371257.

Savko, K.A., Samsonov, A.V., Sal'nikova, E.B., Kotov, A.B., and Bazikov, N.S., 2015, HT/LP metamorphic zoning in the eastern Voronezh Crystalline Massif: Age and parameters of metamorphism and its geodynamic environment: Petrology, v. 23, p. 559–575, doi:10.1134/S0869591115050045.

Schaefer, L.N., Kereszturi, G., Kennedy, B.M., and Villeneuve, M., 2023, Characterizing lithological, weathering, and hydrothermal alteration influences on volcanic rock properties via spectroscopy and laboratory testing: a case study of Mount Ruapehu volcano, New Zealand: Bulletin of Volcanology, v. 85, p. 43, doi:10.1007/s00445-023-01657-w.

Schaller, M., Ehlers, T.A., Lang, K.A.H., Schmid, M., and Fuentes-Espoz, J.P., 2018, Addressing the contribution of climate and vegetation cover on hillslope denudation, Chilean Coastal Cordillera (26°–38°S): Earth and Planetary Science Letters, v. 489, p. 111–122, doi:10.1016/j.epsl.2018.02.026.

Schaller, M., Von Blanckenburg, F., Veldkamp, A., Tebbens, L.A., Hovius, N., and Kubik, P.W., 2002, A 30 000 yr record of erosion rates from cosmogenic ^{10}Be in Middle European river terraces: Earth and Planetary Science Letters, v. 204, p. 307–320, doi:10.1016/S0012-821X(02)00951-2.

Scheibe, A., Sierra, C.A., and Spohn, M., 2023, Recently fixed carbon fuels microbial activity several meters below the soil surface: Biogeosciences, v. 20, p. 827–838, doi:10.5194/bg-20-827-2023.

Scheibe, A., and Spohn, M., 2022, N2 fixation per unit microbial biomass increases with aridity: Soil Biology and Biochemistry, v. 172, p. 108733, doi:10.1016/j.soilbio.2022.108733.

Schenk, H.J., and Jackson, R.B., 2005, Mapping the global distribution of deep roots in relation to climate and soil characteristics: Geoderma, v. 126, p. 129–140, doi:10.1016/j.geoderma.2004.11.018.

Scheuber, E., and Andriessen, P.A.M., 1990, The kinematic and geodynamic significance of the Atacama fault zone, northern Chile: Journal of Structural Geology, v. 12, p. 243–257, doi:10.1016/0191-8141(90)90008-M.

Scheuber, E., and Gonzalez, G., 1999, Tectonics of the Jurassic-Early Cretaceous magmatic arc of the north Chilean Coastal Cordillera (22°-26°S): A story of crustal deformation along a convergent plate boundary: Tectonics, v. 18, p. 895–910, doi:10.1029/1999TC900024.

Schoonejans, J., Vanacker, V., Opfergelt, S., and Christl, M., 2017, Long-term soil erosion derived from in-situ ^{10}Be and inventories of meteoric ^{10}Be in deeply weathered soils in southern Brazil: Chemical Geology, v. 466, p. 380–388, doi:10.1016/j.chemgeo.2017.06.025.

Schoonejans, J., Vanacker, V., Opfergelt, S., Granet, M., and Chabaux, F., 2016, Coupling uranium series and ^{10}Be cosmogenic radionuclides to evaluate steady-state soil thickness in the Betic Cordillera: Chemical Geology, v. 446, p. 99–109, doi:10.1016/j.chemgeo.2016.03.030.

Schuessler, J.A., Botcharnikov, R.E., Behrens, H., Misiti, V., and Freda, C., 2008, Amorphous Materials: Properties, structure, and Durability: Oxidation state of iron in hydrous phono-tephritic melts: American Mineralogist, v. 93, p. 1493–1504, doi:10.2138/am.2008.2795.

Schwertmann, U., 1964, The differentiation of iron oxide in soils by a photochemical extraction with acid ammonium oxalate: Zeitschrift für Pflanzenernährung und Bodenkunde, v. 105, p. 194–201.

Scott, E.E., and Rothstein, D.E., 2014, The dynamic exchange of dissolved organic matter percolating through six diverse soils: Soil Biology and Biochemistry, v. 69, p. 83–92, doi:10.1016/j.soilbio.2013.10.052.

SERNAGEOMIN, 2003, Mapa Geológico de Chile: versión digital , No. 4 CD-R, versión 1.: Servicio Nacional de Geología y Minería, Publicación Geológica Digital, v. No. 4 CD-R, versión 1.

Shotyk, W., and Nesbitt, H.W., 1992, Incongruent and congruent dissolution of plagioclase feldspar: effect of feldspar composition and ligand complexation: Geoderma, v. 55, p. 55–78, doi:10.1016/0016-7061(92)90005-R.

Simon, Q., Bourlès, D.L., Thouveny, N., Horng, C.-S., Valet, J.-P., Bassinot, F., and Choy, S., 2018, Cosmogenic signature of geomagnetic reversals and excursions from the Réunion event to the Matuyama–Brunhes transition (0.7–2.14 Ma interval): Earth and Planetary Science Letters, v. 482, p. 510–524, doi:10.1016/j.epsl.2017.11.021.

Slim, M., Perron, J.T., Martel, S.J., and Singha, K., 2015, Topographic stress and rock fracture: a two-dimensional numerical model for arbitrary topography and preliminary comparison with borehole observations: TOPOGRAPHIC STRESS AND ROCK FRACTURE: Earth Surface Processes and Landforms, v. 40, p. 512–529, doi:10.1002/esp.3646.

Song, X. et al., 2022, Towards a better understanding of the role of Fe cycling in soil for carbon stabilization and degradation: Carbon Research, v. 1, p. 5, doi:10.1007/s44246-022-00008-2.

St. Clair, J., Moon, S., Holbrook, W.S., Perron, J.T., Riebe, C.S., Martel, S.J., Carr, B., Harman, C., Singha, K., and Richter, D. d., 2015, Geophysical imaging reveals topographic stress control of bedrock weathering: Science, v. 350, p. 534–538, doi:10.1126/science.aab2210.

Stallard, R.F., 1995, Tectonic, environmental, and human aspects of weathering and erosion: a global review using a steady-state perspective: Annual Review of Earth and Planetary Sciences, v. 23, p. 11–39.

Steinhilber, F. et al., 2012, 9,400 years of cosmic radiation and solar activity from ice cores and tree rings: Proceedings of the National Academy of Sciences, v. 109, p. 5967–5971, doi:10.1073/pnas.1118965109.

Stierman, D.J., and Healy, J.H., 1985, A study of the depth of weathering and its relationship to the mechanical properties of near-surface rocks in the Mojave Desert: Pure and Applied Geophysics PAGEOPH, v. 122, p. 425–439, doi:10.1007/BF00874609.

Stinchcomb, G.E., Kim, H., Hasenmueller, E.A., Sullivan, P.L., Sak, P.B., and Brantley, S.L., 2018, Relating soil gas to weathering using rock and regolith geochemistry: American Journal of Science, v. 318, p. 727–763, doi:10.2475/07.2018.01.

Stone, J.O., 2000, Air pressure and cosmogenic isotope production: Journal of Geophysical Research: Solid Earth, v. 105, p. 23753–23759, doi:10.1029/2000JB900181.

Stoppe, N., Amelung, W., and Horn, R., 2015, Extracción química de oxi(hidrox)óxidos sedimentario utilizando oxalato de amonio y ditionito sódico revisado - una explicación de los procesos en sedimentos costeros: Agro Sur, v. 43, p. 11–17, doi:10.4206/agrosur.2015.v43n2-03.

Takahashi, Y., Minai, Y., Ambe, S., Makide, Y., and Ambe, F., 1999, Comparison of adsorption behavior of multiple inorganic ions on kaolinite and silica in the presence of humic acid using the multitracer technique: Geochimica et Cosmochimica Acta, v. 63, p. 815–836, doi:10.1016/S0016-7037(99)00065-4.

Tardy, Y., and Roquin, C., 1992, Geochemistry and evolution of lateritic landscapes, *in* Developments in Earth Surface Processes, Elsevier, v. 2, p. 407–443, doi:10.1016/B978-0-444-89198-3.50021-0.

Taylor, L.L., Leake, J.R., Quirk, J., Hardy, K., Banwart, S.A., and Beerling, D.J., 2009, Biological weathering and the long-term carbon cycle: integrating mycorrhizal evolution and function into the current paradigm: Geobiology, v. 7, p. 171–191, doi:10.1111/j.1472-4669.2009.00194.x.

Tessier, A., Campbell, P.G.C., and Bisson, M., 1979, Sequential extraction procedure for the speciation of particulate trace metals: Analytical Chemistry, v. 51, p. 844–851, doi:10.1021/ac50043a017.

Tipper, E.T. et al., 2021, Global silicate weathering flux overestimated because of sediment–water cation exchange: Proceedings of the National Academy of Sciences, v. 118, p. e2016430118, doi:10.1073/pnas.2016430118.

Tornos, F., Hanchar, J.M., Munizaga, R., Velasco, F., and Galindo, C., 2020, The role of the subducting slab and melt crystallization in the formation of magnetite-(apatite) systems, Coastal Cordillera of Chile: Mineralium Deposita, doi:10.1007/s00126-020-00959-9.

Trichandi, R., Bauer, K., Ryberg, T., Heit, B., Araya Vargas, J., Von Blanckenburg, F., and Krawczyk, C.M., 2023a, 3D shear wave velocity imaging of the subsurface structure of granite rocks in the arid climate of Pan de Azúcar, Chile, revealed by Bayesian inversion of HVSR curves: Physical: Geophysics preprint, doi:10.5194/egusphere-2023-1813.

Trichandi, R., Bauer, K., Ryberg, T., Scherler, D., Bataille, K., and Krawczyk, C.M., 2022, Combined seismic and borehole investigation of the deep granite weathering structure – Santa Gracia Reserve case in Chile: Earth Surface Processes and Landforms, p. esp.5457, doi:10.1002/esp.5457.

Trichandi, R., Bauer, K., Ryberg, T., Wawerzinek, B., Araya Vargas, J., Von Blanckenburg, F., and Krawczyk, C.M., 2023b, Shear-wave velocity imaging of weathered granite in La Campana (Chile) from Bayesian inversion of micro-tremor H/V spectral ratios: Journal of Applied Geophysics, v. 217, p. 105191, doi:10.1016/j.jappgeo.2023.105191.

Uecker, R.K., Flinchum, B.A., Holbrook, W.S., and Carr, B.J., 2023, Mapping bedrock topography: a seismic refraction survey and landscape analysis in the Laramie Range, Wyoming: Frontiers in Water, v. 5, p. 1057725, doi:10.3389/frwa.2023.1057725.

Uhlig, D., Amelung, W., and Blanckenburg, F., 2020, Mineral Nutrients Sourced in Deep Regolith Sustain Long-Term Nutrition of Mountainous Temperate Forest Ecosystems: Global Biogeochemical Cycles, v. 34, doi:10.1029/2019GB006513.

Uhlig, D., and von Blanckenburg, F., 2019, How Slow Rock Weathering Balances Nutrient Loss During Fast Forest Floor Turnover in Montane, Temperate Forest Ecosystems: Frontiers in Earth Science, v. 7, p. 159, doi:10.3389/feart.2019.00159.

Uroz, S., Calvaruso, C., Turpault, M.-P., and Frey-Klett, P., 2009, Mineral weathering by bacteria: ecology, actors and mechanisms: Trends in Microbiology, v. 17, p. 378–387, doi:10.1016/j.tim.2009.05.004.

Uroz, S., Kelly, L.C., Turpault, M.-P., Lepleux, C., and Frey-Klett, P., 2015, The Mineralosphere Concept: Mineralogical Control of the Distribution and Function of Mineral-associated Bacterial Communities: Trends in Microbiology, v. 23, p. 751–762, doi:10.1016/j.tim.2015.10.004.

Uroz, S., Picard, L., and Turpault, M.-P., 2022, Recent progress in understanding the ecology and molecular genetics of soil mineral weathering bacteria: Trends in Microbiology, v. 30, p. 882–897, doi:10.1016/j.tim.2022.01.019.

VanLandingham, L.A., Portenga, E.W., Lefroy, E.C., Schmidt, A.H., Bierman, P.R., and Hidy, A.J., 2022, Comparison of basin-scale in situ and meteoric ^{10}Be erosion and denudation rates in felsic lithologies across an elevation gradient at the George River, northeast Tasmania, Australia: Geochronology, v. 4, p. 153–176, doi:10.5194/gchron-4-153-2022.

Vázquez, M., Ramírez, S., Morata, D., Reich, M., Braun, J.-J., and Carretier, S., 2016, Regolith production and chemical weathering of granitic rocks in central Chile: Chemical Geology, v. 446, p. 87–98, doi:10.1016/j.chemgeo.2016.09.023.

Vitousek, P.M., and Farrington, H., 1997, Nutrient limitation and soil development: Experimental test of a biogeochemical theory: Biogeochemistry, v. 37, p. 63–75, doi:10.1023/A:1005757218475.

Von Fromm, S.F. et al., 2021, Continental-scale controls on soil organic carbon across sub-Saharan Africa: SOIL, v. 7, p. 305–332, doi:10.5194/soil-7-305-2021.

Walker, J.C.G., Hays, P.B., and Kasting, J.F., 1981, A negative feedback mechanism for the long-term stabilization of Earth's surface temperature: Journal of Geophysical Research, v. 86, p. 9776, doi:10.1029/JC086iC10p09776.

Wan, J., Tokunaga, T.K., Williams, K.H., Dong, W., Brown, W., Henderson, A.N., Newman, A.W., and Hubbard, S.S., 2019, Predicting sedimentary bedrock subsurface weathering fronts and weathering rates: Scientific Reports, v. 9, p. 17198, doi:10.1038/s41598-019-53205-2.

Wang, W., Chen, P., Dueker, K., Zhang, Y., Lee, E., Mu, D., Keifer, I., and Jiao, J., 2021, Coevolution of Weathering Front and Water Table: Geophysical Research Letters, v. 48, doi:10.1029/2021GL092916.

Wang, F., Michalski, G., Seo, J.-H., Granger, D.E., Lifton, N., and Caffee, M., 2015, Beryllium-10 concentrations in the hyper-arid soils in the Atacama Desert, Chile: Implications for arid soil formation rates and El Niño driven changes in Pliocene precipitation: Geochimica et Cosmochimica Acta, v. 160, p. 227–242, doi:10.1016/j.gca.2015.03.008.

Wang, J., Zhou, W., Shi, Y., Li, Y., Xian, D., Guo, N., and Liu, C., 2022, Uranium sorption on oxyhydroxide minerals by surface complexation and precipitation: Chinese Chemical Letters, p. S1001841722000353, doi:10.1016/j.cclet.2022.01.019.

Weckmann, U., Bauer, K., Krawczyk, C., Kück, J., Übernickel, K., and von Blanckenburg, F., 2020, Geophysical Borehole logging at Santa Gracia, Chile: GFZ Data Publications, doi:10.5880/GFZ.2.7.2020.001.

White, A.F., 2002, Determining mineral weathering rates based on solid and solute weathering gradients and velocities: application to biotite weathering in saprolites: Chemical Geology, v. 190, p. 69–89, doi:10.1016/S0009-2541(02)00111-0.

White, A.F., Blum, A.E., Schulz, M.S., Bullen, T.D., Harden, J.W., and Peterson, M.L., 1996, Chemical weathering rates of a soil chronosequence on granitic alluvium: I. Quantification of mineralogical and surface area changes and calculation of primary silicate reaction rates: Geochimica et Cosmochimica Acta, v. 60, p. 2533–2550, doi:10.1016/0016-7037(96)00106-8.

White, A.F., and Brantley, S.L., 2003, The effect of time on the weathering of silicate minerals: why do weathering rates differ in the laboratory and field? Chemical Geology, v. 202, p. 479–506, doi:10.1016/j.chemgeo.2003.03.001.

White, A.F., Bullen, T.D., Schulz, M.S., Blum, A.E., Huntington, T.G., and Peters, N.E., 2001, Differential rates of feldspar weathering in granitic regoliths: Geochimica et Cosmochimica Acta, v. 65, p. 847–869, doi:10.1016/S0016-7037(00)00577-9.

White, A.F., Bullen, T.D., Vivit, D.V., Schulz, M.S., and Clow, D.W., 1999, The role of disseminated calcite in the chemical weathering of granitoid rocks: Geochimica et Cosmochimica Acta, v. 63, p. 1939–1953, doi:10.1016/S0016-7037(99)00082-4.

White, A.F., and Buss, H.L., 2014, Natural Weathering Rates of Silicate Minerals, *in* Treatise on Geochemistry, Elsevier, p. 115–155, doi:10.1016/B978-0-08-095975-7.00504-0.

White, A.F., Schulz, M.S., Lowenstern, J.B., Vivit, D.V., and Bullen, T.D., 2005, The ubiquitous nature of accessory calcite in granitoid rocks: Implications for weathering, solute evolution, and petrogenesis: Geochimica et Cosmochimica Acta, v. 69, p. 1455–1471, doi:10.1016/j.gca.2004.09.012.

Wiederhold, J.G., Teutsch, N., Kraemer, S.M., Halliday, A.N., and Kretzschmar, R., 2007, Iron isotope fractionation in oxic soils by mineral weathering and podzolization: Geochimica et Cosmochimica Acta, v. 71, p. 5821–5833, doi:10.1016/j.gca.2007.07.023.

Wild, B., Gerrits, R., and Bonneville, S., 2022, The contribution of living organisms to rock weathering in the critical zone: npj Materials Degradation, v. 6, p. 98, doi:10.1038/s41529-022-00312-7.

Willenbring, J.K., and von Blanckenburg, F., 2010a, Long-term stability of global erosion rates and weathering during late-Cenozoic cooling: Nature, v. 465, p. 211–214, doi:10.1038/nature09044.

Willenbring, J.K., and von Blanckenburg, F., 2010b, Meteoric cosmogenic Beryllium-10 adsorbed to river sediment and soil: Applications for Earth-surface dynamics: Earth-Science Reviews, v. 98, p. 105–122, doi:10.1016/j.earscirev.2009.10.008.

Wittmann, H., von Blanckenburg, F., Bouchez, J., Dannhaus, N., Naumann, R., Christl, M., and Gaillardet, J., 2012, The dependence of meteoric 10Be concentrations on particle size in Amazon River bed sediment and the extraction of reactive $^{10}Be/^{9}Be$ ratios: Chemical Geology, v. 318–319, p. 126–138, doi:10.1016/j.chemgeo.2012.04.031.

Wittmann, H., von Blanckenburg, F., Dannhaus, N., Bouchez, J., Gaillardet, J., Guyot, J.L., Maurice, L., Roig, H., Filizola, N., and Christl, M., 2015, A test of the cosmogenic $^{10}Be(meteoric)/^{9}Be$ proxy for simultaneously determining basin-wide erosion rates, denudation rates, and the degree of weathering in the Amazon basin: EROSION FROM METEORIC $^{10}BE/^{9}BE$ IN AMAZON: Journal of Geophysical Research: Earth Surface, v. 120, p. 2498–2528, doi:10.1002/2015JF003581.

Wood, W.W., Sanford, W.E., Cherry, J.A., and Wood, W.T., 2023, “Wrecking the rocks”: Continental weathering by groundwater: Geology, v. 51, p. 1122–1126, doi:10.1130/G51571.1.

Wu, S., Konhauser, K.O., Chen, B., and Huang, L., 2023, “Reactive Mineral Sink” drives soil organic matter dynamics and stabilization: npj Materials Sustainability, v. 1, p. 3, doi:10.1038/s44296-023-00003-7.

Yiou, F. et al., 1997, Beryllium 10 in the Greenland Ice Core Project ice core at Summit, Greenland: Journal of Geophysical Research: Oceans, v. 102, p. 26783–26794, doi:10.1029/97JC01265.

Yuguchi, T., Izumino, Y., and Sasao, E., 2021, Genesis and development processes of fractures in granite: Petrographic indicators of hydrothermal alteration (P. Wang, Ed.): PLOS ONE, v. 16, p. e0251198, doi:10.1371/journal.pone.0251198.

Zhang, J., Hetzel, R., Pan, B., Geng, H., Wolff, R., and Chen, D., 2023, A ^{10}Be-based paleo-erosion record for the Qilian Shan (NE Tibet) over the past 4.2 Ma from a drillcore in the Hexi Corridor: Geomorphology, v. 430, p. 108657, doi:10.1016/j.geomorph.2023.108657.

Zhang, L., and Lüttge, A., 2009, Theoretical approach to evaluating plagioclase dissolution mechanisms: Geochimica et Cosmochimica Acta, v. 73, p. 2832–2849, doi:10.1016/j.gca.2009.02.021.

6. Appendix

6.1 Supplements Chapter 2

The supplement is published as a data publication on GFZ data services as

Physical and geochemical data on a drill core from the semi-arid Coastal Cordillera, Chile

Krone, L. V., Hampl, F. J., Schwerdhelm, C., Bryce, C., Ganzert, L., Kitte, A., Übernickel, K., Dielforder, A., Aldaz, S., Oses-Pedraza, R., Perez, J. P. H., Sanchez-Alfaro, P., Wagner, D., Weckmann, U. & von Blanckenburg, F. (2021); DOI: 10.5880/GFZ.3.3.2021.002.

Table S2-1: Physical properties of the drilling cores derived from boreholes N1 and N1C. Light blue highlighted lines denote bedrock composition.

Table S2-2: Elemental composition derived by OES measurements (corrected for LOI[1]). Major elements were measured with ICP-OES, trace elements with ICP-MS. Light blue highlighted lines denote bedrock composition.

Table S2-3: Modal mineral composition of the bedrock.

Table S2-4: Weathering indicators CDF, volumetric strain ε_{Zr} and τ. Light blue highlighted lines denote bedrock composition.

Table S2-5: Bulk Fe(II)/Fe(III) ratios and extracted oxide Fe, Si, Al concentrations. CBD: citrate dithionite bicarbonate, A and B indicate two replicates, SE: standard error. Light blue highlighted lines denote bedrock composition.

Table S2-6: Elemental composition derived by OES measurements (LOI uncorrected) and reference materials. Light blue highlighted lines denote bedrock composition. Please note that the measured certified reference materials are given in the published supplement.

Table S2-7: *In situ* cosmogenic-derived 10Be denudation-, chemical weathering- and erosion rates.

Table S2-8: Contamination control data derived from tracer particle analysis in drill fluid and rock samples. DL: detection limit.

Supplementary Table S2-1. Physical properties of the drilling cores derived from boreholes N1 and N1C. Light blue highlighted lines denote bedrock composition.

Sample	Zone		Depth	IGSN	Density ρ (bulk)[1]	unc.	Density ρ (matrix)[2]	unc.	He Porosity[3]	unc.	Water-available porosity[4]	unc.	SSA[5]	unc.
			[m]		[g cm^{-3}]	[g cm^{-3}]	[g cm^{-3}]	[g cm^{-3}]	[%]	[%]	[%]	[%]	[m^2 g^{-1}]	[m^2 g^{-1}]
ES03/19-SG-N1C-1-0-25	I	soil	-0.1	GFLVK00KB	na	na	na	na	na	na	na	na	10.97	0.16
ES03/19-SG-N1C-5-0-50	II	saprolite	-2.3	GFLVK00KH	na	na	na	na	na	na	na	na	6.73	0.09
ES03/19-SG-N1C-8-0-40			-3.8	GFLVK00KL	na	na	na	na	na	na	na	na	3.60	0.01
ES03/19-SG-N1-8-33-53			-6.8	GFCHS0002	2.69	0.005	2.70	0.011	0.68	0.01	1.00	1.7E-04	2.45	0.01
ES03/19-SG-N1-11-0-21			-8.6	GFCHS0000	2.81	0.006	2.89	0.010	2.71	0.03	2.46	1.2E-04	6.86	0.06
ES03/19-SG-N1-13-25-47	III	saprock	-11.8	GFCHS000C	2.74	0.005	2.77	0.003	1.20	0.01	1.06	7.5E-05	6.36	0.06
ES03/19-SG-N1-16-50-70			-15.7	GFCHS000E	2.65	0.005	2.79	0.026	4.84	0.05	2.72	3.5E-04	6.73	0.09
ES03/19-SG-N1-18-20-28			-18.1	GFCHS000G	na	na	na	na	na	na	na	na	2.02	0.01
ES03/19-SG-N1-20-16-37			-20.7	GFCHS000K	2.71	0.005	2.75	0.004	1.66	0.02	1.52	8.3E-05	2.35	0.01
ES03/19-SG-N1-22-70-90			-24.1	GFCHS000N	2.72	0.005	2.77	0.006	1.77	0.02	1.61	1.1E-04	4.04	0.02
ES03/19-SG-N1-23-130-145			-26.2	GFCHS000P	2.58	0.005	2.77	0.018	7.03	0.07	5.25	2.4E-04	4.51	0.02
ES03/19-SG-N1-25-0-30			-28.0	GFCHS000Q	2.73	0.005	2.75	0.003	0.88	0.01	0.71	8.4E-05	1.75	0.01
ES03/19-SG-N1-27-12-35			-30.4	GFCHS000S	2.63	0.005	2.77	0.005	4.79	0.05	2.71	7.7E-05	1.14	0.01
ES03/19-SG-N1-29-95-118			-34.3	GFCHS000T	2.76	0.006	2.77	0.003	0.51	0.01	0.63	1.1E-04	1.62	0.01
ES03/19-SG-N1-31-37-62	IV		-36.6	GFCHS000V	2.71	0.005	2.77	0.005	2.28	0.02	1.56	7.4E-05	2.63	0.01
ES03/19-SG-N1-34-17-36			-40.0	GFCHS000W	2.76	0.006	2.78	0.007	0.64	0.01	0.71	1.7E-04	2.33	0.01
ES03/19-SG-N1-36-0-20			-42.3	GFCHS000Y	2.65	0.005	2.75	0.008	4.00	0.04	3.66	9.4E-05	3.98	0.01
ES03/19-SG-N1-38-59-80			-45.8	GFCHS000Z	2.72	0.005	2.74	0.005	0.82	0.01	1.19	1.0E-04	4.44	0.01
ES03/19-SG-N1-40-0-24			-48.2	GFCHS0010	2.75	0.005	2.78	0.012	0.98	0.01	0.86	2.0E-04	1.87	0.01
ES03/19-SG-N1-42-0-22			-50.7	GFCHS0011	2.77	0.006	2.77	0.009	0.02	0.00	0.64	2.4E-04	1.53	0.01
ES03/19-SG-N1-44-40-62			-54.1	GFCHS0013	2.75	0.006	2.78	0.006	0.94	0.01	0.98	1.1E-04	1.37	0.01
ES03/19-SG-N1-46-21-41			-56.9	GFCHS0014	2.79	0.006	2.80	0.005	0.52	0.01	0.83	1.1E-04	2.48	0.02
ES03/19-SG-N1-48-31-51			-60.0	GFCHS0015	na	na	2.74	0.018	na	na	na	na	3.31	0.01

Supplementary Table S2-1 continued.

Sample	Zone		Depth	IGSN	Density ρ (bulk)[1]	unc.	Density ρ (matrix)[2]	unc.	He Porosity[3]	unc.	Water-available porosity[4]	unc.	SSA[5]	unc.
			[m]		[g cm^{-3}]	[g cm^{-3}]	[g cm^{-3}]	[g cm^{-3}]	[%]	[%]	[%]	[%]	[m^2 g^{-1}]	[m^2 g^{-1}]
ES03/19-SG-N1-50-0-22	IV	saprock	-62.4	GFCHS0016	2.73	0.005	2.74	0.002	0.36	0.00	0.90	1.3E-04	2.59	0.01
ES03/19-SG-N1-52-57-77			-65.8	GFCHS0017	2.70	0.005	2.73	0.005	1.26	0.01	1.66	1.0E-04	2.51	0.01
ES03/19-SG-N1-55-32-50	V		-70.0	GFCHS001A	2.63	0.005	2.74	0.006	4.17	0.04	3.16	1.1E-04	2.36	0.01
ES03/19-SG-N1-57-13-36			-71.4	GFCHS001C	2.65	0.005	2.70	0.006	1.85	0.02	2.74	1.2E-04	3.19	0.02
ES03/19-SG-N1-59-6-25			-74.4	GFCHS001E	2.56	0.005	2.76	0.015	7.47	0.07	7.13	2.1E-04	5.21	0.02
ES03/19-SG-N1-60-70-90			-76.5	GFCHS001F	2.73	0.005	2.75	0.010	0.58	0.01	0.76	1.2E-04	2.50	0.02
ES03/19-SG-N1-62-50-70	VI	bedrock	-79.3	GFCHS001H	na	na	na	na	na	na	na	na	2.66	0.04
ES03/19-SG-N1-64-96-120			-82.8	GFCHS001J	2.76	0.006	2.77	0.005	0.50	0.00	0.54	1.3E-04	1.59	0.03
ES03/19-SG-N1-66-95-115			-85.8	GFCHS001L	2.76	0.006	2.76	0.004	0.04	0.00	0.41	1.3E-04	2.36	0.01
ES03/19-SG-N1-67-45-65			-86.8	GFCHS001M	2.75	0.006	2.76	0.012	0.29	0.00	0.47	2.1E-04	1.36	0.01
average bedrock					2.757		2.76		0.27		0.47		1.99	
standard deviation bedrock					0.005		0.004		0.2		0.06		0.5	

[1] Bulk density of the sample including pore volume.

[2] Matrix density describes the density of the solid samples without porosity.

[3] He Porosity derived from He pycnometry.

[4] Water-available porosity derived from sample saturation.

[5] SSA determined on finely powdered samples.

Supplementary Table S2-2. Elemental composition derived by OES measurements (corrected for LOI[1]). Major elements were measured with ICP-OES, trace elements with ICP-MS. Light blue highlighted lines denote bedrock composition.

Major elements (as oxides)					ICP-OES										
Sample	Zone		Depth [m]	IGSN	CO_2 [wt%]	SiO_2 [wt%]	Al_2O_3 [wt%]	Fe_2O_3(T) [wt%]	MnO [wt%]	MgO [wt%]	CaO [wt%]	Na_2O [wt%]	K_2O [wt%]	TiO_2 [wt%]	P_2O_5 [wt%]
				detection limit	0.01	0.01	0.01	0.01	0.001	0.01	0.01	0.01	0.01	0.001	0.01
					LOI corr.	LOI corr.	LOI corr.	LOI corr.	LOI corr.	LOI corr.	LOI corr.	LOI corr.	LOI corr.	LOI corr.	LOI corr.
ES03/19-SG-N1C-1-0-25	I	soil	-0.1	GFLVK00KB	0.19	58.12	17.92	7.51	0.15	2.77	5.22	3.63	2.49	0.78	0.24
ES03/19-SG-N1C-5-0-50	II	saprolite	-2.3	GFLVK00KH	0.09	57.32	17.55	7.93	0.17	3.31	5.19	3.83	2.85	0.76	0.31
ES03/19-SG-N1C-8-0-40			-3.8	GFLVK00KL	0.08	55.25	17.66	7.84	0.16	3.57	6.27	4.07	2.07	0.85	0.31
ES03/19-SG-N1-8-33-53			-6.8	GFCHS0002	0.10	58.15	17.42	6.86	0.14	3.02	5.77	3.77	2.82	0.72	0.25
ES03/19-SG-N1-11-0-21			-8.6	GFCHS0000	0.10	55.53	17.53	7.94	0.17	3.95	5.52	4.10	2.68	0.89	0.38
ES03/19-SG-N1-13-25-47	III	saprock	-11.8	GFCHS000C	0.37	57.94	17.82	6.82	0.13	3.19	5.50	3.62	3.12	0.75	0.26
ES03/19-SG-N1-16-50-70			-15.7	GFCHS000E	0.50	57.85	17.95	6.77	0.12	3.31	3.31	4.48	4.36	0.74	0.29
ES03/19-SG-N1-18-20-28			-18.1	GFCHS000G	0.85	57.03	17.19	7.42	0.16	3.47	6.48	3.46	2.95	0.79	0.27
ES03/19-SG-N1-20-16-37			-20.7	GFCHS000K	0.18	60.13	17.08	6.43	0.13	2.87	4.27	3.79	3.59	0.70	0.22
ES03/19-SG-N1-22-70-90			-24.1	GFCHS000N	0.28	58.33	17.25	7.01	0.14	3.07	4.75	4.11	3.61	0.74	0.25
ES03/19-SG-N1-23-130-145			-26.2	GFCHS000P	0.42	59.44	17.56	6.42	0.13	3.02	4.32	4.31	3.08	0.72	0.25
ES03/19-SG-N1-25-0-30			-28.0	GFCHS000Q	0.05	58.14	17.59	6.97	0.14	2.96	5.84	3.73	2.85	0.67	0.28
ES03/19-SG-N1-27-12-35			-30.4	GFCHS000S	0.10	59.16	17.29	6.76	0.13	2.81	5.55	3.57	2.99	0.73	0.25
ES03/19-SG-N1-29-95-118			-34.3	GFCHS000T	0.09	58.22	17.30	6.89	0.13	2.87	5.27	3.62	3.09	0.75	0.23
ES03/19-SG-N1-31-37-62	IV		-36.6	GFCHS000V	0.28	58.56	17.46	6.55	0.12	2.92	5.59	3.68	3.29	0.75	0.24
ES03/19-SG-N1-34-17-36			-40.0	GFCHS000W	0.06	59.08	17.57	6.79	0.13	2.78	5.50	3.76	2.80	0.71	0.24
ES03/19-SG-N1-36-0-20			-42.3	GFCHS000Y	0.14	57.54	17.29	6.75	0.15	3.24	5.58	3.76	2.90	0.72	0.23
ES03/19-SG-N1-38-59-80			-45.8	GFCHS000Z	0.63	57.84	16.92	6.82	0.14	3.24	4.66	4.42	3.86	0.72	0.25
ES03/19-SG-N1-40-0-24			-48.2	GFCHS0010	0.17	58.38	16.81	6.93	0.14	2.95	5.53	3.54	2.92	0.74	0.25

Supplementary Table S2-2 continued.

					ICP-OES										
Sample	Zone		Depth [m]	IGSN	CO_2 [wt%]	SiO_2 [wt%]	Al_2O_3 [wt%]	Fe_2O_3(T) [wt%]	MnO [wt%]	MgO [wt%]	CaO [wt%]	Na_2O [wt%]	K_2O [wt%]	TiO_2 [wt%]	P_2O_5 [wt%]
				detection limit	0.01	0.01	0.01	0.01	0.001	0.01	0.01	0.01	0.01	0.001	0.01
					LOI corr.	LOI corr.	LOI corr.	LOI corr.	LOI corr.	LOI corr.	LOI corr.	LOI corr.	LOI corr.	LOI corr.	LOI corr.
ES03/19-SG-N1-42-0-22	IV	saprock	-50.7	GFCHS0011	0.10	57.99	17.37	6.99	0.13	2.93	5.64	3.57	2.87	0.74	0.25
ES03/19-SG-N1-44-40-62			-54.1	GFCHS0013	0.11	58.51	17.24	6.93	0.13	2.97	5.64	3.70	2.81	0.72	0.24
ES03/19-SG-N1-46-21-41			-56.9	GFCHS0014	0.12	58.78	17.58	6.68	0.14	2.95	5.31	3.90	2.81	0.72	0.28
ES03/19-SG-N1-48-31-51			-60.0	GFCHS0015	0.34	60.17	15.57	6.78	0.13	3.00	4.59	3.46	4.33	0.79	0.25
ES03/19-SG-N1-50-0-22			-62.4	GFCHS0016	0.11	60.41	17.00	6.21	0.12	2.64	5.05	3.61	3.30	0.67	0.22
ES03/19-SG-N1-52-57-77			-65.8	GFCHS0017	0.10	59.43	17.43	6.20	0.13	2.74	5.05	3.65	3.32	0.68	0.24
ES03/19-SG-N1-55-32-50	V		-70.0	GFCHS001A	0.31	61.33	16.18	5.97	0.12	2.47	3.83	4.01	4.26	0.61	0.20
ES03/19-SG-N1-57-13-36			-71.4	GFCHS001C	2.01	59.34	16.33	6.41	0.12	2.94	5.34	4.49	3.52	0.66	0.24
ES03/19-SG-N1-59-6-25			-74.4	GFCHS001E	0.87	62.34	16.47	5.19	0.10	2.50	3.36	4.59	4.11	0.57	0.19
ES03/19-SG-N1-60-70-90			-76.5	GFCHS001F	0.20	61.68	16.63	5.85	0.12	2.55	4.51	3.60	3.51	0.62	0.22
ES03/19-SG-N1-62-50-70	VI	bedrock	-79.3	GFCHS001H	0.68	58.75	16.87	6.80	0.14	2.97	5.84	3.54	3.14	0.73	0.25
ES03/19-SG-N1-64-96-120			-82.8	GFCHS001J	0.11	59.01	16.74	7.08	0.15	3.09	5.80	3.65	2.88	0.74	0.24
ES03/19-SG-N1-66-95-115			-85.8	GFCHS001L	0.09	59.35	17.31	6.57	0.13	2.73	5.61	3.61	3.00	0.71	0.26
ES03/19-SG-N1-67-45-65			-86.8	GFCHS001M	0.09	59.16	16.91	6.74	0.13	2.76	5.65	3.68	2.88	0.71	0.25
average bedrock					0.24	59.07	16.96	6.80	0.14	2.89	5.72	3.62	2.97	0.72	0.25
standard deviation bedrock					0.06	0.13	0.20	0.18	0.01	0.14	0.07	0.03	0.05	0.01	0.01

Supplementary Table S2-2 continued.

					ICP-MS										
Sample	Zone		Depth [m]	IGSN	Sc [ppm]	Be [ppm]	V [ppm]	Ba [ppm]	Sr [ppm]	Y [ppm]	Zr [ppm]	Cr [ppm]	Co [ppm]	Ni [ppm]	Cu [ppm]
				detection limit	1	1	5	2	2	1	2	20	1	20	10
					LOI corr.	LOI corr.	LOI corr.	LOI corr.	LOI corr.	LOI corr.	LOI corr.	LOI corr.	LOI corr.	LOI corr.	LOI corr.
ES03/19-SG-N1C-1-0-25	I	soil	-0.1	GFLVK00KB	18.5	2.1	162.6	768.9	494.1	26.8	258.3	20.6	18.5	< 20	82.3
ES03/19-SG-N1C-5-0-50	II	saprolite	-2.3	GFLVK00KH	18.5	2.0	154.7	853.2	447.3	25.6	242.1	20.5	17.4	< 20	61.5
ES03/19-SG-N1C-8-0-40			-3.8	GFLVK00KL	19.2	2.0	177.4	626.7	536.0	26.3	207.3	30.3	20.2	< 20	60.7
ES03/19-SG-N1-8-33-53			-6.8	GFCHS0002	17.0	2.0	152.7	812.0	508.5	22.0	212.1	30.0	18.0	< 20	40.0
ES03/19-SG-N1-11-0-21			-8.6	GFCHS0000	21.4	2.0	179.3	687.6	475.8	26.5	213.7	< 20	19.3	< 20	30.5
ES03/19-SG-N1-13-25-47	III	saprock	-11.8	GFCHS000C	16.3	1.0	152.3	1127.1	516.9	16.3	186.1	71.2	17.3	< 20	20.3
ES03/19-SG-N1-16-50-70			-15.7	GFCHS000E	16.4	2.0	155.0	640.7	353.2	22.5	211.6	< 20	17.4	< 20	20.4
ES03/19-SG-N1-18-20-28			-18.1	GFCHS000G	18.6	1.0	169.1	606.1	455.5	23.8	192.5	20.7	18.6	< 20	51.8
ES03/19-SG-N1-20-16-37			-20.7	GFCHS000K	15.1	1.0	144.7	1023.0	465.7	18.1	184.9	40.2	16.1	< 20	60.3
ES03/19-SG-N1-22-70-90			-24.1	GFCHS000N	17.1	1.0	164.3	806.5	461.3	24.2	248.1	20.2	18.2	< 20	20.2
ES03/19-SG-N1-23-130-145			-26.2	GFCHS000P	15.5	1.0	136.5	619.5	214.0	20.7	178.9	< 20	16.5	< 20	20.7
ES03/19-SG-N1-25-0-30			-28.0	GFCHS000Q	15.9	2.0	155.8	697.1	496.0	21.9	157.1	< 20	16.9	< 20	19.9
ES03/19-SG-N1-27-12-35			-30.4	GFCHS000S	15.9	1.0	152.8	769.7	472.1	20.9	193.3	19.9	16.9	< 20	59.8
ES03/19-SG-N1-29-95-118			-34.3	GFCHS000T	15.0	1.0	148.8	881.0	488.8	21.0	204.9	20.0	17.0	< 20	30.0
ES03/19-SG-N1-31-37-62	IV		-36.6	GFCHS000V	16.0	2.0	153.4	785.0	494.8	21.0	168.3	< 20	16.0	< 20	< 10
ES03/19-SG-N1-34-17-36			-40.0	GFCHS000W	16.0	1.0	147.9	777.9	519.6	20.9	173.5	19.9	16.0	< 20	39.9
ES03/19-SG-N1-36-0-20			-42.3	GFCHS000Y	18.2	2.0	149.7	681.5	427.4	21.2	164.7	50.5	17.2	< 20	40.4
ES03/19-SG-N1-38-59-80			-45.8	GFCHS000Z	16.3	1.0	150.9	697.7	307.7	20.4	170.3	< 20	16.3	< 20	51.0
ES03/19-SG-N1-40-0-24			-48.2	GFCHS0010	16.1	1.0	150.6	747.3	469.6	21.1	159.7	< 20	17.1	< 20	90.4

Supplementary Table S2-2 continued.

					ICP-MS										
Sample	Zone		Depth [m]	IGSN	Sc [ppm]	Be [ppm]	V [ppm]	Ba [ppm]	Sr [ppm]	Y [ppm]	Zr [ppm]	Cr [ppm]	Co [ppm]	Ni [ppm]	Cu [ppm]
				detection limit	1	1	5	2	2	1	2	20	1	20	10
					LOI corr.	LOI corr.	LOI corr.	LOI corr.	LOI corr.	LOI corr.	LOI corr.	LOI corr.	LOI corr.	LOI corr.	LOI corr.
ES03/19-SG-N1-42-0-22	IV	saprock	-50.7	GFCHS0011	15.9	1.0	151.8	729.2	501.6	20.9	159.4	29.9	16.9	< 20	59.8
ES03/19-SG-N1-44-40-62			-54.1	GFCHS0013	16.9	2.0	155.7	679.9	498.6	21.9	174.2	29.9	17.9	< 20	29.9
ES03/19-SG-N1-46-21-41			-56.9	GFCHS0014	16.0	2.0	154.7	713.4	507.4	22.0	173.8	20.0	17.0	< 20	30.0
ES03/19-SG-N1-48-31-51			-60.0	GFCHS0015	17.1	1.0	160.2	718.6	411.9	30.1	182.8	20.1	17.1	< 20	< 10
ES03/19-SG-N1-50-0-22			-62.4	GFCHS0016	14.0	2.0	138.9	689.8	461.2	19.9	172.6	< 20	16.0	< 20	< 10
ES03/19-SG-N1-52-57-77			-65.8	GFCHS0017	15.0	2.0	135.0	744.0	475.9	20.0	153.4	< 20	15.0	< 20	10.0
ES03/19-SG-N1-55-32-50	V		-70.0	GFCHS001A	13.1	1.0	123.9	820.9	344.1	19.2	160.7	< 20	13.1	< 20	< 10
ES03/19-SG-N1-57-13-36			-71.4	GFCHS001C	14.5	1.0	131.4	795.1	289.8	19.6	198.2	< 20	15.5	< 20	31.0
ES03/19-SG-N1-59-6-25			-74.4	GFCHS001E	11.3	1.0	107.5	757.6	167.2	15.4	163.8	< 20	12.3	< 20	20.5
ES03/19-SG-N1-60-70-90			-76.5	GFCHS001F	13.0	2.0	129.0	787.6	429.2	19.1	242.7	< 20	14.0	< 20	30.1
ES03/19-SG-N1-62-50-70	VI	bedrock	-79.3	GFCHS001H	15.2	1.0	148.9	802.2	461.4	20.2	168.0	20.2	17.2	< 20	81.0
ES03/19-SG-N1-64-96-120			-82.8	GFCHS001J	17.0	1.0	160.6	746.0	515.4	21.0	172.7	20.0	17.0	< 20	69.9
ES03/19-SG-N1-66-95-115			-85.8	GFCHS001L	14.9	2.0	146.9	776.7	504.7	21.9	148.4	19.9	15.9	< 20	79.7
ES03/19-SG-N1-67-45-65			-86.8	GFCHS001M	15.9	1.0	150.8	767.8	504.6	21.9	178.9	19.9	15.9	< 20	39.8
average bedrock					15.7	1.2	151.8	773.2	496.5	21.2	167.0	20.0	16.5	n/a	67.6
standard deviation bedrock					0.7	0.4	5	12	7	0.4	11	0.05	0.4	n/a	15

Supplementary Table S2-2 continued.

					ICP-MS										
Sample	Zone		Depth [m]	IGSN	Zn [ppm]	Ga [ppm]	Ge [ppm]	As [ppm]	Rb [ppm]	Nb [ppm]	Mo [ppm]	Ag [ppm]	In [ppm]	Sn [ppm]	Sb [ppm]
				detection limit	30	1	1	5	2	1	2	0.5	0.2	1	0.5
					LOI corr.	LOI corr.	LOI corr.	LOI corr.	LOI corr.	LOI corr.	LOI corr.	LOI corr.	LOI corr.	LOI corr.	LOI corr.
ES03/19-SG-N1C-1-0-25	I	soil	-0.1	GFLVK00KB	61.8	20.6	1.0	< 5	71.0	12.4	< 2	0.8	< 0.2	3.1	< 0.5
ES03/19-SG-N1C-5-0-50	II	saprolite	-2.3	GFLVK00KH	71.8	18.5	1.0	< 5	91.3	10.3	< 2	1.3	< 0.2	2.1	< 0.5
ES03/19-SG-N1C-8-0-40			-3.8	GFLVK00KL	70.8	20.2	2.0	< 5	76.9	12.1	< 2	2.3	< 0.2	2.0	< 0.5
ES03/19-SG-N1-8-33-53			-6.8	GFCHS0002	60.0	19.0	2.0	< 5	83.0	153.1	< 2	0.7	< 0.2	2.0	< 0.5
ES03/19-SG-N1-11-0-21			-8.6	GFCHS0000	61.1	19.3	2.0	< 5	94.6	14.2	< 2	0.8	< 0.2	1.0	< 0.5
ES03/19-SG-N1-13-25-47	III	saprock	-11.8	GFCHS000C	50.8	23.4	1.0	< 5	100.7	11.2	< 2	0.7	< 0.2	1.0	0.6
ES03/19-SG-N1-16-50-70			-15.7	GFCHS000E	71.6	18.4	2.0	< 5	127.8	47.0	< 2	0.8	< 0.2	1.0	0.6
ES03/19-SG-N1-18-20-28			-18.1	GFCHS000G	72.5	18.6	1.0	< 5	101.4	13.5	< 2	0.6	< 0.2	1.0	< 0.5
ES03/19-SG-N1-20-16-37			-20.7	GFCHS000K	60.3	18.1	1.0	< 5	106.5	10.0	< 2	0.7	< 0.2	1.0	< 0.5
ES03/19-SG-N1-22-70-90			-24.1	GFCHS000N	60.5	19.2	2.0	< 5	110.9	25.2	< 2	0.8	< 0.2	1.0	< 0.5
ES03/19-SG-N1-23-130-145			-26.2	GFCHS000P	62.1	18.6	1.0	< 5	90.0	11.4	< 2	0.6	< 0.2	1.0	< 0.5
ES03/19-SG-N1-25-0-30			-28.0	GFCHS000Q	59.7	18.9	2.0	< 5	86.5	9.9	8.0	0.6	< 0.2	1.0	< 0.5
ES03/19-SG-N1-27-12-35			-30.4	GFCHS000S	49.8	18.9	1.0	< 5	86.7	12.0	2.0	0.6	< 0.2	1.0	< 0.5
ES03/19-SG-N1-29-95-118			-34.3	GFCHS000T	50.0	19.0	1.0	< 5	97.0	13.0	< 2	0.7	< 0.2	1.0	< 0.5
ES03/19-SG-N1-31-37-62	IV		-36.6	GFCHS000V	40.1	18.0	1.0	< 5	94.2	12.0	< 2	0.5	< 0.2	1.0	< 0.5
ES03/19-SG-N1-34-17-36			-40.0	GFCHS000W	49.9	17.9	2.0	< 5	86.7	10.0	2.0	0.5	< 0.2	1.0	< 0.5
ES03/19-SG-N1-36-0-20			-42.3	GFCHS000Y	60.6	18.2	1.0	< 5	96.0	10.1	< 2	0.5	< 0.2	1.0	< 0.5
ES03/19-SG-N1-38-59-80			-45.8	GFCHS000Z	61.2	18.4	2.0	< 5	112.1	10.2	2.0	0.5	< 0.2	1.0	< 0.5
ES03/19-SG-N1-40-0-24			-48.2	GFCHS0010	70.3	19.1	1.0	< 5	93.4	12.1	2.0	0.6	< 0.2	1.0	< 0.5

Supplementary Table S2-2 continued.

				ICP-MS										
Sample	Zone	Depth [m]	IGSN	Zn [ppm]	Ga [ppm]	Ge [ppm]	As [ppm]	Rb [ppm]	Nb [ppm]	Mo [ppm]	Ag [ppm]	In [ppm]	Sn [ppm]	Sb [ppm]
			detection limit	30	1	1	5	2	1	2	0.5	0.2	1	0.5
				LOI corr.	LOI corr.	LOI corr.	LOI corr.	LOI corr.	LOI corr.	LOI corr.	LOI corr.	LOI corr.	LOI corr.	LOI corr.
ES03/19-SG-N1-42-0-22	IV	-50.7	GFCHS0011	59.8	18.9	2.0	< 5	83.7	11.0	2.0	0.6	< 0.2	< 1	< 0.5
ES03/19-SG-N1-44-40-62		-54.1	GFCHS0013	49.8	21.9	2.0	< 5	89.6	11.0	< 2	0.6	< 0.2	1.0	< 0.5
ES03/19-SG-N1-46-21-41		-56.9	GFCHS0014	49.9	19.0	1.0	< 5	95.9	10.0	< 2	0.6	< 0.2	1.0	< 0.5
ES03/19-SG-N1-48-31-51		-60.0	GFCHS0015	40.2	17.1	2.0	< 5	113.5	20.1	< 2	0.6	< 0.2	2.0	< 0.5
ES03/19-SG-N1-50-0-22	saprock	-62.4	GFCHS0016	49.9	18.0	2.0	< 5	95.8	11.0	< 2	0.6	< 0.2	1.0	< 0.5
ES03/19-SG-N1-52-57-77		-65.8	GFCHS0017	40.1	18.0	1.0	< 5	104.2	11.0	< 2	0.5	< 0.2	1.0	< 0.5
ES03/19-SG-N1-55-32-50		-70.0	GFCHS001A	40.4	16.2	1.0	< 5	117.3	11.1	< 2	0.5	< 0.2	1.0	< 0.5
ES03/19-SG-N1-57-13-36	V	-71.4	GFCHS001C	51.6	17.6	1.0	< 5	111.5	11.4	< 2	0.6	< 0.2	1.0	< 0.5
ES03/19-SG-N1-59-6-25		-74.4	GFCHS001E	61.4	17.4	1.0	< 5	116.7	10.2	< 2	0.5	< 0.2	1.0	< 0.5
ES03/19-SG-N1-60-70-90		-76.5	GFCHS001F	50.1	18.1	1.0	< 5	110.3	10.0	< 2	0.7	< 0.2	1.0	< 0.5
ES03/19-SG-N1-62-50-70		-79.3	GFCHS001H	70.8	18.2	1.0	< 5	99.2	12.1	3.0	0.6	< 0.2	1.0	< 0.5
ES03/19-SG-N1-64-96-120	VI	-82.8	GFCHS001J	59.9	18.0	1.0	< 5	86.9	10.0	4.0	0.6	< 0.2	1.0	< 0.5
ES03/19-SG-N1-66-95-115	bedrock	-85.8	GFCHS001L	59.7	17.9	1.0	< 5	88.6	11.9	2.0	0.6	< 0.2	1.0	< 0.5
ES03/19-SG-N1-67-45-65		-86.8	GFCHS001M	49.7	18.9	1.0	< 5	85.5	10.9	2.0	0.5	< 0.2	1.0	< 0.5
average bedrock				60.0	18.2	1.0	n/a	90.0	11.3	2.8	0.6	n/a	1.0	n/a
standard deviation bedrock				4	0.4	0.002	n/a	2	1	1	0.04	n/a	0.002	n/a

Supplementary Table S2-2 continued.

					ICP-MS										
Sample	Zone		Depth [m]	IGSN	Cs [ppm]	La [ppm]	Ce [ppm]	Pr [ppm]	Nd [ppm]	Sm [ppm]	Eu [ppm]	Gd [ppm]	Tb [ppm]	Dy [ppm]	Ho [ppm]
				detection limit	0.5	0.1	0.1	0.05	0.1	0.1	0.05	0.1	0.1	0.1	0.1
					LOI corr.	LOI corr.	LOI corr.	LOI corr.	LOI corr.	LOI corr.	LOI corr.	LOI corr.	LOI corr.	LOI corr.	LOI corr.
ES03/19-SG-N1C-1-0-25	I	soil	-0.1	GFLVK00KB	4.0	34.4	75.9	9.27	37.5	7.6	1.80	6.3	0.9	4.9	0.9
ES03/19-SG-N1C-5-0-50	II	saprolite	-2.3	GFLVK00KH	3.7	32.2	68.1	8.60	34.4	7.3	1.54	6.2	0.8	4.5	0.8
ES03/19-SG-N1C-8-0-40			-3.8	GFLVK00KL	3.7	35.6	76.3	9.70	38.3	8.0	1.77	6.7	0.9	5.0	0.9
ES03/19-SG-N1-8-33-53			-6.8	GFCHS0002	2.6	31.1	68.2	8.20	33.0	6.8	1.54	5.3	0.8	4.2	0.8
ES03/19-SG-N1-11-0-21			-8.6	GFCHS0000	4.2	30.6	68.2	8.69	36.3	7.4	1.75	6.2	0.9	4.9	0.9
ES03/19-SG-N1-13-25-47	III	saprock	-11.8	GFCHS000C	4.7	28.1	56.7	6.77	28.0	5.4	1.59	4.8	0.6	3.5	0.6
ES03/19-SG-N1-16-50-70			-15.7	GFCHS000E	3.7	30.7	64.9	7.98	32.6	7.1	1.59	5.7	0.8	4.4	0.8
ES03/19-SG-N1-18-20-28			-18.1	GFCHS000G	7.6	33.2	73.5	8.85	36.6	7.2	1.60	5.8	0.8	4.6	0.8
ES03/19-SG-N1-20-16-37			-20.7	GFCHS000K	4.5	25.5	53.9	6.75	27.6	5.9	1.45	4.6	0.7	3.6	0.7
ES03/19-SG-N1-22-70-90			-24.1	GFCHS000N	3.4	33.3	71.9	9.02	36.3	7.6	1.66	5.9	0.8	4.6	0.9
ES03/19-SG-N1-23-130-145			-26.2	GFCHS000P	5.6	31.9	67.3	8.04	32.2	6.6	1.48	5.3	0.7	3.9	0.7
ES03/19-SG-N1-25-0-30			-28.0	GFCHS000Q	2.3	32.9	69.3	8.36	33.9	6.7	1.61	5.5	0.8	4.4	0.8
ES03/19-SG-N1-27-12-35			-30.4	GFCHS000S	2.4	30.9	65.2	7.91	31.3	6.6	1.52	5.5	0.8	4.3	0.8
ES03/19-SG-N1-29-95-118			-34.3	GFCHS000T	2.6	30.5	64.4	7.71	31.4	6.3	1.52	5.1	0.7	3.9	0.8
ES03/19-SG-N1-31-37-62	IV		-36.6	GFCHS000V	2.6	32.0	68.3	8.25	32.4	6.7	1.53	5.2	0.8	4.3	0.8
ES03/19-SG-N1-34-17-36			-40.0	GFCHS000W	2.7	27.3	58.5	7.18	29.7	5.9	1.50	4.9	0.7	3.8	0.7
ES03/19-SG-N1-36-0-20			-42.3	GFCHS000Y	4.1	27.8	60.0	7.43	30.4	6.6	1.44	5.3	0.7	4.0	0.8
ES03/19-SG-N1-38-59-80			-45.8	GFCHS000Z	3.8	28.2	59.9	7.39	30.8	6.3	1.54	5.2	0.7	4.2	0.7
ES03/19-SG-N1-40-0-24			-48.2	GFCHS0010	4.5	31.5	65.0	7.80	31.3	6.2	1.61	5.3	0.7	4.2	0.8

Supplementary Table S2-2 continued.

					ICP-MS										
Sample	Zone		Depth [m]	IGSN	Cs [ppm]	La [ppm]	Ce [ppm]	Pr [ppm]	Nd [ppm]	Sm [ppm]	Eu [ppm]	Gd [ppm]	Tb [ppm]	Dy [ppm]	Ho [ppm]
				detection limit	0.5	0.1	0.1	0.05	0.1	0.1	0.05	0.1	0.1	0.1	0.1
					LOI corr.	LOI corr.	LOI corr.	LOI corr.	LOI corr.	LOI corr.	LOI corr.	LOI corr.	LOI corr.	LOI corr.	LOI corr.
ES03/19-SG-N1-42-0-22	IV	saprock	-50.7	GFCHS0011	3.6	30.1	63.1	7.66	30.8	6.4	1.57	5.4	0.8	4.2	0.8
ES03/19-SG-N1-44-40-62			-54.1	GFCHS0013	2.4	29.5	62.7	7.62	30.8	6.2	1.51	5.2	0.7	4.0	0.8
ES03/19-SG-N1-46-21-41			-56.9	GFCHS0014	3.1	32.4	67.1	8.14	33.0	6.7	1.57	5.3	0.8	4.2	0.8
ES03/19-SG-N1-48-31-51			-60.0	GFCHS0015	2.9	45.4	104.5	12.66	49.7	9.5	1.89	7.4	1.1	5.8	1.1
ES03/19-SG-N1-50-0-22			-62.4	GFCHS0016	2.8	29.2	59.2	7.14	29.0	5.9	1.38	4.9	0.7	3.8	0.7
ES03/19-SG-N1-52-57-77			-65.8	GFCHS0017	3.2	30.0	61.0	7.40	29.6	5.9	1.45	5.0	0.7	3.8	0.7
ES03/19-SG-N1-55-32-50	V		-70.0	GFCHS001A	4.2	29.7	61.7	7.24	28.7	5.8	1.29	4.9	0.6	3.6	0.7
ES03/19-SG-N1-57-13-36			-71.4	GFCHS001C	3.9	31.9	64.4	7.70	30.8	6.3	1.40	4.6	0.7	3.8	0.7
ES03/19-SG-N1-59-6-25			-74.4	GFCHS001E	4.5	27.6	55.7	6.54	25.2	4.8	1.33	4.0	0.6	3.1	0.6
ES03/19-SG-N1-60-70-90			-76.5	GFCHS001F	4.5	27.1	56.5	6.80	28.2	5.6	1.36	4.3	0.6	3.5	0.7
ES03/19-SG-N1-62-50-70	VI	bedrock	-79.3	GFCHS001H	5.1	29.1	62.7	7.70	31.3	6.4	1.62	5.2	0.8	4.0	0.8
ES03/19-SG-N1-64-96-120			-82.8	GFCHS001J	4.1	27.7	58.0	7.15	29.0	6.2	1.53	4.9	0.7	3.9	0.7
ES03/19-SG-N1-66-95-115			-85.8	GFCHS001L	3.8	31.2	65.2	7.93	31.3	6.7	1.48	5.2	0.7	4.0	0.8
ES03/19-SG-N1-67-45-65			-86.8	GFCHS001M	2.7	33.6	68.9	8.26	33.4	6.4	1.64	5.3	0.8	4.2	0.8
average bedrock					3.9	30.4	63.7	7.76	31.2	6.4	1.57	5.1	0.8	4.0	0.8
standard deviation bedrock					1	2	4	0.4	2	0.2	0.1	0.1	0.04	0.1	0.04

Supplementary Table S2-2 continued.

					ICP-MS											
Sample	Zone		Depth [m]	IGSN	Er [ppm]	Tm [ppm]	Yb [ppm]	Lu [ppm]	Hf [ppm]	Ta [ppm]	W [ppm]	Tl [ppm]	Pb [ppm]	Bi [ppm]	Th [ppm]	U [ppm]
				detection limit	0.1	0.05	0.1	0.01	0.2	0.1	1	0.1	5	0.4	0.1	0.1
					LOI corr.	LOI corr.	LOI corr.	LOI corr.	LOI corr.	LOI corr.	LOI corr.	LOI corr.	LOI corr.	LOI corr.	LOI corr.	LOI corr.
ES03/19-SG-N1C-1-0-25	I	soil	-0.1	GFLVK00KB	2.8	0.42	2.8	0.46	7.3	1.0	< 1	0.3	7.2	< 0.4	15.5	3.3
ES03/19-SG-N1C-5-0-50	II	saprolite	-2.3	GFLVK00KH	2.6	0.39	2.7	0.41	6.7	0.8	1.0	0.4	< 5	< 0.4	8.9	2.5
ES03/19-SG-N1C-8-0-40			-3.8	GFLVK00KL	2.8	0.42	2.8	0.48	5.9	0.8	5.1	0.3	< 5	< 0.4	8.8	2.7
ES03/19-SG-N1-8-33-53			-6.8	GFCHS0002	2.3	0.34	2.3	0.36	5.9	1.4	< 1	0.3	6.0	< 0.4	15.2	3.5
ES03/19-SG-N1-11-0-21			-8.6	GFCHS0000	2.6	0.39	2.6	0.40	5.7	0.9	2.0	0.3	< 5	< 0.4	7.0	3.0
ES03/19-SG-N1-13-25-47	III	saprock	-11.8	GFCHS000C	1.8	0.25	1.7	0.28	5.1	0.6	4.1	0.3	5.1	< 0.4	9.9	3.6
ES03/19-SG-N1-16-50-70			-15.7	GFCHS000E	2.6	0.37	2.7	0.41	5.9	1.0	2.0	0.4	< 5	< 0.4	8.1	3.4
ES03/19-SG-N1-18-20-28			-18.1	GFCHS000G	2.6	0.35	2.7	0.40	5.6	0.8	< 1	0.4	< 5	< 0.4	7.8	2.7
ES03/19-SG-N1-20-16-37			-20.7	GFCHS000K	2.0	0.28	1.9	0.28	5.2	0.8	< 1	0.4	5.0	< 0.4	7.0	2.2
ES03/19-SG-N1-22-70-90			-24.1	GFCHS000N	2.6	0.39	2.8	0.45	7.3	1.0	< 1	0.4	< 5	< 0.4	11.8	3.8
ES03/19-SG-N1-23-130-145			-26.2	GFCHS000P	2.2	0.35	2.3	0.36	5.1	0.9	< 1	0.3	< 5	< 0.4	13.1	3.4
ES03/19-SG-N1-25-0-30			-28.0	GFCHS000Q	2.3	0.35	2.3	0.38	4.4	0.8	< 1	0.2	5.0	< 0.4	9.5	2.2
ES03/19-SG-N1-27-12-35			-30.4	GFCHS000S	2.2	0.32	2.3	0.36	5.7	0.9	< 1	0.3	6.0	< 0.4	11.1	2.3
ES03/19-SG-N1-29-95-118			-34.3	GFCHS000T	2.2	0.32	2.1	0.34	5.8	0.9	< 1	0.3	< 5	< 0.4	12.9	4.0
ES03/19-SG-N1-31-37-62	IV		-36.6	GFCHS000V	2.3	0.34	2.3	0.39	4.8	1.1	< 1	0.2	< 5	< 0.4	13.2	5.5
ES03/19-SG-N1-34-17-36			-40.0	GFCHS000W	2.1	0.31	2.1	0.33	5.2	0.8	< 1	0.3	6.0	< 0.4	10.4	3.1
ES03/19-SG-N1-36-0-20			-42.3	GFCHS000Y	2.2	0.35	2.3	0.38	5.1	0.8	< 1	0.3	< 5	< 0.4	11.7	3.8
ES03/19-SG-N1-38-59-80			-45.8	GFCHS000Z	2.2	0.34	2.2	0.37	5.0	0.9	1.0	0.4	< 5	< 0.4	12.2	5.2
ES03/19-SG-N1-40-0-24			-48.2	GFCHS0010	*2.3*	*0.34*	*2.3*	*0.37*	*5.1*	*0.9*	*< 1*	*0.4*	*8.0*	*< 0.4*	*11.3*	*3.7*

Supplementary Table S2-2 continued.

					ICP-MS										
Sample	Zone	Depth [m]	IGSN	Er [ppm]	Tm [ppm]	Yb [ppm]	Lu [ppm]	Hf [ppm]	Ta [ppm]	W [ppm]	Tl [ppm]	Pb [ppm]	Bi [ppm]	Th [ppm]	U [ppm]
			detection limit	0.1	0.05	0.1	0.01	0.2	0.1	1	0.1	5	0.4	0.1	0.1
				LOI corr.	LOI corr.	LOI corr.	LOI corr.	LOI corr.	LOI corr.	LOI corr.	LOI corr.	LOI corr.	LOI corr.	LOI corr.	LOI corr.
ES03/19-SG-N1-42-0-22	IV	-50.7	GFCHS0011	2.3	0.33	2.4	0.40	4.8	0.9	2.0	< 0.1	8.0	< 0.4	14.9	4.5
ES03/19-SG-N1-44-40-62		-54.1	GFCHS0013	2.3	0.32	2.2	0.36	5.0	0.8	2.0	0.2	5.0	< 0.4	12.8	4.3
ES03/19-SG-N1-46-21-41		-56.9	GFCHS0014	2.4	0.33	2.3	0.39	5.3	0.8	< 1	0.2	5.0	< 0.4	13.3	3.6
ES03/19-SG-N1-48-31-51		-60.0	GFCHS0015	3.4	0.51	3.5	0.55	5.9	2.0	< 1	0.3	< 5	< 0.4	15.9	8.7
ES03/19-SG-N1-50-0-22	saprock	-62.4	GFCHS0016	2.2	0.32	2.1	0.35	5.4	1.0	< 1	0.2	< 5	< 0.4	13.1	5.5
ES03/19-SG-N1-52-57-77		-65.8	GFCHS0017	2.1	0.31	2.2	0.33	4.7	1.0	< 1	0.3	6.0	< 0.4	12.6	6.3
ES03/19-SG-N1-55-32-50		-70.0	GFCHS001A	2.0	0.29	2.1	0.35	4.8	1.0	< 1	0.3	< 5	< 0.4	12.4	6.7
ES03/19-SG-N1-57-13-36	V	-71.4	GFCHS001C	2.1	0.32	2.3	0.33	5.7	0.9	1.0	0.3	< 5	< 0.4	14.2	4.9
ES03/19-SG-N1-59-6-25		-74.4	GFCHS001E	1.6	0.27	1.8	0.31	4.7	0.8	2.0	0.4	< 5	< 0.4	14.4	7.4
ES03/19-SG-N1-60-70-90		-76.5	GFCHS001F	2.1	0.30	2.0	0.34	7.2	0.8	< 1	0.3	6.0	< 0.4	16.7	6.4
ES03/19-SG-N1-62-50-70	VI	-79.3	GFCHS001H	2.2	0.31	2.1	0.33	4.9	0.9	< 1	0.4	7.1	< 0.4	12.2	3.9
ES03/19-SG-N1-64-96-120		-82.8	GFCHS001J	2.2	0.31	2.2	0.34	5.1	0.8	< 1	0.3	7.0	< 0.4	9.7	3.1
ES03/19-SG-N1-66-95-115	bedrock	-85.8	GFCHS001L	2.2	0.33	2.3	0.36	4.5	0.9	4.0	0.3	8.0	< 0.4	13.0	4.4
ES03/19-SG-N1-67-45-65		-86.8	GFCHS001M	2.3	0.33	2.3	0.37	5.5	0.8	< 1	0.3	7.0	< 0.4	13.2	3.5
average bedrock				2.2	0.32	2.2	0.35	5.0	0.9	n/a	0.3	7.2	n/a	12.0	3.7
standard deviation bedrock				0.04	0.01	0.04	0.01	0.4	0.04	n/a	0.01	0.4	n/a	1	0.5

Supplementary Table S2-3. Modal mineral composition of the bedrock.

mineral	[%]	mineral	[%]	rest
plagioclase	43.7	apatite	1.8	chlorite
hornblende	16.2	magnetite	1	calcite
K-feldspar	15.7	zircon	0.50	pumpellyite
quartz	10.8	titanite	0.40	ilmenite
biotite	5.8	copper-bearing sulphides *	0.3	sericite
				epidote

* mainly chalcopyrite

Determination of the modal mineral composition

The modal mineral composition of a bedrock sample was investigated using a micro x-ray fluorescence device (µ-XRF M4 Tornado, Bruker, USA) at the Technische Universität Berlin. An area of 57 times 57 mm of a bedrock sample slab (cut perpendicular to the drilling direction) was mapped. As settings, a measuring spot size of 20 µm with a spot distance of 50 µm were chosen and the integration time was 30 ms point^{-1}. The maps were analysed with the open-source image processing program ImageJ and element combinations were attributed to the different minerals (i.e. calculation of area shares which are occupied by the respective element combinations). Complemented by ordinary point counting with an optical light microscope the most abundant bedrock can be classified as quartz monzodiorite in the Streckeisen diagram.

Supplementary Table S2-4. Weathering indicators CDF[1], volumetric strain ε_{Zr}[2] and τ[3]. Light blue highlighted lines denote bedrock composition.

Sample	Zone		Depth [m]	IGSN	CDF (Zr)	Strain ε_{Zr}	τ (Na)	τ (K)	τ (Mg)	τ (Al)	τ (Ca)	τ (Si)	τ (U)	τ (Fe)
ES03/19-SG-N1C-1-0-25	I	soil	-0.1	GFLVK00KB	0.33	na	-0.35	-0.46	-0.38	-0.32	-0.41	-0.36	-0.43	-0.29
ES03/19-SG-N1C-5-0-50	II	saprolite	-2.3	GFLVK00KH	0.29	na	-0.27	-0.34	-0.21	-0.29	-0.37	-0.33	-0.54	-0.20
ES03/19-SG-N1C-8-0-40			-3.8	GFLVK00KL	0.19	na	-0.10	-0.44	0.00	-0.16	-0.12	-0.25	-0.41	-0.07
ES03/19-SG-N1-8-33-53			-6.8	GFCHS0002	0.21	-0.19	-0.18	-0.25	-0.18	-0.19	-0.21	-0.22	-0.26	-0.21
ES03/19-SG-N1-11-0-21			-8.6	GFCHS0000	0.21	-0.23	-0.12	-0.30	0.07	-0.19	-0.25	-0.27	-0.38	-0.09
ES03/19-SG-N1-13-25-47	III	saprock	-11.8	GFCHS000C	0.09	-0.10	-0.10	-0.06	-0.01	-0.06	-0.14	-0.12	-0.14	-0.10
ES03/19-SG-N1-16-50-70			-15.7	GFCHS000E	0.19	-0.18	-0.02	0.16	-0.09	-0.16	-0.54	-0.23	-0.29	-0.21
ES03/19-SG-N1-18-20-28			-18.1	GFCHS000G	0.10	na	-0.17	-0.14	0.04	-0.12	-0.02	-0.16	-0.37	-0.05
ES03/19-SG-N1-20-16-37			-20.7	GFCHS000K	0.09	-0.08	-0.06	0.09	-0.10	-0.09	-0.33	-0.08	-0.46	-0.15
ES03/19-SG-N1-22-70-90			-24.1	GFCHS000N	0.32	-0.32	-0.24	-0.18	-0.29	-0.32	-0.44	-0.34	-0.31	-0.31
ES03/19-SG-N1-23-130-145			-26.2	GFCHS000P	0.03	0.00	0.11	-0.03	-0.02	-0.03	-0.29	-0.06	-0.14	-0.12
ES03/19-SG-N1-25-0-30			-28.0	GFCHS000Q	-0.05	0.07	0.09	0.02	0.09	0.10	0.08	0.05	-0.38	0.09
ES03/19-SG-N1-27-12-35			-30.4	GFCHS000S	0.14	-0.10	-0.15	-0.13	-0.16	-0.12	-0.16	-0.13	-0.47	-0.14
ES03/19-SG-N1-29-95-118			-34.3	GFCHS000T	0.19	-0.19	-0.19	-0.15	-0.19	-0.17	-0.25	-0.20	-0.13	-0.17
ES03/19-SG-N1-31-37-62	IV		-36.6	GFCHS000V	0.01	0.01	0.01	0.10	0.00	0.02	-0.03	-0.02	0.47	-0.04
ES03/19-SG-N1-34-17-36			-40.0	GFCHS000W	0.04	-0.04	0.00	-0.09	-0.07	0.00	-0.07	-0.04	-0.20	-0.04
ES03/19-SG-N1-36-0-20			-42.3	GFCHS000Y	-0.02	0.06	0.05	-0.01	0.14	0.03	-0.01	-0.01	0.05	0.01
ES03/19-SG-N1-38-59-80			-45.8	GFCHS000Z	0.00	-0.01	0.20	0.27	0.10	-0.02	-0.20	-0.04	0.37	-0.02
ES03/19-SG-N1-40-0-24			-48.2	GFCHS0010	-0.05	0.05	0.02	0.03	0.07	0.04	0.01	0.03	0.04	0.07
ES03/19-SG-N1-42-0-22			-50.7	GFCHS0011	-0.04	0.04	0.03	0.01	0.06	0.07	0.03	0.03	0.26	0.08
ES03/19-SG-N1-44-40-62			-54.1	GFCHS0013	0.05	-0.04	-0.02	-0.09	-0.02	-0.03	-0.06	-0.05	0.10	-0.02
ES03/19-SG-N1-46-21-41			-56.9	GFCHS0014	0.04	-0.05	0.04	-0.09	-0.02	0.00	-0.11	-0.04	-0.07	-0.06

Supplementary Table S2-4 continued.

Sample	Zone		Depth [m]	IGSN	CDF (Zr)	Strain ε_{Zr}	τ (Na)	τ (K)	τ (Mg)	τ (Al)	τ (Ca)	τ (Si)	τ (U)	τ (Fe)
ES03/19-SG-N1-48-31-51	IV	saprock	-60.0	GFCHS0015	0.08	na	-0.13	0.33	-0.05	-0.16	-0.27	-0.07	1.14	-0.09
ES03/19-SG-N1-50-0-22			-62.4	GFCHS0016	0.04	-0.02	-0.04	0.07	-0.11	-0.03	-0.15	-0.01	0.43	-0.12
ES03/19-SG-N1-52-57-77			-65.8	GFCHS0017	-0.09	0.11	0.10	0.22	0.03	0.12	-0.04	0.10	0.85	-0.01
ES03/19-SG-N1-55-32-50	V		-70.0	GFCHS001A	-0.05	0.09	0.15	0.49	-0.11	-0.01	-0.30	0.08	0.86	-0.09
ES03/19-SG-N1-57-13-36			-71.4	GFCHS001C	0.11	-0.12	0.04	0.00	-0.14	-0.19	-0.21	-0.15	0.10	-0.21
ES03/19-SG-N1-59-6-25			-74.4	GFCHS001E	-0.05	0.10	0.29	0.41	-0.12	-0.01	-0.40	0.08	1.02	-0.22
ES03/19-SG-N1-60-70-90			-76.5	GFCHS001F	0.31	-0.31	-0.32	-0.19	-0.39	-0.33	-0.46	-0.28	0.19	-0.41
ES03/19-SG-N1-62-50-70	VI	bedrock	-79.3	GFCHS001H	-0.01	na	-0.03	0.05	0.02	-0.01	0.01	-0.01	0.05	-0.01
ES03/19-SG-N1-64-96-120			-82.8	GFCHS001J	0.04	-0.03	-0.02	-0.06	0.03	-0.05	-0.02	-0.03	-0.20	0.01
ES03/19-SG-N1-66-95-115			-85.8	GFCHS001L	-0.12	0.12	0.12	0.13	0.06	0.15	0.10	0.13	0.32	0.09
ES03/19-SG-N1-67-45-65			-86.8	GFCHS001M	0.07	-0.07	-0.05	-0.10	-0.11	-0.07	-0.08	-0.07	-0.13	-0.07
average bedrock					0.00		0.00	0.01	0.00	0.01	0.00	0.01	0.01	0.00
standard deviation bedrock					0.07		0.07	0.09	0.07	0.09	0.07	0.08	0.2	0.06

[1] CDF calculated using eq. [7] in main text

[2] strain calculated using eq. [10] in main text

[3] τ calculated using eq. [8] in main text

Supplementary Table S2-5. Bulk Fe(II)/Fe(III) ratios and extracted oxide Fe, Si, Al concentrations. CBD: citrate dithionite bicarbonate, A and B indicate two replicates, SE: standard error. Light blue highlighted lines denote bedrock composition.

Sample	Zone		Depth	IGSN	$Fe(III)/Fe_{total}$	CBD											
						Fe				**Si**				Al			
			[m]			A [mg/g]	B [mg/g]	average [mg/g]	SE	A [mg/g]	B [mg/g]	average [mg/g]	SE	A [mg/g]	B [mg/g]	average [mg/g]	SE
ES03/19-SG-N1C-1-0-25	I	soil	-0.1	GFLVK00KB	0.65												
ES03/19-SG-S1-80-100			-0.9	GFLVK00CH	na	2.67	2.40	2.54	0.19	1.44	1.45	1.45	0.01	0.24	0.26	0.25	0.01
ES03/19-SG-N1C-5-0-50	II	saprolite	-2.3	GFLVK00KH	0.66												
ES03/19-SG-N1C-8-0-40			-3.8	GFLVK00KL	0.55												
ES03/19-SG-N1-8-33-53			-6.8	GFCHS0002	0.37	6.05	6.19	6.12	0.09	0.78	0.72	0.75	0.04	0.86	0.78	0.82	0.06
ES03/19-SG-N1-11-0-21			-8.6	GFCHS0000	0.51												
ES03/19-SG-N1-13-25-47	III	saprock	-11.8	GFCHS000C	0.53												
ES03/19-SG-N1-16-50-70			-15.7	GFCHS000E	0.49												
ES03/19-SG-N1-18-20-28			-18.1	GFCHS000G	0.49	5.98	5.59	5.78	0.27	0.97	1.43	1.20	0.32	1.07	1.94	1.51	0.62
ES03/19-SG-N1-20-16-37			-20.7	GFCHS000K	0.38												
ES03/19-SG-N1-22-70-90			-24.1	GFCHS000N	0.33												
ES03/19-SG-N1-23-130-145			-26.2	GFCHS000P	0.48												
ES03/19-SG-N1-25-0-30			-28.0	GFCHS000Q	0.35												
ES03/19-SG-N1-27-12-35			-30.4	GFCHS000S	0.38	4.84	4.47	4.65	0.26	0.68	0.65	0.67	0.03	0.74	0.82	0.78	0.05
ES03/19-SG-N1-29-95-118			-34.3	GFCHS000T	0.39												
ES03/19-SG-N1-31-37-62	IV		-36.6	GFCHS000V	0.43												
ES03/19-SG-N1-34-17-36			-40.0	GFCHS000W	0.37	4.28	4.19	4.24	0.06	0.72	0.71	0.71	0.01	0.78	0.85	0.82	0.05
ES03/19-SG-N1-36-0-20			-42.3	GFCHS000Y	0.41												
ES03/19-SG-N1-38-59-80			-45.8	GFCHS000Z	0.46												
ES03/19-SG-N1-40-0-24			-48.2	GFCHS0010	0.35												

Supplementary Table S2-5 continued.

Sample	Zone		Depth [m]	IGSN	$Fe(III)/Fe_{total}$	CBD											
						Fe				Si				Al			
						A [mg/g]	B [mg/g]	average [mg/g]	SE	A [mg/g]	B [mg/g]	average [mg/g]	SE	A [mg/g]	B [mg/g]	average [mg/g]	SE
ES03/19-SG-N1-42-0-22	IV	saprock	-50.7	GFCHS0011	0.39												
ES03/19-SG-N1-43-66-90			-52.9	GFCHS0012	na	12.68	5.21	8.94	5.28	0.55	0.55	0.55	0.00	0.74	0.76	0.75	0.01
ES03/19-SG-N1-44-40-62			-54.1	GFCHS0013	0.36												
ES03/19-SG-N1-46-21-41			-56.9	GFCHS0014	0.34												
ES03/19-SG-N1-48-31-51			-60.0	GFCHS0015	0.40	4.48	4.21	4.35	0.19	0.66	0.66	0.66	0.00	0.78	0.74	0.76	0.03
ES03/19-SG-N1-50-0-22			-62.4	GFCHS0016	0.39												
ES03/19-SG-N1-52-57-77			-65.8	GFCHS0017	0.35												
ES03/19-SG-N1-54-17-34			-68.4	GFCHS0019	na	6.84	7.05	6.94	0.15	1.36	1.14	1.25	0.15	1.30	1.06	1.18	0.17
ES03/19-SG-N1-55-32-50	V		-70.0	GFCHS001A	0.42												
ES03/19-SG-N1-57-13-36			-71.4	GFCHS001C	0.48												
ES03/19-SG-N1-59-6-25			-74.4	GFCHS001E	0.50	6.50	6.22	6.36	0.20	1.33	0.98	1.16	0.25	1.49	0.92	1.21	0.40
ES03/19-SG-N1-60-70-90			-76.5	GFCHS001F	0.42	6.35	6.15	6.25	0.14	0.65	0.67	0.66	0.02	0.77	0.78	0.77	0.01
ES03/19-SG-N1-62-50-70	VI	bedrock	-79.3	GFCHS001H	0.37	3.63	3.56	3.59	0.05	0.77	0.73	0.75	0.03	0.91	0.89	0.90	0.02
ES03/19-SG-N1-64-96-120			-82.8	GFCHS001J	0.32												
ES03/19-SG-N1-66-95-115			-85.8	GFCHS001L	0.39	4.06	3.31	3.68	0.53	1.60	1.50	1.55	0.07	0.52	0.51	0.52	0.01
ES03/19-SG-N1-67-45-65			-86.8	GFCHS001M	0.40												
average bedrock					0.4												
standard deviation bedrock					0.03												
Reference Materials:					mean	2SD											
GA granite					0.40	± 0.02											
GA granite (Schuessler et al., 2008)					0.39	± 0.01											
AC-E granite					0.51	± 0.05											
AC-E granite (Schuessler et al., 2008)					0.53	± 0.01											

Supplementary Table S2-6. Elemental composition derived by OES measurements (LOI uncorrected) and reference materials. Light blue highlighted lines denote bedrock composition. Please note that the measured certified reference materials are given in the published supplement.

Major elements (as oxides)					ICP-OES											
Sample	Zone		Depth [m]	IGSN	CO_2 [wt%]	SiO_2 [wt%]	Al_2O_3 [wt%]	Fe_2O_3(T) [wt%]	MnO [wt%]	MgO [wt%]	CaO [wt%]	Na_2O [wt%]	K_2O [wt%]	TiO_2 [wt%]	P_2O_5 [wt%]	LOI [wt%]
				detection limit	0.01	0.01	0.01	0.01	0.001	0.01	0.01	0.01	0.01	0.001	0.01	
ES03/19-SG-N1C-1-0-25	I	soil	-0.1	GFLVK00KB	0.18	56.47	17.41	7.3	0.142	2.69	5.07	3.53	2.42	0.754	0.23	4.21
ES03/19-SG-N1C-5-0-50	II	saprolite	-2.3	GFLVK00KH	0.09	55.88	17.11	7.73	0.164	3.23	5.06	3.73	2.78	0.744	0.3	3.89
ES03/19-SG-N1C-8-0-40			-3.8	GFLVK00KL	0.08	54.63	17.46	7.75	0.163	3.53	6.2	4.02	2.05	0.839	0.31	2.48
ES03/19-SG-N1-8-33-53			-6.8	GFCHS0002	0.1	58.12	17.41	6.86	0.141	3.02	5.77	3.77	2.82	0.721	0.25	1.41
ES03/19-SG-N1-11-0-21			-8.6	GFCHS0000	0.1	54.57	17.23	7.8	0.166	3.88	5.42	4.03	2.63	0.872	0.37	3.09
ES03/19-SG-N1-13-25-47	III	saprock	-11.8	GFCHS000C	0.36	56.99	17.53	6.71	0.132	3.14	5.41	3.56	3.07	0.741	0.26	3.01
ES03/19-SG-N1-16-50-70			-15.7	GFCHS000E	0.49	56.6	17.56	6.62	0.118	3.24	3.24	4.38	4.27	0.728	0.28	3.54
ES03/19-SG-N1-18-20-28			-18.1	GFCHS000G	0.82	55.09	16.61	7.17	0.151	3.35	6.26	3.34	2.85	0.764	0.26	4.78
ES03/19-SG-N1-20-16-37			-20.7	GFCHS000K	0.18	59.85	17	6.4	0.133	2.86	4.25	3.77	3.57	0.695	0.22	1.83
ES03/19-SG-N1-22-70-90			-24.1	GFCHS000N	0.28	57.84	17.11	6.95	0.139	3.04	4.71	4.08	3.58	0.729	0.25	2.2
ES03/19-SG-N1-23-130-145			-26.2	GFCHS000P	0.41	57.47	16.98	6.21	0.123	2.92	4.18	4.17	2.98	0.696	0.24	4.69
ES03/19-SG-N1-25-0-30			-28.0	GFCHS000Q	0.05	58.47	17.69	7.01	0.145	2.98	5.87	3.75	2.87	0.678	0.28	0.79
ES03/19-SG-N1-27-12-35			-30.4	GFCHS000S	0.1	59.39	17.36	6.79	0.132	2.82	5.57	3.58	3	0.728	0.25	0.97
ES03/19-SG-N1-29-95-118			-34.3	GFCHS000T	0.09	58.25	17.31	6.89	0.133	2.87	5.27	3.62	3.09	0.755	0.23	1.31
ES03/19-SG-N1-31-37-62	IV		-36.6	GFCHS000V	0.28	58.45	17.43	6.54	0.122	2.91	5.58	3.67	3.28	0.751	0.24	1.55
ES03/19-SG-N1-34-17-36			-40.0	GFCHS000W	0.06	59.26	17.62	6.81	0.132	2.79	5.52	3.77	2.81	0.717	0.24	1.06
ES03/19-SG-N1-36-0-20			-42.3	GFCHS000Y	0.14	56.94	17.11	6.68	0.148	3.21	5.52	3.72	2.87	0.71	0.23	2.39
ES03/19-SG-N1-38-59-80			-45.8	GFCHS000Z	0.62	56.73	16.6	6.69	0.134	3.18	4.57	4.34	3.79	0.707	0.25	3.28
ES03/19-SG-N1-40-0-24			-48.2	GFCHS0010	0.17	58.13	16.74	6.9	0.138	2.94	5.51	3.52	2.91	0.738	0.25	1.79

Supplementary Table 2-6 continued.

				ICP-OES											
Sample	Zone		Depth	IGSN	CO_2	SiO_2	Al_2O_3	Fe_2O_3(T)	MnO	MgO	CaO	Na_2O	K_2O	TiO_2	P_2O_5	LOI
			[m]		[wt%]	[wt%]	[wt%]	[wt%]	[wt%]	[wt%]	[wt%]	[wt%]	[wt%]	[wt%]	[wt%]	[wt%]
				detection limit	0.01	0.01	0.01	0.01	0.001	0.01	0.01	0.01	0.01	0.001	0.01	
ES03/19-SG-N1-42-0-22	IV	saprock	-50.7	GFCHS0011	0.10	58.19	17.43	7.01	0.135	2.94	5.66	3.58	2.88	0.738	0.25	1.01
ES03/19-SG-N1-44-40-62			-54.1	GFCHS0013	0.11	58.77	17.32	6.96	0.135	2.98	5.66	3.72	2.82	0.724	0.24	0.92
ES03/19-SG-N1-46-21-41			-56.9	GFCHS0014	0.12	58.86	17.6	6.69	0.136	2.95	5.32	3.91	2.81	0.72	0.28	1.23
ES03/19-SG-N1-48-31-51			-60.0	GFCHS0015	0.34	59.9	15.5	6.75	0.134	2.99	4.57	3.44	4.31	0.788	0.25	1.81
ES03/19-SG-N1-50-0-22			-62.4	GFCHS0016	0.11	60.57	17.04	6.23	0.117	2.65	5.06	3.62	3.31	0.676	0.22	1.1
ES03/19-SG-N1-52-57-77			-65.8	GFCHS0017	0.10	59.29	17.39	6.19	0.126	2.73	5.04	3.64	3.31	0.677	0.24	1.6
ES03/19-SG-N1-55-32-50	V		-70.0	GFCHS001A	0.31	60.66	16	5.91	0.115	2.44	3.79	3.97	4.21	0.604	0.2	2.45
ES03/19-SG-N1-57-13-36			-71.4	GFCHS001C	1.95	57.47	15.82	6.21	0.114	2.85	5.17	4.35	3.41	0.637	0.23	4.53
ES03/19-SG-N1-59-6-25			-74.4	GFCHS001E	0.85	60.91	16.09	5.07	0.1	2.44	3.28	4.48	4.02	0.558	0.19	3.68
ES03/19-SG-N1-60-70-90			-76.5	GFCHS001F	0.20	61.5	16.58	5.83	0.123	2.54	4.5	3.59	3.5	0.619	0.22	1.65
ES03/19-SG-N1-62-50-70	VI	bedrock	-79.3	GFCHS001H	0.67	58.06	16.67	6.72	0.139	2.94	5.77	3.5	3.1	0.722	0.25	2.54
ES03/19-SG-N1-64-96-120			-82.8	GFCHS001J	0.11	59.1	16.77	7.09	0.148	3.09	5.81	3.66	2.88	0.742	0.24	1.2
ES03/19-SG-N1-66-95-115			-85.8	GFCHS001L	0.09	59.6	17.38	6.6	0.129	2.74	5.63	3.63	3.01	0.71	0.26	0.93
ES03/19-SG-N1-67-45-65			-86.8	GFCHS001M	0.09	59.51	17.01	6.78	0.129	2.78	5.68	3.7	2.9	0.711	0.25	0.77

Supplementary Table S2-6 continued.

					ICP-MS										
Sample	Zone		Depth [m]	IGSN	Sc [ppm]	Be [ppm]	V [ppm]	Ba [ppm]	Sr [ppm]	Y [ppm]	Zr [ppm]	Cr [ppm]	Co [ppm]	Ni [ppm]	Cu [ppm]
				detection limit	1	1	5	2	2	1	2	20	1	20	10
ES03/19-SG-N1C-1-0-25	I	soil	-0.1	GFLVK00KB	18	2	158	747	480	26	251	20	18	< 20	80
ES03/19-SG-N1C-5-0-50	II	saprolite	-2.3	GFLVK00KH	18	2	157	866	454	25	236	20	17	< 20	60
ES03/19-SG-N1C-8-0-40			-3.8	GFLVK00KL	19	2	180	636	544	26	205	30	20	< 20	60
ES03/19-SG-N1-8-33-53			-6.8	GFCHS0002	17	2	155	824	516	22	212	30	18	< 20	40
ES03/19-SG-N1-11-0-21			-8.6	GFCHS0000	21	2	182	698	483	26	210	< 20	19	< 20	30
ES03/19-SG-N1-13-25-47	III	saprock	-11.8	GFCHS000C	16	1	155	1147	526	16	183	70	17	< 20	20
ES03/19-SG-N1-16-50-70			-15.7	GFCHS000E	16	2	158	653	360	22	207	< 20	17	< 20	20
ES03/19-SG-N1-18-20-28			-18.1	GFCHS000G	18	1	173	620	466	23	186	20	18	< 20	50
ES03/19-SG-N1-20-16-37			-20.7	GFCHS000K	15	1	147	1039	473	18	184	40	16	< 20	60
ES03/19-SG-N1-22-70-90			-24.1	GFCHS000N	17	1	167	820	469	24	246	20	18	< 20	20
ES03/19-SG-N1-23-130-145			-26.2	GFCHS000P	15	1	139	631	218	20	173	< 20	16	< 20	20
ES03/19-SG-N1-25-0-30			-28.0	GFCHS000Q	16	2	158	707	503	22	158	< 20	17	< 20	20
ES03/19-SG-N1-27-12-35			-30.4	GFCHS000S	16	1	155	781	479	21	194	20	17	< 20	60
ES03/19-SG-N1-29-95-118			-34.3	GFCHS000T	15	1	151	894	496	21	205	20	17	< 20	30
ES03/19-SG-N1-31-37-62	IV		-36.6	GFCHS000V	16	2	156	798	503	21	168	< 20	16	< 20	< 10
ES03/19-SG-N1-34-17-36			-40.0	GFCHS000W	16	1	150	789	527	21	174	20	16	< 20	40
ES03/19-SG-N1-36-0-20			-42.3	GFCHS000Y	18	2	152	692	434	21	163	50	17	< 20	40
ES03/19-SG-N1-38-59-80			-45.8	GFCHS000Z	16	1	154	712	314	20	167	< 20	16	< 20	50
ES03/19-SG-N1-40-0-24			-48.2	GFCHS0010	16	1	153	759	477	21	159	< 20	17	< 20	90

Supplementary Table S2-6 continued.

				ICP-MS										
Sample	Zone		Depth [m]	IGSN	Sc [ppm]	Be [ppm]	V [ppm]	Ba [ppm]	Sr [ppm]	Y [ppm]	Zr [ppm]	Cr [ppm]	Co [ppm]	Ni [ppm]	Cu [ppm]
				detection limit	1	1	5	2	2	1	2	20	1	20	10
ES03/19-SG-N1-42-0-22	IV	saprock	-50.7	GFCHS0011	16	1	154	740	509	21	160	30	17	< 20	60
ES03/19-SG-N1-44-40-62			-54.1	GFCHS0013	17	2	158	690	506	22	175	30	18	< 20	30
ES03/19-SG-N1-46-21-41			-56.9	GFCHS0014	16	2	157	724	515	22	174	20	17	< 20	30
ES03/19-SG-N1-48-31-51			-60.0	GFCHS0015	17	1	163	731	419	30	182	20	17	< 20	< 10
ES03/19-SG-N1-50-0-22			-62.4	GFCHS0016	14	2	141	700	468	20	173	< 20	16	< 20	< 10
ES03/19-SG-N1-52-57-77			-65.8	GFCHS0017	15	2	137	755	483	20	153	< 20	15	< 20	10
ES03/19-SG-N1-55-32-50	V		-70.0	GFCHS001A	13	1	126	835	350	19	159	< 20	13	< 20	< 10
ES03/19-SG-N1-57-13-36			-71.4	GFCHS001C	14	1	136	823	300	19	192	< 20	15	< 20	30
ES03/19-SG-N1-59-6-25			-74.4	GFCHS001E	11	1	110	775	171	15	160	< 20	12	< 20	20
ES03/19-SG-N1-60-70-90			-76.5	GFCHS001F	13	2	131	800	436	19	242	< 20	14	< 20	30
ES03/19-SG-N1-62-50-70	VI	bedrock	-79.3	GFCHS001H	15	1	152	819	471	20	166	20	17	< 20	80
ES03/19-SG-N1-64-96-120			-82.8	GFCHS001J	17	1	163	757	523	21	173	20	17	< 20	70
ES03/19-SG-N1-66-95-115			-85.8	GFCHS001L	15	2	149	788	512	22	149	20	16	< 20	80
ES03/19-SG-N1-67-45-65			-86.8	GFCHS001M	16	1	153	779	512	22	180	20	16	< 20	40

Supplementary Table S2-6 continued.

					ICP-MS										
Sample	Zone		Depth [m]	IGSN	Zn [ppm]	Ga [ppm]	Ge [ppm]	As [ppm]	Rb [ppm]	Nb [ppm]	Mo [ppm]	Ag [ppm]	In [ppm]	Sn [ppm]	Sb [ppm]
				detection limit	30	1	1	5	2	1	2	0.5	0.2	1	0.5
ES03/19-SG-N1C-1-0-25	I	soil	-0.1	GFLVK00KB	60	20	1	< 5	69	12	< 2	0.8	< 0.2	3	< 0.5
ES03/19-SG-N1C-5-0-50	II	saprolite	-2.3	GFLVK00KH	70	18	1	< 5	89	10	< 2	1.3	< 0.2	2	< 0.5
ES03/19-SG-N1C-8-0-40			-3.8	GFLVK00KL	70	20	2	< 5	76	12	< 2	2.3	< 0.2	2	< 0.5
ES03/19-SG-N1-8-33-53			-6.8	GFCHS0002	60	19	2	< 5	83	153	< 2	0.7	< 0.2	2	< 0.5
ES03/19-SG-N1-11-0-21			-8.6	GFCHS0000	60	19	2	< 5	93	14	< 2	0.8	< 0.2	1	< 0.5
ES03/19-SG-N1-13-25-47	III	saprock	-11.8	GFCHS000C	50	23	1	< 5	99	11	< 2	0.7	< 0.2	1	0.6
ES03/19-SG-N1-16-50-70			-15.7	GFCHS000E	70	18	2	< 5	125	46	< 2	0.8	< 0.2	1	0.6
ES03/19-SG-N1-18-20-28			-18.1	GFCHS000G	70	18	1	< 5	98	13	< 2	0.6	< 0.2	1	< 0.5
ES03/19-SG-N1-20-16-37			-20.7	GFCHS000K	60	18	1	< 5	106	10	< 2	0.7	< 0.2	1	< 0.5
ES03/19-SG-N1-22-70-90			-24.1	GFCHS000N	60	19	2	< 5	110	25	< 2	0.8	< 0.2	1	< 0.5
ES03/19-SG-N1-23-130-145			-26.2	GFCHS000P	60	18	1	< 5	87	11	< 2	0.6	< 0.2	1	< 0.5
ES03/19-SG-N1-25-0-30			-28.0	GFCHS000Q	60	19	2	< 5	87	10	8	0.6	< 0.2	1	< 0.5
ES03/19-SG-N1-27-12-35			-30.4	GFCHS000S	50	19	1	< 5	87	12	2	0.6	< 0.2	1	< 0.5
ES03/19-SG-N1-29-95-118			-34.3	GFCHS000T	50	19	1	< 5	97	13	< 2	0.7	< 0.2	1	< 0.5
ES03/19-SG-N1-31-37-62	IV		-36.6	GFCHS000V	40	18	1	< 5	94	12	< 2	0.5	< 0.2	1	< 0.5
ES03/19-SG-N1-34-17-36			-40.0	GFCHS000W	50	18	2	< 5	87	10	2	0.5	< 0.2	1	< 0.5
ES03/19-SG-N1-36-0-20			-42.3	GFCHS000Y	60	18	1	< 5	95	10	< 2	0.5	< 0.2	1	< 0.5
ES03/19-SG-N1-38-59-80			-45.8	GFCHS000Z	60	18	2	< 5	110	10	2	0.5	< 0.2	1	< 0.5
ES03/19-SG-N1-40-0-24			-48.2	GFCHS0010	70	19	1	< 5	93	12	2	0.6	< 0.2	1	< 0.5

Supplementary Table S2-6 continued.

					ICP-MS										
Sample	Zone		Depth [m]	IGSN	Zn [ppm]	Ga [ppm]	Ge [ppm]	As [ppm]	Rb [ppm]	Nb [ppm]	Mo [ppm]	Ag [ppm]	In [ppm]	Sn [ppm]	Sb [ppm]
				detection limit	30	1	1	5	2	1	2	0.5	0.2	1	0.5
ES03/19-SG-N1-42-0-22	IV	saprock	-50.7	GFCHS0011	60	19	2	< 5	84	11	2	0.6	< 0.2	< 1	< 0.5
ES03/19-SG-N1-44-40-62			-54.1	GFCHS0013	50	22	2	< 5	90	11	< 2	0.6	< 0.2	1	< 0.5
ES03/19-SG-N1-46-21-41			-56.9	GFCHS0014	50	19	1	< 5	96	10	< 2	0.6	< 0.2	1	< 0.5
ES03/19-SG-N1-48-31-51			-60.0	GFCHS0015	40	17	2	< 5	113	20	< 2	0.6	< 0.2	2	< 0.5
ES03/19-SG-N1-50-0-22			-62.4	GFCHS0016	50	18	2	< 5	96	11	< 2	0.6	< 0.2	1	< 0.5
ES03/19-SG-N1-52-57-77			-65.8	GFCHS0017	40	18	1	< 5	104	11	< 2	0.5	< 0.2	1	< 0.5
ES03/19-SG-N1-55-32-50	V		-70.0	GFCHS001A	40	16	1	< 5	116	11	< 2	0.5	< 0.2	1	< 0.5
ES03/19-SG-N1-57-13-36			-71.4	GFCHS001C	50	17	1	< 5	108	11	< 2	0.6	< 0.2	1	< 0.5
ES03/19-SG-N1-59-6-25			-74.4	GFCHS001E	60	17	1	< 5	114	10	< 2	0.5	< 0.2	1	< 0.5
ES03/19-SG-N1-60-70-90			-76.5	GFCHS001F	50	18	1	< 5	110	10	< 2	0.7	< 0.2	1	< 0.5
ES03/19-SG-N1-62-50-70	VI	bedrock	-79.3	GFCHS001H	70	18	1	< 5	98	12	3	0.6	< 0.2	1	< 0.5
ES03/19-SG-N1-64-96-120			-82.8	GFCHS001J	60	18	1	< 5	87	10	4	0.6	< 0.2	1	< 0.5
ES03/19-SG-N1-66-95-115			-85.8	GFCHS001L	60	18	1	< 5	89	12	2	0.6	< 0.2	1	< 0.5
ES03/19-SG-N1-67-45-65			-86.8	GFCHS001M	50	19	1	< 5	86	11	2	0.5	< 0.2	1	< 0.5

Supplementary Table S2-6 continued.

					ICP-MS										
Sample	Zone		Depth [m]	IGSN	Cs [ppm]	La [ppm]	Ce [ppm]	Pr [ppm]	Nd [ppm]	Sm [ppm]	Eu [ppm]	Gd [ppm]	Tb [ppm]	Dy [ppm]	Ho [ppm]
				detection limit	0.5	0.1	0.1	0.05	0.1	0.1	0.05	0.1	0.1	0.1	0.1
ES03/19-SG-N1C-1-0-25	I	soil	-0.1	GFLVK00KB	3.9	33.4	73.7	9.01	36.4	7.4	1.75	6.1	0.9	4.8	0.9
ES03/19-SG-N1C-5-0-50	II	saprolite	-2.3	GFLVK00KH	3.6	31.4	66.4	8.38	33.5	7.1	1.5	6	0.8	4.4	0.8
ES03/19-SG-N1C-8-0-40			-3.8	GFLVK00KL	3.7	35.2	75.4	9.59	37.9	7.9	1.75	6.6	0.9	4.9	0.9
ES03/19-SG-N1-8-33-53			-6.8	GFCHS0002	2.6	31.1	68.2	8.2	33	6.8	1.54	5.3	0.8	4.2	0.8
ES03/19-SG-N1-11-0-21			-8.6	GFCHS0000	4.1	30.1	67	8.54	35.7	7.3	1.72	6.1	0.9	4.8	0.9
ES03/19-SG-N1-13-25-47	III	saprock	-11.8	GFCHS000C	4.6	27.6	55.8	6.66	27.5	5.3	1.56	4.7	0.6	3.4	0.6
ES03/19-SG-N1-16-50-70			-15.7	GFCHS000E	3.6	30	63.5	7.81	31.9	6.9	1.56	5.6	0.8	4.3	0.8
ES03/19-SG-N1-18-20-28			-18.1	GFCHS000G	7.3	32.1	71	8.55	35.4	7	1.55	5.6	0.8	4.4	0.8
ES03/19-SG-N1-20-16-37			-20.7	GFCHS000K	4.5	25.4	53.6	6.72	27.5	5.9	1.44	4.6	0.7	3.6	0.7
ES03/19-SG-N1-22-70-90			-24.1	GFCHS000N	3.4	33	71.3	8.94	36	7.5	1.65	5.9	0.8	4.6	0.9
ES03/19-SG-N1-23-130-145			-26.2	GFCHS000P	5.4	30.8	65.1	7.77	31.1	6.4	1.43	5.1	0.7	3.8	0.7
ES03/19-SG-N1-25-0-30			-28.0	GFCHS000Q	2.3	33.1	69.7	8.41	34.1	6.7	1.62	5.5	0.8	4.4	0.8
ES03/19-SG-N1-27-12-35			-30.4	GFCHS000S	2.4	31	65.5	7.94	31.4	6.6	1.53	5.5	0.8	4.3	0.8
ES03/19-SG-N1-29-95-118			-34.3	GFCHS000T	2.6	30.5	64.4	7.71	31.4	6.3	1.52	5.1	0.7	3.9	0.8
ES03/19-SG-N1-31-37-62	IV		-36.6	GFCHS000V	2.6	31.9	68.2	8.23	32.3	6.7	1.53	5.2	0.8	4.3	0.8
ES03/19-SG-N1-34-17-36			-40.0	GFCHS000W	2.7	27.4	58.7	7.2	29.8	5.9	1.5	4.9	0.7	3.8	0.7
ES03/19-SG-N1-36-0-20			-42.3	GFCHS000Y	4.1	27.5	59.4	7.35	30.1	6.5	1.43	5.2	0.7	4	0.8
ES03/19-SG-N1-38-59-80			-45.8	GFCHS000Z	3.7	27.7	58.8	7.25	30.2	6.2	1.51	5.1	0.7	4.1	0.7
ES03/19-SG-N1-40-0-24			-48.2	GFCHS0010	4.5	31.4	64.7	7.77	31.2	6.2	1.6	5.3	0.7	4.2	0.8

Supplementary Table S2-6 continued.

				ICP-MS										
Sample	Zone	Depth [m]	IGSN	Cs [ppm]	La [ppm]	Ce [ppm]	Pr [ppm]	Nd [ppm]	Sm [ppm]	Eu [ppm]	Gd [ppm]	Tb [ppm]	Dy [ppm]	Ho [ppm]
			detection limit	0.5	0.1	0.1	0.05	0.1	0.1	0.05	0.1	0.1	0.1	0.1
ES03/19-SG-N1-42-0-22	IV	saprock	-50.7	GFCHS0011	3.6	30.2	63.3	7.69	30.9	6.4	1.58	5.4	0.8	4.2	0.8
ES03/19-SG-N1-44-40-62			-54.1	GFCHS0013	2.4	29.6	63	7.65	30.9	6.2	1.52	5.2	0.7	4	0.8
ES03/19-SG-N1-46-21-41			-56.9	GFCHS0014	3.1	32.4	67.2	8.15	33	6.7	1.57	5.3	0.8	4.2	0.8
ES03/19-SG-N1-48-31-51			-60.0	GFCHS0015	2.9	45.2	104	12.6	49.5	9.5	1.88	7.4	1.1	5.8	1.1
ES03/19-SG-N1-50-0-22			-62.4	GFCHS0016	2.8	29.3	59.4	7.16	29.1	5.9	1.38	4.9	0.7	3.8	0.7
ES03/19-SG-N1-52-57-77			-65.8	GFCHS0017	3.2	29.9	60.9	7.38	29.5	5.9	1.45	5	0.7	3.8	0.7
ES03/19-SG-N1-55-32-50	V		-70.0	GFCHS001A	4.2	29.4	61	7.16	28.4	5.7	1.28	4.8	0.6	3.6	0.7
ES03/19-SG-N1-57-13-36			-71.4	GFCHS001C	3.8	30.9	62.4	7.46	29.8	6.1	1.36	4.5	0.7	3.7	0.7
ES03/19-SG-N1-59-6-25			-74.4	GFCHS001E	4.4	27	54.4	6.39	24.6	4.7	1.3	3.9	0.6	3	0.6
ES03/19-SG-N1-60-70-90			-76.5	GFCHS001F	4.5	27	56.3	6.78	28.1	5.6	1.36	4.3	0.6	3.5	0.7
ES03/19-SG-N1-62-50-70	VI	bedrock	-79.3	GFCHS001H	5	28.8	62	7.61	30.9	6.3	1.6	5.1	0.8	4	0.8
ES03/19-SG-N1-64-96-120			-82.8	GFCHS001J	4.1	27.7	58.1	7.16	29	6.2	1.53	4.9	0.7	3.9	0.7
ES03/19-SG-N1-66-95-115			-85.8	GFCHS001L	3.8	31.3	65.5	7.96	31.4	6.7	1.49	5.2	0.7	4	0.8
ES03/19-SG-N1-67-45-65			-86.8	GFCHS001M	2.7	33.8	69.3	8.31	33.6	6.4	1.65	5.3	0.8	4.2	0.8

Supplementary Table S2-6 continued.

					ICP-MS											
Sample	Zone		Depth [m]	IGSN	Er [ppm]	Tm [ppm]	Yb [ppm]	Lu [ppm]	Hf [ppm]	Ta [ppm]	W [ppm]	Tl [ppm]	Pb [ppm]	Bi [ppm]	Th [ppm]	U [ppm]
				detection limit	0.1	0.05	0.1	0.01	0.2	0.1	1	0.1	5	0.4	0.1	0.1
ES03/19-SG-N1C-1-0-25	I	soil	-0.1	GFLVK00KB	2.7	0.41	2.7	0.45	7.1	1	< 1	0.3	7	< 0.4	15.1	3.2
ES03/19-SG-N1C-5-0-50	II	saprolite	-2.3	GFLVK00KH	2.5	0.38	2.6	0.4	6.5	0.8	1	0.4	< 5	< 0.4	8.7	2.4
ES03/19-SG-N1C-8-0-40			-3.8	GFLVK00KL	2.8	0.42	2.8	0.47	5.8	0.8	5	0.3	< 5	< 0.4	8.7	2.7
ES03/19-SG-N1-8-33-53			-6.8	GFCHS0002	2.3	0.34	2.3	0.36	5.9	1.4	< 1	0.3	6	< 0.4	15.2	3.5
ES03/19-SG-N1-11-0-21			-8.6	GFCHS0000	2.6	0.38	2.6	0.39	5.6	0.9	2	0.3	< 5	< 0.4	6.9	2.9
ES03/19-SG-N1-13-25-47	III	saprock	-11.8	GFCHS000C	1.8	0.25	1.7	0.28	5	0.6	4	0.3	5	< 0.4	9.7	3.5
ES03/19-SG-N1-16-50-70			-15.7	GFCHS000E	2.5	0.36	2.6	0.4	5.8	1	2	0.4	< 5	< 0.4	7.9	3.3
ES03/19-SG-N1-18-20-28			-18.1	GFCHS000G	2.5	0.34	2.6	0.39	5.4	0.8	< 1	0.4	< 5	< 0.4	7.5	2.6
ES03/19-SG-N1-20-16-37			-20.7	GFCHS000K	2	0.28	1.9	0.28	5.2	0.8	< 1	0.4	5	< 0.4	7	2.2
ES03/19-SG-N1-22-70-90			-24.1	GFCHS000N	2.6	0.39	2.8	0.45	7.2	1	< 1	0.4	< 5	< 0.4	11.7	3.8
ES03/19-SG-N1-23-130-145			-26.2	GFCHS000P	2.1	0.34	2.2	0.35	4.9	0.9	< 1	0.3	< 5	< 0.4	12.7	3.3
ES03/19-SG-N1-25-0-30			-28.0	GFCHS000Q	2.3	0.35	2.3	0.38	4.4	0.8	< 1	0.2	5	< 0.4	9.6	2.2
ES03/19-SG-N1-27-12-35			-30.4	GFCHS000S	2.2	0.32	2.3	0.36	5.7	0.9	< 1	0.3	6	< 0.4	11.1	2.3
ES03/19-SG-N1-29-95-118			-34.3	GFCHS000T	2.2	0.32	2.1	0.34	5.8	0.9	< 1	0.3	< 5	< 0.4	12.9	4
ES03/19-SG-N1-31-37-62	IV		-36.6	GFCHS000V	2.3	0.34	2.3	0.39	4.8	1.1	< 1	0.2	< 5	< 0.4	13.2	5.5
ES03/19-SG-N1-34-17-36			-40.0	GFCHS000W	2.1	0.31	2.1	0.33	5.2	0.8	< 1	0.3	6	< 0.4	10.4	3.1
ES03/19-SG-N1-36-0-20			-42.3	GFCHS000Y	2.2	0.35	2.3	0.38	5	0.8	< 1	0.3	< 5	< 0.4	11.6	3.8
ES03/19-SG-N1-38-59-80			-45.8	GFCHS000Z	2.2	0.33	2.2	0.36	4.9	0.9	1	0.4	< 5	< 0.4	12	5.1
ES03/19-SG-N1-40-0-24			-48.2	GFCHS0010	2.3	0.34	2.3	0.37	5.1	0.9	< 1	0.4	8	< 0.4	11.3	3.7

Supplementary Table S2-6 continued.

					ICP-MS										
Sample	Zone	Depth	IGSN	Er	Tm	Yb	Lu	Hf	Ta	W	Tl	Pb	Bi	Th	U
		[m]	ppm	[ppm]	[ppm]	[ppm]	[ppm]	[ppm]	[ppm]	[ppm]	[ppm]	[ppm]	[ppm]	[ppm]	[ppm]
			detection limit	0.1	0.05	0.1	0.01	0.2	0.1	1	0.1	5	0.4	0.1	0.1
				LOI corr.	LOI corr.	LOI corr.	LOI corr.	LOI corr.	LOI corr.	LOI corr.	LOI corr.	LOI corr.	LOI corr.	LOI corr.	LOI corr.
ES03/19-SG-N1-42-0-22	IV	saprock	-50.7	GFCHS0011	2.3	0.33	2.4	0.4	4.8	0.9	2	< 0.1	8	< 0.4	15	4.5
ES03/19-SG-N1-44-40-62			-54.1	GFCHS0013	2.3	0.32	2.2	0.36	5	0.8	2	0.2	5	< 0.4	12.9	4.3
ES03/19-SG-N1-46-21-41			-56.9	GFCHS0014	2.4	0.33	2.3	0.39	5.3	0.8	< 1	0.2	5	< 0.4	13.3	3.6
ES03/19-SG-N1-48-31-51			-60.0	GFCHS0015	3.4	0.51	3.5	0.55	5.9	2	< 1	0.3	< 5	< 0.4	15.8	8.7
ES03/19-SG-N1-50-0-22			-62.4	GFCHS0016	2.2	0.32	2.1	0.35	5.4	1	< 1	0.2	< 5	< 0.4	13.1	5.5
ES03/19-SG-N1-52-57-77			-65.8	GFCHS0017	2.1	0.31	2.2	0.33	4.7	1	< 1	0.3	6	< 0.4	12.6	6.3
ES03/19-SG-N1-55-32-50	V		-70.0	GFCHS001A	2	0.29	2.1	0.35	4.7	1	< 1	0.3	< 5	< 0.4	12.3	6.6
ES03/19-SG-N1-57-13-36			-71.4	GFCHS001C	2	0.31	2.2	0.32	5.5	0.9	1	0.3	< 5	< 0.4	13.8	4.7
ES03/19-SG-N1-59-6-25			-74.4	GFCHS001E	1.6	0.26	1.8	0.3	4.6	0.8	2	0.4	< 5	< 0.4	14.1	7.2
ES03/19-SG-N1-60-70-90			-76.5	GFCHS001F	2.1	0.3	2	0.34	7.2	0.8	< 1	0.3	6	< 0.4	16.7	6.4
ES03/19-SG-N1-62-50-70	VI	bedrock	-79.3	GFCHS001H	2.2	0.31	2.1	0.33	4.8	0.9	< 1	0.4	7	< 0.4	12.1	3.9
ES03/19-SG-N1-64-96-120			-82.8	GFCHS001J	2.2	0.31	2.2	0.34	5.1	0.8	< 1	0.3	7	< 0.4	9.7	3.1
ES03/19-SG-N1-66-95-115			-85.8	GFCHS001L	2.2	0.33	2.3	0.36	4.5	0.9	4	0.3	8	< 0.4	13.1	4.4
ES03/19-SG-N1-67-45-65			-86.8	GFCHS001M	2.3	0.33	2.3	0.37	5.5	0.8	< 1	0.3	7	< 0.4	13.3	3.5

Supplementary Table S2-7. *In situ* cosmogenic-derived 10Be denudation-, chemical weathering- and erosion rates.

Sample	Depth	IGSN	Density ρ (soil)†	m.a.s.l.	latitude	longitude	^{10}Be concentration
	[cm]		[g cm^{-3}]	[m]			[10^4 atoms g^{-1}]
ES03/19-SG-N1-Q1	12.00	GFLVK00CD	1.5	625	-29.759414	-71.160322	3.54E+05 ± 2.13E+04
ES03/19-SG-N1-Q2	13.00	GFLVK00CE	1.5	625	-29.759414	-71.160322	2.52E+05 ± 1.25E+04
ES03/19-SG-N2-Q	25.00	GFLVK00CF	1.5	627	-29.759822	-71.159853	2.95E+05 ± 1.31E+04
ES03/19-SG-N3-Q	13.00	GFLVK00CG	1.5	617	-29.758999	-71.161077	3.20E+05 ± 2.53E+04

	D			W			E
Sample	Total denudation rate	CDF (total)*	CDF (saprolite; -8.6 m)*	Chemical weathering rate (total)‡	Chemical weathering rate (saprolite)‡	Physical erosion rate#
	[t km^{-2} yr^{-1}]			[t km^{-2} yr^{-1}]	[t km^{-2} yr^{-1}]	[t km^{-2} yr^{-1}]
ES03/19-SG-N1-Q1	24.8 ± 1.5	0.335 ± 0.03	0.206 ± 0.02	8.30 ± 0.84	5.10 ± 0.52	16.50 ± 1.67
ES03/19-SG-N1-Q2	35.6 ± 1.8	0.335 ± 0.03	0.206 ± 0.02	11.92 ± 1.13	7.32 ± 0.69	23.68 ± 2.25
ES03/19-SG-N2-Q	30.3 ± 1.4	0.335 ± 0.03	0.206 ± 0.02	10.14 ± 0.93	6.23 ± 0.57	20.16 ± 1.86
ES03/19-SG-N3-Q	27.6 ± 2.3	0.335 ± 0.03	0.206 ± 0.02	9.24 ± 1.06	5.68 ± 0.65	18.36 ± 2.10
average ± standard deviation	29.6 ± 4.0			9.90 ± 1.33	6.08 ± 0.82	19.68 ± 2.65

† Average soil densities from Oeser et al. (2018)

*"Total" integrating CDF over entire core, determined in the shallowest sample, consisting of soil. "Saprolite" integrating from bedrock up to 8.6m depth.

‡ Weathering rates W = D * CDF. "Total" integrating over entire core. "Saprolite" integrating from bedrock up to 8.6m depth.

Physical erosion rates: E = D-W

Supplementary Table S2-8. Contamination control data derived from tracer particle analysis in drill fluid and rock samples. DL: detection limit.

Core run	Top depth [m]	Bottom depth [m]	IGSN	Particle concentration in drilling fluid [L^{-1}]	Sample	Depth [m]	IGSN	Particle concentration in rock sample [g^{-1}]	Drilling fluid infiltration [$\mu L\ g^{-1}$]
ES03/19-SG-N1-1	0	1.3	GFLVK009X	2.1E+11					
ES03/19-SG-N1-4	2.35	3.65	GFLVK00A3	1.4E+11					
ES03/19-SG-N1-5	3.65	5.15	GFLVK00A6	3.3E+11					
ES03/19-SG-N1-6	5.15	6.15	GFLVK00A1	3.8E+11					
ES03/19-SG-N1-8	6.35	7.45	GFLVK00A5	4.6E+11	ES03/19-SG-N1-8-33-53	-6.8	GFCHS0002	6.3E+04	0.14
ES03/19-SG-N1-9	7.45	8.15	GFLVK00A4	6.0E+11					
ES03/19-SG-N1-10	8.15	8.45	GFLVK00A2	5.3E+11					
ES03/19-SG-N1-11	8.45	9.95	GFLVK00AA	4.4E+11	ES03/19-SG-N1-11-0-21	-8.6	GFCHS0000	1.1E+04	0.03
ES03/19-SG-N1-12	9.95	11.45	GFLVK00AA	4.7E+11					
ES03/19-SG-N1-13	11.45	12.75	GFLVK00A9	2.4E+11	ES03/19-SG-N1-13-25-47	-11.8	GFCHS000C	1.3E+07	54.56
ES03/19-SG-N1-14	12.75	14.25	GFLVK00A8	2.5E+11					
ES03/19-SG-N1-15	14.25	15.05	GFLVK00A7	2.7E+11					
ES03/19-SG-N1-16	15.05	16.45	GFLVK00AE	1.8E+11					
ES03/19-SG-N1-17	16.45	17.9	GFLVK00AD	3.6E+12					
ES03/19-SG-N1-18	17.9	19.4	GFLVK00AC	2.1E+11	ES03/19-SG-N1-18-20-28	-18.1	GFCHS000G	5.1E+05	2.40
ES03/19-SG-N1-19	19.4	20.4	GFLVK00AF	1.9E+11					
ES03/19-SG-N1-20	20.4	21.8	GFLVK00AG	2.5E+11	ES03/19-SG-N1-20-16-37	-20.7	GFCHS000K	1.5E+04	0.06
					ES03/19-SG-N1-20-124-142	-21.7	GFCHS000L	1.0E+05	0.41
ES03/19-SG-N1-21	21.8	23.3	GFLVK00AH	5.6E+11	ES03/19-SG-N1-21-128-150	-23.2	GFCHS000M	1.6E+04	0.03
ES03/19-SG-N1-22	23.3	24.8	GFLVK00AJ	1.9E+11	ES03/19-SG-N1-22-70-90	-24.1	GFCHS000N	1.1E+04	0.06
ES03/19-SG-N1-23	24.8	26.3	GFLVK00AK	2.8E+11	ES03/19-SG-N1-23-130-145	-26.2	GFCHS000P	7.0E+04	0.25
ES03/19-SG-N1-24	26.3	27.8	GFLVK00AL	4.4E+11					
ES03/19-SG-N1-25	27.8	29.2	GFLVK00AM	na	ES03/19-SG-N1-25-0-30	-28.0	GFCHS000Q	2.2E+04	0.05

Supplementary Table S2-8 continued.

Core run	Top depth [m]	Bottom depth [m]	IGSN	Particle concentration in drilling fluid [L^{-1}]	Sample	Depth [m]	IGSN	Particle concentration in rock sample [g^{-1}]	Drilling fluid infiltration [$\mu L\ g^{-1}$]
ES03/19-SG-N1-26	29.2	30.2	GFLVK00AN	3.3E+11					
ES03/19-SG-N1-28	31.7	33.2	GFLVK00AP	2.5E+11					
ES03/19-SG-N1-29	33.2	34.7	GFLVK00AQ	3.0E+11	ES03/19-SG-N1-29-95-118	-34.3	GFCHS000T	1.6E+04	0.05
ES03/19-SG-N1-30	34.7	36.1	GFLVK00AR	1.5E+11	ES03/19-SG-N1-30-30-53	35.1	GFCHS000U	1.9E+04	0.13
ES03/19-SG-N1-31	36.1	37.7	GFLVK00AS	1.3E+11	ES03/19-SG-N1-31-37-62	-36.6	GFCHS000V	3.7E+03	0.03
ES03/19-SG-N1-32	37.7	38.3	GFLVK00AT	2.4E+11					
ES03/19-SG-N1-33	38.3	39.7	GFLVK00AU	1.1E+11					
ES03/19-SG-N1-34	39.7	41.2	GFLVK00AV	4.8E+11					
ES03/19-SG-N1-35	41.2	42.2	GFLVK00AW	2.6E+11					
ES03/19-SG-N1-36	42.2	43.7	GFLVK00AX	1.5E+11	ES03/19-SG-N1-36-0-20	-42.3	GFCHS000Y	1.6E+04	0.10
					ES03/19-SG-N1-36-113-133	-43.4	GFCHS000X	7.7E+05	5.12
ES03/19-SG-N1-37	43.7	45.1	GFLVK00AY	1.8E+11					
ES03/19-SG-N1-38	45.1	46.6	GFLVK00B0	2.2E+11	ES03/19-SG-N1-38-59-80	-45.8	GFCHS000Z	3.3E+04	0.15
ES03/19-SG-N1-39	46.6	48.1	GFLVK00AZ	1.1E+11					
ES03/19-SG-N1-40	48.1	49.6	GFLVK00BU	2.3E+11	ES03/19-SG-N1-40-0-24	-48.2	GFCHS0010	1.3E+04	0.05
ES03/19-SG-N1-41	49.6	50.6	GFLVK00B1	2.2E+11					
ES03/19-SG-N1-42	50.6	52.1	GFLVK00B2	3.2E+11	ES03/19-SG-N1-42-0-22	-50.7	GFCHS0011	2.4E+04	0.08
ES03/19-SG-N1-43	52.1	53.6	GFLVK00B3	2.6E+11	ES03/19-SG-N1-43-66-90	-52.9	GFCHS0012	3.9E+03	0.02
ES03/19-SG-N1-44	53.6	55.1	GFLVK00B4	2.7E+11	ES03/19-SG-N1-44-40-62	-54.1	GFCHS0013	< DL	< DL
ES03/19-SG-N1-45	55.1	56.6	GFLVK00BS	2.0E+11					
ES03/19-SG-N1-46	56.6	58.1	GFLVK00B5	2.1E+11	ES03/19-SG-N1-46-21-41	-56.9	GFCHS0014	1.2E+04	0.05
ES03/19-SG-N1-47	58.1	59.6	GFLVK00B6	1.9E+11					
ES03/19-SG-N1-48	59.6	61.1	GFLVK00BT	1.9E+11	ES03/19-SG-N1-48-31-51	-60.0	GFCHS0015	1.5E+04	0.08
ES03/19-SG-N1-49	61.1	62.3	GFLVK00BA	2.0E+11					

Supplementary Table S2-8 continued.

Core run	Top depth [m]	Bottom depth [m]	IGSN	Particle concentration in drilling fluid [L^{-1}]	Sample	Depth [m]	IGSN	Particle concentration in rock sample [g^{-1}]	Drilling fluid infiltration [$\mu L\ g^{-1}$]
ES03/19-SG-N1-50	62.3	63.6	GFLVK00B7	1.8E+11					
ES03/19-SG-N1-51	63.6	65.1	GFLVK00HH	2.6E+11					
ES03/19-SG-N1-52	65.1	66.6	GFLVK00B9	1.9E+11	ES03/19-SG-N1-52-57-77	-65.8	GFCHS0017	1.2E+04	0.06
					ES03/19-SG-N1-52-130-150	-66.5	GFCHS0018	7.2E+03	0.04
ES03/19-SG-N1-53	66.6	68.1	GFLVK00BB	1.3E+11					
ES03/19-SG-N1-55	69.6	69.7	GFLVK00BD	2.5E+11					
ES03/19-SG-N1-56	69.7	71.2	GFLVK00BE	2.6E+11	ES03/19-SG-N1-56-85-108	-70.7	GFCHS001B	6.9E+04	0.26
ES03/19-SG-N1-57	71.2	72.7	GFLVK00BF	3.2E+11	ES03/19-SG-N1-57-13-36	-71.4	GFCHS001C	1.1E+04	0.03
ES03/19-SG-N1-58	72.7	74.2	GFLVK00BG	2.3E+11					
ES03/19-SG-N1-59	74.2	75.7	GFLVK00BH	3.1E+11	ES03/19-SG-N1-59-6-25	-74.4	GFCHS001E	4.7E+04	0.15
ES03/19-SG-N1-60	75.7	77.2	GFLVK00BJ	3.3E+11					
ES03/19-SG-N1-61	77.2	78.7	GFLVK00BK	3.9E+11					
ES03/19-SG-N1-62	78.7	80.2	GFLVK00BL	2.5E+11					
ES03/19-SG-N1-63	80.2	81.7	GFLVK00BM	4.1E+11					
ES03/19-SG-N1-64	81.7	83.2	GFLVK00BN	1.9E+11	ES03/19-SG-N1-64-96-120	-82.8	GFCHS001J	1.5E+04	0.08
ES03/19-SG-N1-65	83.2	84.7	GFLVK00BP	1.8E+11	ES03/19-SG-N1-65-0-20	-83.3	GFCHS001K	1.6E+04	0.09
ES03/19-SG-N1-66	84.7	86.2	GFLVK00BQ	1.7E+11					
ES03/19-SG-N1-67	86.2	87.2	GFLVK00BR	1.9E+11					

6.2 Supplements Chapter 3

Long method description for *in situ* and meteoric ^{10}Be.

Table S3-1: Sampling site properties, *in situ* Beryllium-10 and calculated denudation, chemical weathering, and physical erosion rates.

Table S3-2: Bedrock ^{9}Be concentrations.

Table S3-3: Sampling site properties, meteoric Beryllium-10, stable Beryllium-9, and calculated denudation, chemical weathering, and physical erosion rates for surface samples.

Table S3-4: Sampling site properties, meteoric Beryllium-10, stable Beryllium-9, and calculated denudation, chemical weathering, and physical erosion rates for depth profiles.

Table S3-5: Meteoric ^{10}Be depositional flux derived from GCM models and calculated using (^{10}Be/^{9}Be) and *in situ* ^{10}Be-derived denudation rate. 1: Heikkilä and von Blanckenburg (2015);2: Graly et al. (2011).

Table S3-6: pH measurements in soil, core, and fracture samples (3 measurements per sample). SD: standard deviation.

Long method description – *In situ* and meteoric ^{10}Be

For *in situ* ^{10}Be analyses, we collected additional soil samples below the respective soil mixing zone that was previously identified in the soil pits. For each soil pit ca. 3 kg sample material was cleaned, dried, and sieved. For quartz isolation, we used the grain-size fraction 0.25 – 1 mm and conducted standard physical and chemical separation methods. For ^{10}Be measurements, each sample was spiked with ^{9}Be carrier for blank correction. After anion and cation column separation and alkaline precipitation of Be (von Blanckenburg et al., 2004), Be was oxidised and pressed into accelerator mass spectrometer (AMS) cathodes and measured at the AMS facility at the University of Cologne (Dewald et al., 2013). To determine denudation rates $D_{in\ situ}$, we used the CRONUS online exposure age calculator (Balco et al., 2008) using the time-dependent scaling scheme of Lal/Stone (St) (Lal, 1991; Stone, 2000) and a sea-level high latitude (SLHL) neutron spallation ^{10}Be production rate of 4.01 at g^{-1} yr^{-1} (Borchers et al., 2016). The denudation rate D_{insitu} (in g cm^{-2} yr^{-1}) can be calculated using equation 1 shown in a simplified form (Lal, 1991):

$$D_{in\ situ} = \left(\frac{P}{[^{10}Be]} - \lambda \right) \Lambda \qquad [1]$$

with the ^{10}Be nuclide concentration $[^{10}Be]$ (atoms $g_{(Quartz)}^{-1}$), the scaled ^{10}Be production rate P (atoms g_{qtz}^{-1} yr^{-1}), λ as the decay constant of ^{10}Be (5 x10^{-7} yr^{-1}). Λ includes the e-folding absorption length for neutrons and muons, respectively.

For meteoric ^{10}Be analyses, we used ~1 g of powdered sample material (processed as described in (Wittmann et al., 2012); oven-dried for 72h at 60 °C) for sequential chemical extraction (Wittmann et al., 2012). We treated each sample with 0.5 M hydrochloric acid to extract amorphous oxyhydroxides (am-ox) followed by 1 M hydroxylamine-hydrochloride to extract crystalline oxyhydroxides (x-ox). After these steps, we decomposed the sample residue (min) with a combination of hydrofluoric acid and aqua regia; for organic-rich samples we also used hydrogen peroxide. Following matrix decomposition, we split the am-ox and x-ox fractions for ^{10}Be and ^{9}Be measurements. We measured ^{9}Be in the distinct am-ox, x-ox, and min fractions by Inductively Coupled Plasma – Optical Emission Spectroscopy (ICP-OES) and combined the measured concentrations to the reactive phase (reac) afterwards. For ^{10}Be measurements, the splits were combined to reac and processed the same way as described for *in situ* ^{10}Be measurements. For blank correction, we used a pooled blank from all (^{10}Be/^{9}Be) measurements of 6.5 ± 5.7 x10^{-15} (n=11).

Supplementary Table S3-1. Sampling site properties, *in situ* Beryllium-10 and calculated denudation, chemical weathering, and physical erosion rates.

site	sample name	IGSN	latitude	longitude	altitude	sample depth	density	quartz mass	^{9}Be carrier mass	(^{10}Be/^{9}Be)	$[^{10}Be]_{quartz}$
					[m.a.s.l.]	[cm]	[g cm^{-3}]	[g]	[mg]	[x10^{-13} atoms atoms^{-1}]	[x10^{5} atoms g^{-1}]
arid (PdA)	ES11/19-PdA-S1-Q	GFLVK00QM	-26.30285	-70.45733	736	6	2.6	1.4	0.159	1.5 ± 0.1	11 ± 0.5
	ES11/19-PdA-S2-Q	GFLVK00QN	-26.30440	-70.45843	761	5	2.6	1.3	0.159	1.6 ± 0.1	13 ± 0.6
	ES11/19-PdA-S3-Q	GFLVK00QP	-26.30197	-70.45587	726	5	2.6	1.5	0.159	1.6 ± 0.1	11 ± 0.5
	average						2.6				12 ± 0.9
Semi-arid[a] (SG)	ES03/19-SG-N1-Q1	GFLVK00CD	-29.75941	-71.16032	625	12	2.6	14.5	0.159	4.9 ± 0.3	3.5 ± 0.2
	ES03/19-SG-N1-Q2	GFLVK00CE	-29.75941	-71.16032	625	13	2.6	14.4	0.159	3.4 ± 0.2	2.5 ± 0.1
	ES03/19-SG-N2-Q	GFLVK00CF	-29.75982	-71.15985	627	25	2.6	11.8	0.160	3.3 ± 0.1	3.0 ± 0.1
	ES03/19-SG-N3-Q	GFLVK00CG	-29.75900	-71.16108	617	13	2.6	13.0	0.159	4.0 ± 0.3	3.2 ± 0.3
	average						2.6				3.0 ± 0.4
mediterranean (LC)	ES02/20-LC-S1-Q	GFLVK00Q5	-33.02838	-71.04371	894	15	2.6	15.8	0.159	2.2 ± 0.1	1.4 ± 0.1
	ES02/20-LC-S2-Q	GFLVK00QB	-33.02859	-71.04127	928	15	2.6	15.6	0.159	1.2 ± 0.1	0.8 ± 0.04
	ES02/20-LC-S3-Q	GFLVK00QD	-33.02872	-71.04717	854	15	2.6	15.8	0.160	1.2 ± 0.1	0.8 ± 0.04
	average						2.6				1.0 ± 0.3
humid (NA)	ES02/20-NA-S1-Q	GFLVK00QL	-37.79371	-72.95065	1113	50	2.6	10.5	0.160	4.6 ± 0.2	4.6 ± 0.2
	ES02/20-NA-S3-Q	GFLVK00QJ	-37.79533	-72.94868	1120	50	2.6	10.5	0.159	2.6 ± 0.1	2.6 ± 0.1
	ES02/20-NA-S4-Q	GFLVK00QK	-37.79517	-72.95206	1084	55	2.6	10.7	0.159	2.5 ± 0.1	2.4 ± 0.1
	average						2.6				3.2 ± 1.0

Supplementary Table S3-1 continued

site	sample name	CDF	Total denudation rate	Chemical weathering rate	Physical erosion rate
		(SG[a])	[t km^{-2} yr^{-1}]	[t km^{-2} yr^{-1}]	[t km^{-2} yr^{-1}]
arid (PdA)	ES11/19-PdA-S1-Q	0.00	7.3 ± 0.3	0.0	7.3
	ES11/19-PdA-S2-Q	0.00	6.4 ± 0.3	0.0	6.4
	ES11/19-PdA-S3-Q	0.00	7.6 ± 0.4	0.0	7.6
	average	0.00	7.1 ± 0.5	0.0	7.1 ± 0.7
semi-arid[a] (SG)	ES03/19-SG-N1-Q1	0.33 ± 0.02	24.8 ± 1.5	8.3 ± 0.8	16.5 ± 1.7
	ES03/19-SG-N1-Q2	0.33 ± 0.02	35.6 ± 1.8	11.9 ± 1.1	23.7 ± 2.2
	ES03/19-SG-N2-Q	0.33 ± 0.02	30.3 ± 1.4	10.1 ± 0.9	20.2 ± 1.9
	ES03/19-SG-N3-Q	0.33 ± 0.02	27.6 ± 2.3	9.2 ± 1.1	18.4 ± 2.1
	average	0.33 ± 0.02	29.6 ± 4.0	9.9 ± 1.3	19.7 ± 3.1
mediterranean (LC)	ES02/20-LC-S1-Q	0.21 ± 0.05	81 ± 3	17.3 ± 3.7	63 ± 14
	ES02/20-LC-S2-Q	0.21 ± 0.05	150 ± 7	32.1 ± 6.9	118 ± 25
	ES02/20-LC-S3-Q	0.21 ± 0.05	147 ± 7	31.5 ± 6.7	116 ± 25
	average	0.21 ± 0.05	126 ± 32	26.9 ± 6.8	99 ± 31
humid (NA)	ES02/20-NA-S1-Q	0.50 ± 0.06	24 ± 1	12.1 ± 1.5	11.9 ± 1.5
	ES02/20-NA-S3-Q	0.53 ± 0.05	44 ± 2	23.6 ± 2.5	20.7 ± 2.2
	ES02/20-NA-S4-Q	0.56 ± 0.02	45 ± 2	25.6 ± 0.8	19.8 ± 0.6
	average	0.53 ± 0.02	38 ± 10	20.4 ± 6.0	17.5 ± 4.8

Supplementary Table S3-2. Bedrock ^{9}Be concentrations.

study site	sample name	IGSN	depth	9Be	9Be
			[m]	[µg g^{-1}]	[x10^{16} atoms g^{-1}]
arid (PdA)	ES11/19-PdA-N1-11-WS9-GC9	GFNAS0068	12.6	1.76 ± 0.09	11.8 ± 0.6
	ES11/19-PdA-N1-19-WS14-GC14	GFNAS0069	20.9	1.55 ± 0.08	10.4 ± 0.5
	ES11/19-PdA-N1-28-WS19-GC19	GFNAS006A	31.0	1.75 ± 0.09	11.7 ± 0.6
	ES11/19-PdA-N1-36-WS22-GC22	GFNAS006B	39.3	1.56 ± 0.08	10.4 ± 0.5
	ES11/19-PdA-N1-42-WS24-GC24	GFNAS006C	49.8	2.96 ± 0.15	19.8 ± 1.0
	average			**1.92**	**12.8**
	standard deviation			**0.53**	**3.5**
semi-arid (SG)	ES03/19-SG-N1-31-37-62	GFCHS000V	36.6	1.18 ± 0.06	7.9 ± 0.4
	ES03/19-SG-N1-34-17-36	GFCHS000W	40.8	1.14 ± 0.06	7.6 ± 0.4
	ES03/19-SG-N1-42-0-20	GFCHS0011	50.7	1.10 ± 0.06	7.4 ± 0.4
	ES03/19-SG-N1-44-40-62	GFCHS0013	54.1	1.17 ± 0.06	7.8 ± 0.4
	ES03/19-SG-N1-46-21-41	GFCHS0014	56.9	1.21 ± 0.06	8.1 ± 0.4
	ES03/19-SG-N1-50-0-22	GFCHS0016	62.4	1.27 ± 0.06	8.5 ± 0.4
	ES03/19-SG-N1-62-50-70	GFCHS001H	79.3	1.19 ± 0.06	7.9 ± 0.4
	ES03/19-SG-N1-64-96-120	GFCHS001J	82.8	1.21 ± 0.06	8.1 ± 0.4
	ES03/19-SG-N1-66-95-115	GFCHS001L	85.8	1.20 ± 0.06	8.0 ± 0.4
	ES03/19-SG-N1-67-45-65	GFCHS001M	86.8	1.38 ± 0.07	9.3 ± 0.5
	average			**1.21**	**8.1**
	standard deviation			**0.07**	**0.5**
mediterranean (LC)	ES02/20-LC-N1-70-WS30-GC30	GFNAS0006	43.3	0.92 ± 0.05	6.2 ± 0.3
	ES02/20-LC-N1-73-WS48-GC48	GFNAS0001	47.7	0.94 ± 0.05	6.3 ± 0.3
	ES02/20-LC-N1-74-WS33-GC33	GFNAS000N	49.7	0.93 ± 0.05	6.2 ± 0.3
	ES02/20-LC-N1-76-WS34-GC34	GFNAS000L	51.9	0.92 ± 0.05	6.1 ± 0.3
	ES02/20-LC-N1-78-WS36-GC36	GFNAS000K	55.7	0.98 ± 0.05	6.6 ± 0.3
	ES02/20-LC-N1-80-WS37-GC37	GFNAS000J	57.9	0.95 ± 0.05	6.4 ± 0.3
	ES02/20-LC-N1-82-WS38-GC38	GFNAS000H	59.6	0.93 ± 0.05	6.2 ± 0.3
	ES02/20-LC-N1-84-WS39-GC39	GFNAS000G	63.5	1.02 ± 0.05	6.8 ± 0.3
	ES02/20-LC-N1-86-WS40-GC40	GFNAS000F	65.2	0.98 ± 0.05	6.5 ± 0.3
	ES02/20-LC-N1-88-WS41-GC41	GFNAS000E	69.1	0.91 ± 0.05	6.1 ± 0.3
	ES02/20-LC-N1-92-WS43-GC43	GFNAS000C	74.8	1.07 ± 0.05	7.1 ± 0.4
	ES02/20-LC-N1-95-WS44-GC44	GFNAS000B	77.8	1.00 ± 0.05	6.7 ± 0.3
	ES02/20-LC-N1-97-WS45-GC45	GFNAS000A	80.7	1.06 ± 0.05	7.1 ± 0.4
	ES02/20-LC-N1-102-WS47-GC47	GFNAS0008	88.1	0.99 ±0.05	6.6 ± 0.3
	average			**0.97**	**6.5**
	standard deviation			**0.05**	**0.3**

Supplementary Table S3-2 continued.

study site	sample name	IGSN	depth	9Be	9Be
			[m]	[µg g^{-1}]	[x10^{16} atoms g^{-1}]
humid (NA)	ES02/20-NA-N1-23-WS6-GC6	GFLVK010B	13.0	1.33 ± 0.07	8.9 ± 0.4
	ES02/20-NA-N1-24-WS7-GC7	GFLVK010C	14.1	1.23 ± 0.06	8.2 ± 0.4
	ES02/20-NA-N1-26-WS8-GC8	GFLVK010D	15.6	1.65 ± 0.08	11.0 ± 0.6
	ES02/20-NA-N1-29-WS9-GC10	GFLVK010E	20.1	2.11 ± 0.11	14.1 ± 0.7
	ES02/20-NA-N1-30-WS10-GC11	GFLVK010F	21.2	1.04 ± 0.05	7.0 ± 0.3
	ES02/20-NA-N1-32-WS11-GC12	GFLVK010G	23.5	1.36 ± 0.07	9.1 ± 0.5
	ES02/20-NA-N1-37-WS13-GC14	GFLVK010H	28.8	1.06 ± 0.05	7.1 ± 0.4
	ES02/20-NA-N1-40-WS16-GC19	GFLVK010J	32.4	1.12 ± 0.06	7.5 ± 0.4
	ES02/20-NA-N1-40-WS15-GC16	GFLVK010K	33.0	1.16 ± 0.06	7.7 ± 0.4
	ES02/20-NA-N1-44-WS18-GC21	GFLVK010L	38.2	2.11 ± 0.11	1.4 ± 0.7
	average			**1.42**	**9.5**
	standard deviation			**0.39**	**2.6**
	ES02/20-NA-N2-32-WS3-GC3	GFLVK010M	17.9	2.10 ± 0.10	14.0 ± 0.7
	ES02/20-NA-N2-32-WS4-GC4	GFLVK010N	18.1	2.07 ± 0.10	13.9 ± 0.7
	ES02/20-NA-N2-34-WS5-GC5	GFLVK010R	20.7	2.11 ± 0.11	14.1 ± 0.7
	ES02/20-NA-N2-43-WS11-GC12	GFLVK010P	33.4	2.27 ± 0.11	15.2 ± 0.8
	ES02/20-NA-N2-49-WS13-GC14	GFLVK010Q	42.4	2.17 ± 0.11	14.5 ± 0.7
	average			**2.14**	**14.3**
	standard deviation			**0.07**	**0.5**

Supplementary Table S3-3. Sampling site properties, meteoric Beryllium-10, stable Beryllium-9, and calculated denudation, chemical weathering, and physical erosion rates for surface samples.

site	sample name	IGSN	latitude	longitude	altitude	sample depth	sample interval	($^{10}Be/^{9}Be$)	$[^{10}Be]_{reac}$	Inventory $[^{10}Be]_{reac}$	$[^{9}Be]_{reac}$
					[m.a.s.l.]	[cm]	[cm]	[x10^{-9} atoms atoms^{-1}]	[x10^{7} atoms g^{-1}]	[x10^{9} atoms cm^{-2}]	[µg g^{-1}]
arid (PdA)	ES11/19-PdA-N1-1-WS1-GC1	GFNAS001P	-26.302717	-70.45735	732	-7.5	0-15	0.14 ± 0.03	1.2 ± 0.2	1.0 ± 0.1	1.26 ± 0.06
semi-arid (SG)	ES03/19-SG-S1-0-5	GFLVK00P2	-29.759037	-71.160226	618	-2.5	0-5	6.4 ±0.4	6.1 ± 0.2	2.4 ± 0.1	0.14 ± 0.01
medieterranean (LC)	ES02/20-LC-S1-0-5	GFFJH009C	-33.028375	-71.04371	894	-2.5	0-5	11.2 ± 1.1	8.1 ± 0.3	6.4 ± 0.2	0.11 ± 0.01
humid-ridge (NA1)	ES02/20-NA-S1-0-5	GFFJH00A4	-37.79371	-72.95065	1113	-2.5	0-5	18.9 ± 1.1	37.6 ± 1.2	59 ± 2	0.30 ± 0.01
humid-slope (NA2)	ES02/20-NA-S4-0-5	GFFJH00J6	-37.79517	-72.95206	1084	-2.5	0-5	18.8 ± 1.1	53.0 ± 1.7	159 ± 5	0.42 ± 0.02
humid average (NA)		-						18.8 ±1.1	45.3 ± 1.5	109 ± 3	0.36 ± 0.06

site	sample name	$[^{9}Be]_{min}$	^{9}Be (*f*reac+*f*diss)	$[^{9}Be]$parent	depositional flux ^{10}Be (model-derived)	Total denudation rate	Chemical weathering rate	Physical erosion rate
		[x10^{16} atoms g^{-1}]		[µg g^{-1}]	[x10^{6} atoms cm^{-2} yr^{-1}]	[t km^{-2} yr^{-1}]	[t km^{-2} yr^{-1}]	[t km^{-2} yr^{-1}]
arid (PdA)	ES11/19-PdA-N1-1-WS1-GC1	9.8 ± 0.5	0.46	1.9 ± 0.5	1.0 ± 0.2	1235 ± 460	0.00	1235
semi-arid (SG)	ES03/19-SG-S1-0-5	7.9 ± 0.4	0.11	1.21 ± 0.07	1.2 ± 0.007	210 ± 22	70 ± 12	140 ± 25
medieterranean (LC)	ES02/20-LC-S1-0-5	5.5 ± 0.3	0.12	0.97 ± 0.05	1.4 ± 0.3	169 ± 39	36 ± 16	133 ± 59
humid-ridge (NA1)	ES02/20-NA-S1-0-5	5.9 ± 0.3	0.25	1.4 ± 0.4	1.8 ± 0.4	40 ± 14	20.0 ± 9.5	19.7 ± 9.4
humid-slope (NA2)	ES02/20-NA-S4-0-5	7.6 ± 0.4	0.27	2.14 ± 0.07	1.8 ± 0.4	24 ± 5	13.4 ± 3.4	10.4 ± 2.6
humid average (NA)		6.8 ± 0.3	0.26	1.8 ± 0.4	1.8 ± 0.4	30 ± 8	15.9 ± 4.7	14.0 ± 4.1

Supplementary Table S3-4. Sampling site properties, meteoric Beryllium-10, stable Beryllium-9, and calculated denudation, chemical weathering, and physical erosion rates for depth profiles.

site	sample name	IGSN	sample type	sample depth	($^{10}Be/^{9}Be$)	$[^{10}Be]_{reac}$	$[^{9}Be]_{reac}$	$[^{9}Be]_{min}$	$[^{9}Be]_{parent}$
					[$x10^{-10}$]	[$x10^{7}$ atoms g^{-1}]	[$\mu g\ g^{-1}$]	[$\mu g\ g^{-1}$]	[$\mu g\ g^{-1}$]
arid (PdA)	ES11/19-PdA-N1-1-WS1-GC1	GFNAS001P	core	-0.075	1.4 ± 0.3	1.2 ± 0.2	1.26 ± 0.06	1.47 ± 0.07	1.9 ± 0.5
	ES11/19-PdA-N1-2-WS2-GC2	GFNAS0056	core	-0.54	0.8 ± 0.3	0.6 ± 0.2	1.14 ± 0.06	1.47 ± 0.07	1.9 ± 0.5
semi-arid (SG)	ES03/19-SG-S1-0-5	GFLVK00P2	soil	-0.025	63.9 ± 3.9	6.1 ± 0.2	0.14 ± 0.01	1.19 ± 0.06	1.21 ± 0.07
	ES03/19-SG-S1-5-10	GFLVK00P3	soil	-0.075	62.3 ± 3.8	5.9 ± 0.2	0.14 ± 0.01	1.20 ± 0.06	1.21 ± 0.07
	ES03/19-SG-S1-10-20	GFLVK00P4	soil	-0.15	55.7 ± 3.5	5.6 ± 0.2	0.15 ± 0.01	1.19 ± 0.06	1.21 ± 0.07
	ES03/19-SG-S1-20-40	GFLVK00P5	soil	-0.3	18.9 ± 1.8	1.5 ± 0.1	0.12 ± 0.01	1.22 ± 0.06	1.21 ± 0.07
	ES03/19-SG-S1-40-60	GFLVK00P6	soil	-0.5	6.5 ± 1.6	0.4 ± 0.1	0.10 ± 0.005	1.24 ± 0.06	1.21 ± 0.07
	ES03/19-SG-N1C-1-0-25	GFLVK00KB	core	-0.125	32.8 ± 5.2	3.8 ± 0.6	0.17 ± 0.01	1.34 ± 0.07	1.21 ± 0.07
	ES03/19-SG-N1C-1-25-50	GFLVK00KC	core	-0.375	15.2 ± 5.0	1.6 ± 0.5	0.16 ± 0.01	1.29 ± 0.06	1.21 ± 0.07
	ES03/19-SG-N1C-2-0-25	GFLVK00KD	core	-0.625	2.1 ± 3.0	0.4 ± 0.5	0.27 ± 0.01	1.31 ± 0.07	1.21 ± 0.07
	ES03/19-SG-N1C-2-25-50	GFLVK00KE	core	-0.875	3.8 ± 3.2	0.6 ± 0.5	0.25 ± 0.01	0.99 ± 0.05	1.21 ± 0.07
	ES03/19-SG-N1C-3-0-50	GFLVK00KF	core	-1.25	2.0 ± 4.6	0.2 ± 0.5	0.17 ± 0.01	1.41 ± 0.07	1.21 ± 0.07
	ES03/19-SG-N1C-5-0-50	GFLVK00KH	core	-2.25	0.7 ± 4.7	0.08 ± 0.53	0.17 ± 0.01	1.26 ± 0.06	1.21 ± 0.07
	ES03/19-SG-N1C-7-0-50	GFLVK00KK	core	-3.25	1.4 ± 10.0	0.07 ± 0.53	0.07 ± 0.004	1.59 ± 0.08	1.21 ± 0.07
	ES03/19-SG-N1C-10-0-30	GFLVK00KM	core	-4.55	2.7 ± 8.6	0.2 ± 0.5	0.09 ± 0.005	1.39 ± 0.07	1.21 ± 0.07
	ES03/19-SG-N1C-13-0-20	GFLVK00KP	core	-5.5	0.9 ± 7.1	0.07 ± 0.52	0.11 ± 0.01	1.37 ± 0.07	1.21 ± 0.07
	ES03/19-SG-N1C-15-50-54	GFLVK00XN	core	-7.1	na	na	0.20 ± 0.01	1.29 ± 0.06	1.21 ± 0.07

Supplementary Table S3-4 continued

site	sample name	IGSN	sample type	sample depth	(^{10}Be/^{9}Be) [x10^{-10}]	[^{10}Be]$_{reac}$ [x10^{7} atoms g^{-1}]	[^{9}Be]$_{reac}$ [µg g^{-1}]	[^{9}Be]$_{min}$ [µg g^{-1}]	[^{9}Be]$_{parent}$ [µg g^{-1}]
mediterranean (LC)	ES02/20-LC-S1-0-5	GFFJH009C	soil	-0.025	112 ± 7	8.1 ± 0.3	0.11 ± 0.01	0.83 ± 0.04	0.97 ± 0.05
	ES02/20-LC-S1-5-10	GFFJH009B	soil	-0.075	110 ± 7	8.2 ± 0.3	0.11 ± 0.01	0.86 ± 0.04	0.97 ± 0.05
	ES02/20-LC-S1-10-20	GFFJH009A	soil	-0.15	104 ± 7	8.7 ± 0.4	0.12 ± 0.01	0.87 ± 0.04	0.97 ± 0.05
	ES02/20-LC-S1-20-40	GFFJH0097	soil	-0.3	67 ± 5	6.7 ± 0.3	0.15 ± 0.01	0.84 ± 0.04	0.97 ± 0.05
	ES02/20-LC-S1-60-80	GFFJH0099	soil	-0.7	28.1 ± 2.7	2.9 ± 0.2	0.15 ± 0.01	0.85 ± 0.04	0.97 ± 0.05
	ES02/20-LC-S1-400-450	GFFJH009L	soil	-4.25	223 ± 8	0.06 ± 0.22	0.04 ± 0.002	0.97 ± 0.05	0.97 ± 0.05
	ES02/20-LC-S1-550-600	GFFJH009Q	soil	-5.75	3.1 ± 7.5	0.08 ± 0.20	0.04 ± 0.002	0.97 ± 0.05	0.97 ± 0.05
humid (NA)	ES02/20-NA-S1-0-5	GFFJH00A4	soil	-0.025	189 ± 11	38 ± 1	0.30 ± 0.01	0.89 ± 0.04	1.4 ± 0.4
	ES02/20-NA-S1-20-40	GFFJH00A2	soil	-0.3	169 ± 10	38 ± 1	0.34 ± 0.02	1.07 ± 0.05	1.4 ± 0.4
	ES02/20-NA-S1-60-80	GFFJH00A5	soil	-0.7	115 ± 7	28 ± 1	0.37 ± 0.02	0.85 ± 0.04	1.4 ± 0.4
	ES02/20-NA-S1-120-140	GFFJH00A9	soil	-1.3	66 ± 4	10.2 ± 0.3	0.23 ± 0.01	0.80 ± 0.04	1.4 ± 0.4
	ES02/20-NA-S1-180-200	GFFJH00A0	soil	-1.9	39 ± 2	4.7 ± 0.2	0.18 ± 0.01	0.98 ± 0.05	1.4 ± 0.4
	ES02/20-NA-S1-300-350	GFFJH009X	soil	-3.25	30 ± 4	3.1 ± 0.4	0.16 ± 0.01	0.99 ± 0.05	1.4 ± 0.4
	ES02/20-NA-S1-400-450	GFFJH009T	soil	-4.25	23.4 ± 3.0	3.7 ± 0.4	0.24 ± 0.01	1.08 ± 0.05	1.4 ± 0.4
	ES02/20-NA-S4-0-5	GFFJH00J6	soil	-0.025	188 ± 11	53 ± 2	0.42 ± 0.02	1.14 ± 0.06	2.14 ± 0.07
	ES02/20-NA-S4-20-40	GFFJH00L4	soil	-0.3	180 ± 11	51 ± 2	0.43 ± 0.02	1.36 ± 0.07	2.14 ± 0.07
	ES02/20-NA-S4-60-80	GFFJH00L6	soil	-0.7	134 ± 8	31 ± 1	0.35 ± 0.02	1.62 ± 0.08	2.14 ± 0.07
	ES02/20-NA-S4-120-140	GFFJH00L3	soil	-1.3	56 ± 4	19.7 ± 0.8	0.53 ± 0.03	1.73 ± 0.09	2.14 ± 0.07
	ES02/20-NA-S4-180-200	GFFJH00KX	soil	-1.9	49 ± 3	18.0 ± 0.7	0.55 ± 0.03	1.74 ± 0.09	2.14 ± 0.07
	ES02/20-NA-S4-300-350	GFFJH00KW	soil	-3.25	49 ± 3	15.3 ± 0.6	0.47 ± 0.02	1.76 ± 0.09	2.14 ± 0.07
	ES02/20-NA-S4-350-400	GFFJH00J8	soil	-3.75	39 ± 3	16.0 ± 0.7	0.62 ± 0.03	1.85 ± 0.09	2.14 ± 0.07

Supplementary Table S3-5. Meteoric ^{10}Be depositional flux derived from GCM models and calculated using ($^{10}Be/^{9}Be$) and *in situ* ^{10}Be-derived denudation rate. 1: (Graly et al., 2011);2: (Graly et al., 2011).

site	GCM-model flux[1]	Precipitation-derived flux[2]	($^{10}Be/^{9}Be$)-derived flux
	[atoms cm^{-2} yr^{-1}]	[atoms cm^{-2} yr^{-1}]	[atoms cm^{-2} yr^{-1}]
arid (PdA)	10.0 ± 1.6	0.15 ± 0.03	0.06 ± 0.02
semi-arid (SG)	11.7 ± 0.07	16.5 ± 0.3	1.6 ± 0.3
mediterranean (LC)	14.2 ± 3.0	10.0 ± 2.0	10.6 ± 2.9
humid-ridge (NA1)	18.1 ± 3.6	29.7 ± 5.9	10.8 ± 3.1
humid-alope (NA2)	18.1 ± 3.6	29.7 ± 5.9	33.0 ± 3.1
humid average (NA)	18.1 ± 3.6	29.7 ± 5.9	22.3 ± 6.7

Supplementary Table S3-6. pH measurements in soil, core, and fracture samples (3 measurements per sample). SD: standard deviation.

study site	sample name	sample type	IGSN	depth	1. pH	2. pH	3. pH	mean pH	2SD
arid (PdA)	ES11/19-PdA-N1-1-WS1-GC1	core	GFNAS001P	-0.15	8.12	7.89	7.97	7.99	0.19
	ES11/19-PdA-N1-2-WS2-GC2	core	GFNAS0056	-0.54	8.29	8.08	7.95	8.11	0.28
	ES11/19-PdA-N1-17-WS13-GC13a	core	GFNAS0055	-19.15	8.19	7.99	7.90	8.03	0.24
	ES11/19-PdA-N1-21-WS15-GC15	core	GFNAS0054	-23.15	8.06	7.90	7.77	7.91	0.23
	ES11/19-PdA-N1-68-WS39-GC39	core	GFNAS0053	-86.30	8.10	7.89	7.82	7.94	0.24
	ES11/19-PdA-N1-9-0-10-bf	fracture	GFLVK00ZW	-9.25	8.12	7.99	7.90	8.00	0.19
	ES11/19-PdA-N1-34-75-85-B-bf	fracture	GFLVK00ZV	-37.50	8.13	8.01	7.84	7.99	0.23
	ES11/19-PdA-N1-45-78-88-A-bf	fracture	GFLVK0100	-53.63	8.09	7.90	7.77	7.92	0.26
	ES11/19-PdA-N1-74-0-25-B-bf	fracture	GFLVK00ZJ	-92.08	8.13	7.92	7.89	7.98	0.22
semi-arid (SG)	ES03/19-SG-S1-0-5	soil	GFLVK00P2	-0.03	7.57	7.52	7.59	7.56	0.06
	ES03/19-SG-S1-5-10	soil	GFLVK00P3	-0.08	7.52	7.44	7.51	7.49	0.07
	ES03/19-SG-S1-10-20	soil	GFLVK00P4	-0.15	7.57	7.52	7.59	7.56	0.06
	ES03/19-SG-S1-20-40	soil	GFLVK00P5	-0.30	7.50	7.42	7.50	7.47	0.07
	ES03/19-SG-S1-40-60	soil	GFLVK00P6	-0.50	7.76	7.66	7.74	7.72	0.08
	ES03/19-SG-S2-10-20	soil	GFLVK00QR	-0.15	7.91	7.91	7.92	7.91	0.01
	ES03/19-SG-S3-10-20	soil	GFLVK00R2	-0.15	7.77	7.81	7.75	7.78	0.04
	ES03/19-SG-N1C-1-0-25	core	GFLVK00KB	-0.13	7.51	7.50	7.55	7.52	0.05
	ES03/19-SG-N1C-1-25-50	core	GFLVK00KC	-0.38	7.48	7.38	7.47	7.44	0.09
	ES03/19-SG-N1C-2-0-25	core	GFLVK00KD	-0.63	7.69	7.61	7.69	7.66	0.08
	ES03/19-SG-N1C-2-25-50	core	GFLVK00KE	-0.88	7.61	7.56	7.61	7.59	0.05
	ES03/19-SG-N1C-3-0-50	core	GFLVK00KF	-1.25	7.70	7.69	7.75	7.71	0.05
	ES03/19-SG-N1C-5-0-50	core	GFLVK00KH	-2.25	7.53	7.73	7.74	7.67	0.19
	ES03/19-SG-N1C-7-0-50	core	GFLVK00KK	-3.25	7.97	8.02	8.04	8.01	0.05
	ES03/19-SG-N1C-10-0-30	core	GFLVK00KM	-4.55	8.35	8.21	8.18	8.25	0.15
	ES03/19-SG-N1C-13-0-30	core	GFLVK00KP	-5.50	8.68	8.52	8.48	8.56	0.17
	ES03/19-SG-N1C-15-50-54	core	GFLVK00XN	-7.10	8.40	8.32	8.27	8.33	0.10
	ES03/19-SG-N1-11-0-21	core	GFCHS0000	-8.56	7.78	7.83	7.81	7.81	0.04
	ES03/19-SG-N1-22-70-90	core	GFCHS000N	-24.10	8.41	8.43	8.38	8.41	0.04
	ES03/19-SG-N1-34-17-36	core	GFCHS000W	-39.97	8.35	8.33	8.10	8.26	0.22
	ES03/19-SG-N1-52-57-77	core	GFCHS0017	-65.77	8.18	8.21	8.16	8.18	0.04
	ES03/19-SG-N1-57-13-36	core	GFCHS001C	-71.45	8.01	7.86	7.84	7.90	0.15
	ES03/19-SG-N1-67-45-65	core	GFCHS001M	-86.75	8.33	8.33	8.30	8.32	0.03

Supplementary Table S3-6 continued.

study site	sample name	sample type	IGSN	depth	1. pH	2. pH	3. pH	mean pH	2SD
mediterranean (LC)	ES02/20-LC-S1-0-5	soil	GFFJH009C	-0.03	5.75	6.21	6.32	6.09	0.49
	ES02/20-LC-S1-5-10	soil	GFFJH009B	-0.08	5.85	6.03	6.30	6.06	0.37
	ES02/20-LC-S1-10-20	soil	GFFJH009A	-0.15	5.87	6.01	6.12	6.00	0.21
	ES02/20-LC-S1-20-40	soil	GFFJH0097	-0.30	6.08	6.18	6.24	6.16	0.13
	ES02/20-LC-S1-60-80	soil	GFFJH0099	-0.70	6.15	6.24	6.28	6.23	0.11
	ES02/20-LC-S1-400-450	soil	GFFJH009L	-4.25	7.28	7.43	7.37	7.36	0.12
	ES02/20-LC-S1-550-600	soil	GFFJH009Q	-5.75	7.06	7.34	7.37	7.26	0.28
	ES02/20-LC-N1-1-WS1-GC1	core	GFNAS001G	-0.20	6.01	6.14	6.20	6.12	0.17
	ES02/20-LC-N1-3-WS2-GC2	core	GFNAS001F	-1.00	6.31	6.43	6.52	6.42	0.17
	ES02/20-LC-N1-5-WS3-GC3	core	GFNAS001E	-1.95	7.00	7.15	7.18	7.11	0.16
	ES02/20-LC-N1-7-WS5-GC5	core	GFNAS001C	-2.93	7.08	7.30	7.30	7.23	0.21
	ES02/20-LC-N1-21-WS7-GC7	core	GFNAS001A	-9.90	7.00	7.14	7.22	7.12	0.18
	ES02/20-LC-N1-28-WS9-GC9	core	GFNAS0018	-13.45	7.32	7.24	7.50	7.35	0.22
	ES02/20-LC-N1-32-WS11-GC11	core	GFNAS0017	-15.43	7.23	7.26	7.37	7.29	0.12
	ES02/20-LC-N1-36-WS13-GC13	core	GFNAS0014	-17.40	7.18	7.18	7.08	7.15	0.09
	ES02/20-LC-N1-43-WS15-GC15	core	GFNAS0012	-20.93	7.35	7.37	7.29	7.33	0.07
	ES02/20-LC-N1-48-WS16-GC16	core	GFNAS0011	-23.43	7.36	7.39	7.31	7.35	0.07
	ES02/20-LC-N1-53-WS18-GC18	core	GFNAS000Z	-26.10	7.50	7.56	7.50	7.52	0.06
	ES02/20-LC-N1-55-WS20-GC20	core	GFNAS000X	-27.03	7.50	7.53	7.60	7.54	0.08
	ES02/20-LC-N1-57-WS21-GC21	core	GFNAS000W	-29.05	7.40	7.45	7.65	7.50	0.22
	ES02/20-LC-N1-59-WS24-GC24	core	GFNAS000V	-30.70	7.41	7.53	7.46	7.47	0.09
	ES02/20-LC-N1-68-WS29-GC29	core	GFNAS000Q	-42.20	7.53	7.66	7.63	7.61	0.12
	ES02/20-LC-N1-76-WS34-GC34	core	GFNAS000L	-51.90	8.40	8.31	8.27	8.33	0.11
	ES02/20-LC-N1-84-WS39-GC39	core	GFNAS000G	-63.50	8.52	8.30	8.29	8.37	0.21
	ES02/20-LC-N1-92-WS43-GC43	core	GFNAS000C	-74.80	8.40	8.28	8.19	8.29	0.17
	ES02/20-LC-N1-102-WS47-GC47	core	GFNAS0008	-88.10	8.30	8.21	8.22	8.24	0.08
	ES02/20-LC-N1-21-5-15-bf	fracture	GFLVK010S	-10.30	7.68	7.74	7.74	7.72	0.06
	ES02/20-LC-N1-48-3-11-bf	fracture	GFLVK010U	-23.07	7.87	7.88	7.85	7.86	0.03
	ES02/20-LC-N1-54-0-8-bf	fracture	GFLVK010V	-26.24	7.90	7.91	7.99	7.93	0.08
	ES02/20-LC-N1-66-108-128-bf	fracture	GFLVK010W	-39.28	7.66	7.76	7.81	7.74	0.12
	ES02/20-LC-N1-85-0-17-bf	fracture	GFLVK010X	-63.69	7.98	8.01	8.00	8.00	0.02

Supplementary Table S3-6 continued.

study site	sample name	sample type	IGSN	depth	1. pH	2. pH	3. pH	mean pH	2SD
humid (NA)	ES02/20-NA-S1-0-5	soil	GFFJH00A4	-0.03	5.24	5.39	5.82	5.48	0.49
	ES02/20-NA-S1-20-40	soil	GFFJH00A2	-0.30	5.28	5.39	5.50	5.39	0.18
	ES02/20-NA-S1-60-80-GCW	soil	GFFJH00A5	-0.70	4.94	5.02	5.10	5.02	0.13
	ES02/20-NA-S1-120-140-GCW	soil	GFFJH00A9	-1.30	4.79	4.90	5.03	4.91	0.20
	ES02/20-NA-S1-180-200-GCW	soil	GFFJH00A0	-1.90	4.66	4.79	4.92	4.79	0.21
	ES02/20-NA-S1-300-350-GCW	soil	GFFJH009X	-3.25	4.76	4.85	5.00	4.87	0.20
	ES02/20-NA-S1-400-450-GCW	soil	GFFJH009T	-4.75	4.80	4.91	5.03	4.92	0.19
	ES02/20-NA-N1-7-WS1-GC1	core	GFLVK010Y	-3.08	7.42	7.37	7.51	7.43	0.11
	ES02/20-NA-N1-14-WS3-GC3	core	GFLVK010Z	-6.51	7.43	7.50	7.48	7.47	0.06
	ES02/20-NA-N1-24-WS7-GC7	core	GFLVK010C	-14.13	8.38	8.23	8.05	8.22	0.27
	ES02/20-NA-N1-30-WS10-GC11	core	GFLVK010F	-21.23	7.99	7.98	8.01	7.99	0.03
	ES02/20-NA-N1-37-WS13-GC14	core	GFLVK010H	-28.82	8.26	8.09	7.95	8.10	0.25
	ES02/20-NA-N1-40-WS16-GC18	core	GFLVK0110	-32.26	7.49	7.43	7.63	7.52	0.16
	ES02/20-NA-N1-40-WS15-GC16	core	GFLVK010K	-33.03	8.12	8.06	8.03	8.07	0.08
	ES02/20-NA-S4-0-5	soil	GFFJH00J6	-0.03	4.81	4.89	5.11	4.94	0.25
	ES02/20-NA-S4-20-40	soil	GFFJH00L4	-0.30	4.95	5.00	5.13	5.02	0.15
	ES02/20-NA-S4-60-80	soil	GFFJH00L6	-0.70	4.91	4.91	4.96	4.92	0.05
	ES02/20-NA-S4-120-140	soil	GFFJH00L3	-1.30	4.89	4.91	5.01	4.94	0.10
	ES02/20-NA-S4-180-200	soil	GFFJH00KX	-1.90	4.84	4.88	4.98	4.90	0.12
	ES02/20-NA-S4-300-350	soil	GFFJH00KW	-3.25	5.16	5.24	5.33	5.24	0.14
	ES02/20-NA-S4-350-400	soil	GFFJH00J8	-3.75	5.02	5.09	5.18	5.10	0.13
	ES02/20-NA-N2-27-WS1-GC1	core	GFLVK0111	-13.47	7.45	7.51	7.55	7.50	0.08
	ES02/20-NA-N2-32-WS3-GC3	core	GFLVK010M	-17.93	7.95	7.99	7.99	7.98	0.04
	ES02/20-NA-N2-35-WS6-GC6	core	GFLVK0112	-21.87	7.95	7.79	7.68	7.81	0.22
	ES02/20-NA-N2-37-WS8-GC8	core	GFLVK0113	-25.24	8.06	7.97	7.96	7.99	0.09
	ES02/20-NA-N2-39-WS9-GC9	core	GFLVK0114	-27.80	7.65	7.67	7.65	7.66	0.01
	ES02/20-NA-N2-43-WS11-GC12	core	GFLVK010P	-33.38	8.16	8.03	8.11	8.10	0.11
	ES02/20-NA-N2-49-WS13-GC14	core	GFLVK010Q	-42.41	8.31	8.29	8.26	8.29	0.04
	ES02/20-NA-N1-8-10-30-bf	fracture	GFLVK0115	-3.65	6.46	6.59	6.62	6.56	0.14
	ES02/20-NA-N1-11-5-15-bf	fracture	GFLVK0116	-5.00	6.58	6.68	6.61	6.62	0.08
	ES02/20-NA-N1-17-39-50-bf	fracture	GFLLH006F	-8.70	7.37	7.38	7.43	7.39	0.05
	ES02/20-NA-N1-24-38-48-bf	fracture	GFLVK00YP	-13.68	7.80	7.80	7.87	7.82	0.06

Supplementary Table S3-6 continued.

study site	sample name	sample type	IGSN	depth	1. pH	2. pH	3. pH	mean pH	2SD
humid (NA)	ES02/20-NA-N1-30-30-37-A-bf	fracture	GFLVK0117	-20.84	8.07	8.00	8.06	8.04	0.06
	ES02/20-NA-N1-41-36-42-bf	fracture	GFLVK0118	-33.69	7.83	7.82	7.91	7.85	0.08
reference material IRMM-443-7	1				4.18				
	2				4.30				
	3				4.19				
	4				4.32				
	5				4.15				
	6				4.31				
	7				4.16				
	8				4.31				
	9				4.17				
	10				4.30				
	11				4.19				
	12				4.28				
	13				4.21				
	14				4.30				
	15				4.21				
	16				4.38				
	17				4.22				
	18				4.37				
	19				4.32				
	20				4.41				

6.3 Supplements Chapter 4

Table S4-1: Extractable major elements for all samples. The given concentrations are mathematically pooled to the extractable phase but here shown separately for each extraction step.

Table S4-2: Elemental mass loss indicated by the weathering indicator τ (tau). Negative values indicate depletion. The dissolved fraction was calculated using this mass loss; where τ indicates enrichment I used 0 to indicate no loss.

Table S4-3: Bulk bedrock elemental composition.

Table S4-4: Calculated fractions for the residual ($F_{residual}$), extractable (F_{ex}) and dissolved (F_{diss}) phase.

Supplementary Table S4-1. Extractable major elements for all samples.

Site	Sample	Type	Depth	0.5M HCl extractable						1M HxHCl extractable					
				Al	Ca	Fe	K	Mg	Na	Al	Ca	Fe	K	Mg	Na
			[m]	[µg g^{-1}]											
arid (PdA)	ES11/19-PdA-N1-1-WS1-GC1	core	0.15	1083	1234	2800	930	366	368	168	580	441	225	120	96
	ES11/19-PdA-N1-2-WS2-GC2	core	0.54	1000	6638	2103	688	245	343	147	350	489	168	97	83
	ES11/19-PdA-N1-17-WS13-GC13a	core	19.15	1324	7635	3627	701	293	542	297	849	850	251	138	82
	ES11/19-PdA-N1-21-WS15-GC15	core	23.15	1710	10403	3601	857	490	454	369	2865	1438	339	287	68
	ES11/19-PdA-N1-68-WS39-GC39	core	86.3	957	22574	3494	801	169	138	148	2920	1207	336	259	36
semi-arid (SG)	ES03/19-SG-S1-0-5	soil	0.025	5603	4703	7761	1432	2059	1001	278	4462	1092	249	327	211
	ES03/19-SG-S1-5-10	soil	0.05	5658	4149	8029	1048	2467	866	291	5160	1236	214	396	215
	ES03/19-SG-S1-10-20	soil	0.15	6770	4760	8702	1148	2788	1128	255	1127	1132	200	260	227
	ES03/19-SG-S1-20-40	soil	0.3	6519	8372	9419	817	3789	865	266	4234	1107	164	395	223
	ES03/19-SG-S1-40-60	soil	0.5	6533	5518	9023	792	3210	1230	209	1181	897	159	243	254
	ES03/19-SG-N1C-1-0-25	core	0.125	6375	3747	5645	1000	2795	707	866	833	3188	637	847	528
	ES03/19-SG-N1C-1-25-50	core	0.375	7620	5977	6721	555	3969	518	236	2524	1070	133	387	111
	ES03/19-SG-N1C-2-0-25	core	0.625	8319	6203	6357	553	3734	793	178	305	850	139	269	142
	ES03/19-SG-N1C-2-25-50	core	0.875	12538	9012	6553	554	3822	989	251	269	987	141	259	141
	ES03/19-SG-N1C-3-0-50	core	1.25	22888	17566	21154	2166	12071	2513	121	239	869	144	301	129
	ES03/19-SG-N1C-5-0-50	core	2.25	8213	6791	7405	732	4626	1110	133	350	2138	149	548	132
	ES03/19-SG-N1C-7-0-50	core	3.25	4295	4214	4317	701	2404	784	123	222	862	128	518	106
	ES03/19-SG-N1C-10-0-30	core	4.55	4869	8734	4571	1062	2989	779	139	210	836	159	593	102
	ES03/19-SG-N1C-13-0-30	core	5.5	9039	6319	7838	2982	3804	1524	159	363	837	243	473	199
	ES03/19-SG-N1C-15-50-54	core	7.1	11896	9211	3861	1998	2255	1039	161	247	1005	181	663	110
	ES03/19-SG-N1-11-0-21	core	8.555	4750	4695	4603	1408	3312	663	77	73	252	112	181	4

Supplementary Table S4-1 continued.

Site	Sample	Type	Depth	0.5M HCl extractable						1M HxHCl extractable					
				Al	Ca	Fe	K	Mg	Na	Al	Ca	Fe	K	Mg	Na
			[m]	[µg g^{-1}]											
semi-arid (SG)	ES03/19-SG-N1-22-70-90	core	24.1	5204	6163	4298	1737	2440	560	700	1588	1439	436	1020	138
	ES03/19-SG-N1-34-17-36	core	39.965	3578	3061	4451	2268	2472	469	98	275	576	48	493	3
	ES03/19-SG-N1-52-57-77	core	65.77	4059	5222	3885	1541	2015	492	758	665	1479	517	924	103
	ES03/19-SG-N1-57-13-36	core	71.445	4689	18709	2703	702	1796	248	74	61	212	83	139	3
	ES03/19-SG-N1-67-45-65	core	86.75	2434	2600	3482	1733	1848	232	933	2102	1118	251	944	55
mediterranean (LC)	ES02/20-LC-S1-0-5	soil	0.025	3239	3185	6571	1109	837	219	415	1056	1519	264	252	80
	ES02/20-LC-S1-5-10	soil	0.075	3792	3545	6493	1126	867	262	307	2669	1050	208	236	84
	ES02/20-LC-S1-10-20	soil	0.15	3698	3934	6666	1097	900	239	297	904	1064	207	178	78
	ES02/20-LC-S1-20-40	soil	0.3	4723	3706	6798	1249	1150	245	347	675	1191	230	209	79
	ES02/20-LC-S1-60-80	soil	0.7	4161	1908	5186	935	1293	189	368	1050	1117	197	268	72
	ES02/20-LC-S1-400-450	soil	4.25	2399	4894	4819	669	1096	311	156	685	828	169	263	101
	ES02/20-LC-S1-550-600	soil	5.75	2462	2305	4605	667	1071	302	152	678	821	174	283	100
	ES02/20-LC-N1-1-WS1-GC1	core	0.2	2702	1089	4486	767	802	173	229	56	975	149	145	40
	ES02/20-LC-N1-3-WS2-GC2	core	1	2415	1191	3944	631	738	197	264	611	983	129	153	65
	ES02/20-LC-N1-5-WS3-GC3	core	1.95	3495	2125	5112	702	1213	444	209	1951	721	145	246	112
	ES02/20-LC-N1-7-WS5-GC5	core	2.93	2806	2238	3609	746	1077	360	205	1443	695	143	212	111
	ES02/20-LC-N1-21-WS7-GC7	core	9.9	3654	2951	3190	500	1008	370	142	542	800	155	258	50
	ES02/20-LC-N1-28-WS9-GC9	core	13.45	2221	3880	3942	578	1204	297	117	341	729	150	271	98
	ES02/20-LC-N1-32-WS11-GC11	core	15.43	2167	2463	3651	558	1194	264	116	1770	757	147	336	94
	ES02/20-LC-N1-36-WS13-GC13	core	17.4	2241	2315	3133	499	1045	192	98	2330	736	143	370	43
	ES02/20-LC-N1-43-WS15-GC15	core	20.93	2282	4132	4236	449	1474	269	120	335	817	129	254	97
	ES02/20-LC-N1-48-WS16-GC16	core	23.43	2695	2622	5537	650	1550	321	100	365	622	112	211	94
	ES02/20-LC-N1-53-WS18-GC18	core	26.1	2365	2182	5233	717	1443	227	86	291	691	144	258	55

Supplementary Table S4-1 continued.

Site	Sample	Type	Depth	0.5M HCl extractable						1M HxHCl extractable					
				Al	Ca	Fe	K	Mg	Na	Al	Ca	Fe	K	Mg	Na
			[m]	[µg g^{-1}]											
mediterranean (LC)	ES02/20-LC-N1-55-WS20-GC20	core	27.03	2605	4544	5622	972	1691	293	112	282	753	151	272	103
	ES02/20-LC-N1-57-WS21-GC21	core	29.05	3179	4455	4293	901	1456	380	134	426	744	153	280	101
	ES02/20-LC-N1-59-WS24-GC24	core	30.7	2447	2041	5428	991	1561	202	101	2325	663	139	335	55
	ES02/20-LC-N1-68-WS29-GC29	core	42.2	4858	3305	6157	1776	2011	432	97	564	702	219	326	52
	ES02/20-LC-N1-76-WS-34-GC34	core	51.9	2566	2292	6767	2015	1918	260	640	1005	1749	558	867	77
	ES02/20-LC-N1-84-WS39-GC39	core	63.5	3186	1732	7974	2507	2276	285	106	2193	403	141	341	45
	ES02/20-LC-N1-92-WS43-GC43	core	74.8	3399	2370	8654	2375	2538	294	123	1995	524	124	391	45
	ES02/20-LC-N1-102-WS47-GC47	core	88.1	4131	3511	8188	2308	2379	367	113	3018	520	143	427	52
humid (NA)	ES02/20-NA-S1-0-5	soil	0.025	12112	2403	8700	516	892	54	1640	248	3499	91	364	25
	ES02/20-NA-S1-20-40	soil	0.3	15316	1088	11854	452	1101	59	1402	205	2636	68	254	26
	ES02/20-NA-S1-60-80-GCW	soil	0.7	11877	952	8422	371	1116	52	1046	840	2270	46	155	28
	ES02/20-NA-S1-120-140-GCW	soil	1.3	6050	2788	5187	604	960	40	545	1547	933	57	112	28
	ES02/20-NA-S1-180-200-GCW	soil	1.9	3734	3586	4288	664	745	44	402	839	581	74	95	28
	ES02/20-NA-S1-300-350-GCW	soil	3.25	2982	171	3674	693	564	47	344	202	570	77	90	29
	ES02/20-NA-S1-400-450-GCW	soil	4.25	2888	211	3856	768	532	50	359	81	659	93	93	30
	ES02/20-NA-N1-7-WS1-GC1	core	3.075	4223	3690	6258	2074	1076	302	235	3160	299	197	396	103
	ES02/20-NA-N1-14-WS3-GC3	core	6.505	3596	3939	7255	2509	1463	279	174	2491	435	207	306	94
	ES02/20-NA-N1-24-WS7-GC7	core	14.13	2701	2947	6036	2176	1178	257	141	2854	282	187	237	91
	ES02/20-NA-N1-30-WS10-GC11	core	21.23	5493	5465	11957	4389	2697	276	153	3760	696	342	446	95
	ES02/20-NA-N1-37-WS13-GC14	core	28.815	3105	1050	6818	2337	1335	294	150	3105	356	195	245	97
	ES02/20-NA-N1-40-WS16-GC18	core	32.26	1828	7110	4022	1374	1496	113	1224	3211	1691	425	595	55
	ES02/20-NA-N1-40-WS15-GC16	core	33.025	4652	4318	10291	3787	2317	309	150	3066	555	300	369	98
	ES02/20-NA-S4-0-5	soil	0.025	17120	1578	10958	503	997	75	1738	233	6048	127	564	41

Supplementary Table S4-1 continued.

Site	Sample	Type	Depth	0.5M HCl extractable						1M HxHCl extractable					
				Al	Ca	Fe	K	Mg	Na	Al	Ca	Fe	K	Mg	Na
			[m]	[µg g^{-1}]											
humid (NA)	ES02/20-NA-S4-20-40	soil	0.3	19435	1398	12247	414	1168	80	1579	209	5585	95	479	39
	ES02/20-NA-S4-60-80	soil	0.7	19606	899	13560	920	2306	79	1072	801	3106	77	316	37
	ES02/20-NA-S4-120-140	soil	1.3	16950	1646	12658	1900	3165	56	919	149	1082	86	382	24
	ES02/20-NA-S4-180-200	soil	1.9	13813	494	9970	1800	2496	49	869	173	620	90	294	23
	ES02/20-NA-S4-300-350	soil	3.25	14675	871	8675	1972	1486	94	772	2459	455	139	247	36
	ES02/20-NA-S4-350-400	soil	3.75	11694	499	7541	1668	1740	65	894	108	509	104	240	25
	ES02/20-NA-N2-27-WS1-GC1	core	13.47	5082	3179	10518	3878	2434	285	155	239	679	334	334	97
	ES02/20-NA-N2-32-WS3-GC3	core	17.93	4840	2681	10347	3904	2408	350	138	286	574	261	274	106
	ES02/20-NA-N2-35-WS6-GC6	core	21.87	6161	3537	12402	4578	2874	418	163	713	719	332	311	88
	ES02/20-NA-N2-37-WS8-GC8	core	25.24	5918	3677	11560	4565	2706	391	168	2483	703	413	384	189
	ES02/20-NA-N2-39-WS9-GC9	core	27.8	7734	5856	9491	3564	2417	460	246	1255	1047	450	417	101
	ES02/20-NA-N2-43-WS11-GC12	core	33.38	5322	3777	10270	3957	2505	405	153	2477	549	246	327	94
	ES02/20-NA-N2-49-WS13-GC14	core	42.41	5663	3619	12078	4926	2950	364	126	468	563	279	256	91

Supplementary Table S4-2. Elemental mass loss (τ) of major elements for all samples; na: not available. Negative values indicate depletion.

Site	Sample	Type	Depth	Elemental mass loss τ					
				Al	Ca	Fe	K	Mg	Na
			[m]						
arid (PdA)	ES11/19-PdA-N1-1-WS1-GC1	core	0.15	0.02	-0.66	-0.27	-0.01	-0.12	0.03
	ES11/19-PdA-N1-2-WS2-GC2	core	0.54	0.07	0.73	-0.25	0.06	-0.27	0.17
	ES11/19-PdA-N1-17-WS13-GC13a	core	19.15	0.05	0.81	0.31	0.01	0.54	-0.12
	ES11/19-PdA-N1-21-WS15-GC15	core	23.15	0.00	0.75	0.58	-0.01	0.99	-0.49
	ES11/19-PdA-N1-68-WS39-GC39	core	86.3	-0.22	4.55	0.30	-0.41	1.31	-0.97
semi-arid (SG)	ES03/19-SG-S1-0-5	soil	0.025	-0.12	-0.24	-0.09	-0.23	-0.24	-0.17
	ES03/19-SG-S1-5-10	soil	0.05	-0.17	-0.29	-0.13	-0.29	-0.27	-0.23
	ES03/19-SG-S1-10-20	soil	0.15	-0.10	-0.22	-0.08	-0.24	-0.23	-0.15
	ES03/19-SG-S1-20-40	soil	0.3	-0.16	-0.25	-0.15	-0.33	-0.26	-0.21
	ES03/19-SG-S1-40-60	soil	0.5	-0.05	-0.10	-0.10	-0.26	-0.21	-0.05
	ES03/19-SG-N1C-1-0-25	core	0.125	-0.32	-0.41	-0.29	-0.46	-0.38	-0.35
	ES03/19-SG-N1C-1-25-50	core	0.375	na	na	na	na	na	na
	ES03/19-SG-N1C-2-0-25	core	0.625	na	na	na	na	na	na
	ES03/19-SG-N1C-2-25-50	core	0.875	na	na	na	na	na	na
	ES03/19-SG-N1C-3-0-50	core	1.25	na	na	na	na	na	na
	ES03/19-SG-N1C-5-0-50	core	2.25	-0.29	-0.37	-0.20	-0.34	-0.21	-0.27
	ES03/19-SG-N1C-7-0-50	core	3.25	na	na	na	na	na	na
	ES03/19-SG-N1C-10-0-30	core	4.55	na	na	na	na	na	na
	ES03/19-SG-N1C-13-0-30	core	5.5	na	na	na	na	na	na
	ES03/19-SG-N1C-15-50-54	core	7.1	na	na	na	na	na	na
	ES03/19-SG-N1-11-0-21	core	8.555	-0.19	-0.25	-0.09	-0.30	0.07	-0.12
	ES03/19-SG-N1-22-70-90	core	24.1	-0.32	-0.44	-0.31	-0.18	-0.29	-0.24
	ES03/19-SG-N1-34-17-36	core	39.965	0.00	-0.07	-0.04	-0.09	-0.07	0.00
	ES03/19-SG-N1-52-57-77	core	65.77	0.12	-0.04	-0.01	0.22	0.03	0.10
	ES03/19-SG-N1-57-13-36	core	71.445	-0.19	-0.21	-0.21	0.00	-0.14	0.04
	ES03/19-SG-N1-67-45-65	core	86.75	-0.07	-0.08	-0.07	-0.10	-0.11	-0.05
mediterranean (LC)	ES02/20-LC-S1-0-5	soil	0.025	-0.19	-0.38	-0.02	-0.24	-0.32	-0.39
	ES02/20-LC-S1-5-10	soil	0.075	-0.19	-0.41	-0.03	-0.25	-0.32	-0.38
	ES02/20-LC-S1-10-20	soil	0.15	-0.15	-0.43	0.00	-0.21	-0.29	-0.39
	ES02/20-LC-S1-20-40	soil	0.3	-0.20	-0.53	-0.11	-0.27	-0.35	-0.49
	ES02/20-LC-S1-60-80	soil	0.7	-0.05	-0.42	-0.06	-0.22	-0.24	-0.38
	ES02/20-LC-S1-400-450	soil	4.25	-0.12	-0.20	-0.08	-0.21	-0.17	-0.18
	ES02/20-LC-S1-550-600	soil	5.75	-0.10	-0.17	-0.10	-0.26	-0.17	-0.17
	ES02/20-LC-N1-1-WS1-GC1	core	0.2	-0.16	-0.45	-0.10	-0.15	-0.36	-0.37
	ES02/20-LC-N1-3-WS2-GC2	core	1	-0.07	-0.42	-0.04	-0.02	-0.36	-0.29
	ES02/20-LC-N1-5-WS3-GC3	core	1.95	-0.13	-0.33	-0.14	-0.14	-0.31	-0.23

Supplementary Table S4-2 continued.

Site	sample	Type	Depth	Elemental mass loss τ					
				Al	Ca	Fe	K	Mg	Na
			[m]						
mediterranean (LC)	ES02/20-LC-N1-7-WS5-GC5	core	2.93	-0.08	-0.24	-0.09	-0.11	-0.24	-0.16
	ES02/20-LC-N1-21-WS7-GC7	core	9.9	-0.07	-0.20	-0.10	-0.10	-0.21	-0.18
	ES02/20-LC-N1-28-WS9-GC9	core	13.45	-0.10	-0.19	-0.13	-0.12	-0.20	-0.13
	ES02/20-LC-N1-32-WS11-GC11	core	15.43	-0.04	-0.11	-0.03	-0.12	-0.11	-0.09
	ES02/20-LC-N1-36-WS13-GC13	core	17.4	-0.09	-0.17	-0.13	-0.13	-0.21	-0.13
	ES02/20-LC-N1-43-WS15-GC15	core	20.93	-0.05	-0.15	-0.10	-0.04	-0.19	-0.09
	ES02/20-LC-N1-48-WS16-GC16	core	23.43	-0.11	-0.18	-0.12	-0.15	-0.20	-0.15
	ES02/20-LC-N1-53-WS18-GC18	core	26.1	-0.08	-0.12	-0.10	-0.14	-0.16	-0.11
	ES02/20-LC-N1-55-WS20-GC20	core	27.03	-0.12	-0.16	-0.12	-0.17	-0.17	-0.13
	ES02/20-LC-N1-57-WS21-GC21	core	29.05	-0.07	-0.13	-0.08	-0.12	-0.16	-0.10
	ES02/20-LC-N1-59-WS24-GC24	core	30.7	-0.15	-0.20	-0.14	-0.19	-0.21	-0.17
	ES02/20-LC-N1-68-WS29-GC29	core	42.2	-0.02	-0.06	0.00	-0.05	-0.05	-0.07
	ES02/20-LC-N1-76-WS-34-GC34	core	51.9	-0.12	-0.12	-0.10	-0.05	-0.09	-0.12
	ES02/20-LC-N1-84-WS39-GC39	core	63.5	-0.09	-0.11	-0.09	-0.04	-0.09	-0.09
	ES02/20-LC-N1-92-WS43-GC43	core	74.8	-0.03	-0.01	0.00	-0.08	-0.02	-0.03
	ES02/20-LC-N1-102-WS47-GC47	core	88.1	0.13	0.20	0.14	0.02	0.16	0.12
humid (NA)	ES02/20-NA-S1-0-5	soil	0.025	-0.37	-0.76	0.11	-0.67	-0.28	-0.89
	ES02/20-NA-S1-20-40	soil	0.3	-0.36	-0.83	0.15	-0.71	-0.31	-0.90
	ES02/20-NA-S1-60-80-GCW	soil	0.7	-0.27	-0.85	0.11	-0.62	-0.24	-0.91
	ES02/20-NA-S1-120-140-GCW	soil	1.3	-0.11	-0.90	-0.06	-0.16	-0.22	-0.89
	ES02/20-NA-S1-180-200-GCW	soil	1.9	-0.06	-0.92	-0.02	-0.16	-0.15	-0.91
	ES02/20-NA-S1-300-350-GCW	soil	3.25	-0.14	-0.91	-0.13	-0.18	-0.20	-0.91
	ES02/20-NA-S1-400-450-GCW	soil	4.25	-0.15	-0.90	-0.08	-0.15	-0.21	-0.88
	ES02/20-NA-N1-7-WS1-GC1	core	3.075	0.17	-0.09	0.04	0.36	-0.05	0.04
	ES02/20-NA-N1-14-WS3-GC3	core	6.505	-0.20	-0.13	0.00	-0.31	0.00	-0.20
	ES02/20-NA-N1-24-WS7-GC7	core	14.13	0.47	0.27	0.05	0.79	-0.03	0.41
	ES02/20-NA-N1-30-WS10-GC11	core	21.23	-0.01	0.16	0.47	-0.10	0.49	-0.14
	ES02/20-NA-N1-37-WS13-GC14	core	28.815	0.00	0.23	-0.03	-0.30	0.00	0.13
	ES02/20-NA-N1-40-WS16-GC18	core	32.26	0.01	-0.43	0.08	0.22	1.25	-0.68
	ES02/20-NA-N1-40-WS15-GC16	core	33.025	0.02	0.01	0.01	0.16	0.03	-0.03
	ES02/20-NA-S4-0-5	soil	0.025	-0.47	-0.55	0.29	-0.85	-0.02	-0.79
	ES02/20-NA-S4-20-40	soil	0.3	-0.45	-0.57	0.31	-0.86	0.01	-0.79
	ES02/20-NA-S4-60-80	soil	0.7	-0.35	-0.52	0.35	-0.82	0.37	-0.77
	ES02/20-NA-S4-120-140	soil	1.3	-0.35	-0.59	0.22	-0.80	0.53	-0.83
	ES02/20-NA-S4-180-200	soil	1.9	-0.29	-0.65	0.22	-0.73	0.51	-0.86
	ES02/20-NA-S4-300-350	soil	3.25	-0.21	-0.53	0.26	-0.52	0.52	-0.75
	ES02/20-NA-S4-350-400	soil	3.75	-0.28	-0.65	0.26	-0.71	0.52	-0.84
	ES02/20-NA-N2-27-WS1-GC1	core	13.47	0.02	-0.10	-0.05	-0.04	-0.14	0.04

Supplementary Table S4-2 continued.

Site	Sample	Type	Depth	Elemental mass loss τ					
				Al	Ca	Fe	K	Mg	Na
			[m]						
humid (NA)	ES02/20-NA-N2-32-WS3-GC3	core	17.93	-0.03	-0.01	0.01	-0.01	-0.02	-0.01
	ES02/20-NA-N2-35-WS6-GC6	core	21.87	0.03	-0.03	0.03	0.01	0.03	0.01
	ES02/20-NA-N2-37-WS8-GC8	core	25.24	0.03	-0.06	0.07	-0.01	0.11	0.01
	ES02/20-NA-N2-39-WS9-GC9	core	27.8	-0.02	-0.05	-0.01	0.02	0.00	-0.09
	ES02/20-NA-N2-43-WS11-GC12	core	33.38	0.12	0.28	0.07	0.06	0.12	0.10
	ES02/20-NA-N2-49-WS13-GC14	core	42.41	-0.02	0.01	-0.03	0.07	-0.05	0.00

Supplementary Table S4-3. Bulk bedrock composition for major elements. SD: standard deviation.

Site		Si	Al	Ca	Fe	K	Mg	Na	Ti	Mn	P
		[%]									
arid (PdA)	**average**	29.22	7.04	0.40	1.15	2.20	0.19	2.38	0.08	0.01	0.02
	SD	0.18	0.11	0.11	0.14	0.11	0.02	0.28	0.00	0.00	0.00
	rel. unc %	0.24	0.79	19.82	8.27	2.03	7.48	10.01	2.40	16.42	8.81
semi-arid (SG)	**average**	22.78	8.97	4.09	4.75	1.23	1.74	3.03	0.43	0.11	0.11
	SD	0.08	0.11	0.07	0.13	0.04	0.09	0.04	0.01	0.01	0.00
	rel. unc %	0.14	0.66	1.23	1.88	1.48	3.09	1.20	1.23	4.73	1.23
mediterranean (LC)	**average**	23.89	8.51	3.46	4.07	1.29	1.51	3.03	0.40	0.08	0.05
	SD	0.20	0.12	0.15	0.14	0.08	0.08	0.07	0.01	0.01	0.00
	rel. unc %	0.33	0.73	3.08	2.32	2.48	3.11	1.85	1.78	5.48	2.57
humid-ridge (granite)	**average**	27.84	7.52	1.80	1.84	1.82	0.39	2.30	0.18	0.03	0.04
	SD	0.23	0.18	0.10	0.10	0.09	0.03	0.10	0.01	0.00	0.00
	rel. unc %	0.32	1.24	4.01	3.98	2.03	4.46	3.53	4.19	8.67	4.77
humid-ridge (granodiorite)	**average**	24.63	8.75	3.15	4.33	1.07	1.00	2.91	0.46	0.06	0.10
	SD	1.26	0.32	0.36	1.05	0.14	0.25	0.12	0.16	0.01	0.04
	rel. unc %	1.98	1.93	8.23	17.01	5.50	15.18	3.43	20.57	13.85	16.30
humid-ridge average (NA)		26.23	8.13	2.47	3.08	1.45	0.69	2.60	0.32	0.05	0.07
humid-slope (granodiorite)	**average**	24.52	8.83	3.47	4.27	1.04	1.12	2.72	0.40	0.07	0.08
	SD	0.04	0.04	0.01	0.09	0.01	0.02	0.02	0.00	0.00	0.00
	rel. unc %	0.07	0.21	0.30	1.46	0.37	0.81	0.62	0.73	0.04	1.94
humid-slope (diorite)	**average**	22.57	9.25	4.07	5.74	1.04	1.63	2.70	0.60	0.10	0.11
	SD	0.37	0.33	0.20	0.38	0.09	0.20	0.07	0.09	0.00	0.01
	rel. unc %	0.63	1.91	3.55	4.57	3.60	7.22	2.14	9.31	2.73	5.44
humid-slope average (NA)		23.54	9.04	3.77	5.00	1.04	1.38	2.71	0.50	0.09	0.10

Supplementary Table S4-4. Calculated fractions for the residual ($F_{residual}$), extractable (F_{ex}) and dissolved (F_{diss}) phase. na: not available.

Site	Sample	Type	Depth	$F_{residual}$						F_{ex}						F_{diss}					
				Al	Ca	Fe	K	Mg	Na	Al	Ca	Fe	K	Mg	Na	Al	Ca	Fe	K	Mg	Na
			[m]	[%]																	
arid (PdA)	ES11/19-PdA-N1-1-WS1-GC1	core	0.15	98	0	45	94	63	98	2	45	28	5	26	2	0	66	27	1	12	0
	ES11/19-PdA-N1-2-WS2-GC2	core	0.54	98	0	52	96	55	98	2	100	23	4	18	2	0	0	25	0	27	0
	ES11/19-PdA-N1-17-WS13-GC13a	core	19.15	98	0	61	96	77	97	2	100	39	4	23	3	0	0	0	0	0	0
	ES11/19-PdA-N1-21-WS15-GC15	core	23.15	97	0	56	93	59	98	3	100	44	5	41	2	0	0	0	1	0	0
	ES11/19-PdA-N1-68-WS39-GC39	core	86.3	77	0	59	54	77	99	2	100	41	5	23	1	22	0	0	41	0	1
semi-arid (SG)	ES03/19-SG-S1-0-5	soil	0.025	81	54	73	64	64	79	7	22	19	14	14	4	12	23	8	22	23	17
	ES03/19-SG-S1-5-10	soil	0.05	76	49	67	62	58	74	7	23	19	10	16	4	17	28	13	28	26	23
	ES03/19-SG-S1-10-20	soil	0.15	83	63	71	66	60	80	8	14	21	11	17	4	10	22	8	24	22	15
	ES03/19-SG-S1-20-40	soil	0.3	76	44	63	60	51	75	8	31	22	8	24	4	16	25	15	32	25	21
	ES03/19-SG-S1-40-60	soil	0.5	87	73	69	67	60	90	8	16	21	8	20	5	5	10	10	25	20	5
	ES03/19-SG-N1C-1-0-25	core	0.125	60	48	53	42	43	60	8	11	19	13	21	4	32	41	28	44	36	36
	ES03/19-SG-N1C-1-25-50	core	0.375	91	79	84	94	75	98	9	21	16	6	25	2	na	na	na	na	na	na
	ES03/19-SG-N1C-2-0-25	core	0.625	91	84	85	94	77	97	9	16	15	6	23	3	na	na	na	na	na	na
	ES03/19-SG-N1C-2-25-50	core	0.875	86	77	84	94	77	96	14	23	16	6	23	4	na	na	na	na	na	na
	ES03/19-SG-N1C-3-0-50	core	1.25	74	56	54	81	29	91	26	44	46	19	71	9	na	na	na	na	na	na
	ES03/19-SG-N1C-5-0-50	core	2.25	62	46	61	60	50	68	9	17	20	7	30	4	29	37	19	33	20	28
	ES03/19-SG-N1C-7-0-50	core	3.25	95	89	89	93	83	97	5	11	11	7	17	3	na	na	na	na	na	na
	ES03/19-SG-N1C-10-0-30	core	4.55	94	78	89	90	79	97	6	22	11	10	21	3	na	na	na	na	na	na
	ES03/19-SG-N1C-13-0-30	core	5.5	90	84	82	74	75	94	10	16	18	26	25	6	na	na	na	na	na	na
	ES03/19-SG-N1C-15-50-54	core	7.1	87	77	90	82	83	96	13	23	10	18	17	4	na	na	na	na	na	na
	ES03/19-SG-N1-11-0-21	core	8.555	75	64	81	59	80	86	5	12	10	12	20	2	19	24	9	29	0	12
	ES03/19-SG-N1-22-70-90	core	24.1	62	38	58	65	53	74	7	19	12	18	20	2	31	44	30	18	27	24

Supplementary Table S4-4 continued.

Site	Sample	Type	Depth	$F_{residual}$						F_{ex}						F_{diss}					
				Al	Ca	Fe	K	Mg	Na	Al	Ca	Fe	K	Mg	Na	Al	Ca	Fe	K	Mg	Na
			[m]	[%]																	
semi-arid (SG)	ES03/19-SG-N1-34-17-36	core	39.965	96	85	86	72	76	98	4	8	11	19	17	2	0	7	4	9	7	0
	ES03/19-SG-N1-52-57-77	core	65.77	95	82	88	83	83	98	5	14	11	17	17	2	0	4	1	0	0	0
	ES03/19-SG-N1-57-13-36	core	71.445	76	33	74	93	75	99	5	46	6	6	11	1	19	21	20	0	14	0
	ES03/19-SG-N1-67-45-65	core	86.75	89	81	83	75	74	94	4	11	10	16	16	1	7	8	7	9	10	5
mediterranean (LC)	ES02/20-LC-S1-0-5	soil	0.025	76	48	79	66	59	59	4	12	20	11	7	1	20	40	2	23	34	40
	ES02/20-LC-S1-5-10	soil	0.075	76	38	79	66	59	60	5	18	19	10	7	1	19	44	2	24	34	39
	ES02/20-LC-S1-10-20	soil	0.15	80	41	81	70	62	59	5	14	19	10	7	1	15	45	0	20	31	40
	ES02/20-LC-S1-20-40	soil	0.3	74	31	70	63	54	49	6	13	20	11	9	1	20	56	10	26	37	50
	ES02/20-LC-S1-60-80	soil	0.7	89	47	79	70	64	61	5	9	15	9	10	1	6	44	5	21	26	39
	ES02/20-LC-S1-400-450	soil	4.25	85	63	79	73	72	80	3	16	14	7	9	1	12	21	7	21	19	18
	ES02/20-LC-S1-550-600	soil	5.75	87	73	78	69	73	82	3	9	13	7	9	1	10	18	8	25	18	17
	ES02/20-LC-N1-1-WS1-GC1	core	0.2	81	49	78	79	56	62	3	3	13	7	6	1	16	48	9	14	38	38
	ES02/20-LC-N1-3-WS2-GC2	core	1	89	50	84	93	56	70	3	5	12	6	6	1	8	44	3	2	38	29
	ES02/20-LC-N1-5-WS3-GC3	core	1.95	82	53	73	80	57	74	4	12	14	7	10	2	14	35	12	14	33	24
	ES02/20-LC-N1-7-WS5-GC5	core	2.93	88	64	81	83	66	82	4	11	11	7	9	2	8	25	8	10	25	16
	ES02/20-LC-N1-21-WS7-GC7	core	9.9	88	69	81	85	69	80	4	10	10	5	8	1	7	21	9	10	22	19
	ES02/20-LC-N1-28-WS9-GC9	core	13.45	87	68	77	83	69	86	3	12	11	6	10	1	10	20	11	11	21	13
	ES02/20-LC-N1-32-WS11-GC11	core	15.43	93	76	86	83	78	90	3	12	11	5	10	1	4	12	3	12	12	9
	ES02/20-LC-N1-36-WS13-GC13	core	17.4	88	69	79	82	69	86	3	13	10	5	9	1	9	18	12	13	22	13
	ES02/20-LC-N1-43-WS15-GC15	core	20.93	92	72	79	91	68	90	3	13	12	4	11	1	5	16	9	4	20	9
	ES02/20-LC-N1-48-WS16-GC16	core	23.43	85	72	74	79	67	84	3	9	15	6	12	1	11	19	10	15	21	15
	ES02/20-LC-N1-53-WS18-GC18	core	26.1	89	80	77	80	72	88	3	7	15	7	11	1	8	13	8	14	17	11
	ES02/20-LC-N1-55-WS20-GC20	core	27.03	84	69	74	75	69	85	3	14	16	9	13	1	13	17	10	17	18	14

Supplementary Table S4-4 continued.

Site	Sample	Type	Depth	$F_{residual}$						F_{ex}						F_{diss}					
				Al	Ca	Fe	K	Mg	Na	Al	Ca	Fe	K	Mg	Na	Al	Ca	Fe	K	Mg	Na
			[m]	[%]																	
mediterranean (LC)	ES02/20-LC-N1-57-WS21-GC21	core	29.05	89	72	81	80	72	88	4	14	12	8	11	2	8	14	7	12	17	11
	ES02/20-LC-N1-59-WS24-GC24	core	30.7	82	66	73	73	65	82	3	13	15	9	13	1	15	21	12	18	22	17
	ES02/20-LC-N1-68-WS29-GC29	core	42.2	92	83	83	80	79	91	6	11	17	15	15	2	2	6	0	5	5	7
	ES02/20-LC-N1-76-WS-34-GC34	core	51.9	84	77	70	75	72	86	4	10	21	20	18	1	12	13	9	5	10	13
	ES02/20-LC-N1-84-WS39-GC39	core	63.5	87	77	71	76	73	90	4	11	21	21	17	1	9	11	8	4	9	9
	ES02/20-LC-N1-92-WS43-GC43	core	74.8	93	86	77	73	79	96	4	13	23	19	19	1	3	1	0	7	2	3
	ES02/20-LC-N1-102-WS47-GC47	core	88.1	95	81	79	81	81	99	5	19	21	19	19	1	0	0	0	0	0	0
humid (NA)	ES02/20-NA-S1-0-5	soil	0.025	42	0	34	49	22	0	18	15	66	3	33	0	40	100	0	48	45	100
	ES02/20-NA-S1-20-40	soil	0.3	39	0	21	47	14	0	22	7	79	3	35	0	39	100	0	50	51	100
	ES02/20-NA-S1-60-80-GCW	soil	0.7	54	0	42	54	28	0	17	10	58	2	33	0	29	100	0	44	39	100
	ES02/20-NA-S1-120-140-GCW	soil	1.3	79	0	58	85	37	0	9	24	33	4	28	0	12	100	9	12	35	100
	ES02/20-NA-S1-180-200-GCW	soil	1.9	88	0	70	85	53	0	6	25	26	4	22	0	7	100	4	11	25	100
	ES02/20-NA-S1-300-350-GCW	soil	3.25	80	0	57	83	50	0	4	2	23	4	17	0	15	100	20	13	33	100
	ES02/20-NA-S1-400-450-GCW	soil	4.25	79	0	63	85	49	0	4	2	25	5	16	0	16	100	12	11	35	100
	ES02/20-NA-N1-7-WS1-GC1	core	3.075	94	50	64	88	54	98	6	38	36	12	38	2	0	12	0	0	8	0
	ES02/20-NA-N1-14-WS3-GC3	core	6.505	73	45	58	63	54	75	5	36	42	15	46	2	22	19	0	22	0	23
	ES02/20-NA-N1-24-WS7-GC7	core	14.13	96	68	66	87	59	98	4	32	34	13	37	2	0	0	0	0	4	0
	ES02/20-NA-N1-30-WS10-GC11	core	21.23	93	71	71	44	68	86	6	29	29	44	32	1	1	0	0	12	0	13
	ES02/20-NA-N1-37-WS13-GC14	core	28.815	95	77	57	65	59	98	4	23	39	14	41	2	0	0	4	21	0	0
	ES02/20-NA-N1-40-WS16-GC18	core	32.26	96	0	69	90	46	19	4	57	31	10	54	1	0	61	0	0	0	81
	ES02/20-NA-N1-40-WS15-GC16	core	33.025	95	77	75	62	73	96	5	23	25	38	27	1	0	0	0	0	0	3
	ES02/20-NA-S4-0-5	soil	0.025	34	42	70	6	89	19	20	4	30	6	10	0	46	54	0	88	2	81
	ES02/20-NA-S4-20-40	soil	0.3	33	41	69	7	90	18	23	4	31	5	10	0	44	55	0	89	0	81

Supplementary Table S4-4 continued.

Site	Sample	Type	Depth	$F_{residual}$						F_{ex}						F_{diss}					
				Al	Ca	Fe	K	Mg	Na	Al	Ca	Fe	K	Mg	Na	Al	Ca	Fe	K	Mg	Na
			[m]	[%]																	
humid (NA)	ES02/20-NA-S4-60-80	soil	0.7	43	45	71	6	84	21	22	4	29	10	16	0	34	51	0	84	0	79
	ES02/20-NA-S4-120-140	soil	1.3	47	38	76	0	78	15	19	4	24	19	22	0	34	57	0	81	0	85
	ES02/20-NA-S4-180-200	soil	1.9	55	36	82	6	83	12	16	2	18	18	17	0	29	63	0	76	0	88
	ES02/20-NA-S4-300-350	soil	3.25	61	30	79	26	85	23	17	10	21	20	15	0	21	60	0	54	0	76
	ES02/20-NA-S4-350-400	soil	3.75	59	35	86	9	88	13	14	1	14	17	12	0	27	63	0	74	0	86
	ES02/20-NA-N2-27-WS1-GC1	core	13.47	94	82	76	55	72	99	6	8	19	40	17	1	0	9	4	4	11	0
	ES02/20-NA-N2-32-WS3-GC3	core	17.93	91	90	74	59	74	97	6	9	26	40	24	2	3	1	0	2	2	1
	ES02/20-NA-N2-35-WS6-GC6	core	21.87	93	85	69	53	72	98	7	12	31	47	28	2	0	3	0	0	0	0
	ES02/20-NA-N2-37-WS8-GC8	core	25.24	93	79	79	52	81	98	7	15	21	48	19	2	0	5	0	1	0	0
	ES02/20-NA-N2-39-WS9-GC9	core	27.8	89	74	74	62	74	88	9	21	25	38	25	2	2	6	2	0	0	9
	ES02/20-NA-N2-43-WS11-GC12	core	33.38	94	85	81	60	83	98	6	15	19	40	17	2	0	0	0	0	0	0
	ES02/20-NA-N2-49-WS13-GC14	core	42.41	92	90	75	50	77	98	6	10	22	50	20	2	2	0	3	0	4	0